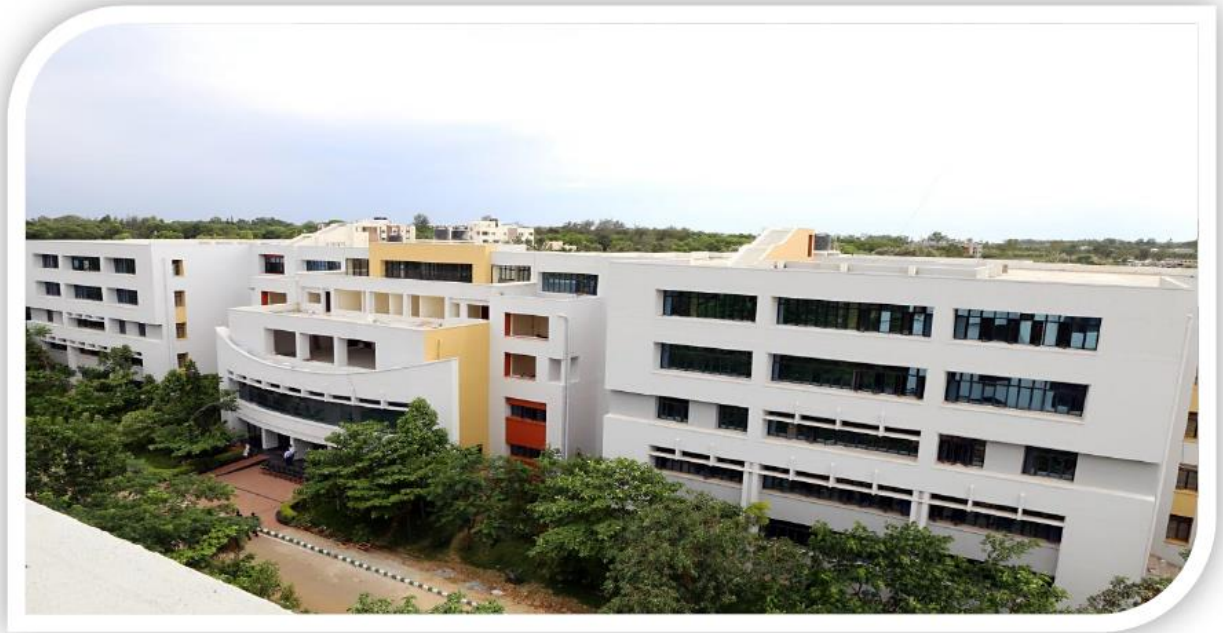


ISSUE - 1, VOLUME - 4, AUG 2019

RESEARCH COMPENDIUM

(Faculty Research Publications)

Department of Mechanical Engineering



2018-19



BMS Institute of Technology & Management

Avalahalli, Yelahanka, Doddaballapura Main Road

Bangalore - 560064

Vision of the Department

To develop technically competent Mechanical Engineering professionals for the benefit of the society

Mission of the Department

Impart quality education in Mechanical Engineering and allied areas by state-of-the-art-infrastructure and dedicated faculty.

Provide conducive environment for both students and faculty to pursue higher education & research and to work ethically for the benefit of society.

Program Educational Objectives

Graduates of the program will:

PEO-1: Be successful professionals in the field of Mechanical Engineering and allied areas.

PEO-2: Exhibit skills to work effectively and ethically in Mechanical and related domains of engineering as part of a team.

PEO-3: Excel in higher studies and research to adapt in a world of constantly developing technology.

Research Publication Details

International Journals 2018-19

Sl No	Faculty Name	Paper Title	Journal Name
1	Dr. H K Govindaraju	Preparation and Mechanical Characterization of Al7075-Silicon Nitride MMC's	International Journal of Mechanical and Production Engineering Research and Development (IJMPERD), ISSN(P): 2249-6890; ISSN(E): 2249-8001 Vol. 8, Issue 4, Aug 2018, 575-584
2	Kiran M D	Modelling and Analysis of Off-Road Rally Vehicle using Adams Car	International Journal of Research and Scientific Innovation (IJRSI) Volume V, Issue IX, September 2018 ISSN 2321-2705
3	Madhu M C	Performance Evaluation of Solar Tracking System with Reflectors	International Journal of Mechanical and Production Engineering Research and Development (IJMPERD) ISSN(P): 2249-6890; ISSN(E): 2249-8001 Vol. 8, Special Issue 8, Oct 2018, 187-194
4	Shripad Diwakar	Effect of Injector Opening Pressure on the Performance and Emission Characteristics of Direct Injection Diesel Engine with Methyl Esters of Calophyllum Inophyllum (Surahonne) oil	International Journal of Mechanical and Production Engineering Research and Development (IJMPERD) ISSN(P): 2249-6890; ISSN(E): 2249-8001 Vol. 8, Special Issue 8, Oct 2018, 67-74
5	S.NithyaPoornima	Moisture Sensors for Automatic Watering System for Indoor Garden	SSRG International Journal of Mechanical Engineering (SSRG - IJME) – Special Issue ICETST Nov 2018
6	Dr. A V Suresh	Effect of MWCNTs on piezoelectric and ferroelectric properties of KNN composites	Materials Science & Engineering B 231 (2018) 40–56, Elsevier Publication
7	G L Anantha Krishna	Finite Element Analysis of Tibia Bone	International Journal of Engineering Science and Computing, December 2018, Volume 8 Issue No.12
8	Kiran M D Dr. H K Govindaraju	Evaluation of fracture toughness of epoxy-nickel coated carbon fiber composites with Al ₂ O ₃ nano filler	Advances in Polymer Composites: Mechanics, Characterization and Application, AIP Conf. Proc. 2057, 020002-1–020002-5;

9	Dr. H K Govindaraju Kiran M D	Development of Wear Resistant Al-Si-Ce Metal Matrix Composites Using Gr as Reinforcement	International Journal of Engineering, Applied and Management Sciences Paradigms (IJEAM), Volume 54 Issue 1 April 2019, 126-131.
10	K.Chandra Sekhara Reddy	Automatic bumper with smart braking system	International Journal of Engineering Science and Computing, June2019, Volume 9 Issue No.6
11	Dr.K.M. Sathish Kumar	Modal Analysis for Optimized Placement of Piezoelectric Patches on a Composite Beam Structure	Materials Today, Volume 5, Issue 10, Part 1, 30 October 2018, ISSN 2214-7853, https://doi.org/10.1016/j.matpr.2018.06.511 , PP.21135-21139, Elsevier Publication.
12	Keerthi Kumar N	Effects of combustion chamber profile on direct injection diesel engine operated with SuOME	AIP Conference Proceedings, Volume-2128, Pages 050001-1 to 050001-13, July 2019, AIP Publishing.
13	Dr. Nandini R	Kinetic Analysis of isothermal solid-state process for synthesized potassium sodium niobate piezoelectric ceramics.	Materials Today Proceedings, 5 (Part-1), 20939–20946, October 2018, Elsevier Publication.
14	S.Nithya Poornima	Outcome Based Education - Need for the Hour	International Journal of advance Research Ideas and Innovations in Technology, Ref No-OAP/IJ/192/771, Volume 2, Issue 2 ISSN-2454-132X
15	Dr. Sangmesh	Heat Transfer Enhancement in a high-Power LED using Heat Sink with Fluid Pockets	Journal of Scientific and Industrial Research. Vol. 77 October 2018
16	Dr. Sangmesh	Mechanical and Wear behaviour of Al6061 reinforced with Graphite and TiC Hybrid MMC's,	Materials Research Innovations, https://doi.org/10.1080/14328917.2019.1628497 .
17	Dr. Sangmesh	Experimental Investigation on HSFP using MWCNT based Nanofluids for high power Light Emitting Diodes,	Journal of Mechanical Engineering and Sciences, Vol. 12 No. 3, (2018),3852-3865.
18	Dr. Sangmesh	Performance studies on cryogenic treated carbide cutting tool for turning of AISI304 steel	Journal of Mechanical Engineering and Sciences, Vol. 12 No. 3, (2018),3927-3941
19	Dr. Sangmesh	Thermal management of vehicle radiator by nanocellulose with one-dimensional analysis	AIP Conference Proceedings 2059, 020043 (2019); https://doi.org/10.1063/1.5085986

20	Dr. Sangmesh	Nanocellulose as heat transfer liquid in heat exchanger	AIP Conference Proceedings 2059, 020044 (2019); https://doi.org/10.1063/1.5085987
21	Dr. Sangmesh	Effect of Cryogenic treatment on Tool Wear, Chip Thickness of Uncoated Carbide Insert during Machining with AISI304 Stainless Steel	International Journal of Innovative Technology and Exploring Engineering, Volume-8, Issue-9, July 2019
22	Dr. Shreya Banerjee	A Timoshenko like model for piezoelectric energy harvester with shear mode	Composite Structures, Elsevier, Volume 204, 15 November 2018, Pages 677-688. DOI: https://doi.org/10.1016/j.compstruct.2018.07.117
23	Dr. Shreya Banerjee	An electromechanically coupled intrinsic, mixed Variational formulation for geometrically nonlinear smart composite beams	Applied Mathematical Modelling, Elsevier, Volume 65, January 2019, Pages 549-565 DOI: https://doi.org/10.1016/j.apm.2018.08.023

PREPARATION AND MECHANICAL CHARACTERIZATION OF AL7075-SILICON NITRIDE MMC'S

MOHAN KUMAR. S¹ & GOVINDARAJU. H. K²

¹Department of Mechanical Engineering, Amrita School of Engineering, Amrita Vishwa Vidyapeetham
Campus, Bengaluru, Karnataka, India

²Department of Mechanical Engineering, BMS Institute of Technology, Bengaluru, Karnataka, India

ABSTRACT

The present work describes the mechanical properties of Al 7075 metal matrix composites reinforced with Si₃N₄. Si₃N₄ particles of size 325 mesh were taken as the reinforcement material to prepare the metal matrix composites by using stir casting technique. The percentage of reinforcement varied from 0 to 12% wt in steps of 3%. Mechanical characterization such as tensile strength hardness test, density tests were conducted as per ASTM standards. Experiment results reveal that there is an improvement in Ultimate tensile strength and hardness properties with the increase in the weight percentage of reinforcement. Optical microscopy technique was used to examine microstructures of the sample specimens and the microstructure revealed uniform distribution, of particles and presence of reinforcements in the matrix phase. A fractured surface on the tensile test specimen was investigated to determine the fracture mechanism by using scanning electron microscope. Experimental studies invoke that the 12%wt of Si₃N₄ increases the tensile strength by 7% and hardness values by 8% compared with that of as cast Al7075. Results also evident that there was a decrease in ductility and percentage of elongation with the increase in the percentage reinforcement.

KEYWORDS: Al 7075, Tensile Strength, Hardness Test, Density Tests & Silicon Nitride

Received: May 19, 2018; **Accepted:** Jun 09, 2018; **Published:** Jul 17, 2018; **Paper Id.:** IJMPERDAUG201859

INTRODUCTION

Bauxite ore is a chief source of aluminum alloy. Aluminum 7075 is a lightweight material hence used for automotive applications and aircraft material. Main alloying element of Al7075 is Zinc and its main advantageous engineering properties are the high strength to weight ratio, moderate machine ability, and resistance to fatigue. Boron carbide is a ceramic material of typically brittle in nature and its crystal structure is of complex nature of icosahedron-based borides. Main properties of Boron carbides are Low thermal conductivity, Susceptible to thermal shock failure, outstanding hardness, extremely brittle, Semiconductor, Good thermal-neutron capture. In the present investigation, Al7075 is used as matrix phase and Silicon Nitride is used as a reinforcement material for the strengthening of the MMC's.

Al 7075 Alloy reinforced with Magnesium oxide nano powder, processed by stir casting has been studied. Al 7075 matrix with 10% of magnesium oxide powder particulates shows higher micro-hardness. Further, it shows more resistance to wear with the increase in magnesium oxide particles. However, with the increase of magnesium oxide beyond 10% does not show any considerable improvement in resistance to wear. Experimental results show that by increasing percentage of reinforcement it founds that increasing wear rate and wear volume.

Aluminum alloy 7075 reinforced with magnesium oxide produced by two-step stir casting method with different weight % [1].

Everton Rodrigues de Araujo et.al fabricated Aluminum 6061 MMC's by using silicon nitride as reinforcement, results shows the decrease in wear rate with the higher hardness number. Results indicated that tensile properties increased with increase in % of Si_3N_4 . Optical microscopy study reveals that uniform dispersion of reinforcement [2].

Mohan et.al investigated the Mechanical and tribological properties of hybrid composites, were AA430 was used as a matrix material, SiC and MgO were used as reinforcement material using the Liquid metallurgical technique. Experimental results showed that increasing the percentage of reinforcement increases the tensile strength and also the hardness. It further showed increasing the percentage of SiC+MgO, the coefficient of friction is decreased. Al6061 alloy reinforced with the TiC is fabricated by using stir casting technique [3]. Aluminum alloy reinforced with ceramic particle like TiC is significantly used in automobile, aircraft, marine, sports and recreation application.

Mohan Kumar and Govindaraju investigated on the fracture behavior of Aluminum 7075 alloy with an Electroless Nickel coating with different thickness. SEM revealed that the adhesion between the 7075 alloy and Nickel coating was strong and the coating was uniform. Fracture toughness of the coated specimen increased significantly with coating thickness [4]. Aluminum 7075 alloys with the different thickness of zinc/cadmium coating also increases Fracture toughness value in compared to that of uncoated aluminum 7075-T6 alloy [5].

Pramod R and Shashi Kumar M. E. evaluated the mechanical and insulation properties of Nomex-T410 and HS glass polymer matrix composites. This had enhanced the mechanical properties and at the same time contributing to the superior electrical insulation properties through the dielectric test when compared to the existing insulators. The PMC also proved its chemical inertness and sustained higher temperatures [7].

J. B. Fogagnolo et.al investigated the mechanical properties of A6061- Si_3N_4 , ZrB_2 MMC with varying percentage of reinforcement. According to the ASTM standards tensile, hardness properties were evaluated. AA6061- Si_3N_4 reinforced MMC exhibited. very good mechanical properties under the T6 heat treatment condition compared to the as-cast MMC of Al6061 alloy and also the dry sliding behavior of AA6061- Si_3N_4 under T6 exhibits a very good wear resistance with the increased wt. % of reinforcement [6].

METHODOLOGY

Liquid Metallurgy Technique

Aluminum 7075 alloy series were used as the base alloy and Silicon Nitride as the reinforcement material. The reinforcement particle size used was 325 μm and was preheated to 500°C. To increase the wettability of molten metal magnesium chips were added, as the molten metal starts to solidify at a faster rate. Adding more than 5% would lead to the porosity of the base metal. Molten Aluminum was stirred with reinforcements at a constant speed of 350 rpm for 10 min so that it creates a vortex and enhances the uniform distribution throughout the matrix phase which is necessary for adjoining the reinforcements with the matrix material. Figure 1 shows the molten metal in the furnace crucible and Figure 2. Show the stirring of Al 7075 with Silicon Nitride reinforcement. Figure 3 shows the pouring of molten metal in to die. Figure 4 showed the casted specimens.



Figure 1: Molten Metal in the Furnace Crucible



Figure 2: Stirring of AA2024 with B4C Reinforcement



Figure 3: Pouring of Molten Metal



Figure 4: Casted Specimens

Density Test

Density is a most predominant factor considered in various applications. To calculate the density of specimens, the mass of the specimen is observed using electronic digital weight scale. The volume is calculated depending on the diameter and height which is measured with the help of Vernier caliper. The specimens prepared for the density test is shown in. Figure 5. Below



Figure 5: Density Test Specimens

Hardness Test

ASTM E18 standard testing method was employed to know the hardness number of the specimen by using Rockwell hardness tester “B” scale. The type of indenter used was hardened steel ball having a dia of 1/16th of inch and the total load applied is 1000 N. The time of application of load is 15sec.

Tensile Test

The Figure 6 gives the dimensions of the tensile test specimens which is in accordance with ASTM E-8M. The test has been done in displacement control mode with a rate of 0.1 mm/min. The load and displacement were measured.

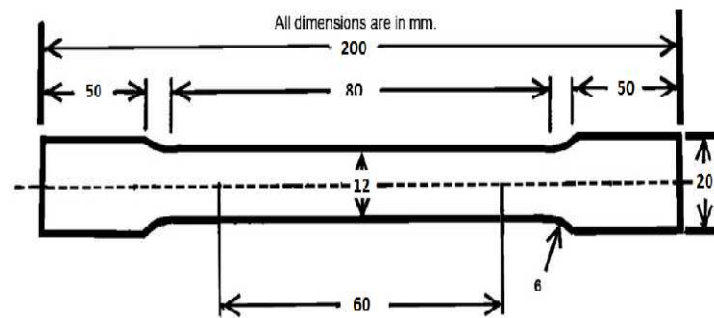


Figure 6: Tensile Test Specimen

RESULTS AND DISCUSSIONS

Density Test and Hardness Test

The density test conducted on the specimens and it revealed that the density of the samples increases as expected on the addition of the reinforcement. The Figure 7 shows that the maximum density was observed for 12% Silicon Nitride reinforcement and also graph reveals that there is no much difference in actual density values to theoretical density values. The hardness of the material improved on the addition of Silicon Nitride. The hardness value improved to a greater extent on the addition of 12% Silicon Nitride with a maximum hardness of 72 HRB. The slope of the curve shows further increase in the Silicon Nitride might improve the hardness but not appreciably.

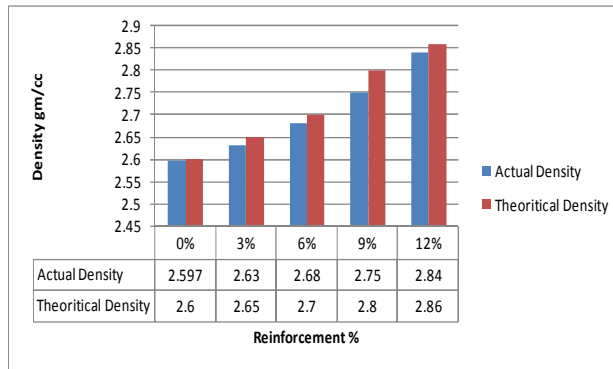


Figure 7: Variation of Density for Different Percentages of Si3N4

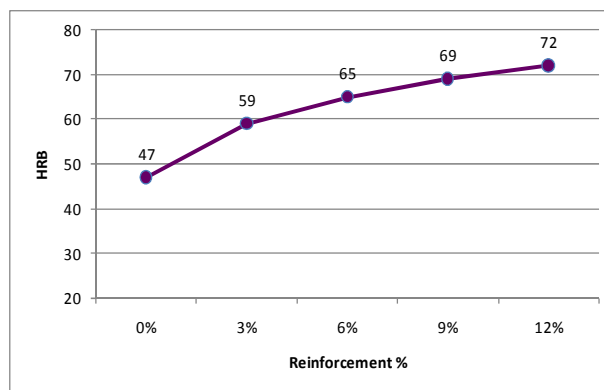


Figure 8: Variation of Hardness for Different Percentages of Si3N4

Tensile Test

The tensile test specimens after fracture are shown in the Figures revealed that the tensile strength increases with increase in weight % of Silicon Nitride. It is also observed that Silicon Nitride improved the yield strength of the material better than base Al 7075 alloy. Interfacial bonds of the material are affected because of the maximum stress experienced by the specimen. The ductility of the material decreases on the addition of the reinforcement materials. A greater reduction in ductility was observed on the addition of 12% Silicon Nitride. Percentage of elongation decreases in increasing the % of reinforcement.

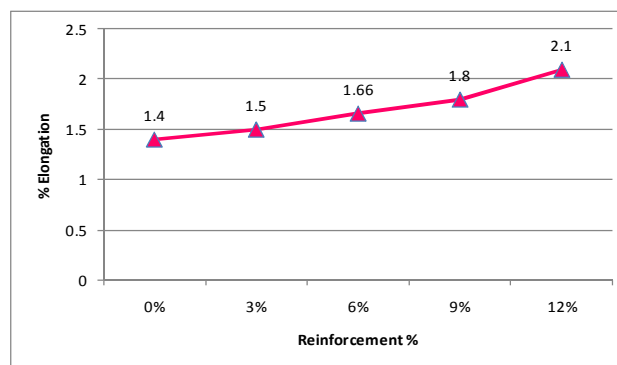


Figure 9: Percentage Elongation for Different Percentages of Si3N4

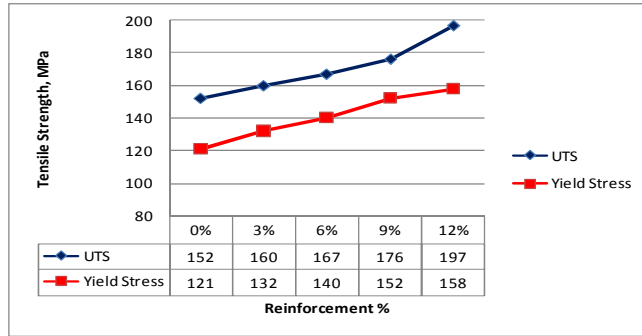


Figure 10: Strength variations for Different Percentages of Si₃N₄

Microstructure

The microstructure of Al 7075 is shown in. Figure 11. The microstructure consists of intermetallic precipitates in a matrix of Dendritic Aluminum solid solution. No segregation or porosity was seen in the section.

The microstructure of Al7075 with 3%, 6% and 9% Silicon Nitride is shown in Figure.12. This also showed the uniform distribution of the Si₃N₄ particles, because of the proper stirring action takes place during the casting process and also it observed from optical microscopy that grain refinement is increased by increasing the wt. % of Si₃N₄ particles.

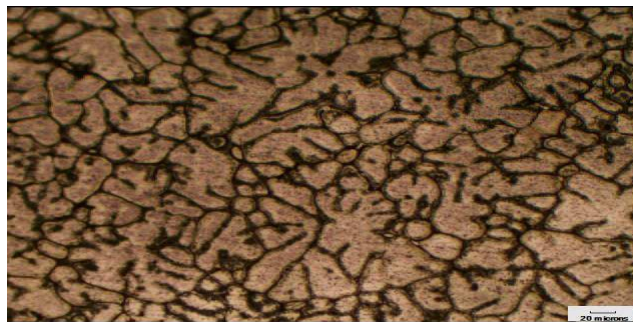


Figure 11: Microstructure of Al 7075

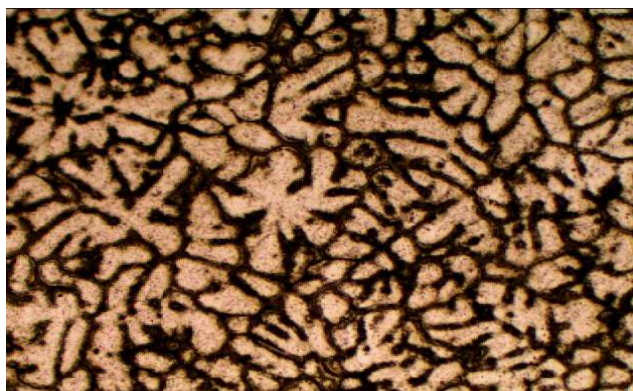


Figure 12(a):.Microstructure of Al 7075 with 3% Si₃N₄

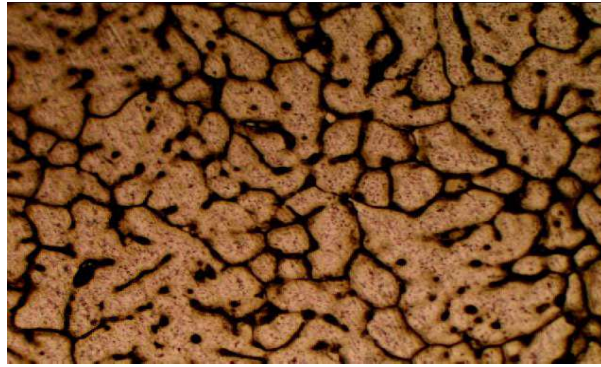


Figure 12(b): Microstructure of Al 7075 with 6% Si₃N₄

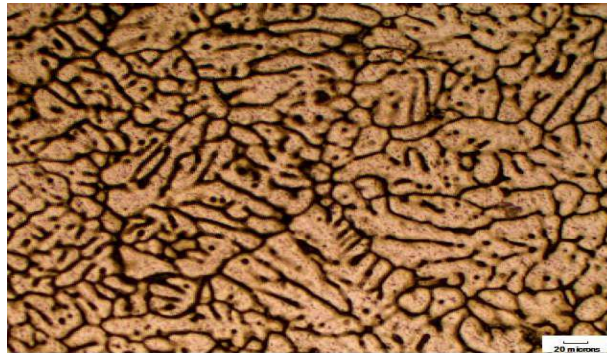


Figure 12(c): Microstructure of Al 7075 with 9% Si₃N₄

SCANNING ELECTRON MICROSTRUCTURE ANALYSIS

Fractured surface of the tensile specimens are subjected to a fractography test. Typical fractographs of Al 7075 tensile test specimen Figure 13 (a) shows an uneven distribution of the large dimples. Experimental studies reveal that the reinforcement particles are rarely fractured. In Figure 13 (C) fractured specimens can be seen reinforcements are breaks up longitudinal and transverse directions. Breaking up of the reinforcements is indicating the increased stress on the specimen. Strain induces on the reinforcements increases as the increase on the loads. Reinforcements pull-out observed in the matrix composite indicating that strong adhesion between the matrix and reinforcement phase in Figure 13(B). There is no gap between the interfacial region on the matrix and reinforcement. Mixed mode failure both ductile and brittle fractures are observed and tear fracture, dimples are seen during SEM analysis

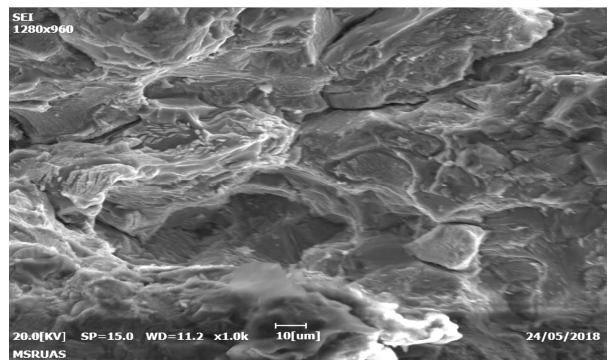


Figure 13(a): Fractographs of the Tensile Specimen Unreinforced Shows Uneven Distribution of the Large Dimples

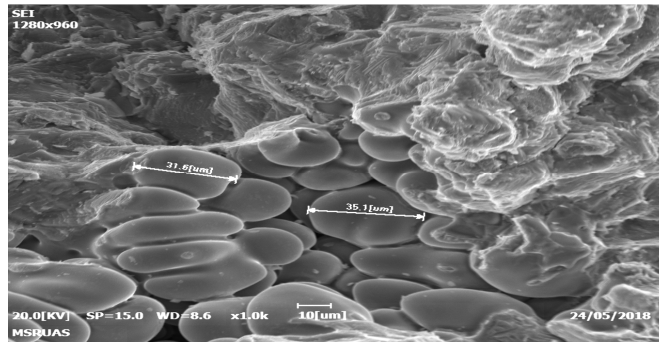


Figure 13 (b): Fractographs of the Tensile Specimen Shows Non-Fractured Reinforcement from the Specimen

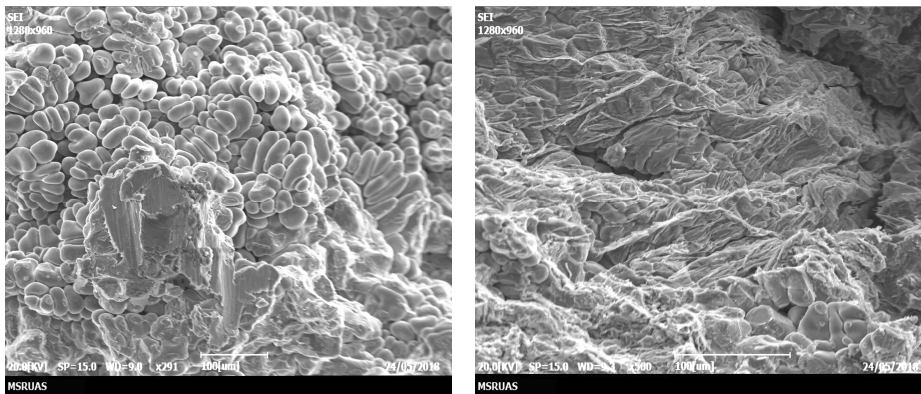


Figure 13 (c): Fractographs of the Tensile Specimen Shows Fractured and Pullout Reinforcement from the Specimen

CONCLUSIONS

The density of the material was observed to increase with the addition of reinforcement materials to the matrix material. Aluminum 2024 reinforced with Boron Carbide is effective in increasing the tensile strength of the composite material. The optimum tensile strength was observed in the sample containing 6% Boron Carbide by weight. Addition of the reinforcement materials results in a reduction in the ductility of the material. It is also observed that Young's modulus of the MMC is increased with the effect of B4C reinforcement in Matrix phase. From the microstructure, it can be seen that the intermetallic precipitates are present and they are uniformly distributed across the matrix material.

REFERENCES

1. T. Prasad, P Chinna Sreenivas Rao and B. Vijay Kiran, "Investigation of Mechanical Properties of Al 7075 with Magnesiumoxide Nano Powder Mmc",. *IOSR J. Mech. Civ. Eng.*, pp. 60-65.
2. Everthon Rodrigues de Araujo, "Preparation of Metal Matrix Aluminum Alloys Composites Reinforced by Silicon Nitride and Aluminum Nitride Through Powder Metallurgy Techniques," *Materials Science Forum Vols...*, pp. 259-262, 2012.
3. S. Mohan Kumar, R. Pramod, and H. K. Govindaraju, "Evaluation of Mechanical and Wear Properties of Aluminium AA430 Reinforced with SiC and Mgo," *Mater. Today Proc.*, vol. 4, no. 2, pp. 509–518, 2017.
4. S. Mohan Kumar, R. Pramod, M. E. Shashi Kumar, and H. K. Govindaraju, "Evaluation of fracture toughness and mechanical properties of aluminum alloy 7075, T6 with nickel coating," *Procedia Eng.*, vol. 97, pp. 178–185, 2014.

5. Youssef, GM. "The Effect Of Etching Current On The Formation Of Antireflection Porous Silicon Coating Fabricated By Electrochemical Technique For Solar Cells."
6. S. Mohan Kumar, V. Ravi Kumar, M. E. Shashi Kumar, and H. K. Govindaraju, "Mechanical characterization and fracture toughness of electroplated cadmium coating of Al -Zn alloy, T6," In AIP Conference Proceedings, 2017, vol. 1859.
7. J. B. Fogagnolo, "Aluminium matrix composites reinforced with Si₃N₄, AlN and ZrB₂ produced by conventional powder metallurgy and mechanical alloying," KONA No22, pp.143–150.
8. R. Pramod and Shashi Kumar M. E., Evaluation of mechanical and insulation properties of nomex-T410 and HS glass polymer matrix composites,.Materials Today: Proceedings, 4 (2017), 3233-3242.

Modelling and Analysis of Off-Road Rally Vehicle using Adams Car

Shreyas B N¹, Kiran M D²

^{1,2}Department of Mechanical Engineering, B.M.S Institute of Technology and Management, Yelahanka, Bangalore, India

Abstract—The paper discusses the modelling of a virtual prototype of the suspension and steering sub systems of a physical rally vehicle available on campus. Upon modelling the front and rear suspensions and the steering on Adams Car, the created model is tested for its correctness using Half Vehicle analysis like K and C analysis, and full car analysis like CRC and Maintain Analysis. Furthermore, the front lower control arm is made flexible to see the stresses acting on it to investigate its reason for failure in the actual prototype.

Keywords-Kinematics; camber; toe; caster; cornering; maintain; flex body

I. INTRODUCTION

An off-road vehicle, as the name suggests, is usually driven on uneven terrains and harsh road conditions. For this project, the rally car has been built with handling properties being given the utmost priority. The chassis is fabricated with steel as the material. The front suspension used it of the double wishbone type, falling under independent type of suspensions. The rear suspension resembles the multilink type. There are 6 suspension struts used in this car. Two are used in front suspension and four struts are used at the rear suspension. The main aim in this project is to find out the reason of failure of the control links in the front suspension.



Figure 1.1 Physical prototype of rally car

II. MODELLING THE VIRTUAL PROTOTYPE USING ADAMS CAR

The aim of this project is to dynamically analyze the performance of the off-road vehicle by creating a replica of the

physical suspension model on the software GUI. This phase is crucial as small errors in the data procured can lead to large changes in the dynamic behavior of the car. Hence, utmost care has to be taken to ensure the hard points extracted from the physical prototype are as accurate as possible.

Once the hard points are fed into ADAMS Car Template Builder, the modelling is progressed by defining parts for the created hard points, creating geometry for the defined parts, assigning relative motion between the created parts by creating joints and bushings where ever required. The mass and inertia properties of individual parts are unavailable on the physical prototype due to various domestic constraints.

The following steps are followed in order to model the suspension accurately.

- Hard Points
- Defining Parts
- Creating Geometry
- Creating Joints and Bushes
- Assigning Communicators

III. MODELLING THE SUSPENSION SUBSYSTEMS

A. Creating the Front Suspension.

The following table shows the different hard points that have been extracted for front suspension template. All the measurements are made in Cartesian co-ordinates.

	FS		
	HP		
Part	X	Y	Z
Drive Shaft Inner	0	-200	225
Lca Front	-140	-320	170
Lca Outer	45	-800	220
Lca Rear	95	-345	180
Lower Strut Mount	-40	-625	325
Subframe Front	-140	-320	170
Subframe Rear	95	-345	180
Tierod Inner	200	-400	300
Tierod Outer	120	-730	360
Top Mount	220	-450	860
Uca Front	-140	-350	315

Uca Outer	-60	-675	330
Uca Rear	85	-365	320
Wheel Center	0	-840	310

Table 3.1 Hard points of front suspension all in mm.

Upon completion of the entire process, the template of front suspension is completed and shown in figure. The car uses double wishbone suspension in the front with rack and pinion steering arrangement.

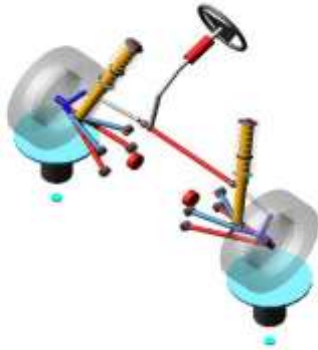


Figure3.1 Isometric View of Front Suspension

B. Creating Rear Suspension.

The rear suspension modelling is done in the same way as the front suspension. The rear suspension largely resembles the multi-link suspension system. There are a few modifications made to the multi-link suspension to closely represent the suspension used in the rally car as much as possible. They are,

- An extra suspension strut is added at the exact location used in the physical prototype.
- The lateral bar is removed as this part isn't present in the actual car.
- Control arm is also removed in the virtual prototype to closely resemble the physical car.
- The location of every part is accurately assigned.

The following image shows the rear suspension.



Fig 3.2 Isometric View of Rear Suspension

C. Creating Assembly

The front suspension which resembles the double wishbone is modelled completely. The steering of rack and pinion type is also modelled.

The rear suspension resembling multi-link suspension is modelled and several changes are made to the model too. Once everything is complete, all the sub systems are called into an assembly including the powertrain and chassis.

The powertrain, chassis and tires are used from the Adams Car library. The full assembly of the car is as shown in figure.

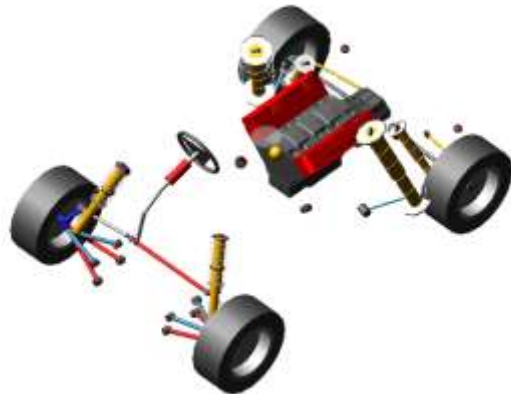


Figure 3.3 Full Vehicle Assembly

IV. KINEMATICS AND COMPLIANCE ANALYSIS

The virtual models of suspension system have to be proven that they are correctly modeled. Correlations can be made by comparing the simulated results with the experimental results. In this project, the model will be built on ADAMS Car and the simulated results are generated. The experimental results are tough to procure due to financial constraints, although these results can be used for verification if the car is analyzed for K and C experimentally in the future.



Figure 4.1 K and C test rig for physical prototypes.

The purpose of performing K and C is to develop and simulate a fully working MBD suspension model of the actual Off-Road Rally Car present in the campus, of Double Wishbone type as the front suspension and the multilink type

for the rear suspension systems. Both the simulated and experimental results only consider the value of the toe change, camber change and wheel rate when subjected to the Vertical In-Phase Test and Vertical Anti-Phase test.

D. Front Suspension K and C Analysis.

Suspension kinematics analysis is the most important part of the chassis tuning, and it is the basic guarantee to ensure the vehicle to control stability. The process is widely referred to as K and C (Kinematics and Compliance) analysis or half vehicle analysis. Joints are used during kinematic analysis and bushes are used during compliance analysis. The MBD models of the double wishbone front suspension and rack and pinion steering systems are established in ADAMS Car, and the model is used to analyze the following:

- Wheel rate
- Toe change
- Camber change

The front suspension along with the wheel and steering is set up on a two post-test rig on ADAMS Car. The different uneven road maneuvers are replicated on the software and plots are made to observe the above mentioned characteristics of the suspension. The different analyses used are as follows:

- Vertical In-Phase
- Vertical Anti-Phase

The following calculations show how preload has been decided.

Total Mass = 312 Kg

Unsprung Mass = 72 Kg

Therefore, Sprung Mass = 240 Kg

Weight distribution = 49:51

Therefore, Front axle load = 0.49*240

Wf = 117.6 Kg acting on two springs.

Therefore, preload on each spring = 117.6/2 = 58.8 Kg

Preload = 58.8*9.81 = 576 N

For the front suspension, we will carry out two simulations. The two being Vertical In-Phase and Vertical Anti-Phase tests. In Vertical In-Phase, the two posts of the test rig lift both wheels and drops them with zero phase lag between the wheels. In Vertical Anti-Phase, while the left wheel experiences bump travel, the right wheel will undergo rebound and vice versa.

The input is given as bounce and rebound. Once the simulation is complete, with the help of ADAMS Post Processor, the kinematics and dynamics of the suspension subsystem are analyzed. Any modifications made to the suspension parameters will be done to achieve better stability of the car.

Analysis Type	K and C
Vehicle	Off Road Rally Vehicle
Spring Stiffness	47 N/mm
Preload	576 N
Wheel Load	18 Kg
Bump	55 mm
Rebound	-30 mm

Table 4.1 K and C Input for Front Suspension

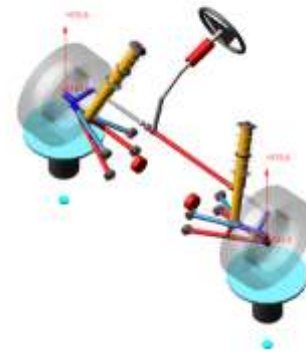


Figure 4.2 K and C Vertical In-Phase at Front Suspension.

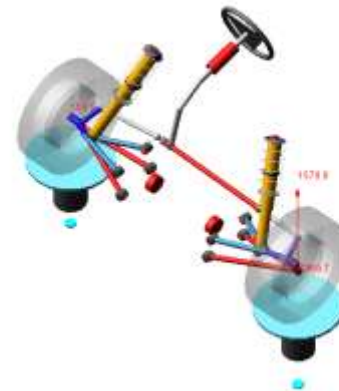


Figure 4.3 K and C Vertical Anti-Phase at Front Suspension.

Wheel Rate

Wheel rate is the vertical stiffness of the suspension relative to the body, measured at the wheel center.

Theoretical Calculation of Wheel Rate

Wheel Rate can be calculated using the relation,

$$\text{Wheel Rate} = \text{Spring Rate} * (\text{Motion Ratio} \wedge 2) * \text{Spring Angle Correction N/mm.}$$

$$\text{Spring Rate} = 47 \text{ N/mm}$$

Motion Ratio = Arm Distance/ Wheel Distance = 305/520 = 0.5865

Spring Angle Correction = cos (18 deg) = 0.9510

Therefore, Wheel Rate = 47*0.35*0.9510

Wheel Rate (Theoretical Value) = 15.7 N/mm

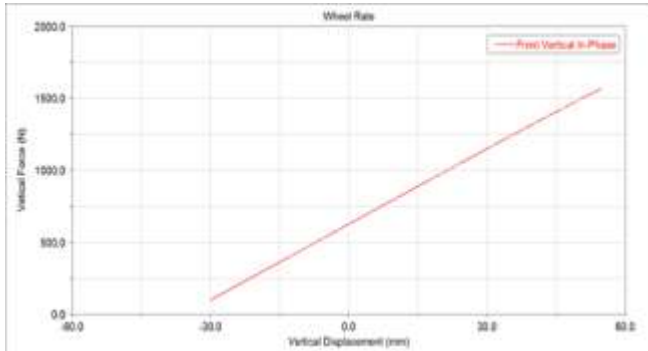


Figure 4.4 Wheel Rate for Front suspension during Vertical In-Phase.

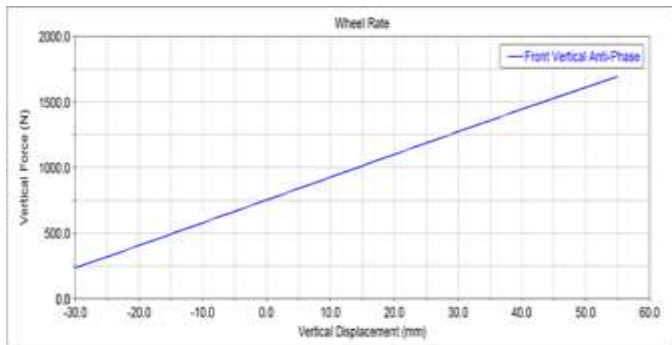


Figure 4.5 Wheel Rate for Front suspension during Vertical Anti-Phase.

Here, the vertical force applied at the left (or right) tire is observed to vary almost linearly to the vertical displacement of the left (or right) tire.

- From the graph, the wheel rate is observed to be equal to 16.39 N/mm.
- This value conforms closely with the calculated value i.e., 15.7 N/mm.
- The slope of the line gives the value of wheel rate in N/mm.
- At 55 mm displacement, i.e., during bump travel, the vertical force at left tire will increase to 1570.88 N.
- When the left wheel rebounds to the full extent i.e., -30 mm, the vertical force at left tire decreases to almost 99.2048 N.

Camber Change

Camber angle is the angle (in degrees), between the perpendicular from the ground and the center line of the wheel, as seen from car’s front. If the center line is inclined inwards, it is called negative camber, and if it is inclined outwards, it is called positive camber.

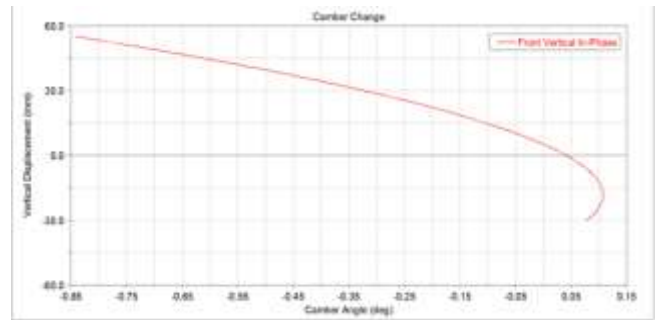


Figure 4.6 Camber Change for Front suspension during Vertical In-Phase.

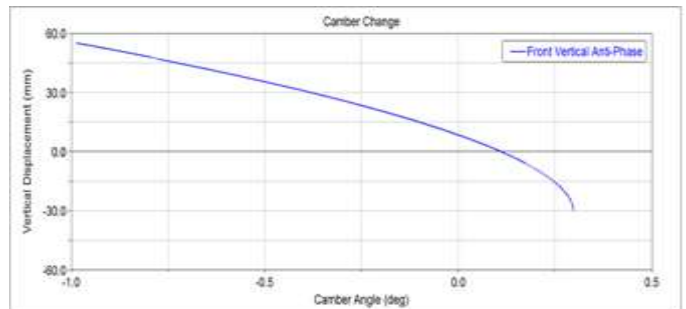


Figure 4.7 Camber Change in Front suspension during Vertical Anti-Phase.

Above graph shows a non-linear relationship between camber angle and vertical wheel travel when both wheels are displaced in-phase and anti-phase with the given values of bump and rebound.

- From the graph it is observed that the wheels will be in negative camber set up for most of its travel, which is desirable in most vehicles as they provide great cornering response.
- When the wheel bumps to an extent of 55 mm in vertical direction, the camber angle will decrease to -0.8417 degrees.
- When the wheel rebounds to an extent of -30 mm in vertical direction, the camber angle will increase to 0.0775 degrees.

Toe Change

The toe angle is the angle to which the wheels are out of parallel, or angle of wheel centerline along the length of the vehicle.

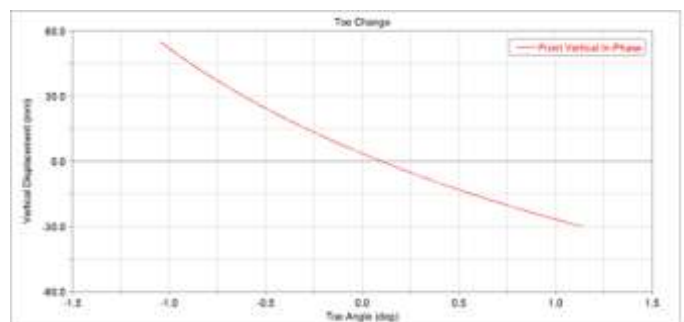


Figure 4.8 Toe Change for Front suspension during Vertical In-Phase.

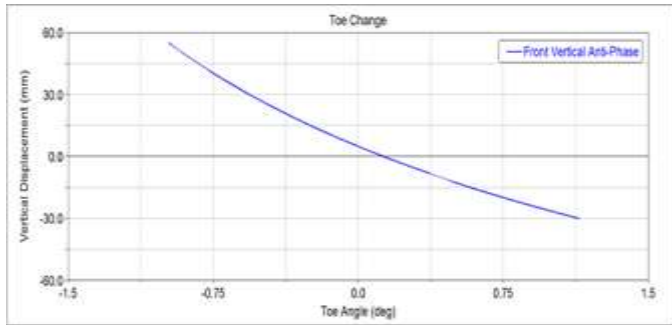


Figure 4.9 Toe Change for Front suspension during Vertical Anti-Phase.

The above graph shows a non-linear relationship between toe angle and vertical wheel travel when both wheels are displaced in-phase and anti-phase with the given values of bump and rebound. From the graph, it can be observed that:

- When the wheel bumps to an extent of 55 mm in vertical direction, the toe angle will increase to -1.0448 degrees.
- When the wheel rebounds to an extent of -30 mm in vertical direction, the camber angle will decrease non-linearly to 1.1391 degrees.
- Bump results in Toe-out which helps the vehicle to negotiate corners faster and offers less straight line stability.
- Rebound results in Toe-in which is preferred for passenger vehicles as they offer straight line stability. It also helps in achieving under steer characteristics.

E. Rear Suspension K and C Analysis

The MBD model of the multilink rear suspension is established in ADAMS Car, and the model is used to analyze the following:

- Wheel rate
- Toe change
- Camber change

The rear suspension along with the wheels is set up on a two post-test rig on ADAMS Car. The different uneven road maneuvers are replicated on the software and plots are made to observe the above mentioned characteristics of the suspension. The different analyses used are as follows:

- Vertical In-Phase
- Vertical Anti-Phase

The following calculations show how preload has been decided.

Total Mass = 312 Kg

Unsprung Mass = 72 Kg

Therefore, Sprung Mass = 240 Kg

Weight distribution = 49:51

Therefore, Rear Axle Load = 0.51*240

$W_r = 122.4 \text{ Kg}$ acting on four springs.

Therefore, preload on each spring = $122.4/4 = 30.6 \text{ Kg}$

Preload = $30.6 * 9.81 = 300.18 \text{ N}$

For the rear suspension as well, we will carry out two simulations. The two being Vertical In-Phase and Vertical Anti-Phase tests. In Vertical In-Phase, the two posts of the test rig lift both wheels and drops them with zero phase lag between the wheels. In Vertical Anti-Phase, while the left wheel experiences bump travel, the right wheel will undergo rebound and vice versa. The input is given as bounce and rebound.

Analysis Type	K and C
Vehicle	Off Road Rally Vehicle
Spring Stiffness	47 N/mm
Preload	300.18 N
Wheel Load	18 Kg
Bump	55 mm
Rebound	-15 mm

Table 4.2 K and C Input for Rear Suspension

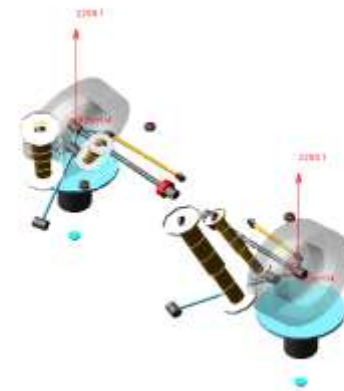


Figure 4.10 K and C Vertical In-Phase at Rear Suspension.

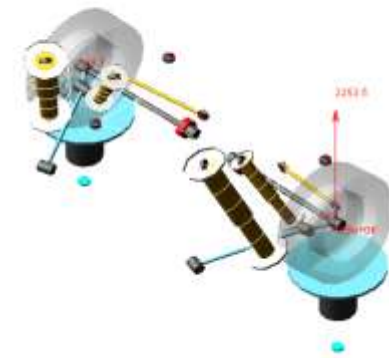


Figure 4.11 K and C Vertical Anti-Phase at Rear Suspension.

Wheel Rate

Wheel rate is the vertical stiffness of the suspension relative to the body, measured at the wheel center. The curve, for both cases, is observed as shown in the graphs.

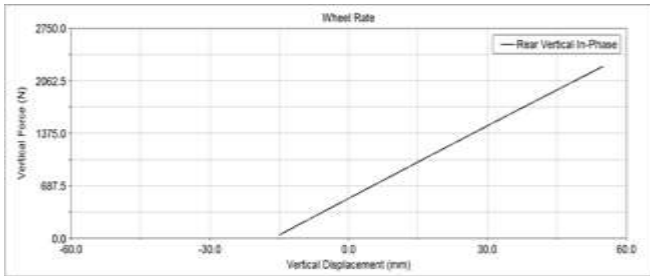


Figure 4.12 Wheel Rate for Rear suspension during Vertical In-Phase.

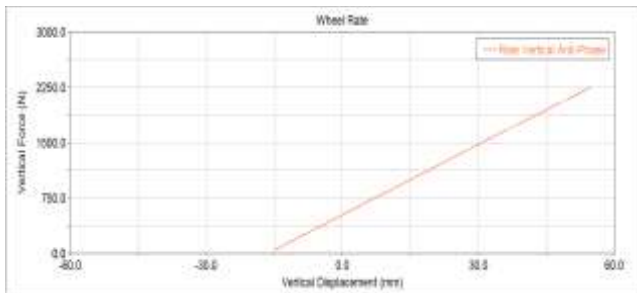


Figure 4.13 Wheel Rate for Rear suspension during Vertical Anti-Phase.

Here we observe that the vertical force applied at the left (or right) tire varies almost linearly as the vertical displacement of the left (or right) tire. From the graph, we can observe the following:

- The wheel rate from the plot is found to be 30.83 N/mm.
- At 55 mm displacement, i.e., during bump travel, the vertical force at left tire will increase to 2253.45 N.
- When the left wheel rebounds to the full extent i.e., -15 mm, the vertical force at left tire decreases to almost 39.18 N.

Camber Change

The change in the camber angle is significantly high in rear suspension as it is missing crucial elements like control arm and lateral link. It is clearly observed in the graphs below during both cases.

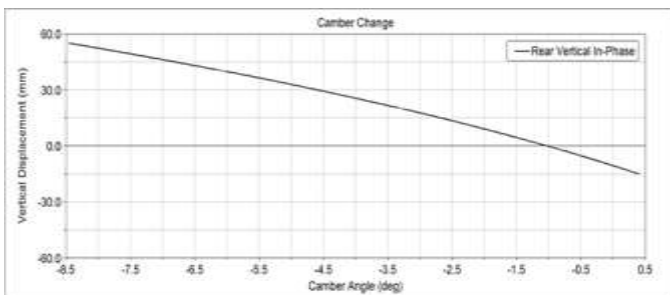


Figure 4.14 Camber Change for Rear Suspension during Vertical In-Phase.

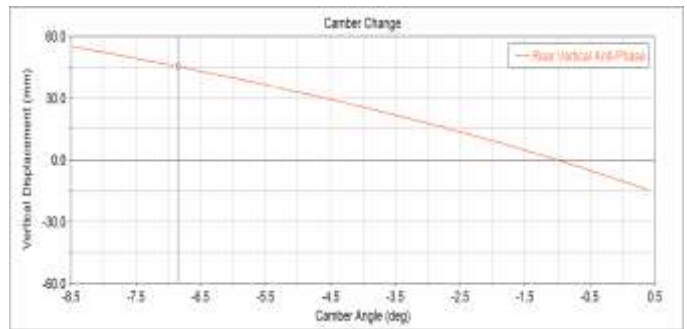


Figure 4.15 Camber Change for Rear suspension during Vertical Anti-Phase.

Above graph shows a non-linear relationship between camber angle and vertical wheel travel when both wheels are displaced anti-phase with the given values of bump and rebound.

- It is seen that the wheels will be in negative camber set up for most of its travel, which is desirable in performance vehicles as they provide great cornering response.
- When the wheel bumps to an extent of 55 mm in vertical direction, the camber angle will decrease to -8.47 degrees.
- When the wheel rebounds to an extent of -15 mm in vertical direction, the camber angle will increase to 0.41 degrees.

Toe Change

Toe can also be described as the difference between the track widths measured at the leading and trailing edges of the tires.

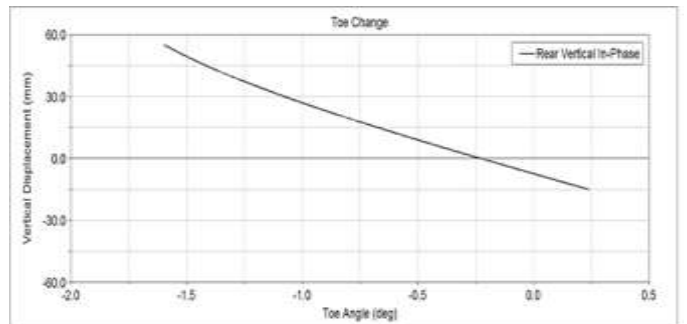


Figure 4.16 Toe Change for Rear suspension during Vertical In-Phase.

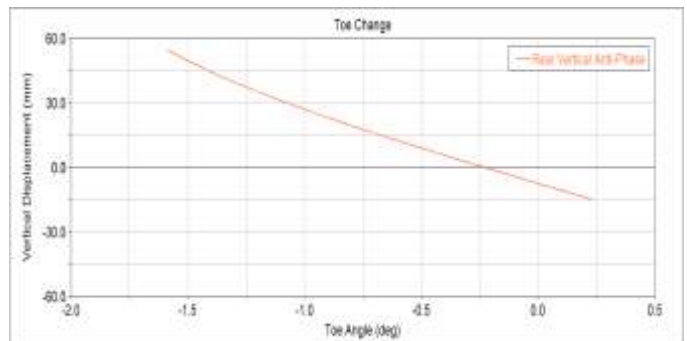


Figure 4.17 Toe Change for Rear suspension during Vertical Anti-Phase.

Above graph shows a non-linear relationship between toe angle and vertical wheel travel during both simulations with the given values of bump and rebound. From the graph, we can observe the following:

- When the wheel bumps to an extent of 55 mm in vertical direction, the toe angle will increase to -1.59 degrees.
- When the wheel rebounds to an extent of -15 mm in vertical direction, the camber angle will decrease non-linearly to 0.2403 degrees.
- Bump results in Toe-out which helps the vehicle to negotiate corners faster and offers less straight line stability.
- Rebound results in Toe-in which is preferred for passenger vehicles as they offer straight line stability. It also helps in achieving under steer characteristics.

V. MAINTAIN ANALYSIS

Maintain analysis or Constant Velocity analysis is a full vehicle analysis performed by automobile engineers to validate the full vehicle built on ADAMS Car.

In Maintain analysis, the full car is made to run along a straight path with a pre-set value of velocity in km/h. A 2D flat road file is used to run the analysis. Here we observe the following,

- Stability of the car and the individual sub systems during the maneuver.
- Behavior of communicators assigned among the different sub systems.
- Weight distribution along the longitudinal axis of the car.
- Forces developed at the tire contact patches.
- Location of CG during maneuver.

By performing maintain analysis, we are able to verify that the location of CG of the virtual prototype conforms closely with the analytical calculations.

The analytical calculations for the physical prototype is shown below.

Analytical Calculation (Physical Prototype)

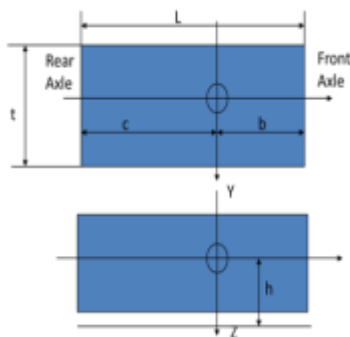


Figure 5.1 Location of C.G in Top and Side views respectively

Sprung Mass = **200 Kg**

Unsprung Mass = **72 Kg**

Total Weight, W = **272 Kg**

Given Weight Distribution = **48:52**

i.e.,

Front Axle Load, W_f = 0.48*272 = **130.5 Kg**

Rear Axle Load, W_r = 0.52*272 = **141.44 Kg**

In static condition,

b= (W_r/W) *L

b= 141.44/272*2100

b= 1092 mm

c= (W_f/W) *L

c=1008 mm

Height of CG, h = 25” = **635mm** (given)

To simulate maintain analysis, the following inputs are taken.

Vehicle	Off-road Rally Vehicle
End Time	10 s
Steps	1000
Road Type	2D flat
Initial Velocity	25 km/hr
Steering Input	Straight Line

Table 5.1 Input data used for Maintain Analysis

After the simulation is complete, we observe the forces developed at each of the four tires in z-direction of the car.



Figure 5.2 Vertical Forces developed at the tire contact patch during maneuver.

Using ADAMS Post Processor, we plot a graph of Normal Force vs Time. Under requests, “wheel tire forces (left and right)” is chosen, and under component, “normal (front and rear)” is chosen. This results in the generation of Normal Force vs Time plot as shown.

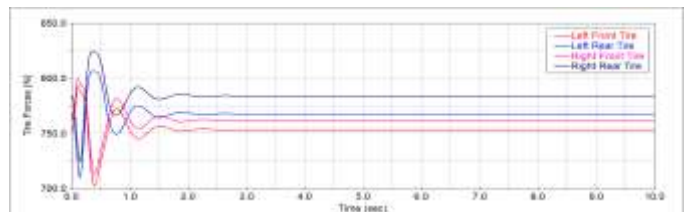


Figure 5.3 Graph of reaction forces developed at tire contact patch w.r.t time

The following forces are obtained at the tire contact patches in z-direction.

Front Left	753 N
Front Right	762 N
Rear Left	767 N
Rear Right	783 N

Table 5.2 Forces at each tire.

To verify the CG location and weight distribution with the analytical results, the following calculations are made.

Total Front Load = 753+762=1515 N

Total Rear Load = 767+783=1550 N

Total Weight = 1515+1550 = 3065 N = 312.4 Kg

Front Load Ratio = 1515/3065 = 0.49 i.e., 49%

Rear Load Ratio = 1550/3065 = 0.51 i.e., 51%

Therefore, Weight Distribution = 49:51

CG location of virtual prototype = (1062.97, 6.92, 436.67)

From the above results, we can observe that the values derived from the MBD model conform closely to the analytically calculated results of the physical prototype.

The table below helps us to get a better idea of this.

Analytical	MBD
Sprung Mass = 200 Kg	Sprung Mass = 240 Kg
Unsprung Mass = 72 Kg	Unsprung Mass = 72 Kg
Total Weight = 272 Kg	Total Weight = 312 Kg
Weight distribution = 48:52	Weight distribution = 49:51
$W_f = 0.48*272 = 130.5$ Kg	$W_f = 0.49*312 = 152.88$ Kg
$W_r = 0.52*272 = 141.44$ Kg	$W_r = 0.51*312 = 159.12$ Kg
B = 1092 mm	B = 1062.97 mm
C = 1008 mm	C = 1037.03 mm
H = 635 mm	H = 436.67 mm

Table 5.3 Comparison of Analytical and MBD vehicle specifications

Hence, with the help of maintain analysis, we are able to show close conformity in the weight distribution ratio between virtual and physical prototypes. The location of CG of both versions is also validated. The change in data between the two specimens exists due to limited data available from the actual car.

VI. CONSTANT RADIUS CORNERING

F. Determination of Understeer Gradient Value K:

Constant radius cornering analysis is second of the two full vehicle analysis performed in this project. The virtual prototype is made to maneuver around a circular path with fixed radius. Input vales of initial and final velocities and time

are given. This test is conducted to determine the understeer gradient value K.

Understeer gradient is crucial to determine the turning response properties of the car. It shows how the steering angle of the car should be altered with trun radius R, or lateral acceleration (V^2/Rg). The equation to determine understeer gradient is given by the expression

$$S = 57.3 * (L/R) + Kay$$

$$K = (W_f/C_{\alpha f}) - (W_r/C_{\alpha r})$$

Where:

S – Steering angle at front wheel (deg)

L – Wheelbase (mm)

R – Radius of turn (mm)

W_f – Load on front axle (N)

W_r – Load on rear axle (N)

$C_{\alpha f}$ – Cornering stiffness of front tires (N/deg)

$C_{\alpha r}$ – Cornering stiffness of rear tires (N/deg)

K – Understeer Gradient (deg/g)

To simulate the constant radius cornering test, the following inputs are given.

Vehicle	Off-road Rally Car
Road	2D flat
Step Size	0.1
Turn Radius	15 m
Turn Direction	Left
Duration of Manoeuvre	17 s
Initial Velocity	10 kmph
Final Velocity	30 kmph

Table 6.1 Input for Constant Radius Cornering analysis.

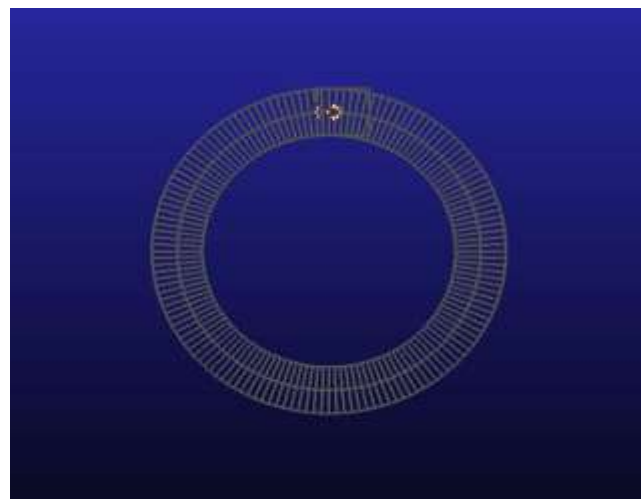


Figure 6.1 Constant Radius Cornering setup

On completion of the simulation, a graph of lateral acceleration vs. steering angle is plotted. The slope of the curve generated gives the value K' i.e., understeer gradient. Depending on the value of K , we can categorize if the vehicle behavior is either of the three,

- Neutral Steer, if $K=0$
- Understeer, if $K>0$
- Oversteer, if $K<0$

In neutral steer condition, no change in steer angle will be required as the speed is varied in a constant radius turn. In understeer condition, the steer angle will have to increase with speed in proportion to K times the lateral acceleration. In oversteer condition, the steer angle will have to decrease as the speed is increased.

The following graph shows steer angle vs lateral acceleration plotted for the virtual prototype of the rally car in Constant Radius Cornering test.

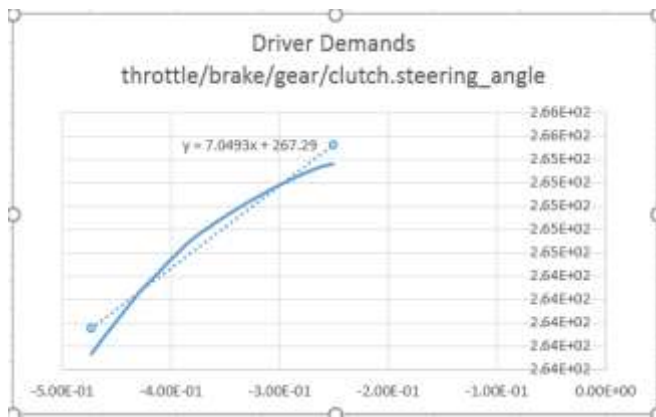


Figure 6.2 Understeer Gradient Characteristic Curve

From the behavior of the graph we can see the slope value K is positive as the curve resembles the straight line of equation $y = mx + c$, where m is K .

Since K is positive, we can conclude that the vehicle behavior is understeer for constant radius of turn with varying speeds. The value of K is approximately = 7.04 deg/g

G. Forces developed in Lower Control Arm (LCA):

The forces generated in the control arms are usually the highest during cornering. Hence, to understand the magnitude and range forces developed, we observe the axial forces acting on the lower control arm pivots, where the control arms connect to the chassis. The two locations where we observe the axial forces in x , y and z directions are:

- LCA front
- LCA rear

Both the LCAs, i.e., on the left and right, are considered.

The following inputs are given to simulate Constant Radius Cornering Analysis.

Vehicle	Off-road Rally Car
Road	2D flat
Step Size	0.1
Turn Radius	15 m
Turn Direction	Left
Duration of Manoeuvre	17 s
Initial Velocity	10 kmph
Final Velocity	30 kmph

Table 6.2 Input for CRC analysis to optimize forces developed in the control arm links.

A graph of LCA front and LCA rear forces vs time is plotted. In order to reduce these forces acting in the control arms, by trial and error, an observation was recorded to show that the forces actually decreased in the control arms when the distance between the LCA front and LCA rear links were further increased in x direction. The two pivots were parted further away from each other by 40mm in x direction.

Entity	Original Location	Modified Location
LCA Front(Left)	-120,-320,170	-140,-320,170
LCA Rear (Left)	75,-345,180	95,-345,180
LCA Front(Right)	-120,320,170	-140,320,170
LCA Rear (Right)	75,345,180	95,345,180

Table 6.3 Modified Hard Point locations of Lower Control Arm.



Figure 6.2 Top View of Original and Modified suspension arm location.

This adjustment in design is done so that the forces are reduced in the control arms. Since in the physical prototype, the front link of the LCA on right side has failed, we observe the forces F_x , F_y , and F_z developed in that link. The forces F_x , F_y and F_z are observed vs time.

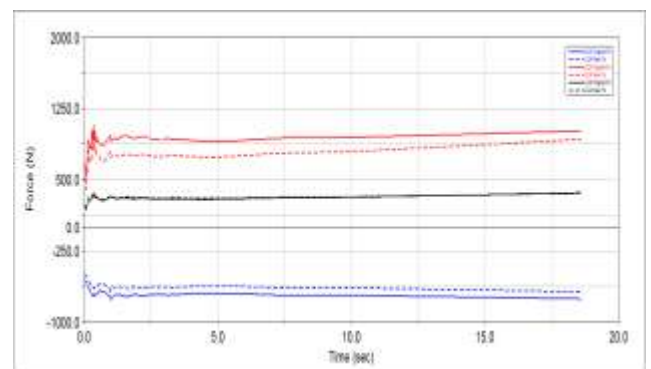


Figure 6.3 Graph of forces developed in the front link of right arm during cornering w.r.t time.

From the above graph it can be observed that the forces in LCA right front link have reduced in the updated design compared to the original design.

We know that,

$$\text{Torque(T)} = \text{Force(F)} * \text{Perpendicular Distance(d)}$$

Since the distance between the two links pivots have been increased, the distance between the point of action of force and the center have also increased. As a result, the effort or force, required to generate the same torque now decreases. This explains the reduction of forces in the link pivots.

The following data shows the values of forces acting in the front link of Right sided LCA.

Fx Original	-700 N
Fx Modified	-620 N
Fy Original	910 N
Fy Modified	748 N
Fz Original	300 N
Fz Modified	307 N

Figure 6.4 Forces developed in the front link of right arm during cornering.

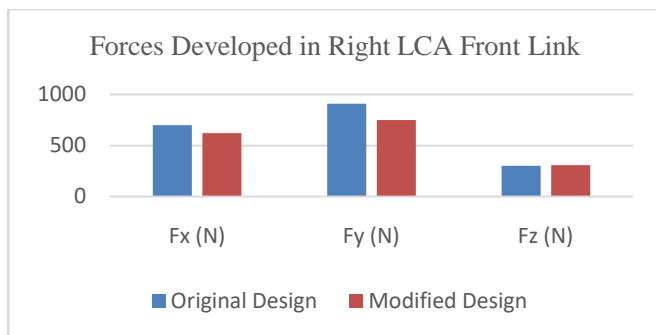


Figure 6.5 Bar Graph depicting the decrease in forces developed in the modified design

Percentage reduction in Fx	11.43 %
Percentage reduction in Fy	17.81 %
Percentage increase in Fz	2.29 %

Table 6.5 Percentage change in forces developed in the front link of right arm.

These improvements shown by altering the design of the LCA are found to be considerable in forces acting in longitudinal and lateral directions at the pivots. However, the forces acting in the vertical direction remain the same. With this modification, we can show that the chance of failure of the lower control arm solely due to dynamic forces produced during maneuver has been decreased.

VII. FLEX BODY ANALYSIS

All the analyses carried out till this stage have been run by using rigid bodies. The flexibility of these bodies are not showing their influence on the MBD results as every part is

assumed to behave rigidly upon application or development of forces.

To understand the reason for failure in the lower control arm in the actual model, we need to understand the stress levels acting in the LCA during any maneuver. This can be done by incorporating a flexible body, in this case, a flexible LCA on both sides of the car. The rigid body is replaced with the flexible body to run the simulation.

H. Generation of Flexible Lower Control Arm:

To replace the rigid body with a flexible component, software tools such as MSC Apex, MSC Patran and MSC Nastran have been used.

The following steps were taken to create flexible LCA on both sides.

- The rigid LCA is exported as an iges file.
- This file is imported into MSC Apex, which is a CAD tool used for modelling and simple meshing.
- The different links in the LCA are merged together to form one geometry. This is done using the Boolean feature.
- A tetrahedral mesh with the following mesh attributes is used.

Mesh Quality Attributes	Good	Fair	Bad	Invalid
Aspect Ratio	1.00	3.00	5.00	>5.00
Warpage Angle	3.00	5.00	10.00	>10.00
Warpage Factor	3.00	5.00	10.00	>10.00
Skew	3.00	10.00	50.00	>50.00
Twist	3.00	5.00	10.00	>10.00
Jacobian	1.00	0.75	0.50	<0.50
Quad Max Interior Angle	90.00	70.00	40.00	<40.00
Quad Min Interior Angle	90.00	110.00	140.00	>140.00
Trio Max Interior Angle	90.00	90.00	20.00	<20.00
Trio Min Interior Angle	90.00	90.00	120.00	>120.00
Quality Index	100.00	75.00	50.00	<50.00

Figure 7.1 Mesh Attributes used while preparing a flexible arm

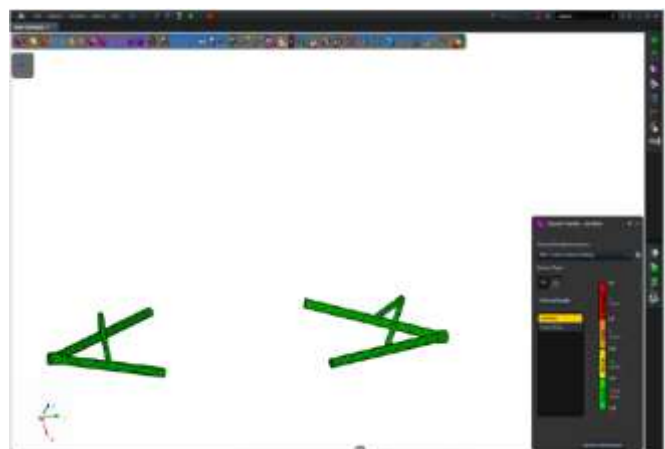


Figure 7.2 Geometry of arm after Boolean and meshing process.

- Once meshing is done, the file is exported as a parasolid and taken into MSC Patran.
- MSC Patran is a pre-processing FEA software tool used to generate mesh, assign properties etc.,
- The model is given three multipoint constraints at the locations where the LCA is pivoted to the knuckle and frame. This is done so that relative motion between the flexible part and the connecting rigid part exists after meshing.
- This file is then taken into MSC Nastran, which is a post-processing FEA tool, to generate the Modal Neutral File or MNF file.
- We can now easily replace the rigid body with the MNF file of the flexible part on ADAMS Car.

I. Constant Radius Cornering using Flexible Lower Control Arm:

Upon generation of the MNF file of the lower control arms, the rigid arms are swapped with the flexible ones on Adams Car. From now on, the stresses and deformation experienced by the LCA will play a role in any simulation the car is made to operate in.

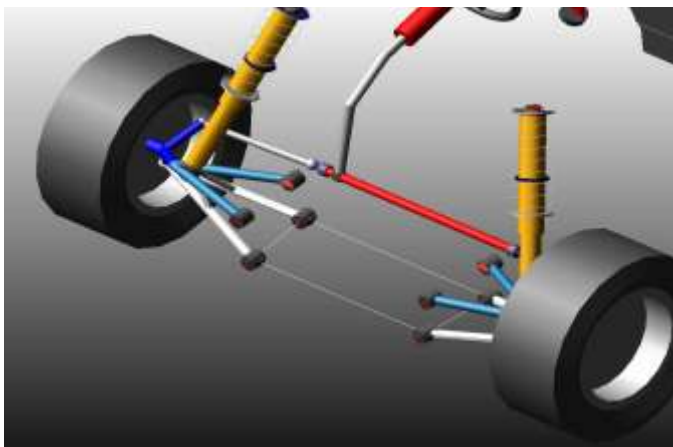


Figure 7.3 Flexible Arms imported into the original assembly.

During maneuvering of the car, the control arms experience the greatest forces when the vehicle is experiencing a cornering event. Hence, to see if the arm has failed due to the dynamic forces generated during cornering, a CRC test is simulated with the flexible arms as part of the assembly.

To simulate the constant radius cornering test, the following inputs are given.

Vehicle	Off-road Rally Car
Road	2D flat
Step Size	0.1
Turn Radius	15 m
Turn Direction	Left
Duration of Manoeuvre	14 s

Initial Velocity	10 kmph
Final Velocity	30 kmph

Table 7.1 Input for CRC analysis using flexible body.

After simulation, using Adams Durability plugin, the hotspots in the control arm on the right side can be observed. Hotspots are the nodes at which there are highest stresses are acting. Von Mises stresses in the arm are observed during CRC test. The hotspots table for right sided LCA are given as follows.

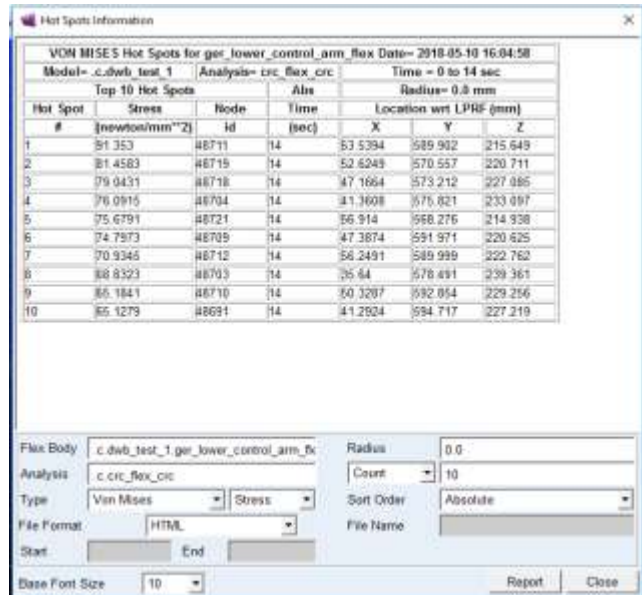


Figure 7.4 Hotspots of Von Mises stresses on the right LCA.

It is seen that the maximum Von Mises stress acting on the arm is around 91.3 MPa. This region which is experiencing the highest stress value is shown in the figure below.

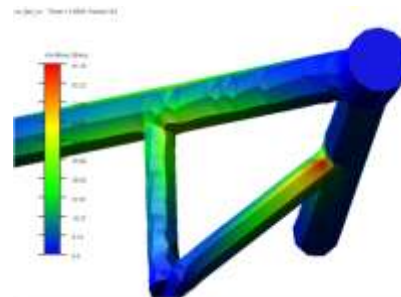


Figure 7.5 High stress region in the lower control arm.

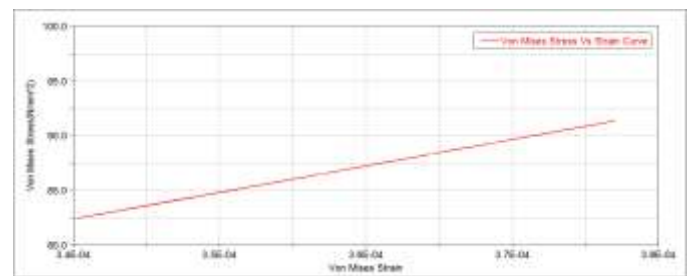


Figure 7.6 Stress Strain curve to observe Von Mises stresses in the right LCA.

The graph shows Von Mises stress strain curve of the LCA on the right side during CRC test. It is seen that the maximum stress developed in the arm is around 91.3 MPa. It is clear from the plot that stress is directly proportional to strain and the material is still behaving elastically. The yielding will only start to take place at 250 MPa for steel.

Hence, it is proved that the control arm failure is not related to any dynamic loading during the maneuver. There are other reasons that could have caused failure in the arm.

On observing the failure area in the real car, it is seen that the arm has failed at the place of weld used to connect two bodies of the link.

The welding region clearly looks like it has been welded with bad welding techniques.

Bad welds lead to voids and sharp corners in the material. These act as high stress concentration regions which are prone to act as sources of macroscopic crack sites. The cracks have propagated through the weld seam upon vehicle dynamic loading and have ultimately given in structurally.

VIII. CONCLUSION AND FUTURE SCOPE

J. Conclusion

Modelling of the vehicle has been carried out by referring the hardpoints. The hard points are extracted from the physical prototype using a measure tape accurately. Using these data, the template for front, rear suspensions and steering are created. The subsystems are developed from this and the full car assembly is created using Adams Car.

Validation of the individual suspension systems have been carried out. The front and rear suspension subsystems have been validated using Kinematics analysis. The MBD model conforms closely with the physical prototype. Along with this, full vehicle analyses are conducted following the validation of individual suspension subsystems.

In Full Vehicle analyses, Maintain Analysis is conducted to observe the reaction forces produced at the tire contact patch when the vehicle is travelling at constant velocity along a straight path. Using this analysis, a close conformity in the results is observed between the MBD model and Physical car when the location of CG was closely observed.

Constant Radius Cornering analysis is conducted to determine the understeer gradient. It is observed that the car behaves with understeer conditions. The forces generated in the front LCA right arm front link are observed during cornering. The design of the Lower Control Arm is slightly modified and CRC test is conducted. The forces developed in the right LCA front link is observed to be lesser in the modified design compared to the original design.

To analyze the failure in right LCA front link, flexible body analysis is carried out using MSC Apex, MSC Nastran and MSC Patran. The resulting Modal Neutral File is switched for the rigid LCA on right and left side. Using Adams Durability, the Hot Spots table is generated to see the highest stress developed at the corresponding node and the von mises stress vs strain graph is plotted. It is clearly observed that the arm experiences only a max of 91 MPa stress and still behaves elastically, i.e., yielding has not started. With this it is concluded that the LCA in the rally car has not failed due to any dynamic loads during maneuver. Reason for failure can be due to poor welding techniques and manufacturing processes employed.

K. Scope for Future Work.

- Hook Joints can be used to mount the struts instead of welding them to the chassis thus providing the suspension with extra degrees of freedom to actuate.
- Bushes with known optimum values can be used in places necessary to conduct Compliance part of K and C analysis.
- The K and C analysis can be conducted physically using SPMM (Suspension Parameter Measuring Machine) test rig. The results obtained can be plotted over the MBD results to see the close conformity more clearly.
- The suggested improvement in design of the LCA can be fabricated and employed into the physical car to see improvement in results.
- Control arms can be employed into the rear suspension of the physical car to see improvement in the handling characteristics.

REFERENCES

- [1] Samuel Joseph (2013), Design and Development of Steering and Suspension System of a Concept Car.
- [2] Thomas D. Gillespie (1992), Fundamentals of Vehicle Dynamics, Society of Automotive Engineers Inc.
- [3] Richard Stone and Geoffrey K. Ball (2004), Automotive Engineering Fundamentals, SAE International.
- [4] Shaopu Yang, Yongjie Lu and Shaohua Li (2013), An overview on vehicle dynamics, Springer-Verlag Berlin Heidelberg.
- [5] Emre Sert and Pinar Boyraz (2017), Optimization of Suspension System and Sensitivity Analysis for Improvement of Stability in a Midsize Heavy Vehicle, Engineering Science and Technology, an International Journal.
- [6] Anoop M. Vasudevan and Jithin Bhaskar, A study on the Handling Characteristics of a Car during Cornering with Variation in Wheel Geometry Parameters, VIT University, Vellore.
- [7] Sarel F. van der Westhuizen, Pieter S. Els (2012), Slow active suspension control for rollover prevention, Journal of Terramechanics.
- [8] N. Ikhsan, R.Ramli and A. Alias (2015), Analysis of the kinematics and compliance of a passive suspension system using Adams Car, Journal of Mechanical Engineering and Sciences

PERFORMANCE EVALUATION OF SOLAR TRACKING SYSTEM WITH REFLECTORS

MADHU MC¹, C S MALA² & K. BADARI NARAYANA³

¹Assistant Professor, Mechanical Engineering, Bmsit&M, Bengaluru, India

²Associate Professor, Telecommunication Engineering, Bmsit&M, Bengaluru, India

³Principal Consultant, COE Aerospace & Defence, VTU Nagarabhavi, Bengaluru, India

ABSTRACT

An automatic solar panel orientation system has been designed to achieve high performance by tracking the sun rays throughout the day. The solar tracking system was connected to the DC motor which is driven by the shaft and the shaft in turn is connected to the solar panel. The main panel rotates to harvest the maximum sunlight. Two reflectors fixed on each side of the panel ensure that the light radiation is directed on to the panel. A bearing was mounted on the column shaft to facilitate the rotation to the tracker. A motor is provided to drive the shaft and it tracks the motion of the sun across the sky and ensures the maximum amount of radiation to fall on the panels. The efficiency of the system was found to be higher using the solar tracking system with reflectors, when compared to the system without reflectors. To achieve this, the solar tracking system was implemented using a DC geared motor, solar photovoltaic panels and geared wheel arrangement.

KEYWORDS: Photo Voltaic Cell, Reflectors, Solar Panel, Solar Panel Efficiency & Solar Tracking System

Received: Jul 24, 2018; **Accepted:** Aug 14, 2018; **Published:** Nov 09, 2018; **Paper Id.:** IJMPERDSPL201822

INTRODUCTION

Solar energy is one of the most promising renewable energy sources. There is a huge conversion potential of solar energy into electrical power. The conversion of solar radiation into electrical energy using Photovoltaic (PV) effect is a very promising technology since it is a clean, silent and reliable technology. The maintenance cost of Solar Photovoltaic Cells is very low. It has been found that this technology has a very small ecological impact. Performance of a photovoltaic array depends primarily on sunlight. Climatic conditions like clouds and fog significantly affect the amount of solar energy that is received by the PV array and therefore impacts its performance.

Literature Review

An extensive literature survey has been carried out. Different types of sun-tracking systems and their merits and demerits have been discussed by Hossein Mousazadeh [1]. The author finds that the most efficient and popular sun-tracking device to be the polar-axis and azimuth/elevation type tracking system.

Ahmed Abu Hanieh [2] explains that two degrees of freedom can be done using part of the power output of the solar panel. In his project, the kinematics of the system used is simple and can easily be controlled using astronomic geometric calculations taking into account the symmetry of the system.

Nader Barsoum [3] has developed and implemented a solar tracking system with two degrees of freedom and it also detects the sunlight using sensors. This Peripheral Interface Controller was the brain of the entire tracking system,

and it was programmed to detect the sunlight through the sensors and then actuate the motor to the position.

Some work has been carried out on the solar radiation falling perpendicular to the Photovoltaic panel. It was found that [4] a system which implemented tracking produced an average of 1.4 times more heat energy in comparison with the stationary collector of the same size.

Methodology

The photovoltaic cell is the basic building block of a photovoltaic system. The individual cells varies from 0.5 inches to 4inches. One cell produces an electrical power between 1 to 2 watts. The PV Panels are fabricated using these cells. The PV panels are connected in series to increase the total power generated. These panels produce electricity as the sun rays fall on them by converting solar radiation into electrical power. Each PV panel produces an approximate of 75 watts of power with an efficiency of around 18%. In order to increase the efficiency of the panels, various methods are adopted. One such method is the automatic solar tracking system. This system facilitates the run rays to fall on the PV panels for the longer duration of time thus enabling higher electrical power generation, which in turn increases the efficiency of the panels.

A solar tracking system basically consists of a DC gear motor to turn the panels in the direction of sunlight. In our work, a DC gear motor, two solar cells, and a gear wheel arrangement are being used for the tracking system. Two reflectors are fixed on each side of the panel. This ensures that the sunlight falling is directed on the panel. A motor is driven by the shaft. The shaft is connected to a solar panel.

It tracks the motion of the sun across the sky and ensures the maximum amount of radiation falls on the panels. The solar panels are positioned to receive sufficient amounts of airflow. This induces natural cooling, which help to keep the efficiency rate high.

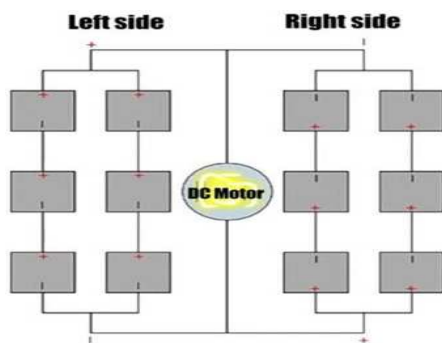


Figure 1: Circuit Diagram For The Solar Tracker Reflectors

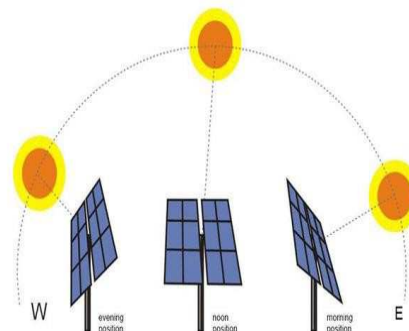


Figure 2: Sun Tracking System

Aluminium foil is prepared in thin metal leaves with a thickness less than 0.2 mm (7.9 mils); The foil is pliable and can be readily bent or wrapped around objects. It has 87-89% reflectivity.

Bevel gears are useful when the direction of a shaft's rotation needs to be changed. They are usually mounted on shafts that are 90 degrees apart but can be designed to work at other angles as well.



Figure 3: Sun Tracking with Reflectors

Experimentation

Experiments were carried out to investigate the performance improvement in the efficiency of solar PV panels. The entire set up for tracking the sunlight falling on the solar PV panels is represented in the Figure 2. Generally, a sun tracker is employed to increase the efficiency of the panel. In our work, a reflector is employed along with the sun tracker, in order to increase the efficiency further.

Experiments were conducted without the reflectors first. The set up of the same is shown in Figure 3. The experimentation results were obtained and the same experiment was conducted with reflectors and the results were noted. It was observed that the efficiency of the panel greatly improved with the addition of the reflectors.

Efficiency of Solar Panel without Reflectors

Solar panels are fixed at an angle of the latitude of the location. The latitude for Bangalore is 12.8° and hence the solar panels are inclined at 13° . This enables maximum rays to fall on the panel, which generally is from 9 am to 3 pm.

Efficiency of Solar Panel with Reflectors

A solar tracker is a device which is fitted on to the solar panels that track the motion of the sun across the sky and ensures the maximum amount of radiation fall on the panels. A bearing is mounted on the column shaft to provide rotation to the tracker. A motor is provided to drive the shaft.

Solar Panel Conversion Efficiency Calculation

Solar panel conversion efficiency is the ratio of the electrical output of a solar cell to the incident energy (falling on the cell) in the form of sunlight.

The energy conversion efficiency (η) of a solar cell is the percentage of the solar energy that is converted into electrical energy. This is calculated by dividing a cell's power output (watts) at its maximum power (P) by the input light (W/m^2) and the surface area of the solar cell (m^2).

$$\text{Solar Conversion Efficiency} = P / (E * A) * 100 \quad (1)$$

$$\text{Solar cells power output is calculated by } P(W) = V * I \quad (2)$$

$$\text{Area of solar panel} = 0.133 \text{ m}^2$$

$$\text{Energy input} = 1000 \text{ W/m}^2$$

RESULTS AND DISCUSSIONS

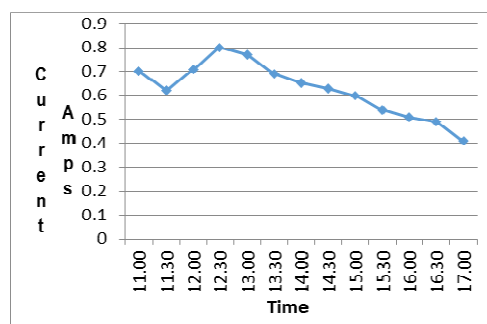
Results for Solar Panels without Reflectors

An extensive research has been carried out to explore the conversion efficiency with and without reflectors for the photovoltaic solar panels.

The observations of the experiments are presented in the tables and graphs. Table 1 presents the results of experiments conducted without reflectors. It is seen that the voltage is at a peak at 16.00. hours and the current measured at that point of time was 0.51 amps, which resulted in yielding a power of 10.618watts with an efficiency of 7.96%. The least voltage observed was in the range 14.00 hours to 14.30hours, at which points the current measured was 0.65Amps and 0.63Amps, yielding a power of 12.62watts and 12.42watts yielding an efficiency of 9.75 and 9.45% respectively. It is observed that at 12.30 hours, the voltage it measured was 20.41Volts and a current of 0.8A which has generated a power of 16.328watts yielding an efficiency of 12.24% which is the maximum recorded during the course of the experiment. The point to be noted here is that at 12.30hours not only is the efficiency the highest but the peak current of 0.8 A is observed. The results of Table 1 is plotted as a graph of current versus time and is presented in Graph 1. and the efficiency versus Time is presented in Graph 2.

Table 1: Experimentation Results for Solar Panels without Reflectors

Time	Voltage (V)	Current (A)	Power (W)	Efficiency (%)
11.00	20.6	0.7	14.42	10.81
11.30	20.7	0.62	12.834	9.62
12.00	20.5	0.71	14.555	10.91
12.30	20.41	0.8	16.328	12.24
13.00	20.03	0.77	15.631	11.72
13.30	20.02	0.69	13.81	10.35
14.00	20	0.65	13	9.75
14.30	20	0.63	12.6	9.45
15.00	20.7	0.6	12.42	9.31
15.30	20.7	0.54	11.178	8.38
16.00	20.82	0.51	10.618	7.96
16.30	20.6	0.49	10.094	7.57
17.00	20.6	0.41	8.446	6.33



Graph 1: Current vs Time for Solar Panels without Reflectors

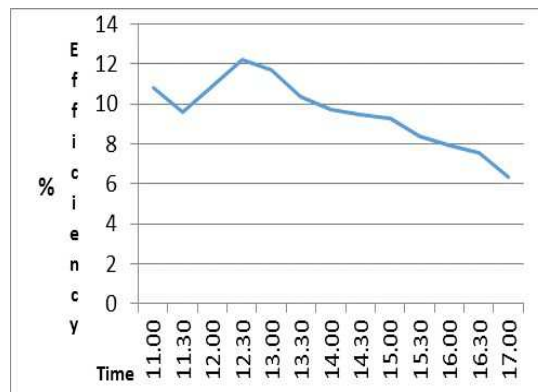
Results for Solar Panels with Reflectors

The results for the experimentation of the Solar Panels with reflectors are presented in Table 2. The experiment observation reveals that the voltage measured is maximum at 11.00hours measuring a current of 0.8 Amps giving a power of 16.64 watts yielding an efficiency of 12.48. It was observed from the Table.2 that the minimum voltage measured at

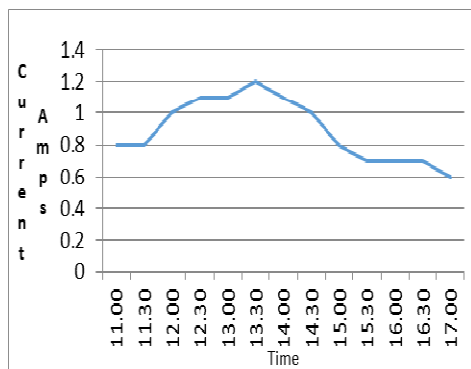
14.00 Hours and at that time the current measured was 1.1amps and power was 22W and an efficiency of 16.5%. The maximum efficiency yielded was at 13.30hours, when the voltage was 20.2 volts and a current of 1.2Amps, generating power of 24W yielding an efficiency of 18.18%. It was also observed that the peak current was obtained at 13.30 hours. The least efficiency and current were seen from 16.00 Hours onwards. The least observed efficiency was 9.27% at 17.00 hours. The graph of current versus time is presented in Graph.3. It was observed from the graph that the current is maximum at 13.30 hours. Graph.4 represents the relationship between time and efficiency.

Table 2: Experimentation Results for Solar Panels with Reflectors

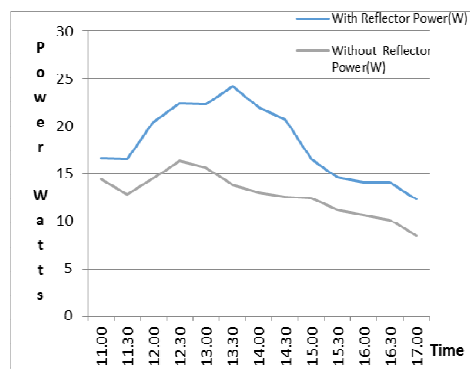
Time	Voltage (V)	Current (A)	Power (W)	Efficiency (%)
11.00	20.8	0.8	16.64	12.48
11.30	20.7	0.8	16.56	12.42
12.00	20.5	1	20.5	15.37
12.30	20.4	1.1	22.44	16.83
13.00	20.3	1.1	22.33	16.74
13.30	20.2	1.2	24.24	18.18
14.00	20	1.1	22	16.5
14.30	20.7	1	20.7	15.52
15.00	20.7	0.8	16.56	12.42
15.30	20.8	0.7	14.56	10.92
16.00	20.6	0.7	14.04	10.53
16.30	20.6	0.7	14.04	10.53
17.00	20.6	0.6	12.36	9.27



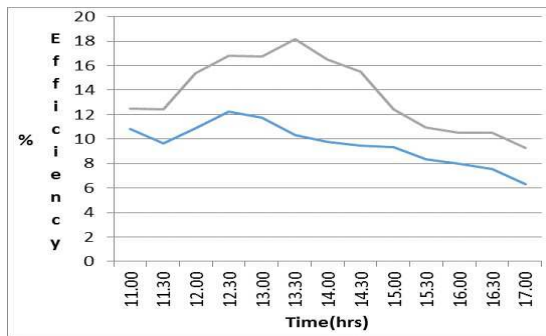
Graph 2: Efficiency vs Time for Solar Panels without Reflectors



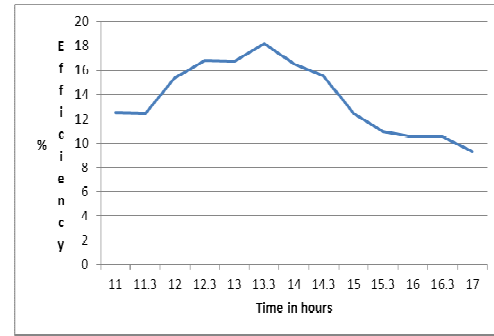
Graph 3: Current vs. Time for Solar Panels with Reflectors



Graph 4: Efficiency vs Time for Solar Panels with Reflectors



Graph 5: Comparison of the Output Power Without Efficiency with and Without Reflectors



Graph 6: Comparison of Solar PV Panel with and Reflectors

After obtaining the results for power generation and efficiency for Solar PV panels with reflectors and without reflectors, a comparison was made and inferences were drawn. Comparisons of the output power is presented in Graph 5 and comparison of efficiencies with and without reflectors are presented in Graph 6.

It was observed from graph 5 that the maximum power generated is 16.328watts for solar panel without reflector, whereas with reflectors the maximum power generated was 24.24W. Table 1 and Table 2 indicate that the efficiency without reflectors was 2.24%, whereas with reflectors was 18.18%

The above results clearly indicated that the power generation in Solar PV Panels has greatly increased by 7.912W by interfacing reflectors to the solar panels. It also indicated the rise in efficiency by 5.94 % due to the introduction of reflectors.

For solar PV panels, an increase in conversion efficiency even by 1% is a significant achievement, as a large number of panels are always connected for higher power generation. For a power generation of 10kW, on an average of 100 solar panels are required. Therefore it was clear that a small increase in efficiency would result in a significant increase when used for larger scale power generation.

We compared the solar tracking system by the use of a solar cell with a fixed solar panel system and found that the efficiency of tracker-based solar tracking system was improved by 23%.

CONCLUSIONS

By using reflectors, it was observed that efficiency of solar panel increased by 8% for a fixed interval of time over a day. Also, a solar cell with the tracking system was more efficient than a fixed solar panel system. This system was found to be more efficient and cost-effective in the long run. From the results, it was found that, by automatic tracking system and reflectors, there was the improvement in efficiency when compared with a non-tracking system.

REFERENCES

1. Hossein Mousazadeh, "A review of principle and sun tracking methods of maximising solar system output," *Renewable and sustainable energy reviews*, Elsevier, Pergamon vol 13(2009), pp1800-1818.
2. Ahmed Abu Hanieh, "Solar Photovoltaic panels tracking system," *Advances in Dynamical systems and control*, Birzeit univ., 15January 2015, pp 30-37.
3. Nader Barsoum, "Fabrication of dual –axis solar tracking controller project", *Intelligent control and automation*, Vol 2, No 2, pp.265-273

4. L. Kancevica et al, "Renewable Energy and Energy Efficiency" Proceedings of the international scientific conference, Jelgava- 2012.
5. R. Condit and D. W. Jones, "Simple DC motor fundamentals," Texas Instruments. Publication AN907, pp. 1 – 22, 2004.
6. S. J. Hamilton, "Sun-tracking solar cell array system," University of Queensland Department of Computer Science and Electrical Engineering, Bachelors Thesis, 1999.
7. M. F. Khan and R. L. Ali, "Automatic sun tracking system," presented at the Engineering Conference,
8. Nader Barsoum, "Fabrication of Dual-Axis Solar Tracking Controller Project", Curtin University, Sarawak, Malaysia, Intelligent Control and Automation, 2011, Vol2, pp. 57-68.
9. Antonio L. Luque; Viacheslav M. Andreev "Concentrator Photovoltaics". Springer Verlag. (2007).
10. David Cooke, "Single vs. Dual Axis Solar Tracking", Alternate Energy eMagazine, April 2011
11. Prof. Pooja K. Chhatwani, Prof. Jayashree Somani, "Intelligent solar tracker system implemented on 8051 microcontroller". International Journal of Engineering Trends and Technology, Vol.4, Issue 9, pp 4267-4271, Sep.2013
12. http://www.nrel.gov/learning/re_photovoltaics.html?print
13. <http://www.solar-facts.com/panels/paneltypes.php>.
14. S. P. Sukhatme, J. K. Nayak, "Solar Energy- Principles of thermal collection and storage", Third Edition, pp.1-460
15. Optimal design of orientation of PV collector with reflectors (<http://www.sciencedirect.com/science/article/pii/S0306261910000462>)
16. A. K. Saxena and V. Dutta, "A versatile microprocessor based controller for solar tracking," in Proc. IEEE, 1990, pp. 1105 – 1109.
17. T. A. Papalias and M. Wong, "Making sense of light sensors," <http://www.embedded.com>, 2006.

EFFECT OF INJECTOR OPENING PRESSURE ON THE PERFORMANCE AND EMISSION CHARACTERISTICS OF DIRECT INJECTION DIESEL ENGINE WITH METHYL ESTERS OF CALOPHYLLUM INOPHYLLUM (SURAHONNE) OIL

SHRIPAD DIWAKAR¹ & RANA PRATAP REDDY²

¹Assistant Professor, Department of Mechanical Engineering, BMSIT &M, Bengaluru, Karnataka, India

²Principal, Department of Mechanical Engineering, Global Academy of Technology, Bengaluru, Karnataka, India

ABSTRACT

Biodiesel is one of the most promising alternatives for diesel needs. Biodiesel produced from edible oils is not economically feasible, and may also create shortage of oil for daily food. This required identification of new kinds of non-edible vegetable oils. Non edible feed stocks such as Mahua, Jatropha, Pongamia Pinnata, Simarouba Glauca, Calophyllum Inophyllum and Neem etc., are reported to be feasible choices for developing countries including India. One of variables, which affect the performance and emission of a fuel engine, is injector opening pressure. Hence, in the present experimental work, effect of Injector opening pressure on the performance and emission characteristics of the engine was studied. A four stroke Direct Injection single cylinder diesel engine was used for experimental work. Three injector opening pressures 180 bar, 200 bar and 220 bar were considered for the present work. The higher injector opening pressure results in better atomization and penetration of methyl ester of Calophyllum Inophyllum oil. The exhaust emission such as Smoke, Unburnt hydro carbon and carbon monoxide of 200 bar injector pressure is lower than other pressures. The experimental investigations reveal that, the better performance and emission characteristics among the biodiesel blends are obtained at Injection opening pressure of 200 bar with C20 blend of Calophyllum Inophyllum Methyl Ester.

KEYWORDS: Biodiesel, Performance, Emission, Calophyllum Inophyllum & Injector Opening Pressure

Received: Jul 24, 2018; **Accepted:** Aug 14, 2018; **Published:** Oct 23, 2018; **Paper Id.:** IJMPERDSPL20188

INTRODUCTION

Due to excess use of the petroleum based fuels for industry and automobile application in present time, the world is facing severe problems like energy crisis environmental pollution and global warming. Therefore, global consciousness has started to grow to prevent for energy crisis by developing alternative fuel sources for engine applications. Many research programs are going on to replace diesel fuel with suitable alternative fuel like biodiesel. Non edible sources like Jatropha oil, Mahua oil, Neem Oil, Karanja Oil, Simarouba Oil etc. are being investigated for biodiesel production. In developing countries like India, it is possible to grow these non-edible oils, but not economically feasible to convert them to methyl esters undergoing different chemical processes. Biodiesel contains no petroleum, but can be blended at any level with petroleum diesel to create a biodiesel blend. Biodiesel blends can be used in Compression Ignition engines with little or no modifications. Several investigators [1-7] have reported experimental investigations on different neat vegetable oil in D.I. diesel

engine without varying injector opening pressure.

MATERIALS AND METHODS

Process of Extracting

The extraction of biodiesel process is carried out by base catalyzed transesterification process. To one liter of raw Calophyllum Inophyllum oil is heated up to 70°C, 300 ml of methanol and 5-7 gms of NaOH(Catalyst) are added and the mixture is maintained at 65-70° C for about 1½ hours and stirred continuously. The mixture is allowed to settle for 20-30 min, until the formation of biodiesel and glycerin layers. The glycerin is removed from the bio diesel in a separating funnel. The biodiesel produced from Calophyllum Inophyllum is ready to use.

Transesterification

It is most widely used and important method to reduce the viscosity of vegetable oils. In this process, triglyceride reacts with three molecules of alcohol in the presence of a catalyst producing a mixture of fatty acids, alkyl ester and glycerol. The process of removal of all the glycerol and the fatty acids from the vegetable oil in the presence of a catalyst is called, transesterification.

Physical and chemical properties are more improved in esterified vegetable oils, because they contain more Cetane number than the diesel fuel. These parameters induce good combustion characteristics in vegetable oil esters. Hence, unburnt hydrocarbon level is decreased in the exhaust. It results in lower generation of carbon monoxide and hydrocarbon in the exhaust compared to diesel fuel. The methyl esters of vegetable oils contain more oxygen and lower calorific value than Diesel. Hence; it enhances the combustion process and generates low emission compared to diesel fuel.

PROPERTIES OF DIESEL AND BIODIESEL BLENDS

After Transesterification process, the properties of Calophyllum Inophyllum blends were determined. It was found that the properties of Calophyllum Inophyllum oil blends were similar to diesel.

Table 1: Properties of Diesel and Calophyllum Inophyllum Blends

Properties	Diesel	C20	C40	C100
Kinematic viscosity at 40°C (Cst)	3	2.9	4	6.3
Calorific Value(kJ/kg)	42856	42705	40105	35811
Density(kg/m ³)	830	850	855	900
Flash point(° C)	54	59	76	174
Fire Point (° C)	64	64	93	186

EXPERIMENTAL SET UP

The experiment setup enables to study performance, emission and combustion characteristics. The experiments have been carried out on a DI compression ignition engine for various blends of Calophyllum Inophyllum oil with diesel (C10, C20, C30, C40 and C100) with varying brake power. The experiment is carried out at constant compression ratio of 17.5:1 and at different injection pressure of 180 bar, 200 bar and 220 bar, respectively. Experimental set up consists of;

Engine

The engine chosen to carry out experimentation in a single cylinder, four Stroke, vertical, water cooled, direct

injection computerized TV-1 Kirloskar make C.I.Engine. This engine can withstand higher pressure encountered, and also being used extensively in agricultural and industrial sectors.



Figure 1: Photograph of Engine Set up

Dynamometer

The engine has a DC electrical dynamometer to measure its output. The dynamometer is calibrated statistically before use. The dynamometer is reversible. i.e., it works on monitoring as well as an absorbing device. Load is controlled by changing the field current. Eddy current dynamometer theory is based on Fleming's right hand rule.

Exhaust Gas Analyzer

The emission test is done with AVL DITEST MDS 480 exhaust gas analyzer 1000 modules. The product has additional features to save a vehicle and customer database, radio connected measuring chamber up to the option of designing the protocols individually. Due to the robust and intuitive application of the device, the tester can be used to get sophisticate and accurate emission measurement.

Table 2: Specifications of the Engine

Particulars	Specifications
Manufacturer	Kirloskar Oil Engines Ltd,India
Model	TV-1 SR, Naturally aspirated
Engine	Single Cylinder, Direct Injection
Bore / Stroke	87.5 mm / 110 mm
Compression Ratio	17.5 : 1
Speed	1500 RPM
Rated Power	5.2 kW
Working cycle	4 stroke
Injection Pressure	200 bar / 23° before TDC
Response time	4 micro seconds
Type of sensor	Piezo electric sensor

RESULTS AND DISCUSSIONS

Performance Characteristics

- **Brake Thermal Efficiency**

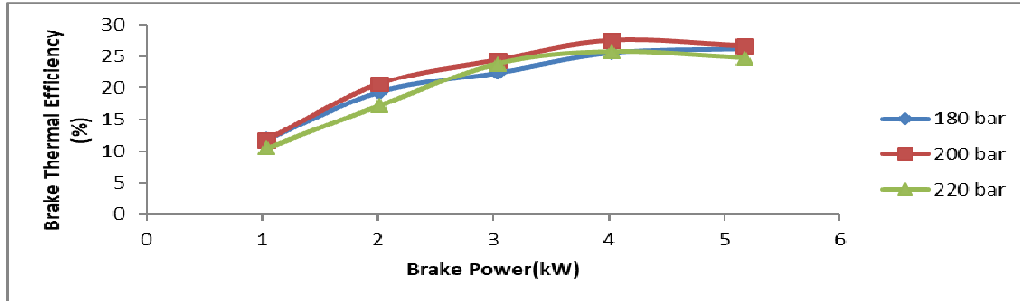


Figure 2: Variation of Brake Power with BTE

Figure 2 shows the variation of brake power with Brake Thermal efficiency. It is observed that the injector opening pressure increases, BTE also increases. The injector opening pressure of 200 bar results in higher BTE.

- **Brake Specific Energy Consumption**

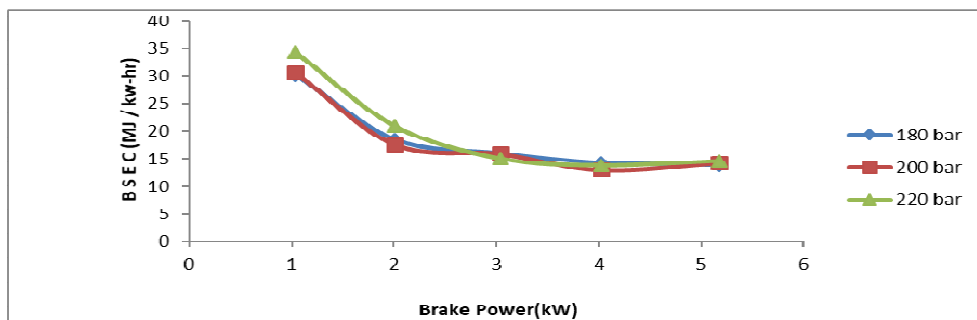


Figure 3: Variation of Brake Power BSEC

The variation of Brake Specific Energy Consumption (BSEC) with load is shown in Figure 3. At low loads, there is a slight variation in BSEC. But as the load increases, BSEC also varies. The injector opening pressure of 180 requires higher energy at full load due to poor combustion of the fuel

- **Exhaust Gas Temperature**

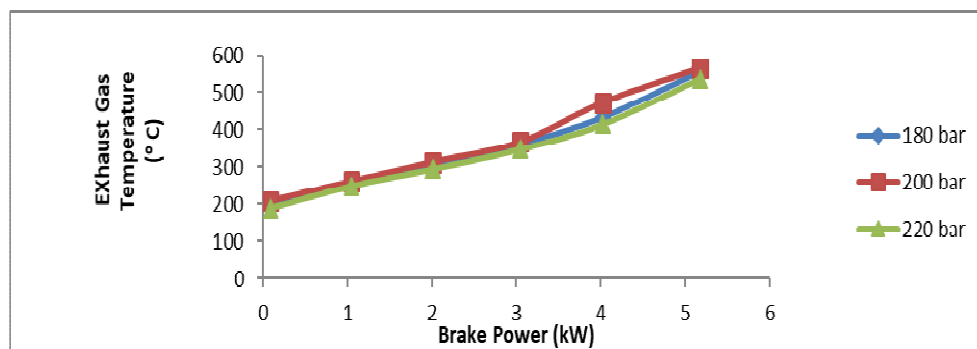


Figure 4: Variation of Brake Power with EGT

Figure 4 shows the variation of smoke emission with load at different injector opening pressures. From the figure it is observed that the injector opening pressure results in higher smoke emission. This is due to poor combustion of the fuel. The injector opening pressure of 200 bar results in lower smoke emission.

- **Air Fuel Ratio**

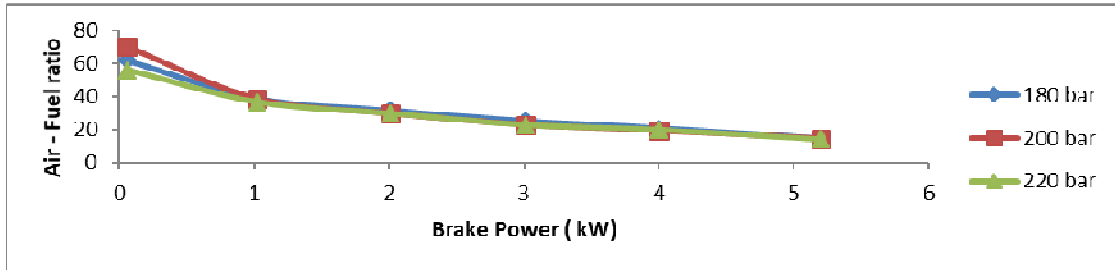


Figure 5: Variation of Brake Power with Air Fuel Ratio

The variation of air fuel ratio with brake power at different injection pressures are shown in the figure 5, from the graph, it is evident that, air fuel ratio decreases as the load increases. This is due to the compensation of the load can only be done with increasing the quantity of the fuel injection to develop the power required to bare the load.

Emission Characteristics

- **Hydro Carbon Emission**

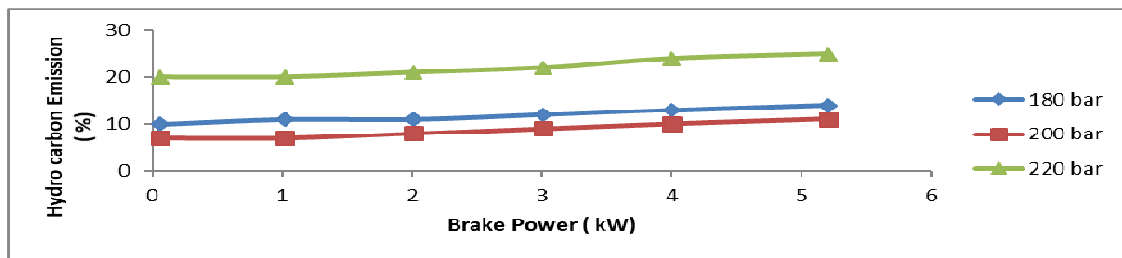


Figure 6: Variation of HC Emission with Brake Power

Figure 6 shows the variation of hydrocarbon emission with brake power for different injection opening pressures. HC emission increases with increase in load. Injection opening pressure of 200 bar shows the less HC emission, as compared to 180 bar and 220 bar IOP.

- **CO Emission**

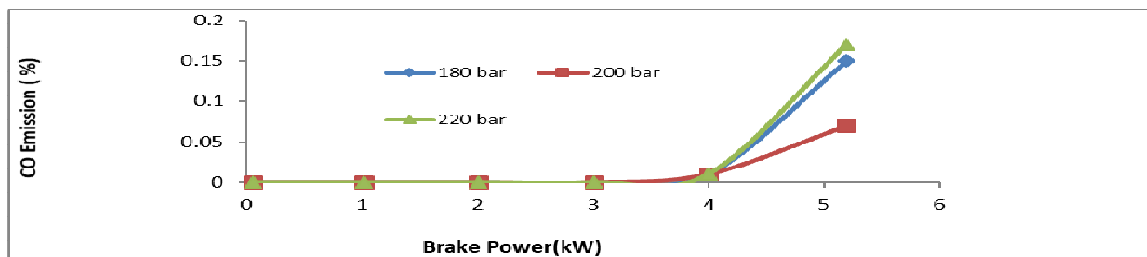


Figure 7: Variation of CO Emission with Brake Power

The variation of carbon monoxide (CO) emission with load at different injector opening pressure is shown in Figure 7. At low loads, there is a slight variation in CO emission at different injector opening pressures. At higher loads,

the injector opening pressure of 180 bar results in higher CO emission due to incomplete combustion of the fuel. But, the injector opening of 200 bar results in lower CO emission than other pressures at higher loads.

Combustion Characteristics

- **Variation of Crank Angle with Cylinder Pressure**

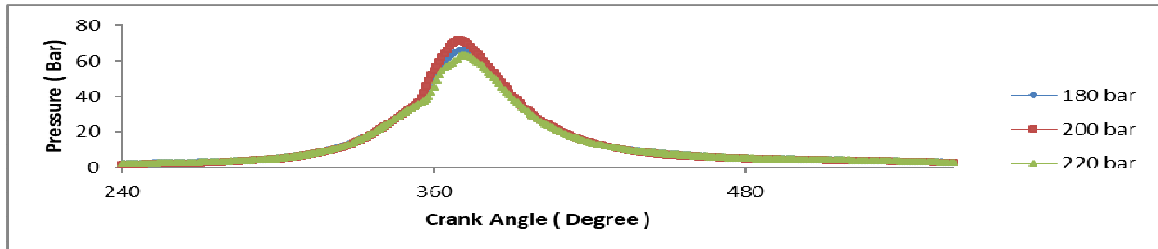


Figure 8: Variation of Crank Angle with Pressure

Figure 8 shows the variation of cylinder pressure with load at different injector opening pressures, a slight variation in pressure was observed at 60% load. At 80% and full loads, 180 bar results in pressure rise after top dead center. This shows that, late burning of fuel and hence knocking is developed. There is a slight variation in pressure rise between 200 bar and 220 bar IOP

- **Heat Release Rate**

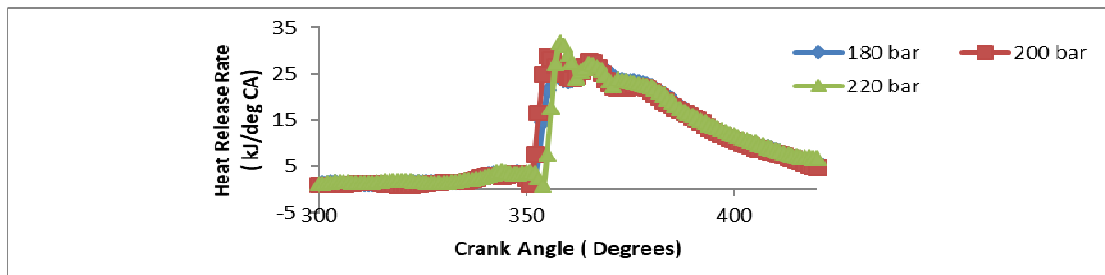


Figure 9: Variation of Crank Angle with Heat Release Rate

Figure 9 shows that the variation of heat release rate with respect to crank angle. It is observed that, all the biodiesel blends at different injection pressures traces the same path. The heat release rate for all tested fuel was slightly less than that of diesel; this may be attributed to low vaporization, high viscosity and low peak pressure of blends as compared to diesel.

- **Variation of Crank Angle with Cumulative Heat Release Rate**

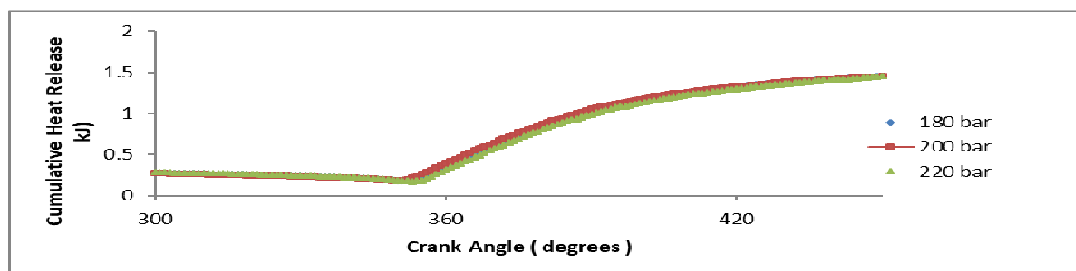


Figure 10: Crank Angle vs Cumulative Heat Release Rate

Figure 10 shows the variation of cumulative heat transfer with crank angle. It is observed that, all the blends of Calophyllum Inophyllum biodiesel and its blends trace the same path as that of diesel at all injection pressures. Initially, cumulative heat transfer decreases at first cycle, and then increases in the second and further cycles, as shown in figure.

CONCLUSIONS

From the test results, the following conclusions are drawn.

- The brake thermal efficiency increases with increase in injection pressure.
- Injector Opening pressure of 200 bar results in higher brake thermal efficiency.
- Injector opening pressure of 180 bar results in poor combustion and knocking.
- Low smoke and CO emissions were observed at the injector opening pressure of 200 bar.
- Higher exhaust gas temperature was observed with the pressure of 180 bar.
- Increased CO emission at higher biodiesel blend with lower injection pressure
- HC emission is lower than diesel. At higher blend and lower injection pressure, HC emission is higher compared with other conditions.

ACKNOWLEDGEMENT

Our special thanks are due to Principal, HoD, Dr.M.C.Navindgi, Professor and Technical staff Mechanical Engineering Department of PDA college of Engineering, Kalaburagi, India for giving the permission to carry out the experimentation work, which includes computerized D.I. diesel engine test rig exhaust gas analyzer and smoke meter.

REFERENCES

1. *Sharanappa, Rana Pratap Reddy, Ch.Suryanarayana Murthy, Mahua oil(Madhuca Indica),Preparation of mahua oil methyl ester, Energy & fuel Users Journal, 2008, 58(2), pp 1-7*
2. *Ramesha D K, B J Ranganath, N Rana Pratap Reddy, Characteristics of Ethanol Esterified Pongamia Pinnata and Madhuca Indica oils for compression Ignition Engine applications, Journal of middle European construction and design of cars, Nov 2007, Vol 5,pp 31-36.*
3. *Ravi S.D, S.R.Hotti, O.D.Hebbal – Performance, Combustion and Emission characteristics of Single cylinder Diesel Engine using Calophyllum Inophyllum(Surahonne oil),International Journal of Engineering Research & Technology,Vol 3,Issue 9, September 2014, pp 378-385.*
4. *L.Jeyraj Kuamr, G.Anbarasu, T.Elangovan, Effects of nano additives on performance and emission characteristics Calophyllum Inophyllum Biodiesel, International Journal of ChemTech research,2016, Vol-09, No-04,pp 210-219*
5. *G.Deepnkumar, Experimental Investigation of Performance and Emission characteristics of Tamanu oil as alternative fuel in C.I.Engine – International Journal of Engineering and Computer Science: ISSN 2319-7242, Volume 4, Issue 6, June2015, pp 12471-12475.*

6. B.K.Venkanna, C.Venkataramana Reddy, *Influence of Injector opening pressures on the performance, emission and combustion characteristics of DI diesel engine running on calophyllum Inophyllum linn oil(honne oil) ,Intl Jour of Renewable Energy*, Vol 6, No 1, June 2011, pp 15-19
7. I.M.Rizwanul Fattah, H.H.Masjuki, Kalam, Abdul wakil, Ashraful Alam, Shahir Shawkat Ali- *Experimental investigations of performance and regulated emissions of a Diesel engine with Calophyllum Inophyllum Bio diesel blends accompanied by oxidation inhibitors*, Article in *Energy conversion and Management* 83:232-240, July 2014.
8. Chavan S.B., Kumbhar R.R. and Deshmukh R.B. "Calophyllum Inophyllum Linn (Honne) Oil, A Source for Biodiesel Production", *Research Journal of Chemical Sciences*, ISSN 2231-606X, Vol. 3(11), November -2013, pp 24-31.
9. Umesh, K. S., Pravin, V. K., & Rajagopal, K. (2014). EXPERIMENTAL INVESTIGATION AND CFD ANALYSIS OF A MULTI-CYLINDER FOUR STROKE SI ENGINE EXHAUST MANIFOLD FOR OPTIMAL GEOMETRY TO REDUCE BACKPRESSURE AND TO IMPROVE FUEL EFFICIENCY. *International Journal of Automobile Engineering Research and Development*, 4, 13-20.
10. Narayana. L, Gattamaneni. R, Subramani. S, "Combustion and emission characteristics of diesel engine fuelled with rice bran oil methyl ester and its diesel blends", *Thermal science* 12, (2008), pp 139-150.
11. K. Nanthagopal, B. Ashok, R. Thundil Karuppa Raj., *Influence of fuel injection pressures on Calophyllum inophyllum methyl ester fuelled direct injection diesel engine. Energy Conversion and Management. Volume 116, 15 May 2016, Pages 165–173.*

Moisture Sensors for Automatic Watering System For Indoor Garden

S.NithyaPoornima

Asisitant Professor, Department of Mechanical Engineering
B.M.S.Institute of Technology and Management
Bangalore ,India.

Abstract

The Main Focus was to design Automatic Watering System for Indoor Gardens regularly. The circuit comprises of sensor parts built using op-amp IC LM358. Op-amp's are configured here as a comparator. Two stiff copper wires are inserted in the soil to sense whether the soil is wet or dry. The Microcontroller is used to control the whole system by monitoring the sensors and when sensors sense the dry condition then the microcontroller will send command to relay driver IC the contacts of which are used to switch on the motor and it will switch off the motor when all the sensors are in wet condition. The microcontroller does the above job as it receives the signal from the sensors through the output of the comparator, and these signals operate under the control of software which is stored in ROM of the MC.

I. INTRODUCTION

The era is all about automation and specially people having small garden and terrace gardens with many fruit bearing trees and plants which require regular watering. The gardener these days are very lazy and often skip watering. This resulted in stunted growth of the plants or in the worst case scenario, some plants starts to withering away. Hence there was a need for some good solution like some form of automation without breaking the bank. Hence this project enabled us in developing an automated watering system for indoor plants with cost effectiveness and less human supervision.

II. BLOCK DIAGRAM

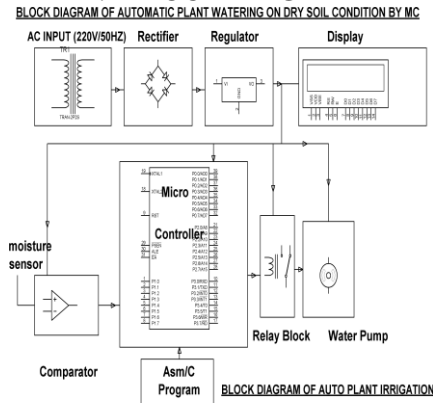


Fig 3.1: Project Block Diagram

III. HARDWARE REQUIREMENTS

Hardware Components

1. TRANSFORMER (230 – 12 V AC)
2. VOLTAGE REGULATOR (LM 7805)
3. RECTIFIER
4. FILTER
5. MICROCONTROLLER (AT89S52/AT89C51)
6. LCD
7. WATER PUMP
8. LM358 OP-AMP
9. BC547 TRANSISTOR
10. RELAY
11. 1N4007
12. LED
13. RESISTORS
14. CAPACITOR.

IV. SOFTWARE REQUIREMENTS

A. Keil C Cross Compiler

Keil is a German based Software development company. It provides several development tools like

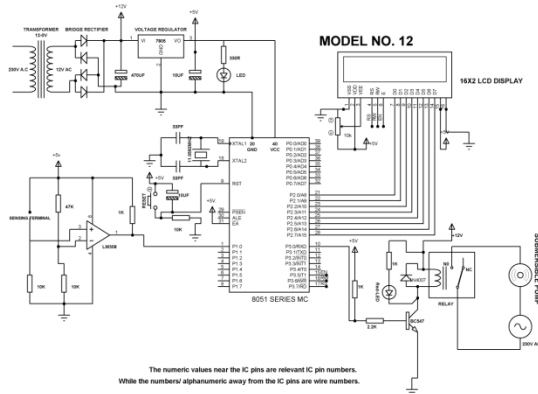
- IDE (Integrated Development environment)
- Project Manager
- Simulator
- Debugger
- C Cross Compiler, Cross Assembler, Locator/Linker

The Keil ARM tool kit includes three main tools, assembler, compiler and linker. An assembler is used to assemble the ARM assembly program. A compiler is used to compile the C source code into an object file. A linker is used to create an absolute object module suitable for our in-circuit emulator.

B. Embedded C

Use of embedded processors in passenger cars, mobile phones, medical equipment, aerospace systems and defense systems is widespread, and even everyday domestic appliances such as dish washers, televisions, washing machines and video recorders now include at least one such device.

V. SCHEMATIC DIAGRAM



A. Description

1) Power Supply

The circuit uses standard power supply comprising of a step-down transformer from 230V to 12V and 4 diodes forming a bridge rectifier that delivers pulsating dc which is then filtered by an electrolytic capacitor of about 470µF to 1000µF. The filtered dc being unregulated, IC LM7805 is used to get 5V DC constant at its pin no 3 irrespective of input DC varying from 7V to 15V. The input dc shall be varying in the event of input ac at 230volts section varies from 160V to 270V in the ratio of the transformer primary voltage V1 to secondary voltage V2 governed by the formula $V1/V2=N1/N2$. As $N1/N2$ i.e. no. of turns in the primary to the no. of turns in the secondary remains unchanged V2 is directly proportional to V1. Thus if the transformer delivers 12V at 220V input it will give 8.72V at 160V. Similarly at 270V it will give 14.72V. Thus the dc voltage at the input of the regulator changes from about 8V to 15V because of A.C voltage variation from 160V to 270V the regulator output will remain constant at 5V.

The regulated 5V DC is further filtered by a small electrolytic capacitor of 10µF for any noise so generated by the circuit. One LED is connected of this 5V point in series with a current limiting resistor of 330Ω to the ground i.e., negative voltage to indicate 5V power supply availability. The unregulated 12V point is used for other applications as and when required.

2) Standard Connections To 8051 Series Micro Controller

ATMEL series of 8051 family of micro controllers need certain standard connections. The 4 set of I/O ports are used based on the project requirement. Every microcontroller requires a timing reference for its internal program execution therefore an oscillator needs to be functional with a desired frequency to obtain the timing reference as $t=1/f$.

A crystal ranging from 2 to 20 MHz is required to be used at its pin number 18 and 19 for the internal oscillator. Typically 11.0592 MHz crystal is used in general for most of the circuits using 8051 series microcontroller. Two small value ceramic capacitors of 33pF each is used as a standard connection for the crystal as shown in the circuit diagram.

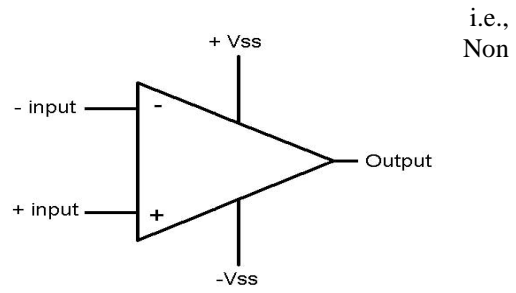
3) Reset

Pin no 9 is provided with a re-set arrangement by a combination of an electrolytic capacitor and a register forming RC time constant.

4) Comparator

How an op-amp can be used as a comparator?

Potential dividers are connected to the inverting and non inverting inputs of the op-amp to give some voltage at these terminals. Supply voltage is given to +Vss and -Vss is connected to ground. The output of this comparator will be logic high (i.e., supply voltage) if the non-inverting terminal input is greater than the inverting terminal input of the comparator.



inverting input (+) > inverting input (-) = output is logic high

If the inverting terminal input is greater than the non-inverting terminal input then the output of the comparator will be logic low (i.e., gnd)

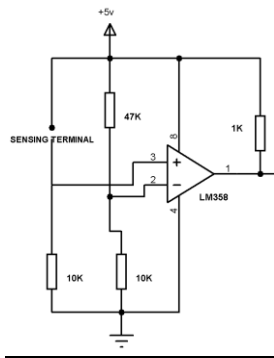
i.e., inverting input (-) > Non inverting input (+) = output is logic low

B. Operation Explanation

1) Connections

The o/p of the power supply which is 5v is connected to the 40 pin of MC and GND is connected to its 20th pin. Now the output of the OPAMP LM358 is connected to Pin 1.0 of Port 1.0. Data lines of LCD or D₀ to D₇ are connected to part 2, Pin 21 – 28 of Microcontroller. Read, Write, Enable pins of LCD are connected to Pin15, Pin16, Pin17 of Port 3 of Microcontroller. When Pin 3.0 of port3 is connected to the transistor (BC547) which drives the relay. When Pin 3.0 is high then the transistor get switch ON so that relay gets ON, since the path is closed. This makes the DC motor run

VI. WORKING



The inverting input of the Comparator LM358 i.e., Pin 2 is given to the fixed voltage i.e., in the ratio 47k: 10k, and the non-inverting input of the comparator is pulled down and is given to moisture sensing arrangement at sensing terminal. When the soil is dry, the soil resistance between the positive supply and the non inverting input is high resulting in positive supply to the non-inverting input less than the inverting input making comparator output as logic low at pin no 1. This command is given to MC. In this condition the MC outputs logic high at pin no. 10 that switches on a relay driving transistor due to which the relay is switched on and the pump motor is in ON condition. Thus water flow is started.

Then while the soil goes sufficiently wet, the soil resistance falls making available a voltage to the non-inverting input higher than inverting input, so that the output of comparator is logic high which is fed to MC. In this condition MC outputs logic low to a transistor which conducts by making the relay 'OFF' and the pump motor stops. Based on the program the conditions appear in the 16x2 lcd display whether the pump is ON or OFF.

VII. LAYOUT DIAGRAM

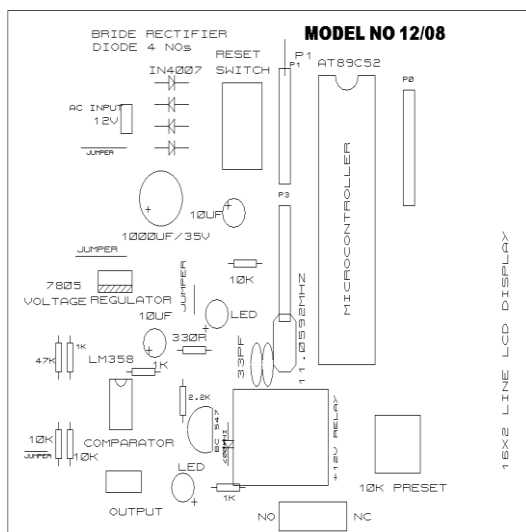


Fig.8.1: Layout Diagram

VIII. RESULT

The system takes the input based on moisture content in the soil and based on it the pump is turned ON/OFF automatically. As long as the moisture is low in the soil the pump is in ON state and once the moisture level is raised to the required level the pump turns OFF.

Watering the indoor garden plants is accurate and efficient with the use of above system. The output of the system depends on the input received based on moisture content.

IX. CONCLUSION

The automatic watering system for indoor gardening plants sensing soil moisture content works very well. As seen from practical application results it automatically sense the moisture content and switches on the pump for watering, thus reduces the human dependency in watering of indoor plants. It effectively waters the plants without human intervention.

Also, the project can be extended to green houses where it can be used for efficient irrigation of the plants by the further improvement of the system. It reduces the overflow and wastage of water effectively.

REFERENCES

- [1] "The 8051 Microcontroller and Embedded systems" by Muhammad Ali Mazidi and Janice GillispieMazidi , Pearson Education.
- [2] ATMEL 89S52 Data Sheets.
- [3] 3.Rishi, Ripul, Dilip Kumar. "Prototype Design of Indigenous GSM based Intelligent Irrigation System." International Journal of Computer Applications 73, no. 18 (2013): 36-39.
- [4] Pulkithanswal, iDesign of a central control unit and soil moisture sensor based irrigation water pump system. IEEE Conference on. IEEE, 2013.



Effect of MWCNTs on piezoelectric and ferroelectric properties of KNN composites

Nandini R. Nadar^a, Krishna M.^{a,*}, Suresh A.V.^b, Narasimha Murthy H.N.^a

^a Research and Development Centre, Department of Mechanical Engineering, R.V. College of Engineering, Bangalore 560059, India

^b Department of Mechanical Engineering, BMS Institute of Technology & Management, Bangalore 560064, India



ARTICLE INFO

Keywords:

KNN
MWCNT
Microwave sintering
Piezoelectric
Ferroelectric
Dielectric

ABSTRACT

The aim of the research work was to investigate the effect of multiwall carbon nanotubes (MWCNTs) reinforcement (0.3–1.2wt.%) on functional properties of microwave sintered Potassium sodium niobate (KNN) composites. Sintered composites are characterized for crystal structure, morphology and temperature stability of piezo-electric, ferroelectric and dielectric properties. KNN composites showed perovskite phase with improved tetragonal symmetry, fine grained porous microstructure, reduced dielectric loss and enhanced effective permittivity. The optimum functional properties and thermal stability obtained for KNN-MWCNT (0.9 wt.%) composites over the range of 20–100 °C, makes the idea of using the addition of MWCNTs to KNN ceramics an interesting approach in searching new structures for temperature stability.

1. Introduction

Ceramic piezoelectric materials find applications in various electronic devices such as sensors, transducers, actuators, micro motors, magneto electric sensor, high power transformers and for energy harvesting due to their robust functional properties [1–3]. Among piezoelectric ceramic materials, potassium sodium niobate (KNN) gained much interest due to its high curie temperature and good electrical properties [4,5]. The presence of morphotropic phase boundary (MPB) between two orthorhombic phases for KNN system shows good piezoelectric and ferroelectric properties similar to standard lead zirconate titanate piezoelectric materials [6,7]. KNN sintered samples showed piezoelectric charge co-efficient (d_{33}) value of 80–160pC/N using solid state method [8,9], 85 pC/N for microwave sintering [10] and 148 pC/N for spark plasma sintered ceramics [11]. But instability of KNN phase above 1140 °C and volatile nature of alkali components at higher temperature restricted them to a limited application.

To overcome the high temperature instability many researchers [12–15] have investigated different dopants on KNN ceramics. This was doped using alkaline (Li^+ , Ba^{2+} , La^{3+} , Bi^{3+}) and transition (Ti^{4+} , Sb^{5+} , Ta^{5+}) elements to enhance functional properties by shifting the polymorphic phase (PPT) transition temperature. Lithium modified KNN samples showed d_{33} value of 235 pC/N, k_p – 44% with the presence of MPB between orthorhombic and tetragonal phases [16]. Extended work by zhang [17] showed the enhanced d_{33} value of 298 pC/N,

k_p – 34.5% and ϵ_r – 945 by adding antimony with lithium doped KNN ceramics, for orthorhombic crystal structure without the presence of MPB. Lithium, antimony and tantalum doped KNN system brought a major breakthrough for reporting d_{33} of 300 pC/N by reactive templated grain growth method (RTGG) [18]. Despite the superior piezoelectric responses, doped KNN ceramics showed the temperature dependent properties with poor stability of the poled domain state. The drastic reduction in phase transition temperature at $T_C \approx 300$ °C and an additional phase transformation at 200 °C degrades the piezoelectric properties of doped KNN ceramics significantly [16]. Hence there is a wide scope for further investigations even though some notable works have been reported [15–19].

Carbon nanotube (CNT) reinforced PZT-PVA 0–3 composite yielded with an increase of 61.3% in piezo-electric charge coefficient (19.8 pC/N), 67% increase in dielectric constant and 89% increase in dielectric loss factor [20,21]. CNT reinforced 1–3 piezoelectric composite had significant piezoelectric and elastic moduli with good frequency responses [22]. Piezo-damping epoxy-matrix composites developed with CNT and PZT contributed to transformation of noise and vibrations to electrical energy, along with shorting of generated electrical current to the external circuit [23]. Non-covalently functionalized graphene oxide (rGO) reinforced polyvinyl alcohol (PVA) composites showed tremendous improvement in its mechanical and thermal properties [24]. The interfacial properties of epoxy resin composites enhanced significantly due to layer by layer grafting of CNTs onto carbon fibre

* Corresponding author.

E-mail address: krishnam@rvce.edu.in (M. Krishna).

<https://doi.org/10.1016/j.mseb.2018.09.001>

Received 7 August 2017; Received in revised form 7 January 2018; Accepted 20 September 2018

0921-5107/ © 2018 Elsevier B.V. All rights reserved.

surface [25], Carbon Nano adsorbents have attracted tremendous interest for metal ion removal from wastewater due to their extraordinary aspect ratios, surface areas, porosities, and reactivities [26]. The robust electrostatic attraction developed in polystyrene/nanocarbon composites helped in achieving ultralow percolation threshold with enhanced conductivity, making a guideway for manufacturing conductive polymer based composites [27]. Polyvinylidene fluoride (PVDF) / polyacrylonitrile (PAN) / multiwalled carbon nanotubes functionalized COOH (MWCNTs-COOH) nanocomposites have shown significant enhancement in impedance and electrical conductivity of PVDF-PAN/MWCNTs composites for a wide frequency range at different temperatures [28]. Epoxy nanocomposites reinforced with SiO₂/MWCNTs helped in developing electrically insulated composite, paying a way for toughen the polymers for electric insulating applications [29].

Even though CNT is a potential candidate for tailoring functional properties of piezoelectric ceramics, no research works are focused on developing CNT reinforced KNN piezoelectric ceramic materials. Hence MWCNT may be a good reinforcement candidate to empower the functional properties of ferroelectric ceramic materials. KNN ceramics is now a potential candidate for intelligent sensing applications such as wheeled mobile robots (unmanned driving car) [30], Multi leap motion / hand tracking sensor (intelligent robots) [31], multi-source power system in electric vehicles based on PI-PD controller [32], virtual sensors, human to machine frame work for requested power demand etc., thereby embedding intelligence in applications [33].

The objective of the present work is to synthesize MWCNT reinforced KNN composites through microwave sintering assisted solid state route. The sintered composites were characterized to determine the effect of MWCNT on crystal structure, microstructure and temperature dependent functional properties of KNN composites such as piezoelectric, ferroelectric and dielectric properties.

2. Materials and methods

The raw materials used for synthesizing (K_{0.5}Na_{0.5})NbO₃ – MWCNT composites are given in Table 1.

2.1. Synthesis of KNN crystalline powders

The elemental powders of Na₂CO₃, K₂CO₃, Nb₂O₅ were precisely measured to yield desired composition of (K_{0.5}Na_{0.5})NbO₃ system and were preheated at 200 °C for 2 h. The preheated elemental powders were subjected to mechanical alloying in a Retsch, GmbH planetary ball mill PM 200 (GmbH) for 15 h. This planetary mono mill has a disc speed of 650 rpm and is programmable for both cycle time and reversing cycles. Milling was carried out with a ball to powder (BPR) weight ratio of 10:1 in a sealed stainless-steel vial using 10 mm stainless steel balls. Milling was performed at a speed of 300 rpm to avoid excessive heating and consequent crystallization of synthesized powder. Ten minutes of idle time after every thirty minutes of milling was programmed to avoid excessive heating of the vial. Reversed milling was used after each cycle of milling. A total of carefully weighed 30 g of powders were added to the vial for the reaction with 3 – 4% of acetone as a process control

Table 1
Specification of the materials used for synthesizing KNN – MWCNT composites.

Element	Na ₂ CO ₃	K ₂ CO ₃	Nb ₂ O ₅	MWCNTs
Purity (%)	99.5	99.0	99.9	95.0
Density	2.53 g/cm ³	2.29 g/cm ³	Density: 4.6 g/cm ³	2.1 g/cm ³
Dimension				Length: 10–30 μm, Surface area: above 200 m ² /gm
Supplier	Alfa Essar, U.K	Alfa Essar, U.K	Alfa Essar, U.K	Chemo pal Industries, Mumbai

agent. To avoid adhesion of the powders to the vial, 1 ml of acetone was added after seven hours for every 7–10 cycles of milling.

2.2. Surface treatment of the MWCNTs and KNN

The MWCNTs was treated by the Fenton / UV method to oxidize, functionalize the multi-walled carbon nanotubes and were vacuum dried at 200 °C for 4 h. The filtrated MWCNTs consisted of agglomerated clusters of MWCNTs due to van der Waals forces. The MWCNTs were surface treated in ethanol and sonicated for four hours in an ultrasonicator, prior to inclusion within the KNN matrix. This non-covalent dispersion method provides surface energy to the multiwall nanotubes to overcome the Vander Waals forces between them. The ball milled KNN powder for 15 h was calcined at 900 °C, 5 h to complete the reaction of the elemental powder and to obtain the desired KNN system. The calcined powder was re-milled for 2 h to avoid the agglomerations formed during solid state reaction. The measured quantity of re-milled powder was uniformly dispersed in liquid media (ethanol) by sonication at RT for 30 min.

2.3. KNN composite preparation

The uniformly dispersed MWCNTs and re-milled KNN nanopowders were ultrasonicated for a period of 2 h to obtain proper inclusion of MWCNT into KNN matrix. The obtained slurry of the KNN composite was vacuum dried, mixed with 2–3 drops of poly vinyl alcohol and was pressed uniaxially at 250 MPa to obtain composite discs of diameter 10 mm and thickness of 1.5 mm. The discs were densified between 1040 and 1120 °C for 30 min using microwave assisted sintering (Microwave furnace 1600 AC, Super (VBCC, Chennai)). The bulk densities of sintered composites were measured by density meter. The densified composite samples were polished using silicon carbide paper and dry grinding. For electrical measurements, high temperature silver paste was coated on both sides of the disc to form electrodes. For piezoelectric activation, all samples were poled in a silicon oil bath under a poling field of 2.5–4 kV/mm DC for 30 min at ambient temperature using parallel plate contact polarization method and a Spellman SL Series high voltage generator.

2.4. Characterization

The crystalline symmetry and lattice parameters were determined by using X-ray diffractometer (XRD, Rigaku Smart Lab), and expert high score software respectively. Morphology, grain size and elemental composition were evaluated on polished samples using scanning electron microscopy-EDS (SEM, ZeissSupra-40). The piezoelectric strain factors of MWCNT-KNN samples were measured by a Piezotest PM300 Pte. Ltd, from RT to 200 °C, under a field of 4 kV/mm. Capacitance, impedance and dissipation factor of specimens were measured by using semiconducting device analyzer (B1500 A), between 1 kHz and 1 MHz. Hysteresis loops were determined using precision premier II ferroelectric tester (Radiant technologies.INC), at room temperature under 5 kV/mm, AC field at 50 Hz with a unit based on sawyer-tower circuit [10]. The dielectric constant of samples was measured using a programmable impedance analyzer (HP4294A, Agilent Technologies), in the frequency range 100 Hz – 1 MHz. The electromechanical coupling factor (k_p) and mechanical quality factor (Q_m) were determined from resonance and antiresonance methods referring to IEEE standards.

3. Results and discussions

3.1. MWCNT and KNN characterization

The surface morphology and distribution of MWCNTs within ethanol after 4 h of sonication were observed with the aid of TEM images as shown in Fig. 1(a). The higher magnification image

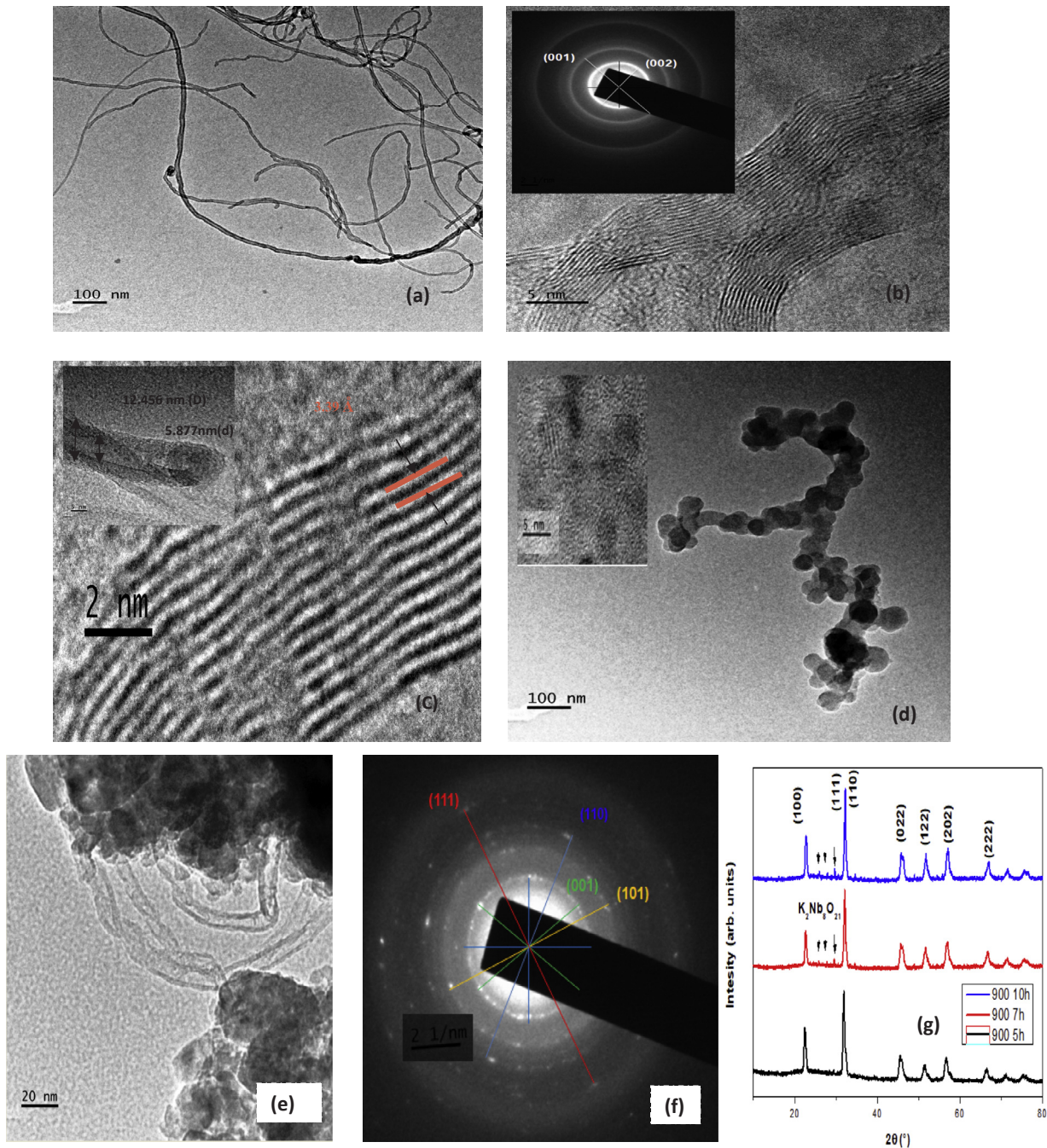


Fig. 1. (a) TEM images of MWCNTs dispersed in ethanol media and sonicated for 4 h, (b) High magnification and diffraction pattern of MWCNT, (c) d spacing, inner and outer diameter of MWCNTs, (d) Low and (e) Higher magnification TEM image of MWCNT reinforced KNN calcined powder, (f) SAED pattern of MWCNT reinforced KNN powder (g) Diffraction pattern of calcined powder at 900 °C, 5–10 h.

(Fig. 1(b)) revealed that the used CNTs are of multiwall in nature. Inset shows the selected area electron diffraction (SAED) pattern of MWCNTs. The diffraction pattern reveals the presence of 4 rings, which may be attributed to the two-dimensional graphite sheets rolled up to form MWCNTs, [34]. Still higher magnification of dispersed MWCNTs (Fig. 1(c)) helped in identifying the d-spacing between the walls of CNTs. Inset reveals the inner and outer diameter of MWCNTs. Fig. 1(d) shows the dispersion of KNN calcined powder in ethanol with spherical shaped particles. Inset shows the average grain size of calcined KNN powder obtained as 5.3035 nm by Image J analysis. Higher magnification (Fig. 1(e)) image shows the existence of MWCNTs in the reinforced matrix of calcined nano-crystalline powder of KNN. The SAED pattern of KNN composite powder reveals the coexistence of MWCNTs

by visibility of diffused rings and polycrystalline phase of calcined KNN powder by the presence of bright spots (Fig. 1(f)). The presence of a ring pattern with relatively continuous rings, proves that the crystallites are small, in the nm range as measured (Inset of Fig. 1(d)) and are in random orientation. Indexed planes in Fig. 1(f) indicates the complete formation of single phase orthorhombic crystal structure of KNN calcined powder. The diffraction pattern of calcined KNN powder (Fig. 1(g)) revealed only orthorhombic peaks with maximum intensity being at (110/111) plane. Since there was no signature of any tetragonal phase it was termed to be as a single phase orthorhombic.

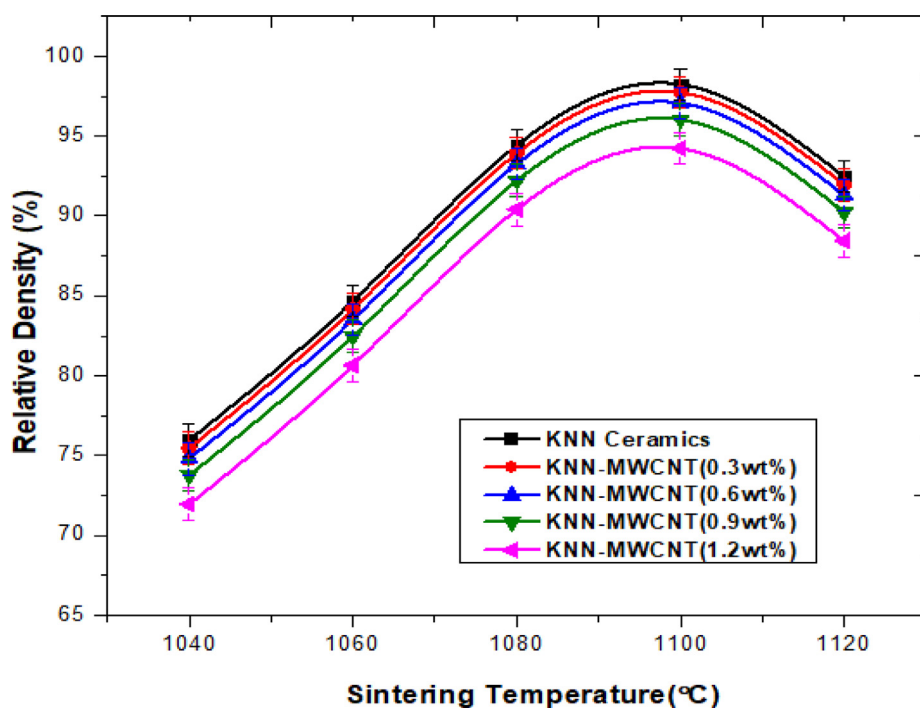


Fig. 2. Relative Density of KNN ceramics and KNN-MWCNT (0.3–1.2 wt%) composites as a function of sintering temperature.

3.2. Density and microstructure of KNN composites

KNN composites were sintered at 1040 °C, 1060 °C, 1080 °C, 1100 °C and 1120 °C to identify the optimized sintering temperature based on relative density achieved. The relative density of KNN composites (Fig. 2) is shown as a function of the microwave sintering temperature. The relative density of all the KNN composites increased gradually with the increase in temperature and were maximum at 1100 °C. At 1120 °C, the relative density of the KNN composite reduced gradually, as the sintering temperature is nearer to its melting point (1140 °C).

It resulted in emergence of secondary phases due to volatile behavior of alkaline elements at higher temperature. Hence 1100 °C, was recommended to be the accurate microwave sintering temperature due to highest relative density achieved. The optimum relative densities obtained for MWCNT addition of 0.3, 0.6, 0.9 and 1.2 wt.% were 97.75, 97.08, 96.04 and 94.23% respectively and were lower than KNN ceramics (98.25%). This is because, addition of even small amount of MWCNTs strongly reduces the sinterability in KNN ceramics, and results in porous and fine-grained microstructures with no significant weight loss.

A typical micrograph of sintered KNN ceramic (Fig. 3), consist of densely packed cubic and sound casting (low porous) microstructure. The reduced porosity yields with good densification properties in case of KNN ceramics. The morphology of sintered KNN composites (0.3–1.2 wt.% are shown in Fig. 4(a–d). KNN composite (0.3 wt.%) showed an initiation for the formation of fine grain microstructure with cubic shaped particles (Fig. 4(a)). The MWCNTs survived after sintering induces porosity, acts as conductive filler inside the KNN matrix, behaves like a bridge between crack and pores, and yields in increasing the conductivity of the KNN composites. The increased conductivity helps in improving the percolation path by interfacial affects, mobility of the electrons and thereby improves the dielectric behavior and reduces the loss factor of the composites. Further, addition of MWCNTs (0.6–0.9 wt.%) into KNN matrix helped in obtaining improved porosity and fine-grained microstructures as shown in Fig. 4(b) and (c). The induced porosity helps in improving the effective permittivity [21] of the KNN composites. Furthermore, addition of MWCNTs into KNN matrix above threshold resulted in enhanced porosity and aggregation

of MWCNTs (Fig. 4(e)) and some closely packed cubical particles as shown in (Fig. 4(d)). High porosity and aggregation of MWCNT clusters yields in low relative density and permittivity. Inferring that, induced porosity plays a vital role in improving the effective permittivity than increased addition of MWCNT into the composite to obtain a fine grain microstructure. The induced porosity and large surface area developed in KNN composites helps in achieving high power conversion efficiency. This can be attributed to easier and faster diffusion of electrons into pores as observed in electrically conductive perovskite strontium ruthenate (SrRuO_3) mesoporous film [35].

3.3. TEM micrograph analysis of KNN-MWCNT bulk composites

The lower and higher magnification TEM images of the sintered KNN composites are depicted in Fig. 5. The densified samples show reinforcement of MWCNTs into KNN composite (Fig. 5(a)) when sintered at 1100 °C. The magnified TEM electron diffraction images show dispersion of MWCNTs into KNN matrix without formation of any agglomerations (Fig. 5(b) and (c)). The SAED pattern of KNN composite (0.6wt.%) (Fig. 5(d)), shows brighter and more distinct spots in the relatively continuous rings. This indicates an improvement in the crystallite size of sintered composites in comparison with calcined diffraction pattern (Fig. 1(f)). The indexed planes in SAED pattern (Fig. 5(d)), ensures formation of tetragonal perovskite structure of KNN. The brighter spots and diffused rings indicates uniform reinforcement of 0.6 wt.% of MWCNTs into polycrystalline tetragonal phase KNN ceramics.

3.4. Crystalline structure of KNN composites

The X-ray diffraction pattern of as received MWCNTs (Fig. 6(a)) shows two broad peaks at $2\theta \sim 26.24^\circ$ and 43.52° correspond to the diffraction from (0 0 2) and (0 0 1) reflection planes of MWCNTs. The (0 0 2) peak is originated due to the residual inner nanotubes and the presence of the (0 0 1) peak is due to partial unzipping of carbon nanotube and resulting in the expansion of interlayer distance [58].

The XRD patterns of sintered KNN composites in comparison with pure KNN are shown in Fig. 6(b)–(d). The partial scan of KNN samples

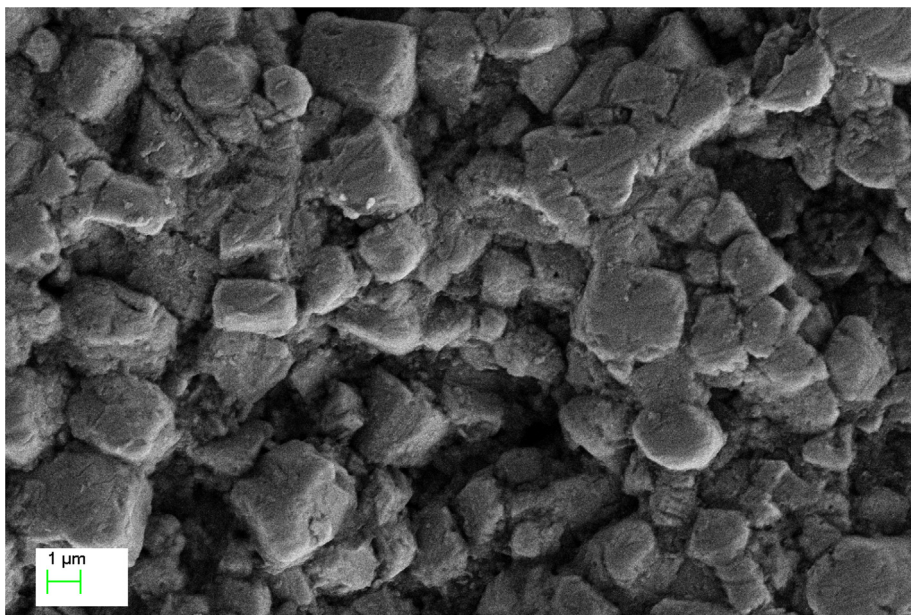


Fig. 3. Micrograph of $(K_{0.5}Na_{0.5})NbO_3$ ceramics, microwave sintered at 1100 °C for 30 min.

for 2θ from 20° to 34° (Fig. 6(b)) shows the existence of the perovskite phase at (1 0 0) and (1 1 0) planes (peaks indexed according to JCPDS file no: 32-822). The unit cell parameters of KNN ceramic samples were reported with c/a ratio of 1.015 for lattice parameters, $a = 3.9480$ nm, $c = 4.0007$ nm with cell volume of 62.3570 (Å³). The presence of minute peaks at 25.59° (0 0 2) in Fig. 6(b) for all KNN composite samples indicate the presence of MWCNTs after sintering and resulting in the formation of the required KNN composites. In this regard, it is expected that the majority of MWCNTs have been preserved into KNN matrix, but their amount is at the detection limit of the XRD instrument.

The intensity of the peak (1 1 0) plane at 32° was sharp and maximum for KNN composites (0.9 wt.%), (Fig. 6(b)) ensuring high intensity perovskite phase. Upon the careful examination of the XRD patterns between 2θ from 40 to 54° (Fig. 6(c)), the emergence of distortion (splitting) of the tetragonal (0 0 2) and (2 0 0) diffraction peaks indicates the formation of KNN composites towards a pure tetragonal ratio of 0.50. The modification of the peak was observed at ~52° for KNN-MWCNT samples with an increase in the amount of MWCNT addition from 0.3 to 1.2 wt.%. This indicates, the tendency of KNN composites to move towards a more tetragonal state for higher MWCNT addition. This distortion of the tetragonal structure increases the calculated c/a ratio from 1.0093 to 1.015 which is due to coexistence of orthorhombic and tetragonal structure [36]. Moreover, addition of MWCNT may act as a nucleating agent during crystallization process, and thereby yield to a high degree of crystallinity as observed in PVDF/PAN/CNT composites [37].

3.5. Dielectric properties

The variation of dielectric constants as a function of temperature for KNN samples sintered in microwave furnace are shown in Fig. 7(a)–(d). The curve deviates twice for all the samples (i) one near 100 °C (attributed to phase transition from orthorhombic to tetragonal) and (ii) ~ 420 °C, peak corresponding to the ferroelectric – paraelectric phase transition. The KNN composites reveal high Curie temperature similar to pure KNN ceramics ensuring temperature stability. In addition, the dielectric constant of all KNN samples show thermal and frequency dependency. The maximum relative permittivity value is shifted towards high temperature with the increase in frequency for all KNN samples.

The dielectric constant of KNN ceramics measured at 1 kHz, was 792

at RT (Fig. 7(a)). Whereas the permittivity of all KNN composites were higher than KNN ceramics and increased with the addition of MWCNT content. The maximum relative permittivity value of 858 at RT obtained for KNN composites (MWCNT-1.2 wt.%), enhanced towards T_c . However, at 100 kHz, pure KNN and KNN – MWCNT (0.9 wt.%) composite had a maximum ϵ_r of 760 and 819 as shown in Fig. 7(b). In addition, the permittivity for 1.2 wt.% of MWCNT sample shows lesser value than other composites including pure KNN. Similarly, the variation in the permittivity value of KNN ceramics measured at 1 MHz, (738 at RT) (Fig. 7(c)) and 1.3 MHz (702 at RT) (Fig. 7(d)) were lesser than ϵ_r values of KNN-MWCNT (0.3–0.9 wt.%) composites with maximum being 832 (1 MHz) and 959 (1.3 MHz) at RT for 0.9 wt.% of MWCNT. This was nearer to the permittivity value of $Pb(Zr_{0.52}Ti_{0.48})O_3$ ceramics sintered by microwave sintering [38]. It can be seen from Fig. 7, that the relative permittivity was high for low frequencies (1 kHz) and decreased with the increase of frequency (1 MHz) which are in agreement with the values reported in the literature [39–41]. Similar trend of increased dielectric constant was observed in MWCNT/PVDF composite and hybrid films of MWCNTs/ $BaTiO_3$ composites [42,43]. Also, high dielectric permittivity at two percolation thresholds were observed in carbon nanotube / elastomer composite [44]. A stable ϵ_r of 30 was achieved for $BaTiO_3$ perovskite films for the frequency range from 0 Hz to 1 MHz [45]. The measurement of permittivity value of KNN composite for 1.2 wt.% of MWCNT, between 100 kHz and 1.3 MHz confirmed that, the effective permittivity is influenced mainly by the porosity induced by CNTs addition, rather than with the highest amount of added MWCNTs. Moreover, divergence observed in ϵ_r for 1.2 wt.% of MWCNT can be associated to approach of conductivity threshold from either side [46]. Since the ϵ_r values of the composite for 1.2 wt.% addition of MWCNT are not thermally stable, 0.9 wt.% addition of MWCNT is considered as the optimized reinforcement mixture to obtain fine grained microstructure with improved effective permittivity. The reduction of permittivity down to a few hundred at higher temperature is usually required for specific applications.

3.6. Dielectric losses

The loss tangent ($\tan\delta$) of the KNN samples sintered in microwave furnace were measured between 1 kHz and 1.3 MHz as shown in Fig. 8(a) to (e). The $\tan\delta$ value of all KNN samples increased with the increase in temperature and frequency. The raise in the loss tangent

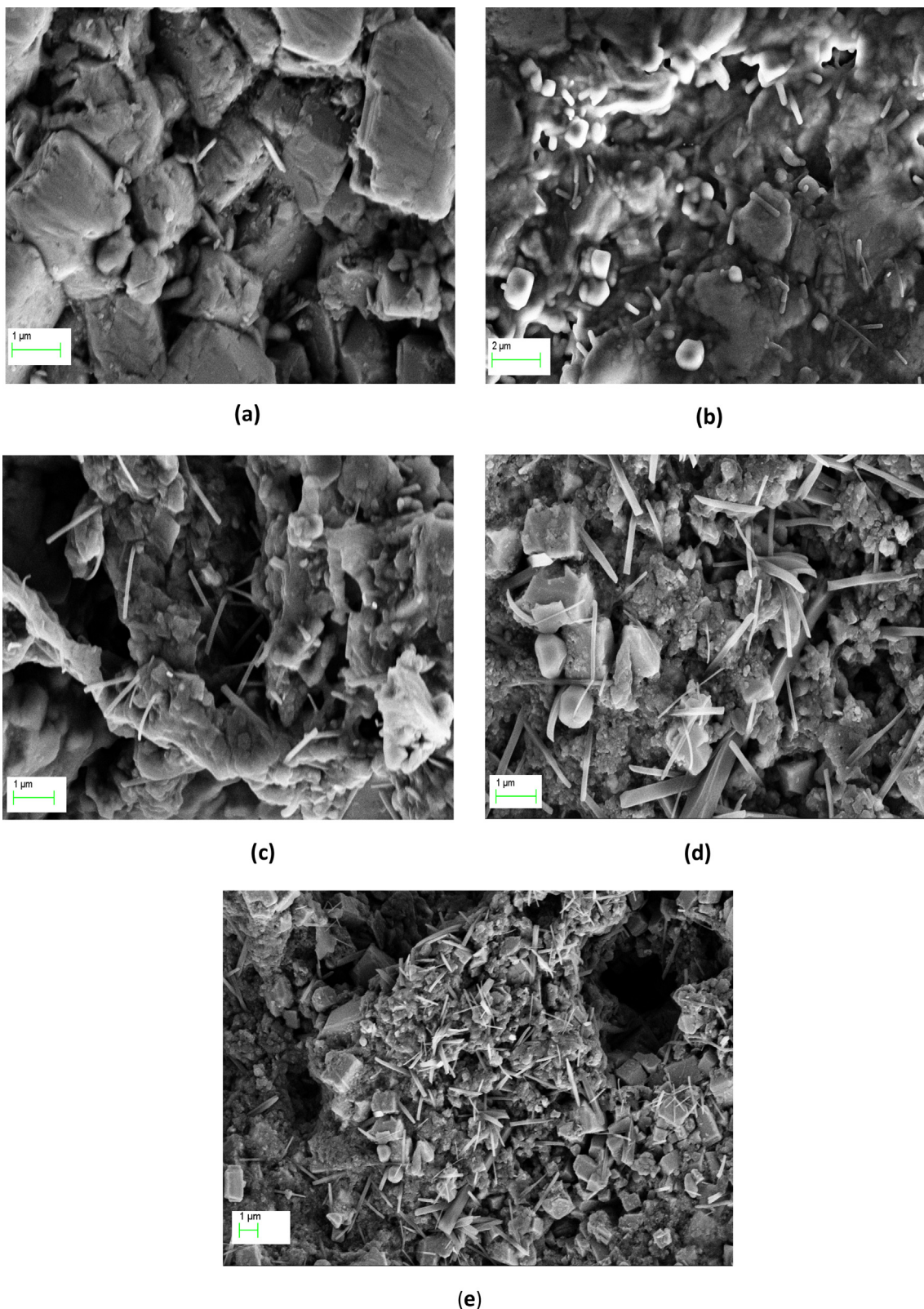


Fig. 4. Micrographs of KNN – MWCNT Composites, microwave sintered at 1100 °C for 30 min. (a) 0.3 wt.% MWCNT, (b) 0.6 wt.% MWCNT, (c) 0.9 wt.% MWCNT, (d) 1.2 wt.% MWCNT (e) High porous structure (1.2 wt.% MWCNT).

might be due to increased ion mobility and certain imperfections in the material [15].

The $\tan\delta$ of KNN composites (0.3–1.2 wt.% measured at 1 kHz) was between 0.014 and 0.029 at RT, (Fig. 8(a)). These values were lesser than the losses measured for KNN ceramics (0.032) at the same

condition. This is due to the combined effect of increased conductivity and improved percolation path on the dielectric loss. Similarly, the dielectric loss at 10 kHz (Fig. 8(b)), was between 0.021 and 0.034 at RT for KNN composites with 0.036 for KNN ceramics. In addition, the loss tangent at 100 kHz was between 0.033 and 0.040 at RT for KNN

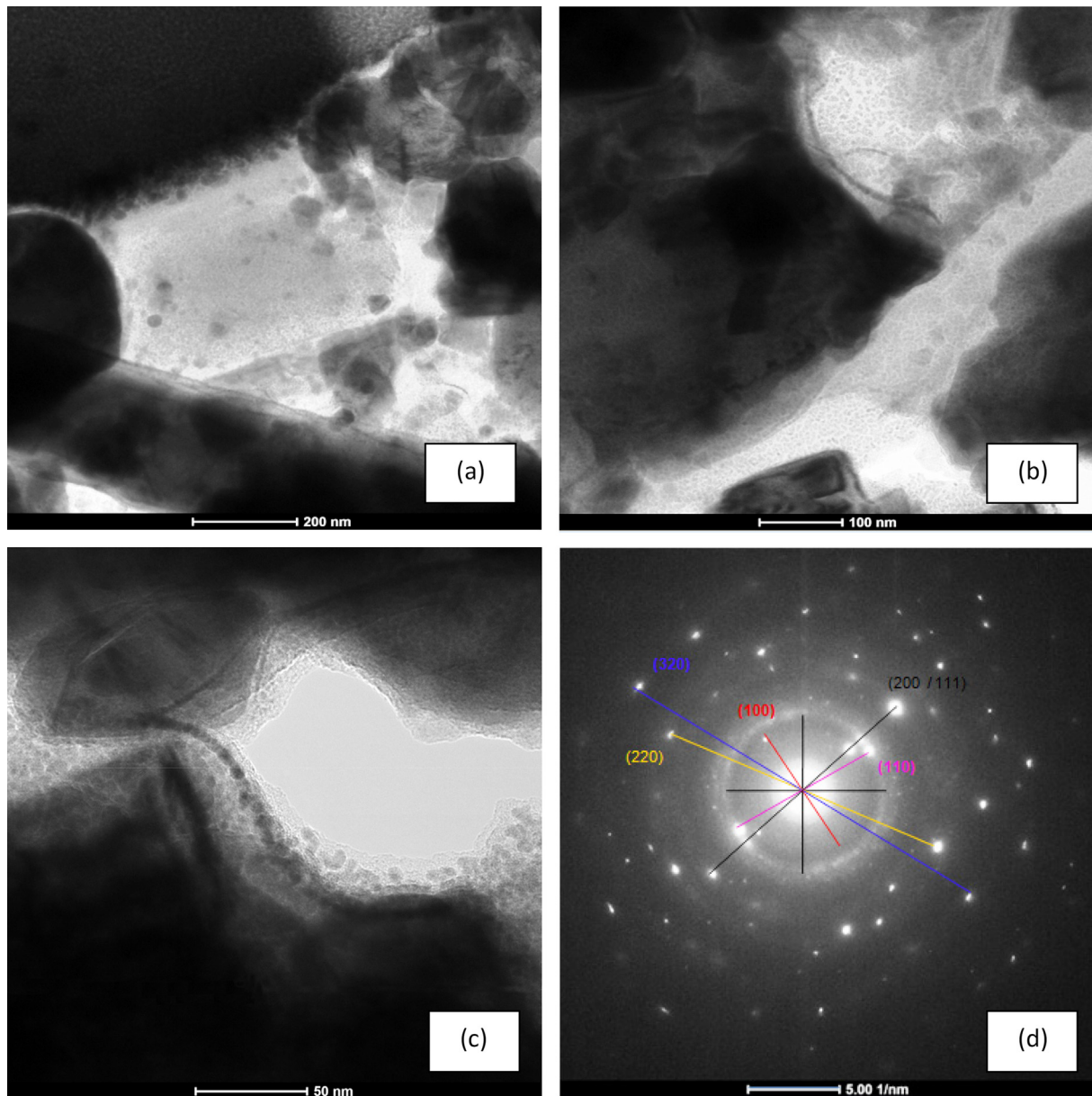


Fig. 5. TEM micrograph of the 2-phase composite shows MWCNTs embedded in the KNN matrix. (a) Lower, (b) high, and (c) higher magnification (d) Diffraction pattern of the bulk KNN-MWCNT (0.6 wt.%) showing diffused rings and spots. The diffused rings and spots corresponds to the MWCNTs and polycrystalline structure of the KNN phase.

composites in comparison with 0.044 for KNN ceramics (Fig. 8(c)). Whereas, the $\tan\delta$ values measured at 1 MHz showed 0.038–0.045 for KNN composites along with 0.054 being obtained for KNN ceramics at RT (Fig. 8(d)). However, the $\tan\delta$ values of KNN and its composites measured at 1.3 MHz was 0.052 and between 0.041 and 0.050 respectively at RT (Fig. 8(e)). Finally, the variation in $\tan\delta$ with temperature at measured frequency range (1 kHz–1 MHz) revealed reduced dielectric loss for all KNN composites than pure KNN. However, the loss factor of the KNN composites were lesser than reported dielectric loss for microwave sintered ceramics [38] and were similar to that of BaTiO₃ ceramics [47]. Since fine grained porous microstructures (Fig. 4(c)) and enhanced permittivity (Fig. 7(c)) are obtained for 0.9 wt.% addition of MWCNTs into the KNN matrix, the dielectric loss for the same composition is recommended for measured frequency range to compare the dielectric loss at enhanced permittivity.

However, KNN-MWCNT (0.3 wt.%) composite posse's lowest loss value for the wide range of temperature and frequency range

(1 KHz–100 KHz). This is because addition of 0.3 wt.% MWCNTs helps in dispersion of nanotubes within the matrix and increases the mobility of electrons to move from valence band to conduction band. This is due to improved percolation path and it yields in increasing the conductivity. But the obtained percolation path was not sufficient to enhance the permittivity due to lack of conducting path between the two electrodes. Hence the losses were less for loading of 0.3 wt.% MWCNTs. Whereas at threshold (0.9 wt.%), the dielectric loss increased with temperature indicating percolation has happened due to formation of more conductive networks, and corresponding to increased dielectric loss. Hence dielectric loss for 0.9 wt.% addition of MWCNT were considered.

3.7. Relationship among dielectric constant, dielectric loss and conductivity

KNN composite consist of a conducting phase (MWCNT) clusters and an insulating dielectric phase (KNN). So, when a system contains

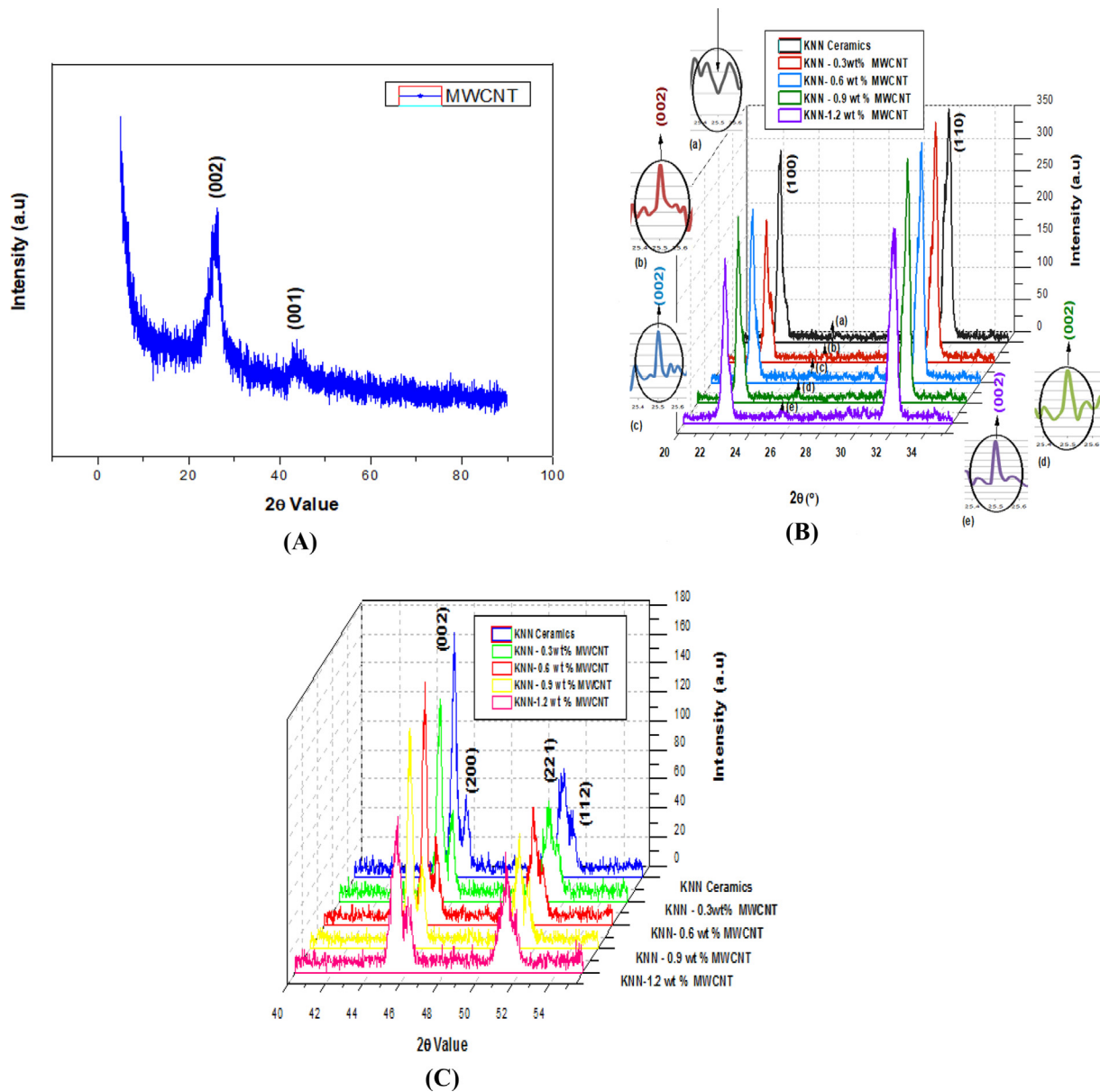


Fig. 6. X-ray diffraction patterns of (A) MWCNT, (B) KNN samples sintered at 1100 °C, 30 min for 2θ from 20° to 34, (C) KNN samples sintered at 1100 °C, 30 min. for 2θ from 40° to 54°.

conductive fillers (MWCNT), the frequency dependence on the dielectric constant and effective conductivity. It can be analyzed in the vicinity of the percolation threshold by Bergman derived power law (Eqs. 1(a) & (b)) and anomalous diffusion of electrons within each cluster of nanotubes [48].

$$\text{Effective conductivity} = \sigma'(2\pi\nu, f_c) \alpha (2\pi\nu)^x \tag{1(a)}$$

$$\text{Dielectric Constant} = \epsilon(2\pi\nu, f_c) \alpha (2\pi\nu)^{-y} \tag{1(b)}$$

where f_c and ν are the percolation threshold and frequency, respectively. The x & y are the critical exponents from percolation theory. In addition, the dielectric constant of the composite increases remarkably, when addition of MWCNT is near the percolation threshold due to its critical behavior near the threshold and the polarization effects between the clusters inside the composite [49]. Based on polarization effects between clusters, researchers have derived the following relation [49].

$$x = t/(t + s), \quad y = s/(t + s) \tag{2}$$

Here t, s are the critical exponents from the power law for percolation theory.

3.8. Frequency dependent dielectric behaviour and its losses

Fig. 9(a) and (b), shows the frequency dependence of the dielectric constant and dielectric loss of KNN composites respectively. From Fig. 9(a) and (b), it could be noticed that dielectric constant and loss of KNN composites were frequency dependent. The dielectric constant of KNN ceramics decreased with increase in frequency because at lower frequency the motion of free charges is constant and hence the relative permittivity is constant. As the frequency increases, the charge carriers will migrate and gets trapped against a defect site and induces an opposite charge in its vicinity, thereby yields with reduced motion of charge carriers and dielectric constant. Whereas, the dielectric constant of KNN composite (0.3 wt.%) were higher than KNN ceramics, it decreased with the increase in frequency (up to 100 KHz), similar to KNN ceramics. It is due to resonance in percolative clusters formed by random dispersion of MWCNTs with no physical interaction between

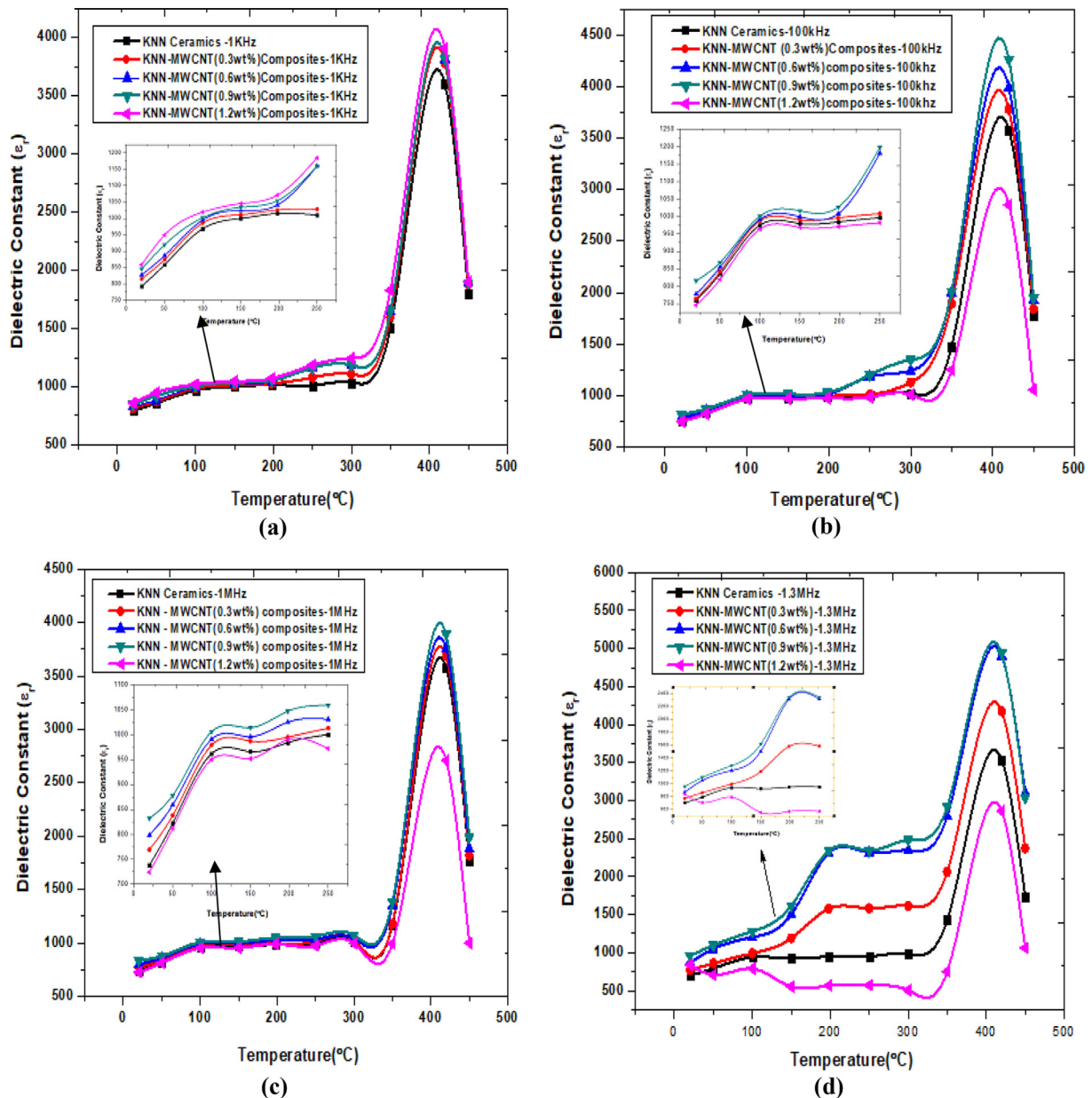


Fig. 7. Dielectric constant (ϵ_r) of the KNN samples as a function of temperature, (a) 1 KHz, (b) 100 KHz, (c) 1 MHz and (d) 1.3 MHz.

MWCNT and KNN ceramics. In KNN composite (0.3 wt.%), permittivity value increased linearly due to improved mobility of charge carriers by addition of MWCNTs into the matrix and reduced opposite charge in its vicinity. The behavior of dielectric constant in KNN-MWCNT (0.6–0.9 wt.%) composite was similar to that of 0.3 wt.% of MWCNTs till 100 KHz and further increased gradually at 1 MHz due to enhanced mobility of percolation clusters and formation of linkages within the composite. But for addition of MWCNTs (1.2 wt.%) above percolation threshold, the composite yielded with reduced permittivity at higher frequency range due to lack of percolating clusters and leakage of currents. Eqs. (1) and (2) indicates that polarization effects between the clusters plays a vital role in frequency dependence of dielectric constant and effective conductivity of the composite. Moreover, the conductivity of the composite is mainly determined by the paths of the percolating clusters rather than the effect of the capacitors. Hence, we can conclude that, the dielectric constant of the composite is enhanced by addition of MWCNTs towards low frequency. The maximum permittivity of 860 obtained for KNN-MWCNT (1.2 wt.%) composite at the frequency of 1 KHz, suggests that addition of MWCNTs is a promising way to enhance

the dielectric constant. Due to variation in the permittivity values for KNN-MWCNT (1.2 wt.%) composite over the range of frequency studied, KNN-MWCNT (0.9 wt.%) composite could be considered as ideal material with stable permittivity.

The dielectric loss of the composites exhibited similar tendency as that of dielectric constant, but loss increased with the increase of MWCNTs addition into the matrix as a function of frequency due to formation of conductive paths (Fig. 9(b)). As the content of MWCNT addition was increased within the threshold, some of them connect to each other and induces dielectric loss. But addition of MWCNT above percolation threshold results with high conductive network, large leakage current, and increased dielectric loss as observed but were lesser than KNN ceramics. The losses were the least at low frequency (1 KHz) and where maximum towards higher frequency in case of KNN composites, but the loss reduced slightly after 1 MHz in case of KNN ceramics.

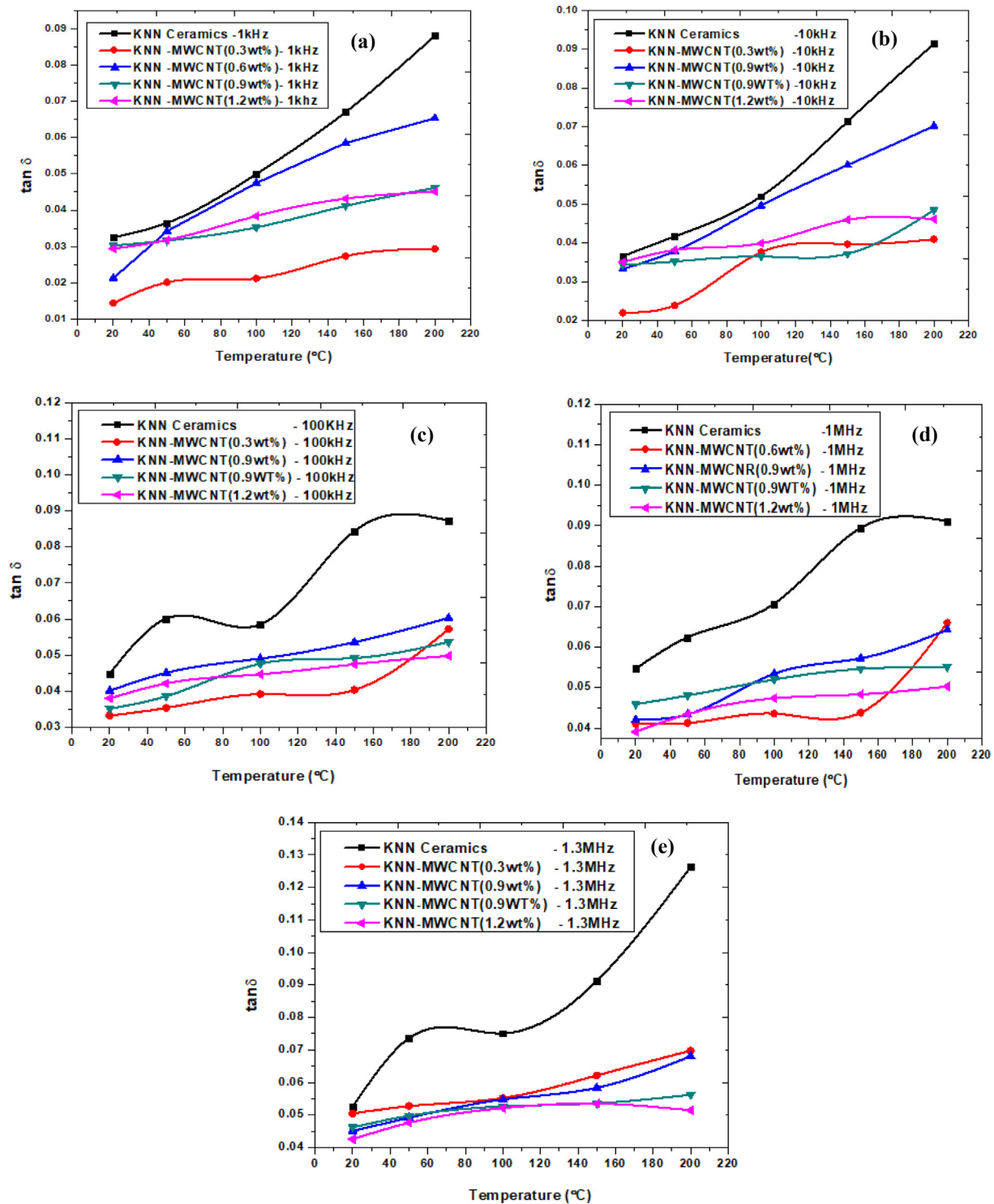


Fig. 8. Dielectric loss of KNN samples as a function of temperature. (a) 1kHz, (b) 10 kHz, (c) 100 kHz, (d) 1 MHz, and (e) 1.3 MHz.

3.9. Strain vs. electric field behavior

Fig. 10 shows the bipolar field-induced strains of KNN ceramics and composites. The typical butterfly shaped loops reported, indicates the piezoelectric nature of the KNN samples. The strain-electric field (S-E) hysteresis loop is formed due to converse piezoelectric effect of the lattice, switching and movement of domain walls [50]. The pure KNN ceramics reported remnant strain ~0.07%, whereas for KNN-MWCNT (0.3–0.9 wt.%) composites, the remnant strain increased gradually and reached maximum strain value (0.34%) for 0.9 wt.% addition of

MWCNTs in comparison to PLZT 8/60/40 [51]. The higher value of remnant strain reported for KNN-MWCNT composites is due to reduction of the potential barrier between polarization states and increased non-180° domain wall motion. Because addition of MWCNT helps in increasing the mobility of the charge carriers, interfacial properties and percolation path within the matrix and thereby increases the domain wall motion of nanocomposites during polarization. However, there was drastic reduction in the remnant strain values of KNN composites for 1.2 wt.% addition of MWCNT due to aggregation of lump mass of MWCNT within the matrix. This results in decreased mobility of the

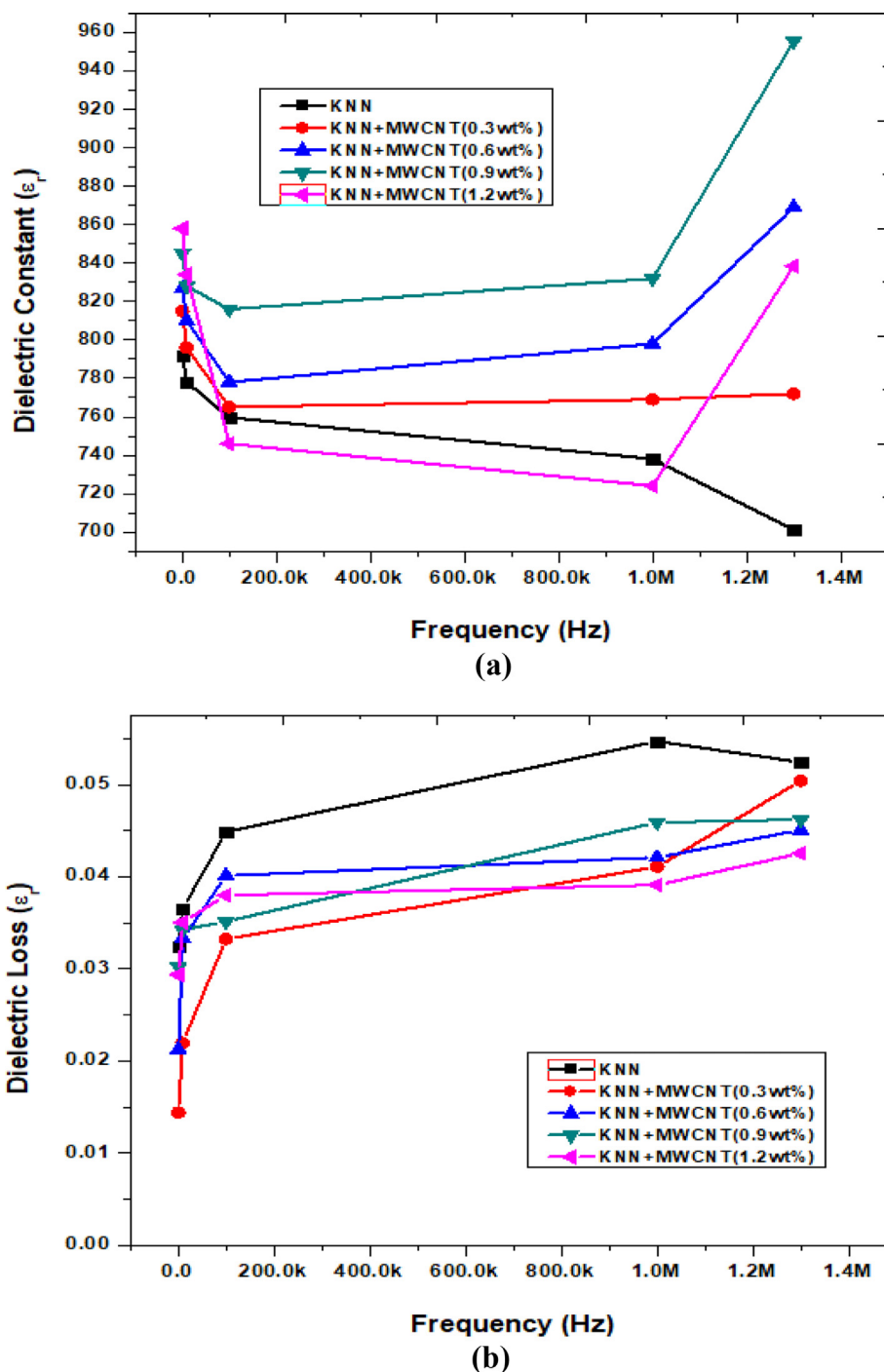


Fig. 9. The relative permittivity (a) and dielectric loss (b) of KNN samples as a function of frequency (1 kHz-1.3 MHz) at RT.

charge carriers, low percolation path and thereby results in reduced connectivity between the electrons and movement of non-180° domain wall respectively.

3.10. Ferroelectric properties

To examine the ferroelectric nature of KNN samples, the polarization vs. electric field (P-E) loops were measured as shown in Fig. 11. The KNN ceramics show a typical ferroelectric loop with narrow loop area and it can be contributed to low hysteresis loss. The macroscopic (remnant) polarization (P_r) retained at zero field, permanent electric dipole moment, (Spontaneous polarization, P_s) exhibited and coercive field to bring the polarization to zero in case of pure KNN material was

reported to be 14.28 $\mu\text{C}/\text{cm}^2$, 15.4 $\mu\text{C}/\text{cm}^2$ and 21.02 kV/Cm respectively.

However, the hysteretic behavior of polarization vs. field dependence, changes in case of KNN composites due to addition of MWCNTs (0.3–1.2 wt.%). For all the KNN-MWCNT composites, hysteresis becomes symmetric and its area reduces with increased addition of MWCNTs between 0.3 wt.% and 1.2 wt.%. Here a transition from typical ferroelectric hysteresis loop into round loop was observed. This is due to increased conductivity observed in KNN composites. The increased conductivity observed in KNN composites yields in large loop area due to faster switching of the domain wall and thereby results in high hysteresis loss. Hence KNN-MWCNT (0.3–0.9 wt.%) composites possess high retentivity and coercivity which makes them more

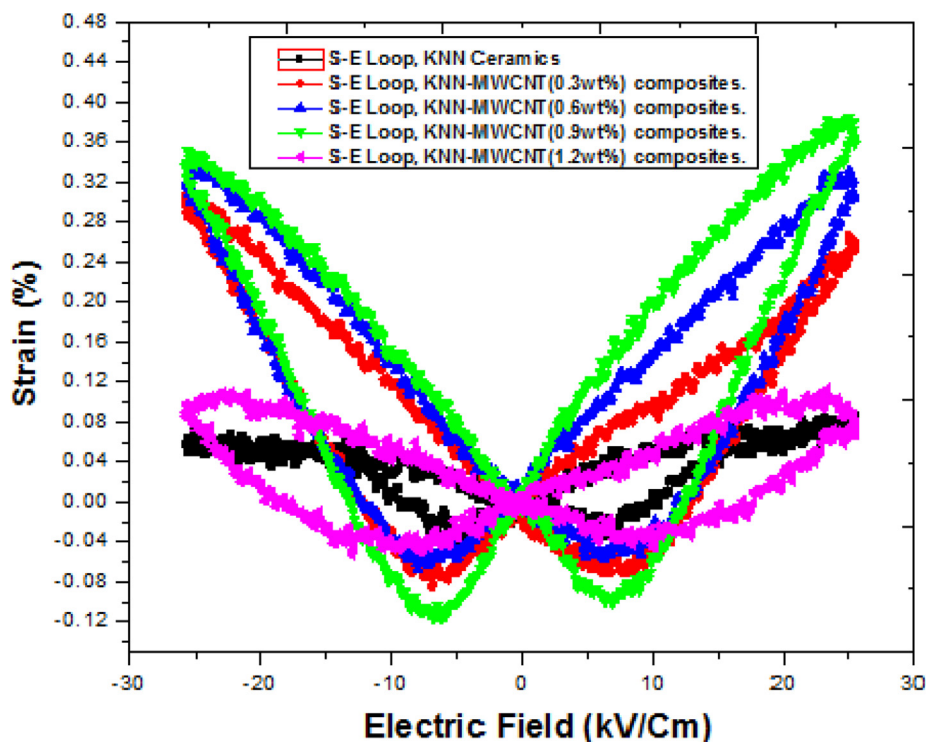


Fig. 10. Strain vs. Electric field (S-E) loops of KNN ceramics and KNN – MWCNT (0.3–1.2 wt%) composites.

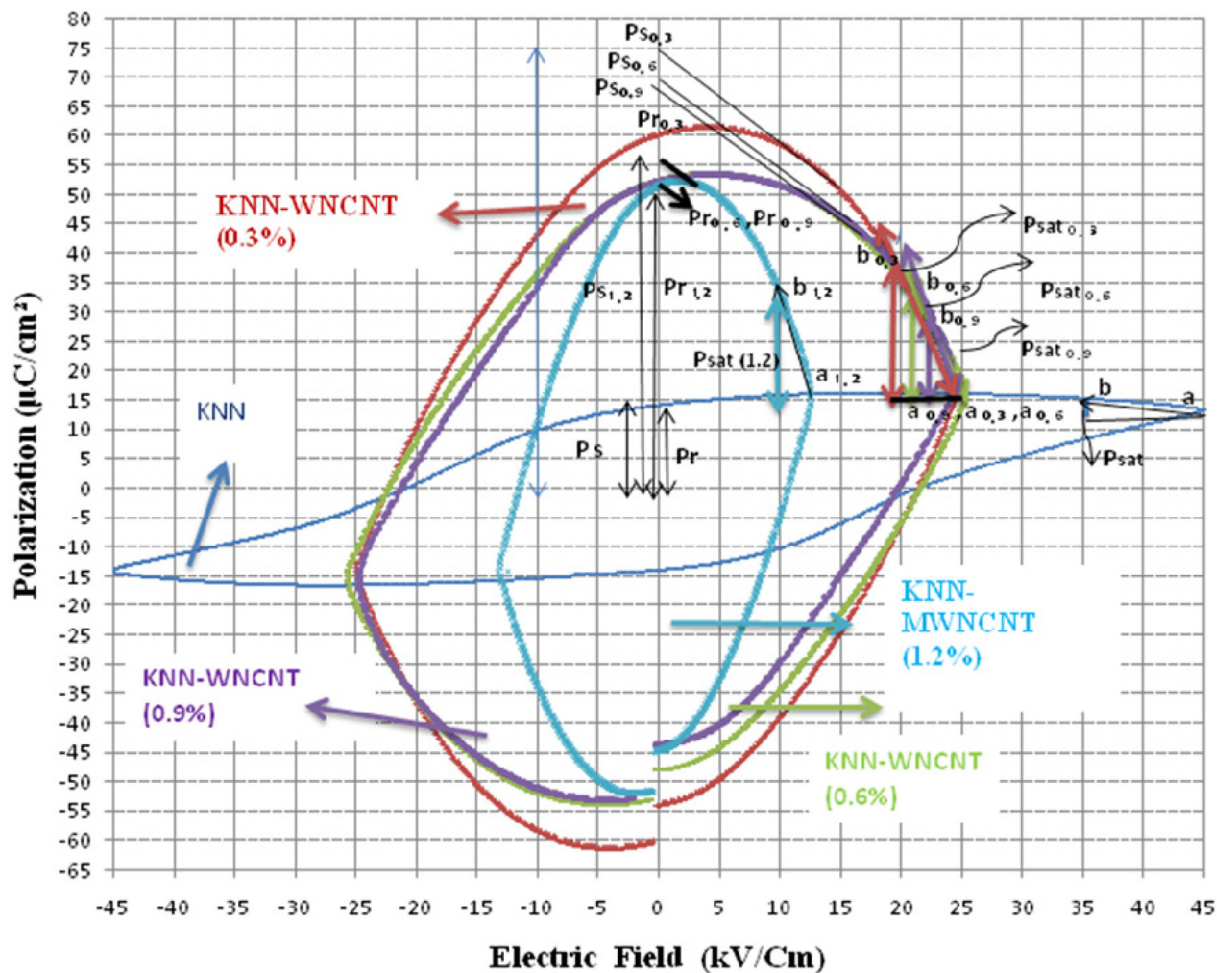


Fig. 11. Polarization VS. Electric field (P-E) loops of KNN ceramics and KNN-MWCNT (0.3–1.2 wt%) composites.

suitable for magnetic applications. Reinforcement of MWCNT into KNN ceramics facilitates poling and results in increase of piezoelectric properties by forming percolation path through the composites. Due to which, observance of saturated polarization becomes difficult in the combined system. However, addition of MWCNT above threshold, results in large enough conductivity and the polarization contributed by switching of the domain wall will be totally submerged. This is due to formation of continuous pathway, electrical leakage and the increased ferroelectric loss within the composite. As a result, the connectivity gap observed in P-E loop for KNN composites increases.

Hence the hysteresis loop of KNN composites is a combination of a linear resistor and a ferroelectric crystal. This combination has the evidence for ferroelectricity but may possess difficulty in extracting from conductivity within the matrix. The observed squareness in hysteresis loop of KNN composites indicates these are magnetic ceramics (ferrite materials). Since squareness of the hysteresis loop is tilted in case of KNN composite, the extrapolation of the linear part a (P_{sat}) will also be tilted. The spontaneous polarization at zero external field (P_s , $P_{s\ 0.3}$, $P_{s\ 0.6}$, $P_{s\ 0.9}$, $P_{s\ 1.2}$), remnant polarization (P_r $P_{r\ 0.3}$, $P_{r\ 0.6}$, $P_{r\ 0.9}$, $P_{r\ 1.2}$), saturated polarization (P_{sat} , $P_{\text{sat}\ 0.3}$, $P_{\text{sat}\ 0.6}$, $P_{\text{sat}\ 0.9}$, $P_{\text{sat}\ 1.2}$) for KNN and its composites (0.3–1.2 wt.%) were represented as mentioned above. The saturated polarization of the samples was calculated by measuring the linear part a, $a_{0.3}b_{0.3}$, $a_{0.6}b_{0.6}$, $a_{0.9}b_{0.9}$ and $a_{1.2}b_{1.2}$ respectively. The squareness ratio was measured by P_r / P_s for all the samples. The measured remnant polarization, spontaneous polarization, coercive field, squareness ratio and saturated polarization is as shown in Table 2.

The measured spontaneous polarization of KNN and its composites were significantly high as they are polycrystalline material. Its actual calculation needs the knowledge of actual switching mechanism, nucleation and growth of non-180 domain. However the tilted squareness of the hysteresis loop itself strongly suggest switching to involve 90° and 180° domains. The squareness ratio was maximum for KNN ceramics and it reduced gradually with addition MWCNTs within the percolation threshold as observed due to reduced cross-sectional area. The obtained remnant polarization for the composites were higher than KNN ceramics with maximum being measured for 0.3 wt.%MWCNTs/KNN composite. In addition the saturation polarization values of the composites increased with addition of MWCNTs in comparison to KNN ceramics due to the effect of enhanced percolation clusters.

Also, the obtained remnant polarization values were higher than reported values for PZT, KNN & BiTO₃ ceramics obtained by microwave sintering [39,52,48,10]. High remnant polarization reported for KNN composites indicates the presence of proper domain states, electromechanical boundary conditions near grain boundaries and good surface area due to reinforcement of MWCNTs into KNN ceramics. whereas in case of PDMS/MWCNTs composites, negative permittivity was obtained due to induced electric dipoles [53].

3.11. Temperature dependence of electromechanical properties

The planar mode electromechanical coupling coefficients (K_p) of KNN samples as a function of temperature is shown in Fig. 12. The higher value of K_p was observed for all the KNN samples near PPT. The

Table 2

Remnant, spontaneous, saturated polarization, coercive force and squareness ratio of KNN ceramics and composites.

Sl. No	Material	Pr ($\mu\text{C}/\text{cm}^2$)	Ps ($\mu\text{C}/\text{cm}^2$)	Ec (kV/Cm)	Squareness ratio	Psat
1	KNN	14.28	15.4	21.02	0.9272	0.25
2	KNN + 0.3 wt%	60.20	75	21.60	0.8006	4.6
3	KNN + 0.6 wt%	53	69.5	21.50	0.7625	5
4	KNN + 0.9 wt%	53	69	20.41	0.7681	5.7
5	KNN + 1.2 wt%	50	56	11.22	0.8928	7

presence of many polarization states near PPT enhances the piezoelectric properties [54]. The maximum K_p value of 0.36 was reported for KNN ceramics at RT. However, the K_p value of KNN composites were higher than KNN ceramics with maximum value of 0.46 reported for 0.9% MWCNT composites due to increased mobility of charge carriers during polarization. The improved mobility of the electrons results in high energy conversion, and develops a strong electromechanical coupling system. Similar effect of charge carriers is attributed to the coupling effect of nanocomposites in case of photo catalytic activity of TiO₂/SnO₂ Nanofibers [55]. Similarly enhanced electromagnetic interference were observed at ultralow percolation threshold in poly(L-lactide)/multi-walled carbon nanotube composites [56] The values of k_p for all samples reduced drastically after PPT, and reached ~ 0 at T_c . This is due to thermal depoling of the samples at higher temperatures.

3.12. Temperature dependence of mechanical quality factor

The Mechanical Q (Q_m) of the KNN samples as a function of temperature is shown in Fig. 13. The Q_m value of 404 was reported for KNN ceramics at RT, with maximum being 507 at 100 °C. However, the Q_m of KNN composites (0.3–1.2 wt.%) were higher at RT than the values for pure KNN ceramics. The highest value of 501 was reported for 0.9% MWCNT composites similar to PZT [38] at RT which was almost same up to 100 °C. The Q_m for KNN-MWCNT (0.3–1.2 wt.%) composites being 420, 484, 501, and 286 at RT corresponded to mechanical loss factor (reciprocal of Q_m) of 0.0023, 0.0020, 0.0019, and 0.0034 respectively. However, the addition of MWCNTs by 1.2 wt.% reduced Q_m drastically due to increased conductivity in the KNN composites.

3.13. Temperature dependence of natural frequency constant

The planar surface oscillation (N_p) of KNN samples as a function of temperature is shown in Fig. 14. The N_p of pure KNN ceramics was 13,928 Hz.m at RT and was almost same at measured temperature range between 20 and 200 °C. The maximum value of 15,000 Hz.m was reported for KNN composite (1.2 wt.%) measured at same condition. Whereas the frequency coefficients of KNN-MWCNTs (0.3–0.9 wt.%) composites were lesser than pure KNN and almost same up to 150°C as shown in the figure. The low N_p value reported near PPT (200 °C) for KNN composites is due to increased elastic compliance and change in hardness or the bonding strength of ionic constituents. However, the obtained N_p values for KNN composites (0.3–0.9 wt.%) within percolation threshold are lower than that of reported N_p values for pure KNN ceramics. The addition of MWCNT above percolation threshold (1.2 wt.%) yielded in enhanced frequency co-efficient due to reduced elastic compliance and variation in ionic constituents.

3.14. Poling temperature dependence of piezoelectric charge coefficient

Fig. 15 shows the variation in piezoelectric charge coefficient (d_{33}) of KNN samples as a function of poling temperature. The d_{33} values of pure KNN (~ 124 pC/N) at RT increased gradually with the increase in poling temperature. However, the improved piezoelectric charge constant reported for KNN composites such as ~ 131 pC/N, 140 pC/N and 168 pC/N for 0.3, 0.6 and 0.9 wt.% addition of MWCNTs respectively, is due to the existence of conductive filler inside the KNN matrix which facilitates poling and forms percolation path through KNN composites. Further these KNN composites showed improvement in d_{33} with increased poling temperature. Because MWCNTs are capable of enhancing the impedance, electric conductivity of the composite in wide frequency range and at different temperatures [37]. This change in piezoelectric co-efficient correspond to sharp rise in conductivity due to increased number of localized MWCNT percolation clusters, which leads to formation of conductive pathways due to electron tunneling and direct contact [57]. Whereas the least d_{33} value of 111 pC/N obtained for KNN composite (1.2 wt.%) at RT, reduced further with

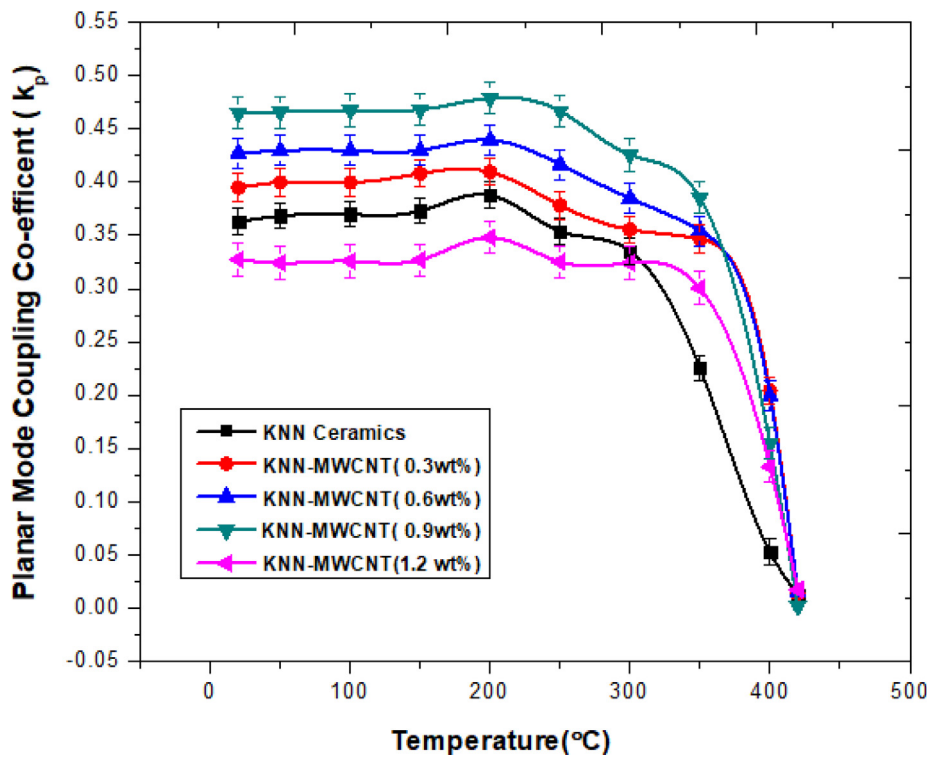


Fig. 12. Temperature dependence of Electro – mechanical coupling coefficient, (k_p) of KNN ceramics and KNN-MWCNT composites.

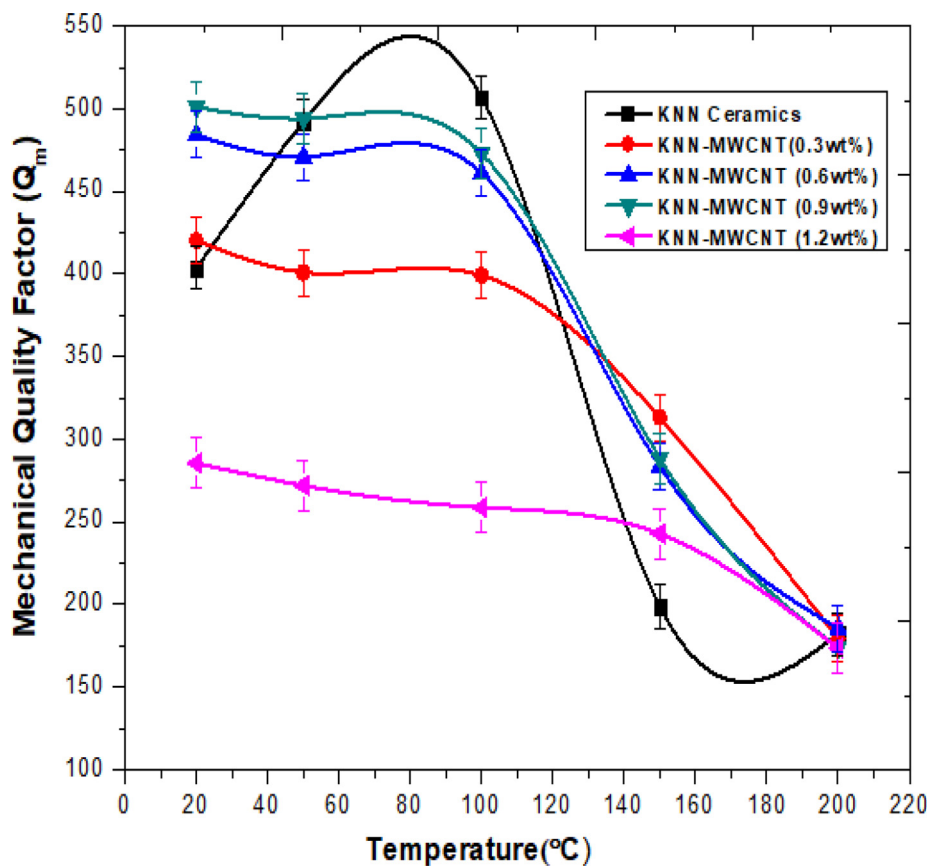


Fig. 13. Temperature dependence of Mechanical quality factor (Q_m) of KNN ceramics and KNN-MWCNT composites.

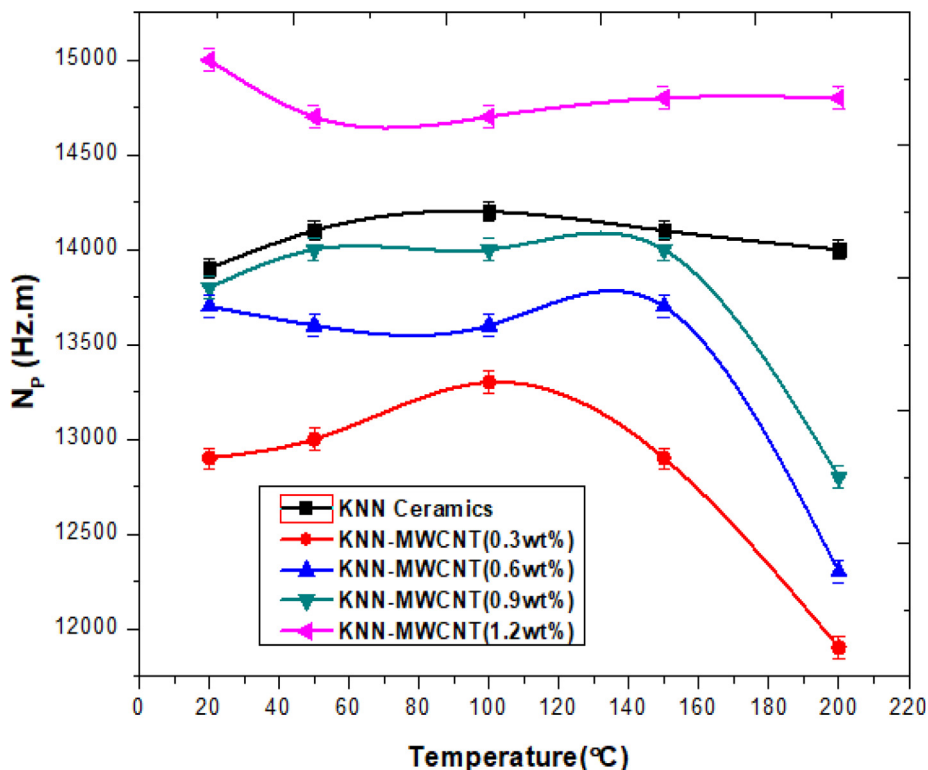


Fig. 14. Temperature dependence of the frequency constant (N_p) of KNN ceramics and KNN-MWCNT (0.3–1.2 wt.%) composites.

increased poling temperature. This is because, increased addition of MWCNTs results in the formation of agglomerations and porous structure (Fig. 1(e)) above threshold, hence there will be loss of connectivity and reduced percolation path. Hence there will be no much percolation of the charges during polarization and results in reduced piezoelectric charge coefficients [21]. Moreover, the higher

loading of MWCNT above threshold will increase the leakage current and dissipate part of electrical potential energy by piezoelectric effect. However, the obtained d_{33} values were comparatively higher than reported values for microwave sintered KNN ceramics [10].

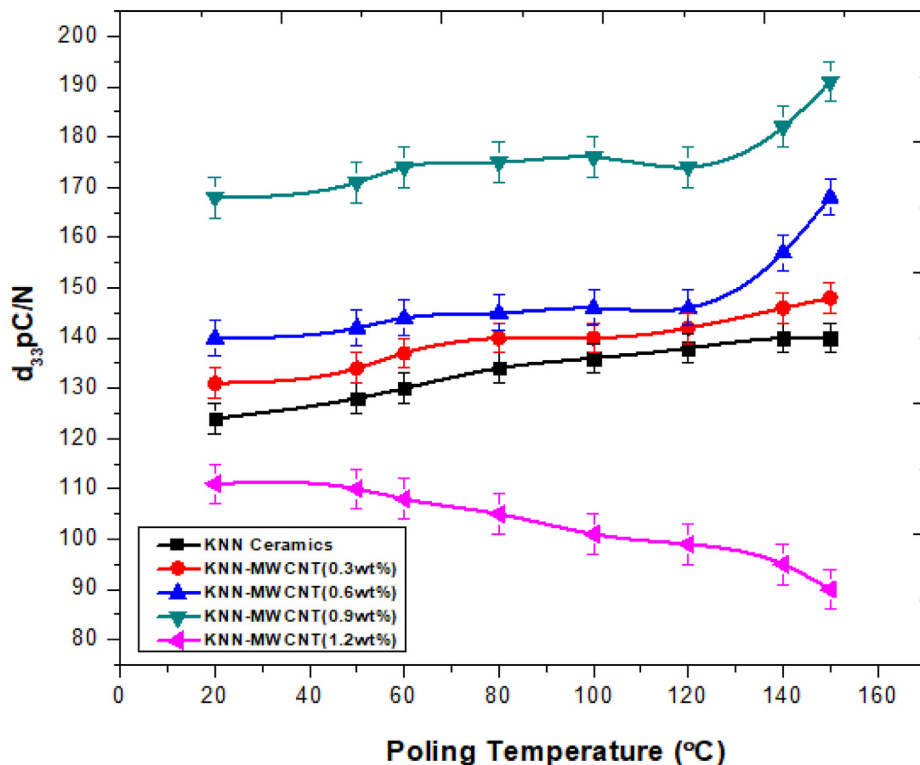


Fig. 15. Piezoelectric co-efficient (d_{33}) of KNN ceramics and KNN-MWCNT (0.3–1.2 wt.%) composites as a function of poling temperature.

4. Conclusion

In this investigation, the effect of MWCNTs reinforcement on the dielectric and piezoelectric properties of KNN composites prepared by microwave assisted sintering has been studied. MWCNTs reinforced KNN matrix resulted in the formation of porous fine grain microstructure with the presence of conductive fillers across pores and cracks in the sintered composites. Distortion and modified behaviour of the tetragonal diffraction peaks at 45° and 52° made the KNN composites to move towards high tetragonal state with increased c/a ratio from 1.0093 to 1.015. KNN – MWCNT (0.3–0.9 wt.%) composites sintered at optimized temperature of 1100 °C showed reduction in its relative density between 0.5 and 4.02% in comparison with pure KNN ceramics. Dielectric (ϵ_r), ferroelectric (P_r , P_s , E_c), piezoelectric (d_{33} , Q_m , K_p , N_p) properties and remnant strain of KNN-MWCNT (0.3–0.9 wt.%) composites improved gradually with increased addition of MWCNTs and were maximum for KNN (0.9 wt.%) composites. Dielectric losses of KNN composites were below 4% for measured frequency range of 1 kHz–1 MHz and were comparatively lesser than that of pure KNN ceramics. However, the reduction in the effective permittivity for 1.2 wt.% addition of MWCNTs to few hundred can be focused further for tunability applications. Thus, the reinforcement of MWCNTs into KNN composites have shown a significant change in electrical properties of KNN composites. The composite with 0.9 wt.% of conductive fillers helped in achieving highest relative permittivity, remnant strain, coupling coefficient (K_p), quality factor (Q_m), and piezoelectric co-efficient. This makes them suitable for nanogenerators, energy storage devices, transducers etc. Furthermore, low dielectric loss and highest remnant polarization achieved for 0.3 wt.% of nanotubes makes itself suitable for tunable capacitor device applications. In addition, high squareness ratio (0.76–0.92) of the hysteresis loop obtained for KNN samples makes them find applications in switching circuits, and storage elements.

Acknowledgement

The authors would like to acknowledge the financial support of R.V.C.E, Bangalore under TEQIP-II Subcomponent 1.2, Characterization facilities support at CENSE Department under INUP (Indian Nano Electronics user Program) funded by Department of MCIT (Ministry of Communication and Information Technology), DST, DRDO and Ministry of Defence, Government of INDIA, Material engineering department at IISC, Bangalore, and technical guidance from Dr. Nagaboopathy Mohan, CENSE dept., IISC Bangalore.

References

- [1] H. Kim, Y. Tadesse, S. Priya, Piezoelectric energy harvesting, energy harvesting technologies, in: S. Priya, D.J. Inman, (Eds.), Springer (2009) 3–39.
- [2] S. Priya, Advances in energy harvesting using low profile piezoelectric transducers, *J. Electroceram.* 19 (2007) 167–184.
- [3] E. Hollenstein, D. Damjanovic, N. Setter, Temperature stability of the piezoelectric properties of Li-modified KNN ceramics, *J. Eur. Ceram. Soc.* 27 (2007) 4093–4097.
- [4] E. Ringgaard, T. Wurlitzer, W. Wolny, Properties of lead-free piezoceramics based on alkali niobates, *Ferroelectrics* 319 (2005) 97–107.
- [5] L. Egerton, D.M. Dillon, Piezoelectric and dielectric properties of ceramics in the system potassium – sodium niobate, *J. Am. Ceram. Soc.* 42 (1959) 438–442.
- [6] G. Shirane, R. Newnham, R. Pepinsky, Dielectric properties and phase transitions of NaNbO_3 and $(\text{Na}, \text{K})\text{NbO}_3$, *Phys. Rev.* 96 (1954) 581–588.
- [7] G.H. Haertling, Properties of hot-pressed ferroelectric alkali niobate ceramics, *J. Am. Ceram. Soc.* 50 (1967) 329–330.
- [8] H. Birol, D. Damjanovic, N. Setter, Preparation and characterization of $(\text{K}_{0.5}\text{Na}_{0.5})\text{NbO}_3$ ceramics, *J. Eur. Ceram. Soc.* 26 (2006) 861–866.
- [9] H.L. Du, Z.M. Li, F.S. Tang, S.B. Qu, Z.B. Pei, W.C. Zhou, Preparation and piezoelectric properties of $(\text{K}_{0.5}\text{Na}_{0.5})\text{NbO}_3$ lead-free piezoelectric ceramics with pressure-less sintering, *Mater. Sci. Eng. B* 131 (2006) 83–87.
- [10] M. Feizpour, H.B. Bafroei, R. Hayati, T. Ebadzadeh, Microwave assisted synthesis and sintering of potassium sodium niobate lead free piezoelectric ceramics, *Ceram. Int.* 40 (2014) 871–877.
- [11] R. Wang, R. Xie, T. Sekiya, Y. Shimajo, Fabrication and characterization of potassium–sodium niobate piezoelectric ceramics by spark-plasma-sintering method, *Mater. Res. Bull.* 39 (2004) 1709–1715.
- [12] R. Zuo, C. Ye, Structures and piezoelectric properties of $(\text{Na K Li})_{1-x}(\text{Bi Na Ba})_x\text{Nb}_{1-x}\text{Ti}_x\text{O}_3$ lead-free ceramics, *Appl. Phys. Lett.* 91 (2007) 062916.
- [13] Y. Saito, H. Takao, High performance lead-free piezoelectric ceramics in the $(\text{Na}_{0.5}\text{K}_{0.5})\text{NbO}_3\text{-LiTaO}_3$ solid solution system, *Ferroelectrics* 338 (2006) 17–32.
- [14] B.Q. Ming, Piezoelectric properties of (Li, Sb, Ta) modified $(\text{Na}, \text{K})\text{NbO}_3$ lead free ceramics, *J. Appl. Phys.* 101 (2007) 054103.
- [15] R. Zuo, J. Fu, Rhombohedral tetragonal phase coexistence and piezoelectric properties of $(\text{Na K})(\text{Nb Sb})\text{O}_3\text{-LiTaO}_3\text{-BaZrO}_3$ lead-free ceramics, *J. Am. Ceram. Soc.* 94 (2011) 1467–1470.
- [16] Y. Guo, P. Kakimoto, H. Ohsato, Phase transitional behavior and piezoelectric properties of $(\text{Na}_{0.5}\text{K}_{0.5})\text{NbO}_3\text{-LiNbO}_3$ ceramics, *Appl. Phys. Lett.* 85 (2004) 4121–4123.
- [17] Q. Zhang, Effects of Sb content on electrical properties of lead-free piezoelectric $(\text{Na}_{0.535}\text{K}_{0.48}\text{O})_{0.942}\text{Li}_{0.058}(\text{Nb}_{1-x}\text{Sb}_x)\text{O}_3$ ceramics, *J. Alloys Compd.* 490 (2010) 260–263.
- [18] Y. Saito, Lead-free piezoceramics, *Nature* 432 (2004) 84–87.
- [19] J. Wu, D. Xiao, Y. Wang, W. Wu, B. Zhang, J. Zhu, Microstructure and electrical properties of (Li, Ag, Ta, Sb) modified $(\text{K}_{0.50}\text{Na}_{0.50})\text{NbO}_3$ lead-free ceramics with good temperature stability, *J. Phys. D: Appl. Phys.* 41 (2008) 125405.
- [20] V. Prince, P. Ram Pratap, Manmeeta, S. Dhiraj, Study of dielectric and piezo-electric properties of CNT reinforced PZT-PVA 0-3 composite, *AIP Conf. Proc.* 1728 (2016) 020341-5.
- [21] E.C. Cristina, L. Paduraraju, P.C. Lavinia, L. Nicoleta, L. Isabelle, M. Deluca, T. Sorin, G. Carmen, L. Mitiseriu, Using multiwalled carbon nanotubes in spark plasma sintered $\text{Pb}(\text{Zr}_{0.47}\text{Ti}_{0.53})\text{O}_3$ ceramics for tailoring dielectric and tunability properties, *J. Appl. Phys.* 116 (2014) 164110.
- [22] M.C. Ray, R.C. Batra, A single-walled carbon nanotube reinforced 1–3 piezoelectric composite for active control of smart structures, *Smart Mater. Struct.* 16 (2007) 1936–1947.
- [23] T. Sheng, C. Fangjin, X. Wang, New type of Piezo-damping epoxy-matrix composites with multiwall carbon nanotubes and lead zirconate titanate, *Mater. Lett.* 62 (2008) 3859–3861.
- [24] X.D. Wang, X. Liu, H. Yuan, H. Liu, C. Liu, T. Li, C. Yan, X. Yan, C. Shen, Z. Guo, Non-covalently functionalized graphene strengthened poly (vinyl alcohol), *Mater. Des.* 139 (2018) 372–379.
- [25] M. Zhao, L. Meng, M. Lichun, M. Lina, X. Yang, Y. Huang, J.E. Ryu, S. Akash, T. Li, C. Yan, Z. Guo, Layer-by-layer grafting CNTs onto carbon fibres surface for enhancing the interfacial properties of epoxy resin composites, *Compos. Sci. Technol.* 154 (2018) 28–36.
- [26] G. Yu, Y. Lu, J. Guo, P. Manisha, B. Adarsh, X. Wang, B. Qiu, C. Jeffryes, S. Wei, Z. Guo, K.W. Evan, Carbon nanotubes, graphene, and their derivatives for heavy metal removal, *Adv. Compos. Hybrid Mater.* (2017), <https://doi.org/10.1007/s42114-017-0004-3>.
- [27] J. Cui, S. Zhou, Facile fabrication of highly conductive polystyrene/nanocarbon composites with robust interconnected network via electrostatic attraction strategy, *J. Mater. Chem. C* (2018), <https://doi.org/10.1039/C7TC04752E>.
- [28] S.M. Aqeel, Z. Huang, J. Walton, C. Baker, D.L. Falkner, Z. Liu, Z. Wang, Polyvinylidene fluoride (PVDF)/polyacrylonitrile (PAN)/carbon nanotube nanocomposites for energy storage and conversion, *Adv. Compos. Hybrid Mater.* (2017), <https://doi.org/10.1007/s42114-017-0002-5>.
- [29] Z. Wu, S. Gao, L. Chen, D. Jiang, Q. Shao, B. Zhang, Z. Zhai, C. Wang, M. Zhao, Y. Ma, X. Zhang, L. Weng, M. Zhang, Z. Guo, Electrically insulated epoxy nanocomposites reinforced with synergistic core-shell $\text{SiO}_2\text{@MWCNTs}$ and montmorillonite bifillers, *Macromol. Chem. Phys.* (2017), <https://doi.org/10.1002/macp.201700357>.
- [30] X. Zhang, G. Hongbo, G.M. Guo, G. Li, Y. Liu, D. Li, A study on key technologies of unmanned driving, *CAAI Trans. Intelligence Technol.* 1 (2016) 4–13.
- [31] H. Jin, Q. Chen, Z. Chen, Y. Hu, J. Zhang, Multi-Leap Motion sensor based demonstration for robotic refine tabletop object manipulation task, *CAAI Trans. Intelligence Technol.* 1 (2016) 104–113.
- [32] P. Sasmita, P. Siddhartha, A hybrid stochastic fractal search and pattern search technique based cascade PI-PD controller for automatic generation control of multisource power systems in presence of plug in electric vehicles, *CAAI Trans. Intelligence Technol.* 2 (2017) 12–15.
- [33] CAAI Transactions on Intelligence technology 1(2016) 1–3.
- [34] H.J. Sandoval, Nano-tailoring photo cross linkable epoxy resins with multi-walled carbon nanotubes for stereo lithography layered manufacturing, *J. Mater. Sci.* 42 (2007) 156–165.
- [35] T. Liu, K. Yu, L. Gao, H. Chen, N. Wang, L. Hao, T. Li, H. He, Z. Guo, A graphene quantum dot decorated SrRuO_3 mesoporous film as an efficient counter electrode for high performance dye-sensitized solar cells, *J. Mater. Chem. A* 5 (2017) 17848.
- [36] F. Rubio Marcos, P. Marchet, T. Merle Mejean, J.F. Fernandez, Role of sintering time, crystalline phases and symmetry in the piezoelectric properties of lead free KNN-modified ceramics, *Mater. Chem. Phys.* 123 (2010) 91–97.
- [37] M. Saleem Aqeel, Z. Huang, J. Walton, C. Baker, D.L. Falkner, Z. Liu, Z. Wang, Polyvinylidene fluoride (PVDF)/polyacrylonitrile (PAN)/carbon nanotube nanocomposites for energy storage and conversion, *Adv. Compos. Hybrid Mater.* (2017), <https://doi.org/10.1007/s42114-017-0002-5>.
- [38] W.C. Lee, K.S. Liu, I.N. Lin, Microwave sintering $\text{Pb}(\text{Zr}_{0.52}\text{Ti}_{0.48})\text{O}_3$ piezoelectric ceramics, *Ferroelectrics* 262 (2001) 293–298.
- [39] J. Fu, R. Zuo, X. Wang, L. Li, phase transition characteristics and piezoelectric properties of compositionally optimized alkaline niobate based ceramics, *J. Alloys Compd.* 486 (2009) 790–794.
- [40] Y. Dai, X. Zhang, G. Zhou, Phase transitional behavior in $(\text{Na}_{0.5}\text{K}_{0.5})\text{NbO}_3\text{-LiTaO}_3$ ceramics, *Appl. Phys. Lett.* 90 (2007) 262903.

- [41] X. Pang, J. Qiu, K. Zhu, Nana Dong, Phase transition behavior and temperature stable piezoelectric properties of new quaternary (K Na) NbO₃ based ceramics, *Ceram. Int.* 39 (2013) 641–647.
- [42] L. Wang, Z. Dang, Carbon nanotube composite with high dielectric constant at low percolation threshold, *Appl. Phys. Lett.* 87 (2005) 042903-3.
- [43] I. Madni, S. Yu, R. Sun, Carbon nanotubes based composites with high dielectric constant and low loss, *IEEE* (2012) 978-1-4673-4944-4.
- [44] K. Shehzad, A.A. Hakro, Y. Zeng, S.H. Yao, Y.X. Hong, M. Mumtaz, K. Nadeem, N.S. Khisro, Z.M. Dang, Two percolation thresholds and remarkably high dielectric permittivity in pristine carbon nanotube/elastomer composites, *Appl. Nano Sci.* 5 (2015) 969–974.
- [45] Z. Sun, L. Zhang, F. Dang, Y. Liu, Z. Fei, Qian Shao, Hong Lin, Jiang Guo, Lichen Xiang, Narendranath Yerra, Zhanhu Guo, *CrystEngComm* 19 (2017) 3288–3298.
- [46] L. Shen, Y.H. Han, C. Xiang, H. Tang, A. Mukherjee, S. Kim, S.I. Baeb, Qing Huang, Phase transformation behavior of ZrO₂ by addition of carbon nanotubes consolidated by spark plasma sintering, *Scr. Mater.* 69 (2013) 736–739.
- [47] R.K. Sonia, Patel, P. Kumar, C. Prakash, D.K. Agrawal, Low temperature synthesis and dielectric, ferroelectric and piezoelectric study of microwave sintered BaTiO₃ ceramics, *Ceram. Int.* 38 (2012) 1585–1589.
- [48] D.J. Bergman, Y. Imry, Analyticity and critical behavior of the complex dielectric constant near the percolation threshold of a heterogeneous system, *Proc. Stat. Phys.* 13 (1978) 467.
- [49] S.L. Shi, L.Z. Zhang, J.S. Li, Electrical and dielectric properties of multiwall carbon nanotube/polyaniline composites, *J. Polymer Res.* 16 (2009) 395–399.
- [50] D. Damjanovic, Ferroelectric, dielectric and piezoelectric properties of ferroelectric thin films and ceramics, *Rep. Prog. Phys.* 61 (1998) 1267–1324.
- [51] K. Ajeet, K.C. James Raju, A.R. James, enhanced piezo response in mechanically activated and microwave sintered PLZT 8/60/40 ceramics, 2016, *IEEE international symposium*.
- [52] K.S. Pramod, Z. Ounaies, V.V. Varadan, V.K. Varadan, Dielectric and piezoelectric properties of microwave sintered PZT, *Smart Mater. Struct.* 5 (2001).
- [53] K. Sun, P. Xie, Z.Y. Wang, T. Su, Q. Shao, J.E. Ryu, X. Zhang, J. Guo, S. Akash, J.F. Li, R. Fan, D. Cao, Z. Guo, Flexible poly dimethyl siloxane/multi-walled carbon nanotubes membranous meta composites with negative permittivity, *Polymer* 125 (2017) 50–57.
- [54] Y.P. Guo, K. Kakimoto, H. Ohsato, (Na_{0.5}K_{0.5}) NbO₃-LiTaO₃ lead-free piezoelectric ceramics, *Mater. Lett.* 59 (2005) 241–244.
- [55] L. Zhang, W. Yu, C. Han, J. Guo, Q. Zhang, H. Xie, Q. Shao, Z. Sun, Zhanhu Guo, Large scaled synthesis of heterostructured electro spun TiO₂/SnO₂ Nanofibers with an enhanced photo catalytic activity, *J. Electrochem. Soc.* 164 (2017) H651–H656.
- [56] K. Zhang, G.H. Li, L.M. Feng, N. Wang, J. Guo, K. Sun, K.X. Yu, J.B. Zeng, T. Li, Z. Guo, M. Wang, Ultralow percolation threshold and enhanced electromagnetic interference shielding in poly (L-lactide)/multi-walled carbon nanotube nanocomposites with electrically conductive segregated networks, *J. Mater. Chem. C* 5 (2017) 9359–9369.
- [57] W.S. Bao, et al., Tunneling resistance and its effect on the electrical conductivity of CNT nanocomposites, *J. Appl. Phys.* 111 (2012) 093726.
- [58] D.J. Bergman, Y. Imry, Critical behavior of the complex dielectric constant near the percolation threshold of a heterogeneous material, *Phys. Rev. Lett.* 39 (1977) 1222.



Finite Element Analysis of Tibia Bone

Naveen Tippanagoudar¹, Anantha Krishna G L²

M.Tech in Machine Design¹, Assistant Professor²

Department of Mechanical Engineering

BMS Institute of Technology and Management Bengaluru, India

Abstract:

The present research in the field of automotive industry incorporates the analysis of lower region of the human body in order to bring more accidental safety to human life. The lower skeleton is composed of thigh, knee, lower limb and foot. The lower limb bone in medical term coined as Tibia bone. The Tibia bone is more prone to damage during accidents; it is the second strongest bone to take major body weight. The bone has the ability to withstand large loads without fracture, but the bone fails during impact loads. Present work considers the analysis of the Tibia bone for impact loads. 3D model was generated using Catia software after taking CT scan of a typical Tibia bone. Finite Element Model (FEM) was developed using Hypermesh software. Finite Element Analysis (FEA) was carried out by using Nastran software.

Keywords: CT scan , FEM, Hypermesh, Nastran

I. INTRODUCTION:

There has been lots of research regarding safety of human life in the field of automotive industry. Most of the cases, the research has been done on the upper part of the body and injury has been eliminated to an enormous extent, like by incorporating air bags and strengthening the vehicle body. But the lower part of the body is not considered until now, which is also a major part of the body. The recent Automotive Crash Analysis research has been found that, the driver's tendency is to depress the brake pedal just before the impact and crash. This action deserves the greatest impact in the lower leg. This led to lower leg research, study on composition of human bone, knowing its strength to withstand injury and rethink in the design of cars so as to reduce the impact force on lower bone. Tibia is the second largest and strongest bone in the human body. The Tibia bone is also known as shine bone. The lower leg consists of two types of bone, which in biologic term called as Tibia and fibula. Tibia is classified as a long bone and consists of two epiphyses and a diaphysis. The diaphysis is the middle section of the Tibia, also called the body or shaft. While the epiphysis is the two bone limbs, the upper (also known as superior or proximal) closest to the thigh and the lower (also known as distal or inferior) closest to the foot. In the lower third, the Tibia is most contracted and the distal end is smaller than the proxima. The Tibia bone is a composite material made up of hard and soft, spongy material Called Cortical bone and Cancellous bone or trabecular bone respectively. Bone Cancellous is one of type of human tissue found in the body. Cancellous bone occurs at the extreme ends of large bones and also in columns of pelvic bones.

II. LITERATURE REVIEW:

M. TothTascau et al [1] made an experimental study to evaluate the adult canine bone mechanical properties (Tibia), using mechanical bending test and numerical analysis. The results are correlated using finite element analysis. The geometry of Tibia

bone is obtained from Computed tomography (CT) and numerical analysis was performed using ANSYS. The test concludes that, deficiency induced in Tibia proximal area bone doesn't have any significant influence on the mechanical behaviour of Tibia bone considering bending test. The fracture lines tend slightly to defect zone. BAO Chun-yu and MENG Qing-hua [2] made an analysis study on Tibial stress during jumping moment using finite element analysis. The geometry of the bone is obtained from CT. Stress and displacement was simulated using finite element software. The results are used as theoretical basis for sports training, sports injury and treatment. The study concludes that, the stress is concentrated on the mid location of Tibia bone. The stress located on the foreside of Tibia is higher than rear. SaileshRajani and Bhavin V Mehata [4] focused on studying the development of stress on Tibia bone under static loads and studying the effects of different material properties on stresses, used Magnetic Resonance Imaging and solid modelling software to build a 3D model. The behaviour and stress pattern concludes that Cancellous bone act as a damper and distribute maximum stress to compact bone.

III. OBJECTIVES:

- 1) To find out stress, strain of Tibia bone subjected to static loading using Nastran for loads of 5KN and 10KN to understand impact load.
- 2) To calculate impact strength and check with Yield strength of bone material.
- 3) To find out deformation of Tibia bone to understand the type of fracture and displacement of bone.

IV. METHODOLOGY:

The following are the steps followed for analysis of Tibia bone.

- CT Scan
- 3D Slicer
- Catia

- Hypermesh
- Nastran

CT Scan:

Computed Tomography is an imaging technique, used to scan the human body. Special x-ray equipment is used in scanning the body.

3D Slicer:

3D slicer is an open source medical imaging software platform. It is used for image processing and three-dimensional visualization. Using this software, a three- dimensional view of Tibia bone is created using CT data as input.

Catia:

Computer Aided Three- dimensional Interactive Application is abbreviated as CATIA. It is well-known multi-platform modelling software, used to create 2D, 3D geometry. The CAD model is created using the geometry of scanned 3D model.

Hypermesh:

Hypermesh is a multi-disciplinary finite element pre-processor and post- processor software. It is one of the most effective tool for meshing largest and most complex models. The Tibia bone mode is imported from Catia for mesh generation. Tetrahedral elements are used for mesh generation of 3D models.

Nastran:

Nastran is finite element analysis software, used for analysing the given data. Nastran is one of the most used software in field of aerospace and other field.

Material Properties of Tibia Bone:

For the stress and displacement analysis, the bone is assumed to be isotropic material. The properties of the bone are shown in Table I.

Table.1. Material properties of Tibia bone

Sl. no	Material	E in GPA	δ in g/cm ³	μ	σ_y in MPa
1	Tibia bone	14	2	0.3	177

Analysis of Tibia bone:

The bone is created and meshed using tetrahedral mesh elements. The boundary conditions are fixed –free. A compressive load of 5KN and 10KN are applied at the proximal end of Tibia bone individually. The Tibia bone with mesh and constraints are shown in fig I.

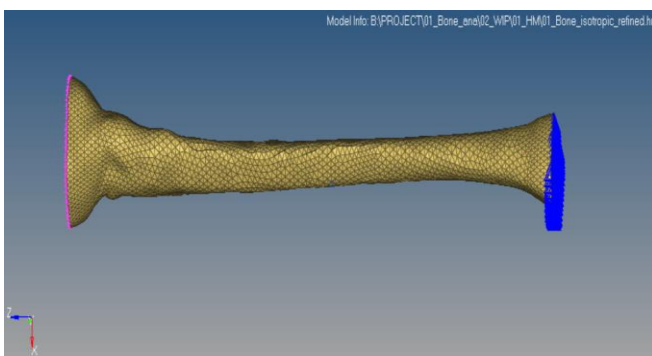


Figure.I. The loading and boundary condition

Constraints:

The Tibia bone is considered as single bone without considering the joints at distal and proximal end; hence the distal end is completely fixed.

The stresses and deformation for 5KN and 10KN are shown in Fig II to V.

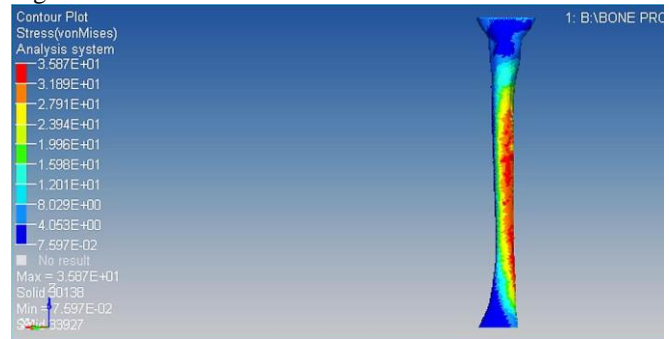


Figure.II. Stress for 5KN

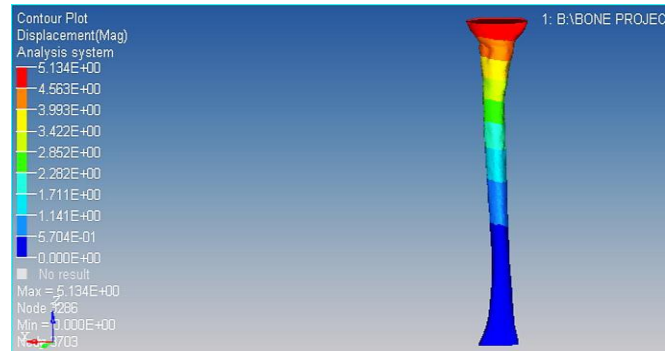


Figure.III. Displacement for 5KN

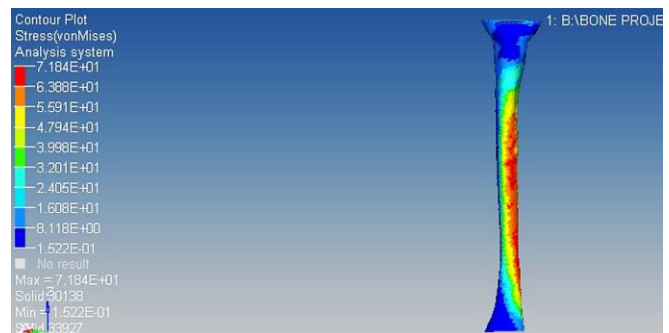


Figure.IV. Stress for 10KN

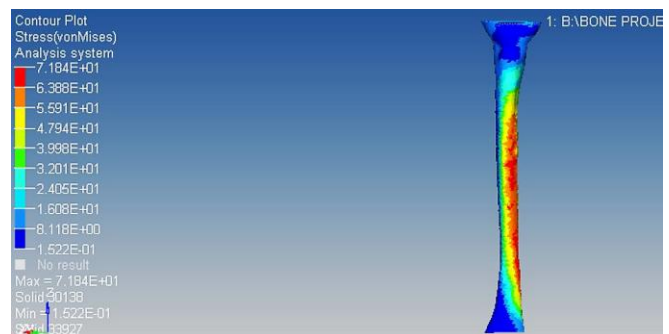


Figure.V. Displacement for 10 KN

The impact stress for the given loads, is determined from the formula.

$$\sigma_i = \sigma [1 + \sqrt{1 + 2h \delta}]$$

Where σ_i = impact stress; h= height; δ = static deflection;

σ = static stress.

1) σ_i for 5KN

$$\delta = 2.4 \text{ mm}; h = 100\text{mm}; \sigma = 35.8 \text{ MPa}$$

$$\sigma_i = 363.4 \text{ MPa}$$

2) σ_i for 10KN

$$\delta = 4.8 \text{ mm}; h = 100\text{mm}; \sigma = 71.8 \text{ MPa}$$

$$\sigma_i = 536 \text{ MPa}$$

The moment of inertia of the bone is determined from the formula.

$$\delta = \frac{wl^3}{384EI}$$

Where δ = static deflection; l = length of the bone; w = weight on the bone; E = young's modulus; I = moment of inertia.

for $\delta = 4.8 \text{ mm}$; $l = 360\text{mm}$;

$$I = 1.44 \times 10^5 \text{ mm}^4$$

A graph of Tibia bone on variation of polar moment of inertia with the area is shown in Fig VI.

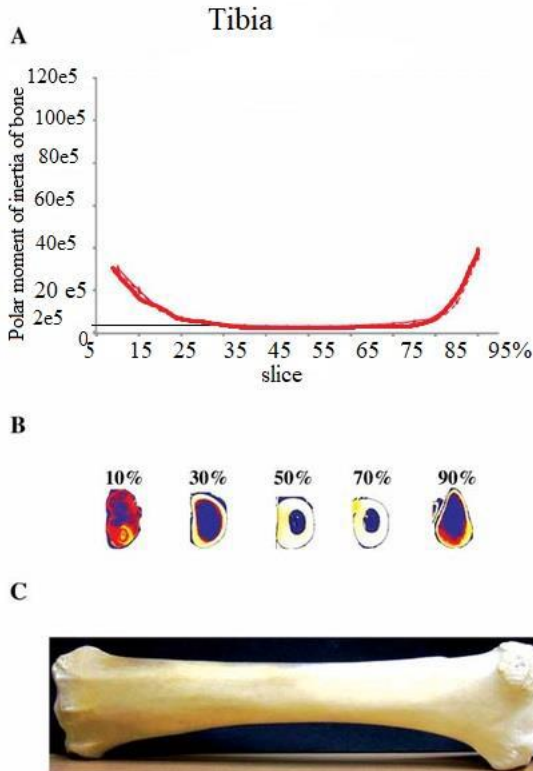


Figure.VI. variation of polar moment of inertia with area of the bone.

Results of Tibia bone subjected to static and impact load

Stress and displacement results are shown in Table II.

Table.II. Displacement and stresses in Tibia bone

SI. no	Load in N	Displacement in mm	Stress in MPa
1	5000	5.3	35.8
2	10000	10.2	71.8
3	5000 (impact)	-	363.4
4	10000 (impact)	-	536

From the results of the analysis it is found that, the bone can withstand static load and stress induced is well within the Yield point, but the bone fractured at impact loads, because of high stresses which are higher than the Yield strength of the bone. Hence fracture of the bone takes place.

V. CONCLUSIONS:

The analysis was carried out to study the behaviour of Tibia bone during static loading and during impact loading. The loads (5KN and 10 KN) were applied on the Tibia bone in static condition. The Yield strength of Tibia bone is 177 MPa. The analysis results showed that, the maximum stress induced in Tibia bone was 35.8 MPa and 71.8 MPa respectively at above said loads. The bone fractures during impact loading condition. This is due to high value of induced impact stresses. The impact stresses were calculated analytically and are found to be 363 MPa and 536 MPa respectively at aforesaid loads. Since, impact stresses were more than Yield strength of the bone, the bone would fracture under impact loading during crash.

VI. REFERENCES:

[1].M TothTascau, M Dreucean , L Rusu, Biomechanical behaviour of canine Tibia based on bending tests and numerical analysis, University of Timisora/ mechatronics Department, Timisoara, Romania.978-1-4244-4478-6/09

[2]. Bao Chun- yu, Meng Qing – hua, Three- dimensional finite element analysis of Tibia stress during jumping moment, Tianjin University of sport, china 978-0-7695-4270-6/10

[3]. S Pal , S Gupta, Fem- analysis of Tibia and computer aided design of Tibial component of TKR, school of BioSc&Engg Jadavpur university, Culcutta, India, 0-7803-7085-2/92

[4]. B v Mehta, s Rajani, Finite element analysis of human Tibia, department of mechanical engineering, Ohio University, Athens, USA,ISSN 1743-3525

[5]. SandeepkumarParashar, Jai kumarsharma, A review on application of finite element modelling in bone biomechanics, Rajasthan University, Kota, India 2213-0209

[6]. M O Kaman, N Celik, S Karakuzu, Numerical stress Analysis of the plate used to treat the Tibia bone fracture, FiratUniversity ,Elazig, Turkey 2,304-309

[7]. Rishi Kumar Srivastav, Syed Nizamulla, J Jagadesh Kumar, G Ravi Teja, Fatigue life prediction of Tibia and fibula bones using finite element method, Vidhyajothi institute of Technology Hydertabad.

[8]. Tyler A. Kress, David J. Porta, characterization of leg injuries from motor vehicle impact, Engineering Institute for Trauma & Injury Prevention The University of Tennessee, U.S.A. Paper number 443.

[9]. S. Karuppudaiyan1, J. Daniel Glad Stephen2, V. Magesh, finite element analysis of Tibia bone by reverse engineering approach, International Journal of Pure and Applied Mathematics Volume 118 No. 20 2018, 839-846.

[10]. WanchalermTarapooma and TumrongPuttapitukpornb, Stress Distribution in Human Tibia Bones using Finite Element Analysis, Department of Mechanical Engineering, Faculty of Engineering, Kasetsart University, Bangkok 10900, Thailand

[11]. Ehsan Taheri¹, Behrooz Sepehri², Reza Ganji, Mechanical Validation of Perfect Tibia 3D Model Using Computed Tomography Scan, Mashhad Branch, Islamic Azad University, Mashhad, Iran, 2012, 4, 877-880

[12]. A.N. Natal and E.A. Meroi, A review of the biomechanical properties of bone as a material, Universiti di Padova, Istituto di Scienza e TecnicadelleCostruzioni.Via F. Marzolo, 9 - 35131, Padova, Italy

[13]. Design Data Hand book volume one, two

[14]. Philip S Pastides, Stephen Ng ,Man Sun ,Alison Hulme, Stuart Evans, Paediatric fractures of the Tibia, Department of Paediatric Orthopaedic Surgery, Chelsea and Westminster NHS Trust, London, UK

Evaluation of fracture toughness of epoxy-nickel coated carbon fiber composites with Al_2O_3 nano filler

Cite as: AIP Conference Proceedings 2057, 020002 (2019); <https://doi.org/10.1063/1.5085573>

Published Online: 11 January 2019

M. D. Kiran, H. K. Govindaraju, and T. Jayaraju



View Online



Export Citation

AIP | Conference Proceedings

Get **30% off** all
print proceedings!

Enter Promotion Code **PDF30** at checkout



Evaluation of Fracture Toughness of Epoxy-Nickel Coated Carbon Fiber composites with Al₂O₃ Nano Filler.

M. D. Kiran^{1, a)} H. K. Govindaraju¹ and T. Jayaraju²

¹ BMS Institute of Technology and Management, Bengaluru 560064, India.

² NIE Institute of Technology, Mysuru, India

^{a)} kiranmdg@gmail.com

Abstract. Carbon short fibers reinforced polymer composites are commonly used composite materials in automotive and aerospace industries. In the present work, nickel coated carbon polyacrylonitrile (PAN)-based carbon fibers/epoxy manufactured by open molding method were studied. Also, nickel coated carbon fiber /epoxy composites with aluminium oxide nano filler were evaluated. Addition of small proportions of 100 nm size Al₂O₃ fillers significantly enhanced the mechanical properties of polymer matrix composites. In nickel coated carbon fiber /epoxy composites the Al₂O₃ nano fillers were added with different weight percentage varied from zero to six percent in steps of two percent. All the tests were conducted according to ASTM standards. The results revealed that Al₂O₃ nano fillers reinforced composites exhibited enhanced mechanical properties such as tensile strength, impact strength and fracture toughness.

INTRODUCTION

Composite materials are the combination of two or more constituents in macroscopic level with different properties and which are chemically insoluble with each other. Conventional materials are replaced by the different polymer matrix composites in various applications such as automotive, structural, sporting goods, household appliances, due to their advantages such as high specific strength and stiffness, ease of processing/production [1]. In polymer matrix composites various types of polymers such as epoxy, polyamide, polyvinyl, polystyrene etc. are used as matrix materials along with different reinforcements such as carbon fiber, glass fiber etc., in the form of continuous/short fiber [2]. Ductility of the polymer matrix composite reinforced with carbon fiber is higher as compared to other fiber reinforced composites [3]. Since the destitute wettability and detrimental interfacial reaction among Carbon fibers and matrix material make it very arduous to obtain the composites with great interface bonding among matrix and fiber. Coating technology on carbon fibers surface remain an effective method to overcome these problems. And Nickel coating on carbon fiber surface increases the interface bonding between matrix and oxidization resistance at high temperature [4] [5].

Addition of fillers to composites modifies the mechanical properties in different ways [6] [7]. The incorporation of various filler materials such as aluminium oxide, titanium dioxide, silicon carbide, zinc oxide, graphite, clay, fly ash etc. to the polymer composite which helps in improving the mechanical properties since the fillers have greater stiffness and modulus than polymer matrix [8]-[10]. To reduce the cost of composites low cost and easily available filler material may be used. The main reason of using filler is to improve the properties of material in addition to curtail the cost of the component. In most of the cases number of materials are used as filler materials in the polymers and in some cases filler materials are used along with different fibers [11] [12]. The mechanical properties along with fracture toughness of particulate micro and nano polymer composites are overwhelmed by particle size, particle/matrix adhesion and also particle loading on composite. This is due to the fact that strength depends on effective stress transfer between filler and matrix [13]. And, the critical size of particle, generally in nanoscale and below the composite stiffness is significantly enhanced due to the substantial effect of the size of particle, apparently caused by the much greater surface areas imparting a “nano”-effect [14]. Composites filled with aluminium oxide showed superior ultimate tensile strength since aluminium oxide consist of ceramic particles, and these particles are distributed unvaryingly throughout the composites which exhibits greater bonding strength among polymer, filler and fiber and

also due to relatively high hardness, good oxidation resistance and chemical stability of aluminium oxide [15] [16]. The epoxy composites exhibit significantly improved fracture toughness with the addition of short fiber relative to the neat resin. Short carbon fiber reinforced composites have better fracture toughness as compare to glass short fiber reinforced composites [17]-[19].

In the present investigation nickel coated carbon fibers are used as a reinforcement for epoxy matrix polymer matrix composites along with Al₂O₃ nano fillers. The composites were developed for different proportions of fillers along with the nickel coated carbon fibers. The mechanical properties of developed hybrid composites were evaluated.

Materials Used

Epoxy resin (Lapox L-12 (ARL-12)) with the density 1162 kg/m³ and epoxide equivalent 182-192 and Hardener K6 Triethylene Tetro amine (TETA) of grade K6 having density of 950 kg/m³ was used. Polymer matrix was made by mixing epoxy and hardener K6 with ratio of 10:1. Nickel coated carbon fibers were used in present work supplied by Blu Dot Asia Pte Ltd, Singapore. Fibers coated with nickel exhibits an eventual mixture of toughness, high strength, high conductivity with low density. Coating process develops a conductive fiber with greater handling properties along with admirable conductivity/shielding competence. Properties of Nickle coated carbon fibers are listed in Table 1.

TABLE 1. Properties of Nickle coated carbon fibers.

Property	Commercial, standard modulus
Filament diameter	7 μm
Tensile strength	2.5 GPa
Coating Thickness	0.25-0.3 μm
Electrical Conductivity	8.2*10 ³ S/cm
Thermal conductivity	400-500 W/mK
Max. Strain	1.2%
Density	1.82gm/cc

Aluminium oxide with the particles having spherical shape was used. Aluminium oxide is most commonly used filler material for polymer matrix composites because it is easily filled with many kinds of resins and rubbers, it can even control wear in kneading machines or moulds when checked with other fillers. Due to its relatively high hardness, good oxidation resistance and chemical stability it is most widely used filler material. Properties of Aluminium Oxide (Al₂O₃) fillers are listed in Table 2.

TABLE 2: Properties of Aluminium Oxide (Al₂O₃) fillers

Average Particle size	Purity	Crystal form	Density	SSA
<100 nm	99.9%	Alpha	3.95gm/cc	15-20m ² /gm

EXPERIMENTS

Epoxy based polymer composites reinforced with Nickel coated carbon fiber (60% Epoxy +40% Fiber) were prepared by adding filler as aluminium oxide particles (<100nm) by 2%, 4% and 6% weight fraction by using open mould process and following tests has been conducted as per ASTM standards.

Tensile test

To study the ability of the material to withstand a static load under the tension tensile has been conducted. The test samples were prepared based on ASTM D638 standard of dimensions 165 mm x 19 mm x 4 mm. A universal testing machine with capacity of maximum of 400kN is used to conduct the test under displacement control.

Impact test

Izord impact test was conducted on the specimens using Izord impact tester. The dimensions of the specimens were 63.5mm x 12.7 mm x 3.2 mm as per ASTM D256 standard, the capacity of the impact tester is up to 25 joules and release angle of the pendulum is 150°.

Mode I Fracture Test

The three-point bending test was used to evaluate the fracture toughness of materials in the form of critical-stress-intensity factor K_{IC} as per the ASTM D5045-99. The three-point bending test involves loading a notched specimen consists of pre-crack as per standard. The validity of the value of K_{IC} determined by three-point bending test depends with the formation of a sharp-crack condition at the crack tip and acceptable size of specimen to obtain linear elastic behavior. Initially, the specimen was prepared carefully by machining and afterwards, natural crack was initiated by using fresh razor blade. The specimen have been kept on supporting points on three-point bending method as shown in figure 1. and applied static load with displacement control at the rate of 10 mm/min. The load v/s displacement curve has been plotted to find out the critical load(P_Q).



FIGURE 1. Three-point Bending setup

To find out the stress intensity factor (K_{IC}) for mode-I the conditional value of K_Q has been calculated using Equation(1)

$$K_Q = \left(\frac{P_Q}{B\sqrt{W}} \right) f(x) \quad (1)$$

Where,

B = Thickness of the specimen in mm $x = a/w$ where ($0 > x > 1$).

W = Width of the specimen in mm.

a = Length of crack in mm

$$f(x) = 6x^{1/2} \frac{[1.99 - x(1-x)(2.15 - 3.93x + 2.7x^2)]}{(1+2x)(1-x)^{3/2}} \quad (2)$$

P_Q is found by load v/s displacement curve.

To make sure the condition of plain strain condition, the dimensional criteria is validated from the equation

$$B.a (w-a) > 2.5 (K_Q/\sigma_{ys}) \quad (3)$$

If Equation (3) satisfies then the K_Q value is considered as K_{IC} .

RESULTS AND DISCUSSION

Generally, nickel coated carbon fiber epoxy has lesser tensile strength than particulate filled nickel coated carbon fiber epoxy composites. Mechanical properties of unfilled and particulate filled NiC-Epoxy composites are tabulated

in Table 3. The aluminium oxide filled NiC fiber reinforced epoxy composites has a tensile strength of 29.73MPa compared to 21.178MPa of unfilled NiC fiber epoxy composites. The addition of aluminium oxide nano filler enhanced the tensile strength N-C epoxy composites when compared to unfilled N-C epoxy composite which due to good adhesion among matrix with filler/ fiber. However, the interface between the particle size dispersal and the aluminium oxide loading is extremely important. Impact test results of particulate filled and unfilled N-C Epoxy composites are shown in Table 3. Addition of alumina nano fillers to N-C Epoxy composites shows remarkable impact strength of the N-C Epoxy composite. The impact strength has increased by around 200% with 6 wt% aluminium oxide in N-C Epoxy composite.

TABLE 3. Mechanical properties of unfilled and particulate filled NiC-Epoxy composites

Composites	Tensile Strength, (N/mm ²)	Impact Strength (kJ/m ²)	Fracture Toughness K _{IC} in MPa √m
Epoxy+N-C	21.178	90.9	88.45
2Al ₂ O ₃ +Epoxy+N-C	27.393	136.36	106.72
4Al ₂ O ₃ +Epoxy+N-C	29.327	136.36	116.92
6Al ₂ O ₃ +Epoxy+N-C	29.73	181.81	151.39

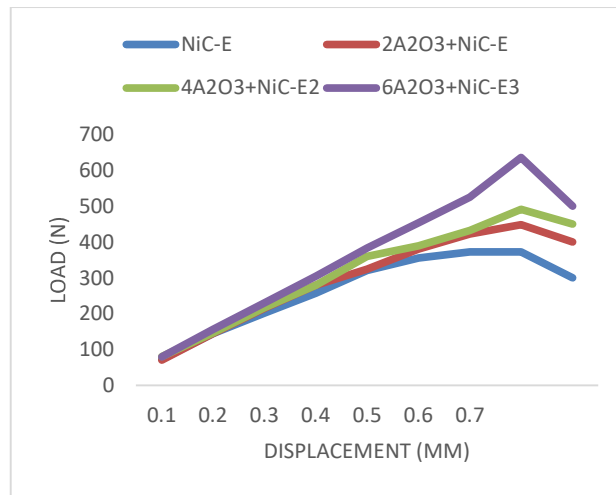


FIGURE 2. Load-displacement curves

In the present investigation, the crack propagation of filled and unfilled N-C Epoxy composites is also studied. For the unfilled N-C Epoxy composite, the value of K_{IC} is smaller than that of aluminium oxide filled N-C Epoxy composites. Fracture toughness increased with addition of aluminium oxide to N-C Epoxy composites. The exemplary load v/s deflection graph for particulate filled and unfilled N-C Epoxy composite as shown in Figure 2. The Load v/s displacement graph of all samples shows linear curve initially and it becomes increasingly non-linear and load drops which shows fast steady growth of crack because crack primarily propagates in stable manner and finally unstable behavior was observed at maximum load.

CONCLUSION

Study on polymer matrix composites with fillers is gaining better interest now a days because of its exceptional properties. Different experiments were conducted on nickel coated carbon fiber /epoxy composites with aluminium oxide filler. The conclusions drawn from the experimental investigation of mechanical strength performance on polymer matrix composite with filler revealed that the addition of aluminium oxide filler significantly contributed to the improvement in fracture, impact and tensile strengths when compared to nickel coated carbon fiber /epoxy composites which can be attributed to the high stiffness and modulus of fillers than matrix.

REFERENCES

1. Vinay H B, H K Govindaraju, Prashanth Banakar —Processing and Characterization of Glass Fiber and Carbon Fiber Reinforced Vinyl Ester Based Composites| IJRET: International Journal of Research in Engineering and Technology eISSN: 2319-1163 | PISSN: 2321-7308.
2. A. Yasmin and I. M. Daniel, “Mechanical and Thermal Properties of Graphite Platelet/ Epoxy Composites,” *Poly-mer*, Vol. 45, No. 24, 2004, pp. 8211-8219.
3. T D Jagannatha and G Harish,” Mechanical properties of Carbon /Glass Fiber Reinforced Epoxy Hybrid Polymer Composites”, International Journal of Mechanical Engineering and Robotics Research, Vol. 4, No. 2, April 2015.
4. Zhongsheng Hua, Yihan Liu, Guangchun Yao, Lei Wang, Jia Ma, and Lisi Liang, “Preparation and Characterization of Nickel Coated Carbon Fibers by Electroplating”, *Journal of Materials Engineering and Performance*, (2012) 21:324–330.
5. Nithin Kumar, H. C. Chittappa, Albert Allen D. Mello, and M. D. Kiran “Fatigue Behaviour of Carbon Fiber Reinforced Aluminum Metal Matrix Composites” *Advanced Science, Engineering and Medicine*. 10, 1–4, 2018.
6. Radford, K.C. (1971) The Mechanical Properties of an Epoxy Resin with a Second Phase Dispersion. *Journal of Materials Science*, 6, 1286-1291.
7. Fu, S.Y and Lauke, B. (1998) Characterization of Tensile Behavior of Hybrid Short Glass Fiber Calcite Particle ABS Composites. *Composite Part A: Applied Science*, 29, 575-583.
8. Eirich, F.R. (1984) Some Mechanical and Molecular Aspects of the Performance of Composites. *Journal of Applied Polymer Science*, 39, 93-102.
9. Fu, S.Y. and Lauke, B. (1997) Analysis of Mechanical Properties of Injection Molded Short Glass Fiber (SGF)/Calcite/ABS Composites. *Journal of Materials Science and Technology*, 13, 389-396.
10. Spanoudakis, J. and Young, R.J. (1984) Crack Propagation in a Glass Particle Filled Epoxy-Resin. Effect of Particle-Volume Frtion and Size. *Journal of Materials Science*, 19, 473-486.
11. Katz H.S., Mileski J.V. Handbook of Fillers for Plastics, (1987), November 30, A Von Nostrand Reihold book.
12. Wasim Akram, Sachin Kumar Chaturvedi, Syed Mazhar Ali “Comparative Study of Mechanical Properties of E-Glass/Epoxy Composite Materials with Al₂O₃, CaCo₃, SiO₂ AND PBO Fillers” International Journal of Engineering Research & Technology (IJERT) Vol. 2 Issue 7, July - 2013.
13. Hsueh, C.H. (1989) Effects of Aspect Ratios of Ellipsoidal Inclusions on Elastic Stress Transfer of Ceramic Composites. *Journal of American Ceramic Society*, 72, 344-347.
14. Shao-Yun Fu, Xi-Qiao Feng, Bernd Lauke, Yiu-Wing Mai “Effects of particle size, particle/matrix interface adhesion nd particle loading on mechanical properties of particulate polymer composites” www.elsevier.com, Composites: Part B 39 (2008) 933–961.
15. Biswas, S. and Satapathy, A. “A study on tribological behavior of alumina filled glass-epoxy composites using Taguchi experimental design”, *Tribol. Trans.*, Vol. 53, 2010.
16. K. Devendra, T. Rangaswamy ‘Strength Characterization of E-glass Fiber Reinforced Epoxy Composites with Filler Materials” *Journal of Minerals and Materials characterization and Engineering*, 2013, 1, 353-357 Published Online November 2013.
17. G. Agarwal, A. Patnaik, R. K. Sharma, “Mechanical and Thermo–Mechanical Properties of Bi-Directional and Short Carbon Fiber Reinforced Epoxy Composites” *Journal of Engineering Science and Technology*. Vol. 9, No. 5 (2014) 590 – 604.
18. Wei Dong, Heng-Chang Liu, Soo-Jin Park, Fan-Long Jin, “Fracture toughness improvement of epoxy resins with short carbon fibers” *Journal of Industrial and Engineering Chemistry* 20 (2014) 1220–1222.
19. J.M.L. Reis, A.J.M. Ferreira, “Assessment of fracture properties of epoxy polymer concrete reinforced with short carbon and glass fibers” *Construction and Building Materials* 18 (2004) 523–528.

Development of Wear Resistant Al-Si-Ce Metal Matrix Composites Using Gr as Reinforcement

H K Govindaraju¹, Lokesh H S², Kiran M D³

^{1,3}*Department of Mechanical Engineering, BMS Institute of Technology and Management, Bengaluru, Karnataka, India*

²*Department of Mechanical Engineering, Mahnad College of Engineering, Hassan, Karnataka, India*

Abstract- In the present investigation wear resistant of Aluminium Matrix Composites (AMCs) were developed by using Graphite as reinforcement and Cerium as a grain refiner. Al-Si-Ce alloys and Al-Si-Ce-Gr AMCs were casted using stir casting metallurgy techniques and the castings were T6 heat treated. Cerium was added from 0.15 wt% to 0.3 wt% and Graphite of 4 wt% was added as reinforcement in the manufacture of AMCs. Wear tests were conducted as per ASTM G-99 test standards. The experiments were conducted with two different speeds and loads of 100 rpm - 500 rpm and 10 N – 50 N. From the wear testing analysis, it was found that at higher speed and lower load wear loss and coefficient of friction was minimum in all the investigating alloys and composites. Maximum wear loss was observed at lower speed (100 rpm) with highest (50 N) load.

Keywords – Cerium, Aluminium Alloys, Metal Matrix Composites, Wear Behavior.

I. INTRODUCTION

Composite materials can be defined in many ways. Some improved or desired properties can be obtained in Composite materials. The Matrix is a dispersed phase(s), dispensed in continuous medium and should maintain its uniqueness even after processing, during service or reprocessing [1]. They have heterogeneous composition. Metal Matrix Composites of Aluminum have extensive use in automotive, aerospace and defense industries because of their light weight, high strength to wear ratio, stiffness, and good wear resistance and enhanced electrical and thermal properties [2-3]

Graphite particles dispersed in Aluminum alloys are known as potential materials for tribological applications [4-7]. Aluminum alloy matrix yields at low stresses and deforms. This improves the deformation and fragmentation of the surface and sub-surface graphite particles. It provides a continuous film of graphite, which prevents metal to metal contact and seizure.

Rohit Sharma et al [8] analyzed dry sliding behavior of Aluminum alloy LM6 reinforced with dual hybrid titanium dioxide and graphite particles. With increase in reinforcement percentage, wear rate decreased linearly and with above 15% reinforcement levels, wear rate started increasing. Wear rate increased at higher loads with decrease in COF. Also, presence of reinforcement improved the micro hardness. Ravindran et al [9] used technique to study the wear behavior of hybrid aluminum composites. The loss of material and COF were influenced by the applied normal load and sliding distance. Wear resistance of 5% SiC + 5% graphite reinforced hybrid composite was more compared to 5% SiC reinforced composites. Soft graphite with hard carbides increased wear resistance. Anru et al [10] published that the strength of the alloy increases by adding Ce at room and high temperature. It also helps to refine Eutectic structure, harden by dispersion, decrease ductility, and influence the rate and precipitation of solid phases. The solubility of Ce in Aluminum increases with increasing temperature. Secondary intermetallic phases forms during solidification and heat treatment for decrease in solubility from high concentrations at high temperatures to relatively low solubility.

Anasyida Abu Seman et al [11] studied the effect of cerium addition on the Microstructure and Microhardness of Al-12.5Si-4Mg alloy. With the addition of 0.5 to 3.0 Wt% of cerium dispersed fine cells having a mixture of α -Al, Eutectic Si and intermetallic Al₄Ce phase was formed in Al-matrix. With increase in Ce content Microhardness of as cast alloy increases due to precipitated phase. Diffusion of Si and Ce induced by ageing at 2000C lead to clustering of Si and Precipitation of fine Al₄Ce phase resulted in increase of the microhardness of as cast alloy. Vivek Babu et al [12] evaluated the hardness of LM6 (aluminum)/Gr (Graphite) particulate metal matrix composite. With the addition of Gr particle up to a particular limit, the hardness value of LM6/Gr composite increased and then suddenly decreased. For around 4% Gr composition Maximum value of hardness was found. Wear loss analysis of 18% silicon-based Aluminum alloy was studied by Anirudh Biswas et al [13]. wear rate reached maximum value at 15N and decreased as applied load increased to 20N. At higher loads work-hardening of matrix due to plastic deformation helped in reduction of wear. Temperature increases appreciably at higher loads, lowers the strength of materials in contact and results in increase in contact area and COF. A.S.Anasyida et al [14] studied the wear behavior of as-cast Al-4Si-4Mg alloys with cerium addition. Cerium addition to Al-4Si-4Mg resulted in

intermetallic phase formation of Al-Ce and Al-Si-Ce. Enhanced wear resistance and lowered friction coefficient of as-cast alloy was obtained with increase of cerium up to 5Wt%. Amro M. Al-Qutub et al [15] studied Al₂O₃/6061 Aluminum particulate composite for dry wear behavior. Higher concentration of Al₂O₃ and higher load lead to higher wear rates. Friction coefficient had negligible effect due to Al₂O₃. S. Srivastava et al [16] used Al-Sn-based alloy with different amount of Graphite for tribological properties at different normal loads and sliding speeds. Mechanical properties and tribological properties due to presence of graphite in the matrix Improved. Increase of Graphite content increased the ductility of composite materials. With increase in Graphite content the COF decreases. Wang and Rack [17], recorded that higher wear resistance is exhibited by overaged composites compared to underaged. Straffellini et al [18] also concluded that higher wear resistance is exhibited in over aged composites than under aged one in extruded and also in forged condition.

From the above literature survey, it was found that still scope exists to work on Aluminum Metal matrix composites. In this investigation Graphite is reinforced in Al-Si-Ce alloys and its wear behaviour has been evaluated.

II. MATERIALS AND METHODS

Based on the necessity mechanical properties of the Metal Matrix composites and alloy, the method of casting process varies. The properties of the casting primarily depend upon alloying elements, melting, casting operations, and heat treatment. The properties attained from one particular combination of these factors may not be same to those obtained with the same alloy in a different metal casting facility.

Molten aluminum has many characteristics that can be controlled to maximize casting properties. It is susceptible to picking up hydrogen gas and oxides in the molten state. It is very sensitive to minor trace elements. Tight control of melt and specialized molten metal processing techniques produce improved mechanical properties.

The composition of the alloy used in casting is as shown in the Table 1. In the process of casting, permanent dies of size 300 mm x 200 mm x 18 mm were used. The alloy which is used as a matrix consisted of pure aluminum, copper, nickel, magnesium etc.

Table 1 Chemical composition of investigating alloys (wt%)

Material	Cu	Mg	Si	Fe	Mn	Ni	Zn	Pb	Sn	Ti	Al	Ce	Gr
Alloy – 1	0.1	0.1	10	0.6	0.5	0.1	0.1	0.1	0.05	0.2	Rem	0.15	-
AMC – 1	0.1	0.1	10	0.6	0.5	0.1	0.1	0.1	0.05	0.2	Rem	0.15	4
Alloy – 2	0.1	0.1	10	0.6	0.5	0.1	0.1	0.1	0.05	0.2	Rem	0.3	-
AMC – 2	0.1	0.1	10	0.6	0.5	0.1	0.1	0.1	0.05	0.2	Rem	0.3	4

Melting was carried in an induction furnace in a graphite crucible up to a temperature of 7200 C. After degassing, master alloy of cerium was added for grain refinement. The melt, stirred for 30 sec with a stirring speed of 140-160 rpm after adding the grain refiner and graphite, held for 5 min and poured to dies. The dies were heated up to 2500C before pouring the molten metal, to avoid the sudden cooling of the melt.

III. HEAT TREATMENT

Aluminum-Silicon alloys having other elements like Mg, Si etc., offer the highest combination of high temperature resistant properties in cast/ wrought form. Heat treatment is a process to change the mode of occurrence of the soluble alloying elements, especially Copper, Magnesium, Silicon and Zinc, which can combine with one another to form inter metallic compounds. Different heat treatment processes include quenching, solution heat treatment, precipitation hardening or aging, cold working and tempering.

Solution heat treatment alludes to a thermal hardening process. Material is immersed at fairly high temperature for a number of hours. During which the alloying elements are put into solid solution. Usually the temperature is rapidly lowered (quenched) which leaves an unstable structure. During aging at room temperature the internal structure stabilizes itself. This is also called T6 Heat treatment is as shown in Fig. 1

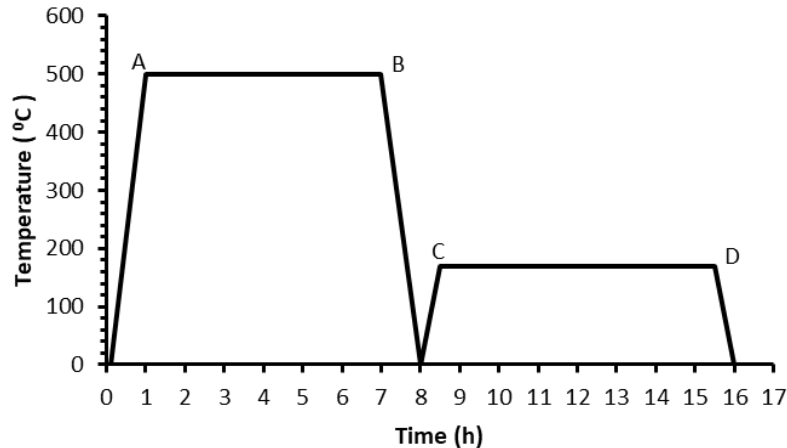


Fig. 1. Graphical representation of Heat treatment
(0AB - Solution heat treating, B8 - Quenching, CD - Heat treatment Aging)

Generally, the cracks are developed in components due to stresses produced during the structural transformation with its accompanying increase in volume. Many heat treatment processes will soften the material. The scale formation is another problem of heat-treated materials. The fracture toughness of the heat-treated materials depends primarily on the method of the heat treatment and the temperature.

IV. SLIDING WEAR TEST

Wear tests were carried using computerized Pin on Disc Tester of Ducom make. Tests were carried at ambient temperature. In the present dry sliding wear investigation of heat treated (T6) Alloy-1, Alloy-2, AMC-1 and AMC-2 was conducted according to ASTM G-99 standard testing procedure. Experiment was conducted using a computerized Pin-on-Disc Tester to find mass loss, Volume loss, frictional force and co-efficient. The machine had wear disc of specification EN31 with wear track diameter 10- 120 mm. The Cylindrical specimens of 8 mm diameter and height 25 mm were used. Test was carried out at track diameter of 100mm for a sliding distance of 3.142 km. The specimens were weighted before and after the experiment and the corresponding weight loss, volume loss, wear loss and coefficient of friction were calculated. During conduction of each test both disc and specimen were cleaned thoroughly with silver nitrate liquid and dried in order to avoid the contamination.

An instrument used was DUCOM make. Test rig was Wear and Tear Monitor, TR-20L, with Electronics controller, Winducom 2010 software and computer of Pentium 4, 512 MB RAM, 2GB. Wear test was conducted out on Pin-on-Disc tester to evaluate the Weight loss, Volume loss, Specific wear loss, COF properties.

The tests were conducted for the following material system. The following material system is used in the sliding wear test analysis (Table 2).

Table 2 List of investigating alloys and AMCs

Specimen	Material Composition
Alloy - 1/T6*	Al-Si-1.5%Ce
Alloy - 2/T6*	Al-Si-3.0 %Ce
AMC - 1/T6*	Al-Si-1.5%Ce-Gr
AMC - 2/T6*	Al-Si-3.0 %Ce-Gr

*Heat treatment

Four sets of experiment were conducted for a combination of different load and speed i.e. a minimum speed of 100 rpm and a maximum speed of 500 rpm along with a minimum load of 10 N and a maximum load of 50 N. The specimens were weighted before and after the experiment and the corresponding weight loss, volume loss, wear loss and coefficient of friction were calculated. During conduction of each test both disc and specimen were cleaned thoroughly with silver nitrate liquid and dried in order to avoid the contamination.

V. EFFECT OF LOAD AND SPEED ON WEIGHT LOSS

All the specimens were tested with four different combinations of load and speed as shown in Fig. 2. From the analysis it was found that at a speed of 100 rpm with an applied load of 10 N, wear loss progressively decreased with the increase of percentage of cerium in both the alloys and composites.

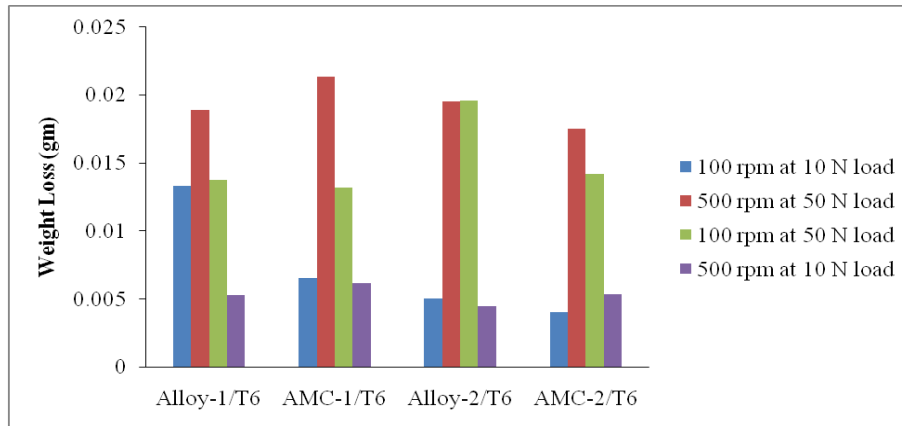


Fig. 2. Wear weight loss (gm) in alloys and composites at different load (N) and speed (rpm)

At an applied load of 50 N with a speed of 500 rpm the wear loss was increased in all the alloys and composites. The weight loss was increased in AMC-1/T6 when compared with Alloy-1/T6 and then it reduced progressively with the increase in cerium percentage. At an applied load of 50 N with a speed of 100 rpm the highest wear loss was observed in Alloy-2/T6 when compared with all other alloys and composites. At an applied load of 10 N with a speed of 500 rpm wear loss was uniform in all the alloys and composites and also minimum wear loss was observed in all the composites and alloys when compared with other speed and load conditions.

VI. EFFECT OF LOAD AND SPEED ON HEIGHT LOSS

From the analysis (Fig. 3) it was found that at an applied load of 10 N with 100 rpm height loss was progressively reduced with the addition of graphite and increase in percentage of cerium. At an applied load of 50 N with 500 rpm height wear loss was observed in Alloy-1/T6 when compared with other alloys and composites and also at different loads and speeds height loss was decreased.

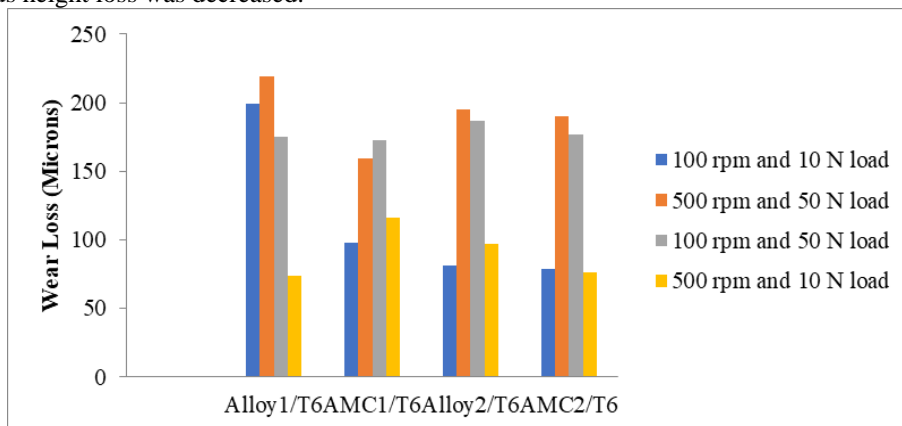


Fig. 3. Heightloss (gm) in different investigating alloys and composites at different load (N) and speed (rpm)

At high load (10 N) and low speed (100 rpm) the height loss is more in all the alloys and composites. Whereas at high speed (500 rpm) and low load height loss is minimum when compared with all other testing conditions

VII. EFFECT OF LOAD AND SPEED ON VOLUMATRIC LOSS

From Fig. 4, it is observed that at low load (10 N) with low speed (100 rpm) volumetric loss was very high in Alloy-1/T6 and progressively reduced in other alloys and composites. At high load and high speed and also at low speed and high load volumetric loss was high are all the alloys and composites when compared with other loads and speeds. Whereas at high speed (500 rpm) and low load (10N) volumetric loss was very less in all the alloys and composites

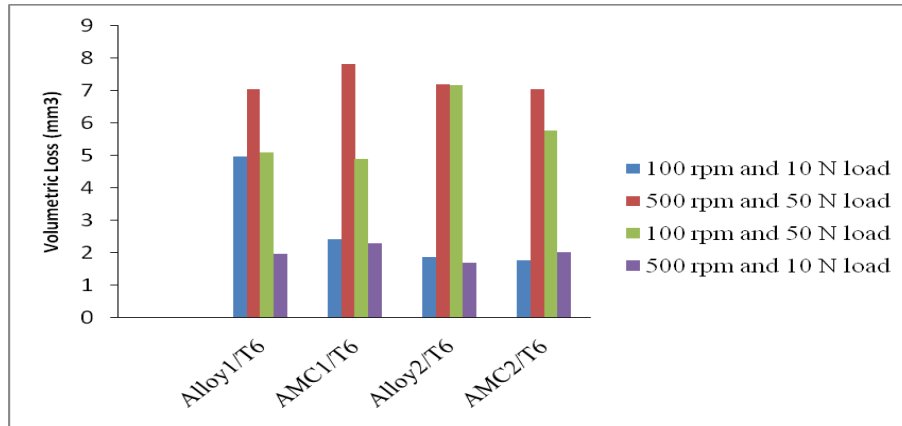


Fig. 4. Volumetric loss (gm) in different investigating alloys and composites at different load (N) and speed (rpm)

VIII. EFFECT OF LOAD AND SPEED ON COEFFICIENT OF FRICTION

Frictional coefficient was calculated from the recorded frictional force and the applied load. From the Fig. 5 it was found that the coefficient of friction in Alloy-1/T6 and Alloy-2/T6 is lesser than AMC-1/T6 and AMC-2/T6 at low load (10 N) and speed (100 rpm), the presence of graphite particles in the matrix increased the COF.

The coefficient of friction is lower at 0.15 wt% Ce mixed alloys and composites when compared with 0.3 wt% cerium mixed alloys and composites at high speed and low load. At low speed and high load AMC-1/T6 and AMC-2/T6 coefficient of friction is lesser than the investigating alloys. At high speed and low load, the coefficient is progressively increased in Alloy-1/T6, Alloy-2/T6, AMC-1/T6 and decreased in AMC-2/T6.

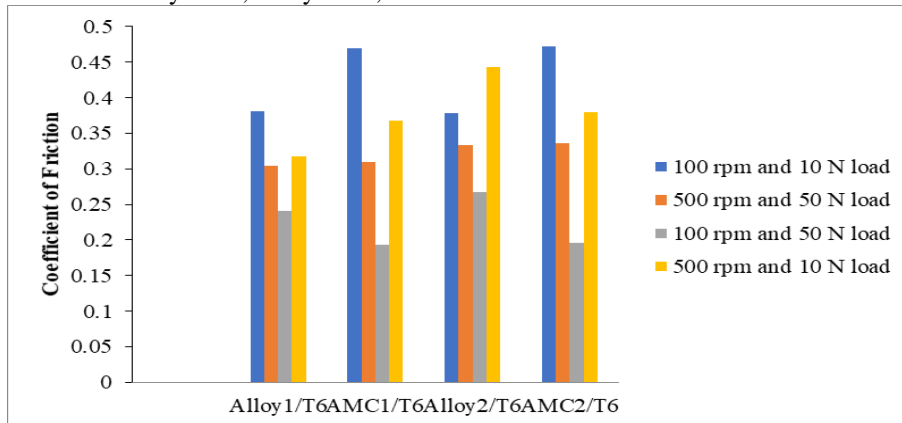


Fig. 5. Coefficient of friction in wear in alloys and composites at different load (N) and speed (rpm)

From the analysis it was found that the coefficient of friction was decreased at higher speed and lower load in alloys and composites with 0.3 wt% Ce. The Gr particulates were found to act as bearing material between specimens and rotating disc. Wear worn surface consists of wear debris includes coarse metallic particles of the surfaces and Gr particles, which act as abrasive particles between the specimen and disc. The oxide film formed on the wearing surface prevents the metal to metal contact. The hard-brittle oxide formed on aluminum provides protection against wear. The oxide layer formed is harder than the base material which reduces the friction and wear of the specimen.

According to Rohatgi et al. [19] at large volume fractions of graphite the composites showed very low wear rates with independent of sliding velocity. This is due to graphite film stability. The existence of graphite in the matrix enhances its oil spreadability over the contact surface, thus decreasing the tendency to score or seize. Graphite has carbon atoms arranged in a layer like structure. It shows a very low COF while sliding on another clean surface [20]. Ramesh et al [21] reported that the coefficient of friction was decreased with the increase in percentage of reinforcement in Al6061-Ni-P-Si3N4 hybrid composites [49], due to the improvement in anti-frictional behaviour of reinforced particles which behaves as a load bearing element [22, 23]. Liu et al. [24] studied friction and wear behaviour of Aluminum – Silicon alloy matrix composites with graphite particles. The coefficient of friction and wear were considerably lower in MMHCs, as compared to MMCs due to the formation graphite film formation between the rubbing surfaces.

IX. CONCLUSION

The experiments were conducted for all the investigating alloys and composites and the following conclusions were drawn on the wear behaviour. Wear volume was progressively reduced and coefficient of friction was increased at low speed and low load in all the investigating alloys and composites. At high load and high-speed highest wear loss was observed when compared with all other loading conditions. At low speed and high load higher wear loss and higher coefficient was observed in alloys when compared with composites. At high speed to low load wear loss was minimum in all the investigating alloys and composites. Also, high coefficient of friction was observed in alloys when compared with composites

X. REFERENCES

- [1] M. Balasubramanian, Composite Materials and Processing, CRC Press, Taylor & Francis Group, 2014.
- [2] M.K Surappa, P.K Rohatgi, Preparation and properties of cast aluminum-ceramic particle composites, Journal of materials science, 16(1981), P983-993.
- [3] J.W.Kaczmar, K.Pietrzak, W. Wlosinski, The production and application of metal matrix composite materials, Journal of material processing technology, 106(2000), p106:58-67.
- [4] M.G Vassilaros, D.A.Davis, G.L.Stecker, J.P.Gudas, in "Proceedings of the Tri- Service Conference on Corrosion" US Air Force Academy, Colorado, November 1980, Vol II
- [5] A.I.Onen, B.T.Nwufo, E.E.Ebenso, R.M.Hlophe. Int.J.Electrochem.Sci., 5 (2010) 1563.
- [6] N.A.P.Rao, S.Biswas, P.K.Rohatgi, A. Santhanam, K.Narayanawamy, Tribol, Int., 1(1980)
- [7] M.Saxena, B.K.Prasad, T.K.Dan, J.Mater.Sci., 27 (1992) 4805-4812
- [8] Rohit Sharma, Pushpinder Sharma, Gagandeep Singh, Dry sliding behavior of aluminium alloy reinforced with hybrid ceramic particles, International Journal of Multidisciplinary Research and Development, 2015, volume: 2, Issue:10, p485-491
- [9] Ravindran P, manisekar K, narayanamy P, selvakumar N, Narayanamy R, Application of factorial techniques to study the wear of Al hybrid composites with graphite addition. Mater Des 2012; 39:42-54.
- [10] WUAnru, XIA Changqing and WANG Shaowu, (2006) Rare Metals, 25, 371-376.
- [11] WUAnru, XIA Changqing and WANG Shaowu, (2006) Rare Metals, 25, 371-376.
- [12] Vivekbabu, Rajamohan, P.A Abdul Samad, Hardness evaluation of LM6/Gr PMMC prepared by stir casting method, International Journal of emerging Technology and Advanced Engineering (2013), Vol:3, Issue7
- [13] AnirudhBiswas, NehaRastogi, AyushSoni and Rajendrasingh, Wear loss analysis of 18% silicon based Aluminum alloy, International Journal of Emerging Technology and Advanced Engineering (2014), Vol:4, special Issue 1,p196-202.
- [14] A.S.Anasyida, A.R.Daud and M.J.Ghazali, Dry sliding wear behavior of Al-4Si-4Mg alloys by addition of cerium, International Journal of Mechanical and Materials Engineering Vol.4, No.2, 2009, p127-130.
- [15] Amro M. Al-Qutub, Ibrahim M. Allam M. A. Abdul Samad, Wear and friction of Al-Al₂O₃ composites at various sliding speeds, Journal of Material Science, 43, (2008), 5797-5803
- [16] S.Srivastava, S. Mohan, YogeshSrivastava and Aman J. Shukla, Study of the wear and friction behavior of immiscible as-cast-Al-Sn/Graphite composite, International Journal of Modern Engineering Research (IJMER), Vol.2, Issue.2, (2012), 025-042.
- [17] Wang A, Rack HJ. Transition wear behavior of SiC-particulate and SiC-whisker-reinforce 7091 Al metal matrix composites, Mater SciEng 1991;A147:211-24
- [18] Straffelini G, Bonollo F, Molinari A, tiziani A, Influence of matrix hardness on the dry sliding behavior of 20 vol% Al₂O₃ particulate reinforced 6061 Al metal matrix composite. Wear 1997; 211: 192-7
- [19] P.K. Rohatgi, P.J. Blau, C.S. Yust, (1990), "Friction and wear in metal-matrix graphite particle composites, in: P.K. Rohatgi, P.J. Blau, C.S. Yust
- [20] S.K. Biswas, B.N. PramilaBai, (1981), "Dry wear of Al-graphite particlecomposites", Wear, Vol.68, pp. 347-359.
- [21] C. S. Ramesh, Keshavamurthy, B. H. Channabasappa, S. Pramod, (2010),"Friction and Wear behavior of Ni-P coated Si₃N₄ reinforced Al6061, composites", Elsevier, TribologicalInternational, Vol. 43, pp. 623-634.
- [22] C. S. Ramesh, R. Keshavamurthy, B. H. Channabasappa, A. Ahmed (2009),"Microstructure and mechanical properties of Ni-P coated Si₃N₄ reinforced Al6061 composites", Master science Engg. A, Vol. 502, pp. 99-106.
- [23] J. F. Archard, (1953), "Contact and rubbing of flat surfaces", J AppliedPhysics, Vol. 24, pp. 981.
- [24] Y. Liu, P.K. Rohatgi, S. Ray, (1993), Tribological characteristics of aluminum graphite composite, Metallurgical and Materials Transactions A, Vol. 24, pp. 151-159.



Automatic Bumper with Smart Braking System

Anuroop Showri. S¹, Sachin Kumar Singh², Shreyas P. S³, Bala Muralidhar Reddy⁴, K. Chandra Sekhara Reddy⁵
Student^{1, 2, 3, 4}, Assistant Professor⁵

Department of Mechanical Engineering
BMS Institute of Technology and Management, Karnataka, India

Abstract:

The pneumatic bumper is utilized to give protection to the man and vehicle. Presently multi day's vehicle mishaps are the serious issue. This savvy bumper is a creative undertaking to avoid mishaps or lessen the effect of frontal mishap occurs in the limited roadways. The motivation behind this framework depends on keen electrically control programmed bumper and brake actuation framework. Our idea is to plan and produce a control framework dependent on keen electrically controlled programmed guard and smart braking. This framework comprises of Ultrasonic sensor, Control Unit, Double acting Pneumatic bumper and braking unit. In the event that there is any snag nearer to the vehicle, inside the predefined go, The Ultra-sonic sensor detects the deterrent and the control signal is given to the control unit and pneumatic guard at the same time, because of which the bumper opens/reaches out to shield the vehicle from harm and at the same time brakes are applied once the guard stretches out.

Keywords: Pneumatic Cylinder, Ultrasonic sensor, Air compressor, Braking unit.

I. INTRODUCTION

India is a developing country. The population is quite high and is still increasing at a very large rate. The use of automobiles due to this has also increased which can be a liberal cause for road accidents. these accidents cannot be unseen yet they can be reduced by taking few measures and introducing new technologies into the automobiles for both vehicle and human safety. Our Aim is to improve the safety. Usually when a vehicle is manually operated, the chances of surviving an accident is purely based on driver's instincts. the driver may not ready to give total consideration when driving during the evening. So there are numerous odds of mishaps. Dire use of brakes can bring about veering of the vehicles due to sliding of tire. In addition, because of abrupt utilization of brakes there are odds of different vehicles dashing from back. Consequently, there is no arrangement to limit the harm of vehicles. In this manner, the current structured framework just reasonably lessens the harm of vehicle as well as travelers. To improvise this condition and to give the vehicle safety other than drivers instincts we introduce "Additional automatic bumper with smart braking system". This System helps to reduce the damage by extension the bumper and applying the brakes simultaneously reducing the efforts of driver in any worst case scenario and provides additional safety

at-risk situation of frontal impact to prepare the vehicle for a subsequent crash and retract when that risk subsides. The Extendable and Retractable impact energy will provide additional safety to the occupant without affecting the styling of the vehicle structure.

Aditya Gandhi, Amey Deshmukh, Rahul Aniyankunju^[2]
This paper "Automated bumper for damage reduction" distributed in 2016 is a hypothesis dependent on safety in the present vehicles for both the vehicle and people inside the vehicle. The author says that even after all the added safety measures today the damage or fatality of the damage reduction is reduced by 60%. 60% is not 100%. So they endeavor to plan a framework for crisis brake that can be utilized as a progressive game plan for the current hand brake mechanism. The presumption made in their idea is that the group of effect would be an impeccably inflexible and stationary body. The guard should assimilate however much effect as could reasonably be expected with the utilization of different vitality absorption materials

J.T Wang ^[3]

In this paper "An extendable and retractable bumper", A E/R bumper is presented which is intended to automatically extend in situations in which there is a high risk of frontal impact to prepare the vehicle for crash and retract when the risk subsides. A demo vehicle and two probing vehicles were built with the E/R bumper. Analytical and nonlinear FEM models were used to aid in the design of these vehicles, and to predict their crash performance in full, offset and oblique impact tests. The tests, along with nonlinear FEM analysis, showed that the additional crush space realized by extending the bumper could reduce the severity of the crash pulse and the amount of structural intrusion to the vehicle compartment. Thus improving the safety of the vehicle.

Takahiro Wada, Shun'ichi Doi, and Shoji Hiraoka ^[4]

The author explains that it is important to judge necessity of deceleration assistance quickly and initiate the assistance naturally. On the other hand, author has derived a mathematical model of driver's perceptual risk of proximity in

II. LITERATURE SURVEY

Pravin E. Fulpagar, Dr.S.P.Shekhawat^[1]

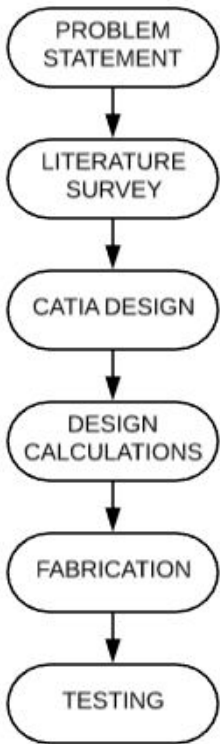
In this paper, the author studies the energy absorption capabilities of an energy absorber attached to a vehicle. in this paper "Crashworthiness Evaluation of an Impact Energy Absorber in a Car Bumper for Frontal Crash Event - A FEA Approach", the author illustrates that the crash test gives us a measure of how well a passenger vehicle would protect its occupants in the event of a serious real world frontal crash. A conceptual crash preparation feature, called the Impact energy absorber is presented to reduced damage to occupant in situations in which there is a high risk of frontal impact to prepare the vehicle for crash. Also, the Extendable and Retractable bumper may provide additional crush space in an

car following situation and successfully derived driver deceleration model to describe deceleration patterns and brake initiation timing of expert driver. In this research, an automatic braking system for collision avoidance was proposed based on the formulated brake profile model and brake initiation model of expert driver to realize smooth, secure brake assistance naturally. It will be shown that the proposed control method can generate smooth profile for various conditions. In addition, experimental results using a driving simulator were showed to prove the validity of the proposed system based on subjective evaluation

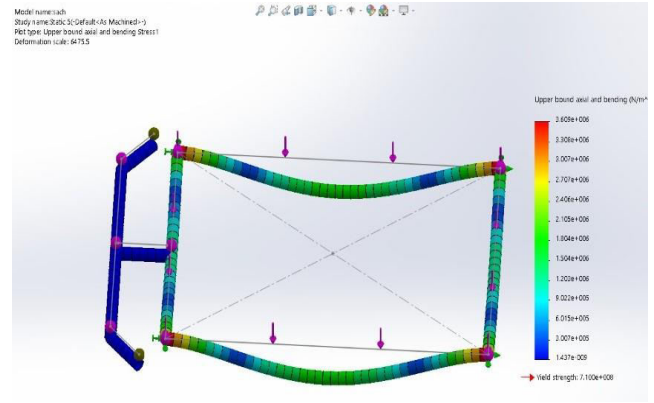
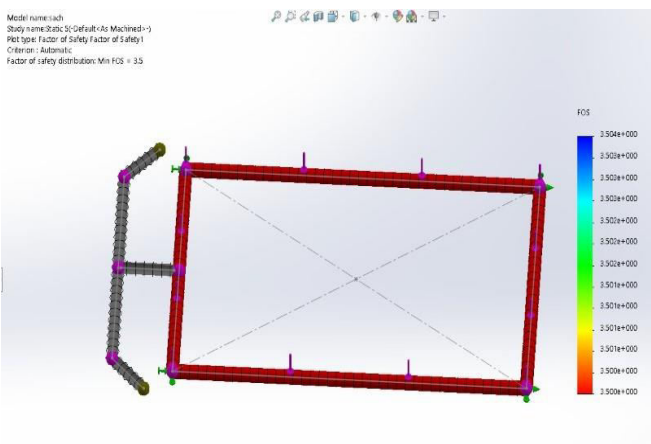
III. OBJECTIVES

- To Decrease the rate of accidents
- To Improve the pre-crash safety
- To Provide additional safety for vehicles and passengers
- To have a capacity to quantify the nearness of the risk and to act appropriately
- To Improve the reaction time of the braking frame work

IV. METHODOLOGY



V. ANALYSIS



VI. COMPONENTS

This project is interdisciplinary. It is a combination of mechanical and electronics, usually known as mechatronics. Mechatronics, which is also called mechatronic engineering, is a multidisciplinary branch of engineering that focuses on the engineering of both electrical and mechanical systems.

ULTRASONIC SENSOR

Ultrasonic sensors work on the principle of reflected sound waves and are used to measure distance. One sensor can detect others operating nearby. Sound waves are emitted by the ultrasonic sensor and they're reflected back if there is an object in front of it. The sensor detects these waves and measures the time it takes between transmitting and receiving those sound waves. Distance is then estimated by the time interval between sensor and object

HC-SR04 Sensor Features:

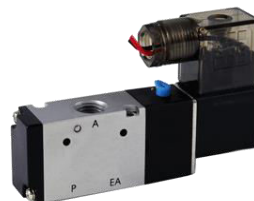
- Operating voltage: +5V
- Theoretical Measuring Distance: 2cm to 450cm
- Practical Measuring Distance: 2cm to 80cm
- Accuracy: 3mm
- Measuring angle covered: <15°
- Operating Current: <15mA
- Operating Frequency: 40Hz

DOUBLE ACTING CYLINDER

A double-acting cylinder is a cylinder in which the working fluid acts alternately on both sides of the piston. Many hydraulic and pneumatic cylinders use them where it is needed to produce a force in both directions. A double-acting hydraulic cylinder has a port at each end, supplied with hydraulic fluid for both the retraction and extension of the piston. A double-acting cylinder is used where an external force is not available to retract the piston or it can be used where high force is required in both directions of travel.

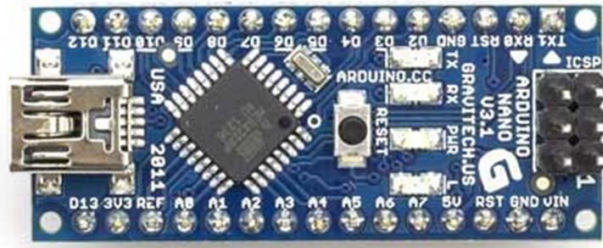
SOLENOID VALVE

Directional control valves (DCV) are a standout amongst the most essential parts in hydraulic driven apparatus also and pneumatic hardware. They permit fluid flow into various ways from one or more sources. Solenoid as a rule comprise of a spool inside the chamber which is precisely or electrically controlled. The development of the spool limits or allows the stream, in this way it controls the fluid stream.



ARDUINO

Arduino is an open-source electronics platform based on easy-to-use hardware and software. Arduino boards are able to read inputs - light on a sensor, a finger on a button, or a Twitter message - and turn it into an output - activating a motor, turning on an LED, publishing something online. You can tell your board what to do by sending a set of instructions to the microcontroller on the board. To do so you use the Arduino programming language (based on Wiring), and the Arduino Software (IDE), based on Processing. The Arduino software is easy-to-use for beginners, yet flexible enough for advanced users. It runs on Mac, Windows, and Linux



VII. RESULTS

To Try and achieve the best results, we had to gather large amounts of data pertaining to the working of bumper and sensors under various conditions for research to know which combination of different factors yields the best results. Based on multiple trails with different input factors, we observed that the ideal range of the ultrasonic sensor is around 13-17 inches, to get a minimum delay of less than one second, which allows the system to react in any situation. After experimenting in different scenarios, we observed that the bumper extends when an object, either moving or stationary, is at the range of less than or equal to 13 inches. Brakes apply simultaneously without any delay. The sensor senses the threat and sends the signal to arduino, it restricts the motor action, so brakes are applied. Then, the solenoid valve allows the air to the pneumatic cylinder and hence bumper extends without any delay. The bumper stays in the extended position for around 2 seconds and retracts backwards. The brakes release and motor action restores after the bumper retracts, i.e., after 2 second

VIII. CONCLUSIONS

The main purpose behind this idea was to reduce the rate of accidents and to minimize the risks and casualties in accidents. General usage cars which are not high end and are generally not affordable by common people do not get enough safety in the vehicles which increases their chances to be prone to higher risks in a case of an accident. We aim to replace or add the usual car bumpers with the automatic bumper to improve the safety of the vehicle and passengers. This is cost friendly and would be completely affordable to a common man. Towards the end of completion of this idea into a working model, we felt that the project has helped us to bridge the gates between institution and industries

IX. REFERENCES

- [1]. "Evaluation Of An Impact Energy Absorber In A Car Bumper" Pravin E. Fulpagar, Dr.S.P.Shekhawat, Department of Mechanical Engineering, SSBTS COET Jalgaon.
- [2]. "Automated Bumper for Damage Reduction" Aditya Gandhi, Amey Deshmukh, Rahul Aniyankunju, and

Prathamesh Kalasakar. Mechanical engineering, MITCOE Pune, Savitribai Phule Pune University, Pune, Maharashtra, India

[3]. J. T. Wang General Motors Corporation, United States, Paper No. 05-0144

[4]. A Deceleration Control Method of Automobile For Collision Avoidance 1.Takahiro Wada, 2.Shun'ichi Doi 3. Shoji Hiraoka.

[5]. "Crash Analysis For Energy Absorption of Frontal Rails of A Passenger Car" Raymond Joseph, Dr. M.A. Kamoji, International Research Journal of Engineering and Technology. (IRJET)

[6]. "Smart Breaking System with Pneumatic Bumper", Shinde Aniket S., Hivrekar Akshay P., Dherange Nitin S., Shegar Ganesh B. Students, Department of Mechanical Engineering D.Y. Patil College of Engineering, Pune, India

[7]. "Impact And Injury Patterns In Frontal Crashes of Vehicles", Matthew L. Brumbelow, David S. Zuby, Insurance Institute for Highway Safety, United States of America

[8]. "Pneumatic Bumper System For Four Wheeler" Tushar Kale, Vaibhav Kute, Sandeep Pokharkar, Shubham Rakshe, Anil katarkar Students, Mechanical Department, P K Technical Campus, Chakan.

Effects of combustion chamber profile on direct injection diesel engine operated with SuOME

Cite as: AIP Conference Proceedings **2128**, 050001 (2019); <https://doi.org/10.1063/1.5117973>
Published Online: 23 July 2019

N. Keerthi Kumar, T. K. Chandrashekar, and N. R. Banapurmath



View Online



Export Citation

ARTICLES YOU MAY BE INTERESTED IN

[Performance analysis of NACA2411 ice accreted original and optimized airfoils](#)

AIP Conference Proceedings **2128**, 050002 (2019); <https://doi.org/10.1063/1.5117974>

[Investigations on performance and emission characteristics of single cylinder four stroke CI engine fueled with diesel - Azadirachtaindica oil blends](#)

AIP Conference Proceedings **2128**, 050006 (2019); <https://doi.org/10.1063/1.5117978>

[Experimental and numerical investigation of thin cylindrical shell subjected to axial compression loading](#)

AIP Conference Proceedings **2128**, 050012 (2019); <https://doi.org/10.1063/1.5117984>

Lock-in Amplifiers

Find out more today



Zurich Instruments

Effects of Combustion Chamber Profile on Direct Injection Diesel Engine Operated with SuOME

N. Keerthi Kumar^{1, a)}, TK. Chandrashekar^{2 b)}, NR. Banapurmath^{3, c)}

¹ Assistant Professor, Department of Mechanical Engineering, BMS Institute of Technology and Management, Bangalore, India.

² Professor, Department of Mechanical Engineering, Mangalore Institute of Technology & Management, Moodabidri, India.

³ Professor, BVB College of Engineering and Technology, Mechanical Engineering, Hubli, India.

^{a)}Corresponding author: keerthikumarn@bmsit.in

^{b)}tkcmite@gmail.com

^{c)} nrbapurmath@gmail.com

Abstract. Present work is focused on experimental investigation of performance, combustion and emission of DI diesel engine using Simarouba Oil Methyl Ester (SuOME). Control of combustion process in order to achieve better performance with reduced emission has been achieved by varying the shape of combustion chamber. In order to study the effect of shapes of different combustion chambers on performance of diesel engine, Toroidal Re-entrant Combustion Chamber (TRCC), Lateral Swirl Combustion Chamber (LSCC), Dual Swirl Combustion Chamber (DSCC) and Lateral Dual Swirl Combustion Chamber (LDSCC) were developed without changing compression ratio of standard diesel engine. Experiments were carried out using optimum injection timing of 27^obTDC, injector opening pressure of 240 bar and nozzle geometry of 6 holes with 0.2 mm diameter. Results of DI diesel engine operated with SuOME revealed that the LSDCC shape resulted in improved engine brake thermal efficiency with minimum HC and CO emission levels compared to other selected combustion chamber shapes.

Keywords: Combustion Chamber, Performance, Combustion characteristics, Simarouba oil Methyl Esters, CI Engine.

INTRODUCTION

Fuel consumption is directly proportional to the development of any country, which demands the use of transport vehicle [1]. Resources of fossil fuels are diminishing very rapidly due to indiscriminate usage in transport and energy sectors. Fossil resources are in the stage of depletion and emit debatable amounts of emissions. Hence, it is important to find and switch over to other alternative renewable fuel sources produced from plants, animals and newer technologies [2]. However, before considering substitute fuel sources for diesel, it is necessary to ensure that the engine performance remains uncompromised. The biodiesels produced from the animal fats leads to higher cost and does not contribute to green energy. Hence, liquid biodiesel derived from honne, rubber seed, mahua, karanja, calophyllumin, nigellasateva, jatropa, polanga, neem seed, rapeseed simarouba etc were used as substitutes for diesel [3-10]. Seed oils produced from non-edible plant seeds provide major contribution by providing rural employment

and avoiding greenhouse effect. By transesterification process, the properties of biodiesel produced from plant seeds can be made comparable to diesel [11-12]. Other major advantages of using biodiesel produced from plant seed are biodegradability, lower sulfur content, and renewability, with higher cetane number. Biodiesel produced will also support nations to reduce the import of fossil fuels or extend the depletion time of available resources of fossil fuel [13]. Simarouba plant is considered as promising non-edible plant, which contributes both for medical and engineering field. Raw oil comprises more than 60% of its weight in Simarouba seeds. Furthermore, the choice of Biodiesel produced from simarouba seeds is desirable due to its harmless, recyclable, and low emission profile, which reduces the negative environmental impacts [14]. Many researchers have conducted experiments to evaluate the effect of biodiesel in diesel engine by adopting different biodiesel conversion techniques, blends, using additives in biodiesel, pre heating of inlet fuel, fine atomizing and many more. Generally, a slight loss in power, with increased specific fuel consumption was observed in case of biodiesel fuelled engine operation. Use of biodiesel reduces the emissions of CO, HC, and PM. However, a majority of research results have identified an increase in nitrogen oxides [15-17].

It has been observed there is a decrease of power by 6% and torque by 3% of CI engine operating using cotton seed biodiesel compared to neat diesel, and it has been concluded that reduced heating value of cotton seed oil is the major reason for reduced trend of power and torque, but they contributed more towards atomization of fuel [18]. Use of jatropha carcus and palm biodiesel and their blends gave noticeable higher specific fuel consumption when compared to diesel at all loads with reduced thermal efficiency. They have also reported higher tail pipe temperature under all operating conditions [19- 21]. The major reason for the reduction in brake thermal efficiency is of higher viscosity of biodiesel and hence improper mixture of biodiesel fuel with air. Many researchers have carried out both experimental and simulation studies to improve the tendency of fuel air mixture which has been achieved by creating forced turbulence in the combustion chamber [22-23].

Change in the performance and emission of cylindrical, Toroidal and Trapezoidal combustion chamber over conventional hemispherical combustion chamber for Neem and Mahua biodiesel operated diesel engine were studied and reported that use of Toroidal combustion chamber increased the combustibility with reduced emission levels due to higher in-cylinder velocity complemented by increased turbulence [23]. Use of jatropha fuel blends in toroidal, spherical and re-entrant combustion chamber shapes have resulted in higher efficiency with reduced emissions like HC, Smoke, CO₂ where as higher NO_x emissions when compared with spherical and re-entrant combustion chambers. This may be due to higher turbulence and fuel air mixture quality [24]. Simulation study has been carried out using KIVA-GA code for Re-entrant type combustion chamber shape to highlight the effect of Swirl ratio, start of injection, EGR, IP, Cr and found reduced emission levels like CO, CO₂, and also in NO_x with reduced fuel consumption [25]. Simulation work has been carried out to optimize the combustion chamber based on reduction of HC and CO emissions and enhancement in combustion efficiency, due to higher tumble and squish, reduced emission were obtained compared to the baseline piston [26]. Simarouba biodiesel was used in cylindrical, toroidal and toroidal re-entrant combustion chamber and it was concluded that simarouba biodiesel is a better substitute for diesel fuels. Result showed that for torodial re-entrant combustion chamber, reduced ignition delay with higher peak in-cylinder pressure were observed than cylindrical, hemispherical and totoidal combustion chambers. This may be due to creation of forced swirl motion of fuel air mixture [27].

Though many researchers have worked on biodiesel, modification of combustion chamber geometries, it has been found that very few researchers have worked on use of 100% simarouba biodiesel with selected combustion chamber shapes. Hence, in this work, the focus is towards the use of 100% simarouba biodiesel in diesel engine with little modification and use of LSCC, DSCC and LDSCC. Use of LDSCC gave the advantage of both LSCC and DSCC in improving the engine performance and to reduce emission levels.

CHARACTERIZATION OF SIMAROUBA OIL METHYL ESTER

Simarouba Oil Methyl Ester (SuOME) was derived from simarouba seeds by crushing and transisterification process. The properties of the fuels were determined as per Indian standards and found to be in line with the diesel fuel. Table 1 and Table 2 show the properties of diesel, SuOME and Fatty acid composition of simarouba methyl ester used in the present study. Average of five trials for each composition has been reported.

TABLE 1. Properties of Simarouba Oil Methyl Ester.

Properties	Diesel	SuOME
Description of sample	--	Yellow Coloured Liquid
Gross Calorific Value, Cal/g	10,275	9,399
Flash point, °C (Open Cup)	56	184
Kinematic viscosity at 40°C, cSt	3-5	4.9
Density, g/ml at 15°C	0.832	0.813
Cloud Point, °C	-17	22
Acid value, mg of KOH/g	--	1.76

TABLE 2. Fatty Acid Composition of Simarouba Oil Methyl Ester.

Parameters	Palmitic Acid	Stearic Acid	Oleic Acid	Linoleic Acid	Linolenic Acid	Arachidonic Acid
SOME	23.9%	13.2%	50.8%	5.6%	3.9%	1.2%

EXPERIMENTAL SETUP

Experiments were carried out on Kirloskar TV 1 type, four-stroke single cylinder water-cooled engine with maximum speed of 1500 rpm 5.2 kW loading capacity. Figure 1 shows experimental setup. Major technical specifications of the selected engine are given in table 3. Eddy current type dynamometer was coupled with engine for loading the engine. Cooling of the engine block and cylinder head is achieved by circulating water all around. Cylinder pressure was measured with Piezo electric transducer fitted on the cylinder head with crank angle encoder attached to flywheel. Combustion analyzer is used to find combustion characteristics with respect to crank angle. The emission characteristics of exhaust gas were measured by using HARTRIDGE smoke meter and DELTA 1600 S, non-dispersive infrared technology exhaust gas analyzer have been used to find quantitate the emission levels. Mechanical Fuel Injection System (MFIS) was adopted for fuel spray having a capacity to inject the fuel with pressure of 205 to 260 bar. In the present study, experiments were carried out by adopting 6 hole 0.2 mm nozzle operating at 240 bar of injection pressure with compression ratio of 17.5. To study the influence of CC shapes on engine performance, combustion and emissions characteristics, four different shape of piston bowl/ combustion chamber shapes namely TRCC, LSCC, DSCC and LDSCC have been considered. Figure 2 shows the geometry of different CC used. All the CC shapes were developed by keeping the bowl volume constant to ensure constant compression ratio. Tests were carried out for standard operating condition using diesel and SuOME as a fuel followed by tests carried out for modified engine having different CC. The tests were carried for different brake power varying from 0% to 100% load with step of 20%. For every load, five set of readings were generated to ensure the accuracy of the data recorded and averaged out data was considered for study. Finally, the results of different CC shapes were compared and analyzed with standard engine results.

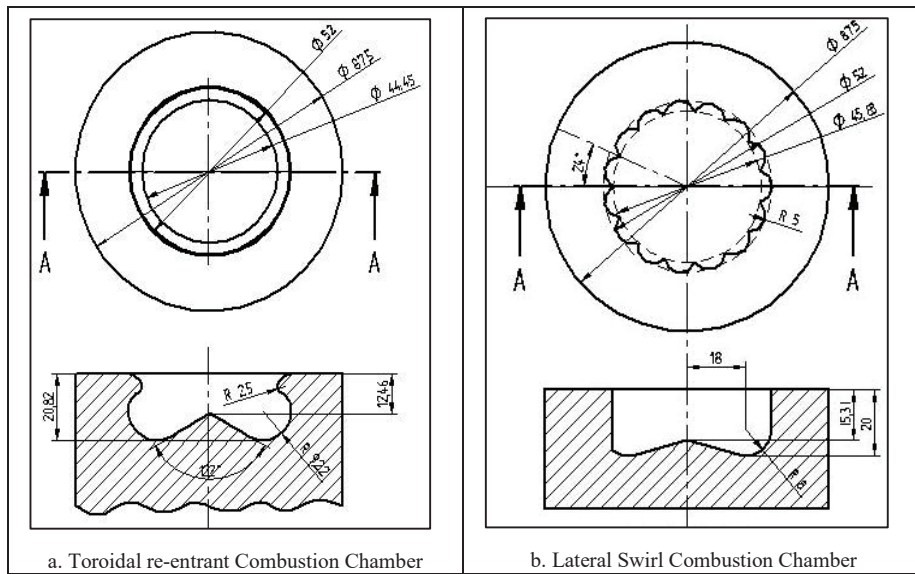
TABLE 3. Technical Specifications of the engine test rig

Sl No	Parameters	Specification
1	Type of engine	Kirloskar make Single cylinder four stroke water cooled DI diesel engine.
2	Rated power	5.2 KW (7 HP) @1500 RPM
3	Nozzle opening pressure	Range - 205 to 260 bar
4	Cylinder diameter (Bore)	87.5 mm
5	Stroke length	110



FIGURE 1. Experimental Setup

COMBUSTION CHAMBER SHAPES USED



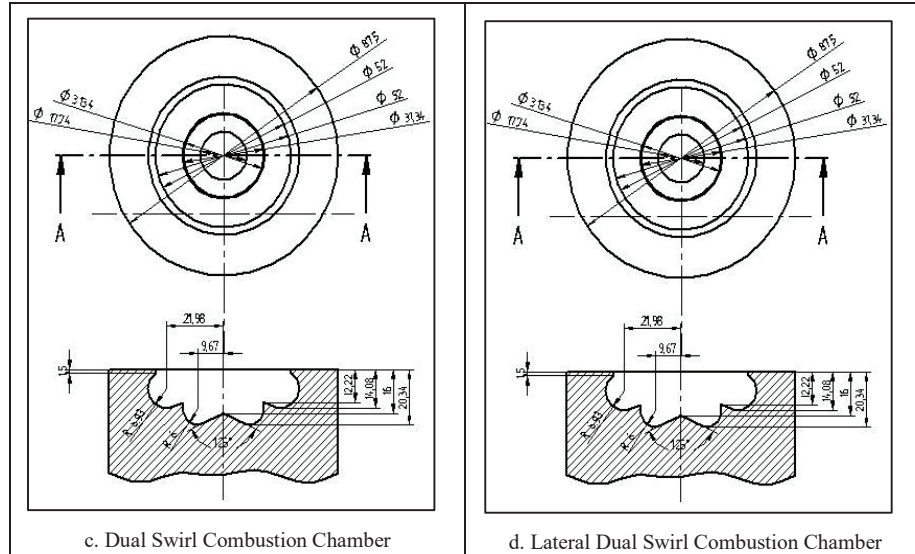


FIGURE 2. Different Combustion Chamber Used

METHODOLOGY

MODIFICATION OF TEST ENGINE

Use of 100% biodiesel directly in to the base line engine is not possible due to higher viscosity of biodiesel. Hence, modification in fuel injection system and geometry of combustion chamber is essential since, they encourage change in performance and emissions. Formation of fuel air mixture depends on combustion chamber shape. In this regard, it is found that many CC shapes namely, shallow depth, cylindrical, and reentrant have been adopted by many researchers. In the present study, HCC was modified to obtain desired shapes namely, TRCC, LSCC, DSCC and LDSCC. All combustion chambers were designed by keeping same piston bowl volume of hemispherical combustion chamber (piston bowl volume = 36,811.088 mm³) so that compression ratio was the same for all shapes. Use of HCC provides small squish which may not be sufficient to use biodiesel and accumulation of fuel takes in mid region of combustion chamber shape. Hence, to provide desired squish and to obtain higher performance ratio of depth to diameter may be varied. By changing the shape of traditional HCC by modified combustion chambers to TRCC, LSCC, DSCC, LDSCC the fuel/air mixture formation could be improved and the soot emission could be reduced accordingly because of higher squish.

ERROR ANALYSIS

Uncertainties and errors during the experimentations may arise either from selection of instruments, operating conditions, observations, readings and method of testing. In the present study, uncertainties in measurements are found by considering accuracy, precision and repeatability of engine test sequence. Each experiment was carried out three times and results were averaged to avoid random uncertainty.

Total uncertainty:

$$\sqrt{[(\text{Load})^2 + (\text{engine speed})^2 + (\text{temperature})^2 + (\text{fuel consumption})^2 + (\text{HC})^2 + (\text{CO})^2 + (\text{NO}_x)^2 + (\text{smoke})^2 + (\text{BTE})^2 + (\text{HRR})^2]} = 4.704$$

RESULTS AND DISCUSSIONS

Combustion, performance and emission characteristics of 4 stroke CI engine were experimentally studied using SuOME biodiesel for modified shapes of CC viz., TRCC, LSCC, DSCC and LDSCCC. In the previous work, TRCC showed higher BTE than Toroidal, Cylindrical and Hemispherical combustion chamber for engine operated using SuOME. This paper is in continuation to previous paper [27]. In the present paper HCC for diesel and TRCC for SuOME is considered as the base to compare with LSCC, DSCC and LDSCC. The experiments were carried out for optimized engine parameters of IOP, IT, Nozzle Geometry. Detailed analysis was carried out based on the experimental results obtained. Effects of various combustion chamber shapes on combustion, performance and emission characteristics were presented in the following sections. The results of the above experiments are tabulated and shown in table 4.

TABLE 4. Comparison of results with reference [27].

	Diesel (HCC)	SuOME (HCC)	SuOME (CCC)	SuOME (TCC)	SuOME (TRCC)	SuOME (LSCC)	SuOME (DSCC)	SuOME (LDSCC)
BTE	30	27	28	28.5	29.15	28.5	28.94	29.5
EGT	510	536	531	525	523	536	528	518
HC	52	62	60	58	58	62	60	56
CO	0.17	0.195	0.195	0.19	0.185	0.195	0.19	0.18
NOx	1242	1220	1222	1224	1230	1222	1225	1234
ID	9.1	9.3	9.2	9.1	9.4	9.6	9.5	9.2
CD	46	46	45	45	48	49	50	47
PP	87	78	79	80	83	80	81	84
Smoke	66	72	70	68	70	74	72	68

Results of reference 30

Results of present paper

Results of reference 30 and present paper

PERFORMANCE ANALYSIS

Brake Thermal Efficiency:

Brake thermal efficiency of SuOME with modified and standard engine for optimized operating parameters against load is shown in Figure 3. It is observed that BTE for diesel operation was slightly higher than SuOME operation for all loads and CC shapes. This may be branded by lower heating value and volatility of the SuOME. On the other hand BTE of TRCC was greater than other CC [27] whereas for LDSCC further higher than TRCC including new CC used in present study operated with SuOME. The possible reason for this may be, LDSCC avoids the flame from prolonged over the squish band hence, results in higher mixing quality. At all the loads BTE of LSCC is lower than LDSCC, while BTE of TRCC and DSCC lies between those of LSDCC and LSCC. At full load with SuOME for the LSDCC, the BTE was 29.5% compared to 28.5% for LSCC. There is an increment of about 3.5% of BTE for LDSCC.

Exhaust Gas Temperature:

Variation of exhaust gas temperature of SuOME for different CC operating with pre-optimized parameters with various brake power is shown in Figure 4. At all the loading EGT is higher marginally with SuOME compared to diesel and the same trend is continued for all the CC. High oxygen content of SuOME is the reason for higher EGT which results in higher combustion tendency when SuOME is used. Use of SuOME in LDSCC at full load gave exhaust gas temperature of 518⁰C which is 18⁰C higher than LSCC. Whereas for LDSCC it is 8⁰C higher than diesel fuel operated using HCC under standard operating condition. The variation of EGT is less in engine operation with LSDCC compared to CC shapes with respect to diesel at full load condition. At full load with SuOME for the LSDCC, the EGT was less of about 3.35% when compared with LSCC

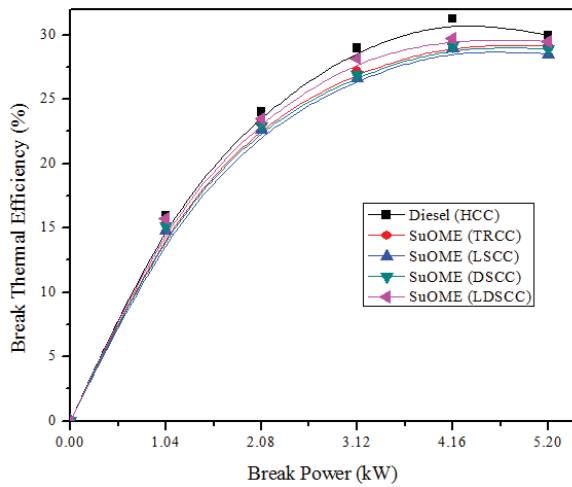


FIGURE 3. Brake Thermal Efficiency with Brake Power

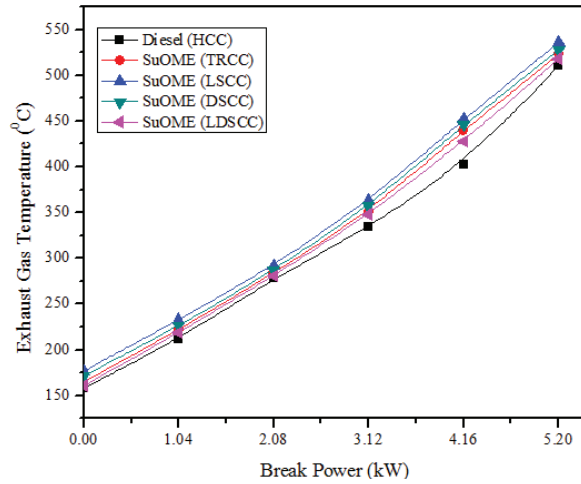


FIGURE 4. Exhaust Gas Temp with Brake Power

EMISSION ANALYSIS

Unburnt Hydrocarbon Emissions:

The unburnt hydrocarbon emission for LDSCC, LSCC, DSCC and TRCC are compared with the baseline HCC fuelled with diesel and SuOME and shown in Figure 5. UBHC emissions comprise a fuel that is partially burned. Formation of HC is due to poor distribution of fuel, higher excess air with reduced EGT and un-burnt fuel found in tail pipe. UBHC emissions increases when load increases and the same trend were observed for all kind of CC. UBHC are reduced over all range of loads for LDSCC when compared with other CC for SuOME operation. The reason for this trend may be due to better eddy formation and higher air fuel mixture rate with LDSCC. However, LSCC did not gave appropriate mixing of fuel and air which led to partial combustion. From the plot it is observed that use of LDSCC reduces HC emissions compared to other combustion chamber shapes when operated using SuOME. At full load with SuOME for the LSDCC, the HC emission was 56 ppm compared to 62 ppm for LSCC. There is a decrease of about 9.67% UBHC emissions for LDSCC. Use of TRCC showed lowered levels of emission compared to various CC used [27].

Carbon Monoxide Emissions:

Figure 6 shows the variation of CO emission with load for four types of CC operating with SuOME for pre-optimized condition. CO is a transitional combustion product and is mainly formed due to rich mixture, deficiency of oxygen to form CO₂, less adiabatic flame temperature and incomplete combustion of carbon leads to form CO. CO emissions for all CC are higher than Standard engine operated using diesel. However CO emissions are lesser with LDSCC compared with TRCC, LSCC, DSCC shapes. This may be attributed due to increased disordered motion of air and oxygen content in SuOME lead to reduced heat losses for the cylinder wall with better oxidation of CO. At full load with SuOME for the LSDCC, the carbon monoxide emission was 0.18% compared to 0.195% for LSCC. There is a decrease of about 7.69% CO emissions for LDSCC. However TRCC showed reduced CO emission compared to other CC used [27].

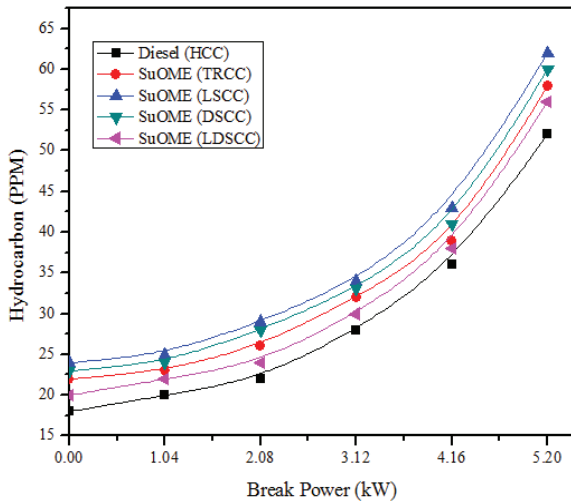


FIGURE 5. HC Emissions with Brake Power

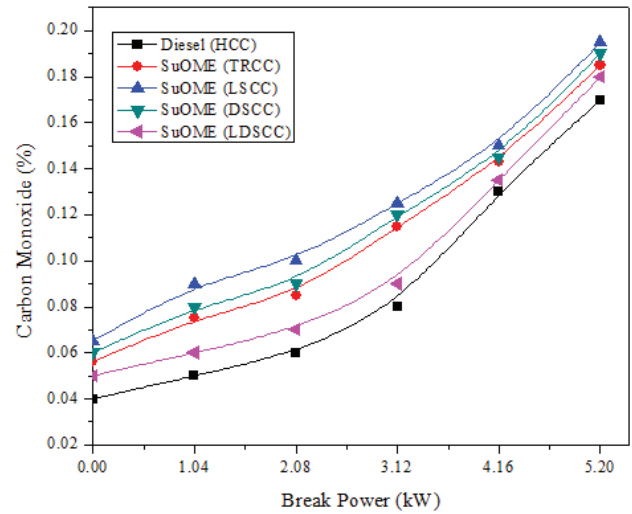


FIGURE 6. CO Emission with Brake Power

Smoke Opacity:

The smoke formation mainly due to high temperature at rich zone (Core region of fuel droplet) and partial burning of the HC with incomplete reacted carbon content in the injected fuel. Fig 7 shows the smoke opacity comparisons for four types of CC with SuOME and diesel. The smoke opacity for all CC is higher when compared with those of base line engine, also increases as the engine load increases. This may be due to higher FFA content of SuOME, higher viscosity. However, LSDCC produces less smoke compared with LSCC due to the effect of both lateral swirl and duel swirl which gives good combustion and oxidation of soot particles and intermediate smoke emissions were observed for TRCC and DSCC. At full load with SuOME for the LSDCC, the smoke opacity emission was 68 HSU compared to 74 HSU for LSCC. There is a decrease of about 8.1% smoke emissions for LSDCC. Use of TRCC in standard engine was suggested over other CC based on results obtained [27].

Oxides of Nitrogen:

Figure 8 shows the variation of oxides of nitrogen with BP for diesel and SuOME operated in standard and modified engine using pre-optimized IT, IOP and nozzle geometry. NO_x emission is highly subjective by the temperature of fuel and air during combustion. It is evident from the figure that, NO_x emission levels are bit higher for diesel fuel operation compared to biodiesel over the entire load range. This may be attributed to amplified rate of heat release during premixed combustion stage with diesel compared with SuOME. NO_x emissions are marginally higher in LDSSCC compared to TRCC, LSCC, DSCC shapes. TRCC showed slightly higher No_x emission compared to HCC, CCC and TCC [27]. This may be attributed to greater combustion temperature due to better mixture formation. Higher oxygen content in SuOME is also responsible for this tendency. However, NO_x emissions can be controlled by employing suitable catalytic converters and adopting Exhaust Gas Recirculation. At 100% with SuOME for the LSDCC, the NO_x emission was 1234 ppm compared to 1222 ppm for LSCC. There is an increase of about 0.98% NO_x emissions for LSDCC.

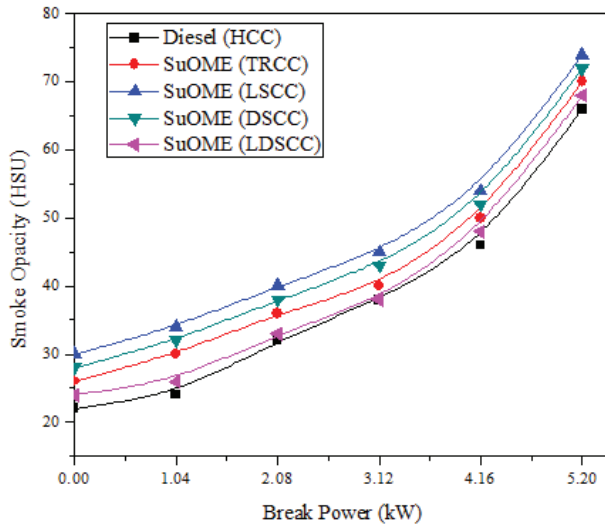


FIGURE 7. Smoke Opacity with Brake Power

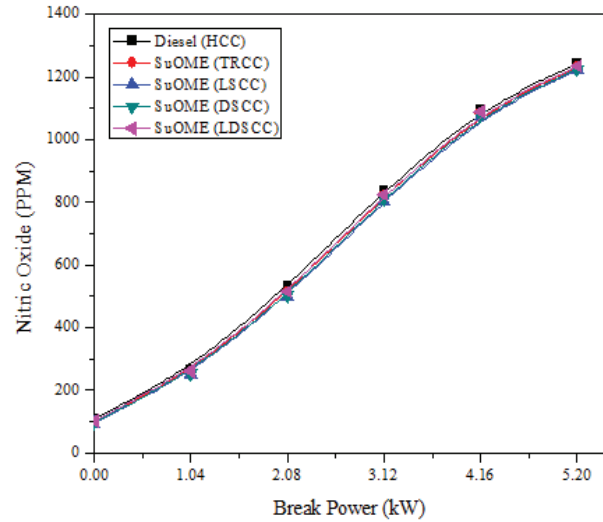


FIGURE 8. Nitric Oxide with Brake Power

COMBUSTION CHARACTERISTICS

Combustion tendency of standard CI engine will differ when SuOME is used as fuel in CI engine, and it mainly governed by the properties of fuel used like viscosity, heating value, auto ignition temperature and quality of fuel air mixture. Use of LDSCC in a CI engine considerably affects the fuel distribution, intensity of fuel air mixture and combustion characteristics of fuel because of forced swirl created by the combination of Lateral and Dual swirl. The different combustion characteristics for SuOME fuel operated diesel engine tested under pre-optimized values constant speed of 1500 rpm and Cr 17.5 are summarized below.

Ignition Delay Period:

Ignition delay of fuel is important parameter for explaining the tendency of knock in CI engines. Variation of Ignition delay for base and modified engine at two loads of 80% and 100% is shown in Figure 9. The ignition delay period depends on the cetane number, specific gravity and viscosity of the fuel. From graph it is noticed that for CC geometries reduction in ignition delay increases with the amplification of brake power. This may be attributed to amplified fuel burnt inside combustion chamber, higher combustion and wall temperatures with reduced exhaust gas dilution. Similar trend were observe for TRCC when compared to HCC, CCC and TCC [27]. Ignition delay period of LDSCC is significantly lower than that of other combustion chambers for SuOME when tested in standard engine. At full load with SuOME for the LSDCC, the ignition delay was 9.2 °CA compared to 9.6 °CA for LSCC. There is a decrease of about 4.16% in ignition delay for LDSCC.

Combustion Duration:

Variation in combustion duration with load for 80% and 100% conditions for both diesel and SuOME fuels is represented in Figure10. It is noticed that for all CC, combustion duration increases as BP is increased. This may be attributed to increase in the quantity of fuel injected. LDSCC gave reduced combustion duration compared to other CC due to increased mixing rate and improved squish hence complete combustion. Higher combustion duration is observed with other combustion chamber except LDSCC due to lack of squish which needs extended time period for mixing of fuel air resulting in partial combustion with extended diffusion combustion duration. At full load with SuOME for the LSDCC, the combustion duration was 47 °CA compared to 50 °CA for DSCC. There is a decrease of about 6% in combustion duration for LDSCC. It is evident that as the rate of fuel air mixture increases, reduction in combustion duration is observed and similar results were observed with HCC, CCC and TCC [27].

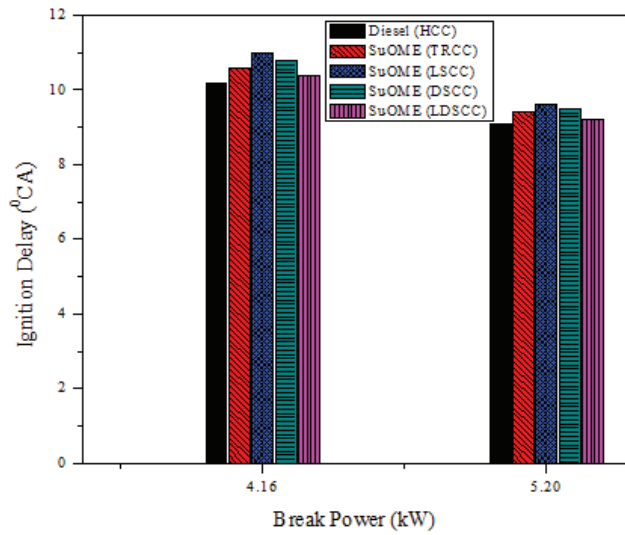


FIGURE 9. Ignition Delay with Brake Power

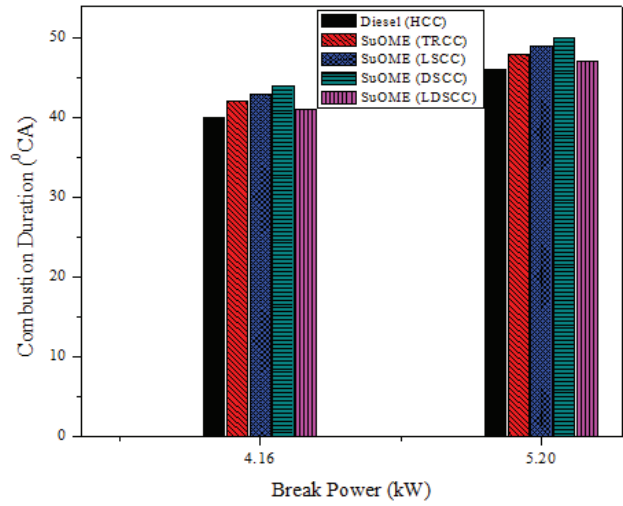


FIGURE 10. Combustion Duration with Brake Power

Cylinder Peak Pressure:

The comparison of cylinder peak pressure with respect to brake power at 80% and 100% load for both modified and base engine with diesel and SuOME fuels operating under the same engine parameters used for previous study. Variation of cylinder peak pressure is shown in Figure 11. It may be noticed that the cylinder peak pressure is lower for SuOME when compared to diesel. This may be attributed to inappropriate mixing of SuOME with air due to higher density, low volatility and lower calorific value. On the other hand the peak pressure of LDSCC is higher than other CC using SuOME as fuel under same operating conditions. This trend is observed due to better combustion because of higher air mixture rate in LDSCC as a result of enhanced air motion. At 100% with SuOME for the LSDCC, the cylinder peak pressure was 84 °CA compared to 80 °CA for LSCC. There is an increase of about 5% in cylinder peak pressure for LDSCC.

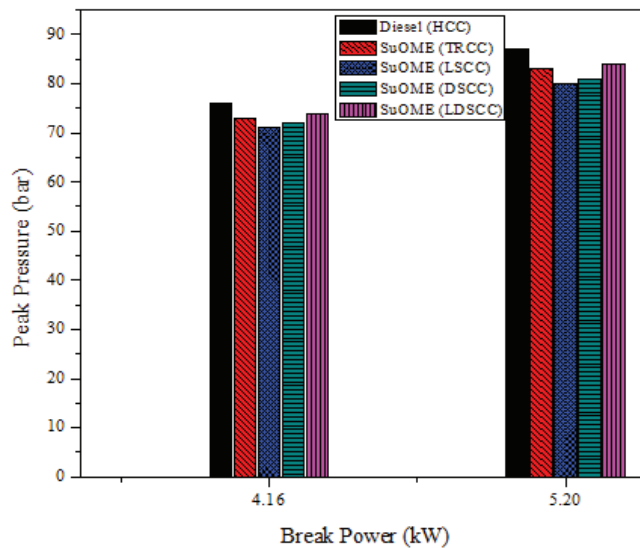


FIGURE 11. Peak Pressure with Brake Power

In cylinder Pressure and Heat Release Rate:

The cylinder pressure–crank angle history was acquired for 100 cycles and the averaged pressure variation with crank angle at 80% load is depicted in Figure 12 for different combustion chamber shapes. The peak pressure depends on the rate of combustion process and portion of fuel that take part in rapid combustion period. The mixture formation during ID and extent of ID regulates uncontrolled combustion phase. This mixture preparation during ID is responsible for the maximum rate of pressure rise. Slightly lower peak pressure was noticed when engine was running on SuOME fuel with different combustion chamber shapes as compared to diesel. The reason could be higher viscosity and slower heat release of SuOME. Similarly, HRR variation with crank angle is provided in Figure 13. SuOME showed slightly lower HRR as compared to diesel with all combustion chamber employed. It could be due to slower combustion of SuOME on account of higher viscosity and inhomogeneous mixture formed. LDSCC enhanced SuOME fueled engine performance due to increase in peak pressure and higher HRR followed by TRCC.

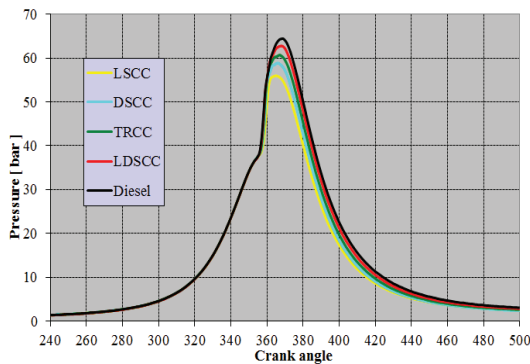


FIGURE 12. Pressure with Crank Angle

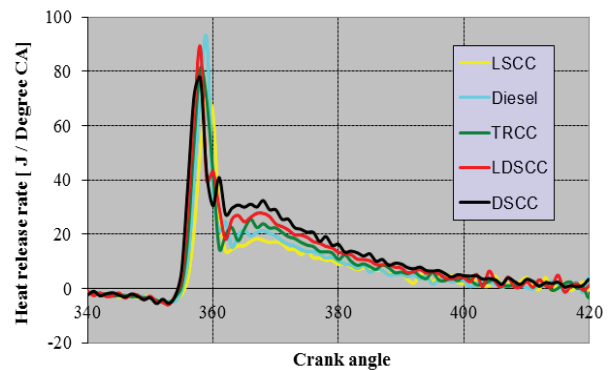


FIGURE 13. Heat Release Rate with Crank Angle

CONCLUSIONS

From the detailed experimental test conducted using SuOME and different CC in single cylinder diesel engine, following conclusions are arrived:

1. Presence of higher oxygen in SuOME results in complete burning of fuel and hence, higher combustion and exhaust gas temperature.
2. Enhanced fuel air mixture was observed in LDSCC due to combined effect of lateral and dual swirl with increased efficiency when compared with other CC shapes.
3. Use of LDSCC increases rate of fuel air mixture, resulting in shorter ignition delay period with high initial rate of heat release with short combustion duration when compared with other CC.
4. Improved air motion results in LDSCC gave higher cylinder pressure compared to LSCC, DSCC, TRCC when SuOME is used.
5. Emissions of CO, UBHC and smoke were noticeably lower for LDSCC than other types of CC when SuOME is used as fuel.
6. NO_x emission was found to be higher with LDSCC when SuOME is used as fuel than other CC which can be reduced by exhaust gas treatments.

Better mixture formation and reduced smoke emissions are the major factors for good CI engine performance. From the above experiment it is concluded that SuOME is a best substitute for diesel at all loads with little modification in engine, for further increase in performance use of LDSCC can be adopted in place of base HCC. Except NO_x and exhaust gas temperature emissions like CO, UBHC and smoke emission from modified engine were of lesser magnitude with the use of SuOME in LDSCC when compared with other CCs.

REFERENCES

1. S.Ch. Rao ,M.SrinivasaRao, Srikakulam, “Performance Analysis of DI Diesel Engine Fuelled with Diesel along with Nano Additives”. [International Journal of Engineering Trends and Technology](#), Vol.24, pp. 107, 2015.
2. Naik, S. N., Vaibhav, V., Goud Prashant, K., Rout, A. and Dalai, K. “Production of first and second generation biofuels: A comprehensive review”. [Renewable and sustainable energy reviews](#), 14, pp. 578-597, 2010.
3. Banapurmath NR, Chavan AS, Bansode SB, Keerthi Kumar N, Tandale MS, “Effect of Combustion Chamber Shapes on the Performance of Mahua and Neem Biodiesel Operated Diesel Engines”, [Journal of Petroleum and Environmental Biotechnology](#), Vol.6, 230, 2015.
4. GajendraBabu MK, Chandan Kumar, Das LM, “Experimental Investigations on a Karanja Oil Methyl Ester Fuelled DI Diesel Engine”, Society of Automotive Engineers, Paper No.: 2006-01-0238, 2006.
5. Karnwal A, Naveen Kumar MM, Chaudhary HR, Siddiquee AN, Khan ZA, “Production of Biodiesel from Thumba Oil: Optimization of Process Parameters”, [Iranica Journal of Energy & Environment](#), Vol.1, pp.352-358, 2010.
6. Onga HC, Mahlia TMI, Masjukia HH, Norhasyimab RS, “Comparison of palm oil, Jatropha curcas and Calophyllum for Biodiesel”, [Renewable and Sustainable Energy Reviews](#), Vol.15, pp.3501-3515, 2011.
7. Ramadhas AS, Muraleedharan C, Jayaraj S, “Performance and emission evaluation of a diesel engine fueled with methyl esters of rubber seed oil”, [Renewable Energy](#), Vol.30, pp.1789-1800, 2005.
8. Raheman H, Phadataré AG, “Diesel engine emissions and performance from blends of karanja methyl ester and diesel”, [Biomass and Bioenergy](#), Vol.27, pp.393-397, 2004.
9. Sahoo PK, Das LM, Babu MKJ, Arora P, Singh VP, “Comparative evaluation of performance and emission characteristics of Jatropha, karanja and polanga based biodiesel as fuel in a tractor engine”, [Fuels](#), Vol. 88, pp.1698-1707, 2009.
10. Venkanna BK, Reddy CV, “Performance, emission and combustion characteristics of direct injection diesel engine running on calophyllum oil (honne oil)”. [International Journal of Agricultural & Biological Engineering](#), Vol.4, 2011.
11. Capuano D, Costa M, Fraia SD, Massarotti N, Vanoli L. “Direct use of waste vegetable oil in internal combustion engines”, [Renewable and Sustainable Energy Reviews](#), Vol.69, pp.759–770,2017.
12. Barnwal BK, Sharma MP. “Prospects of biodiesel production from vegetable oils in India”, [Renewable and Sustainable Energy Reviews](#), Vol.9(4), pp.363–378, 2005.
13. Singh P, Varun, Chauhan SR. “Feasibility of a new non-edible feedstock in diesel engine: investigation of performance, emission and combustion characteristics”, [Journal of Mechanical Science and Technology](#), Vol.31 (4), pp.1979–1986, 2017.
14. NabnitPanigrahi, Mahendra Kumar Mohanty, SrutiRanjan Mishra, Ramesh Chandra Mohanty, “Energy and Exergy Analysis of a Diesel Engine Fuelled with Diesel and Simarouba Biodiesel Blends”, [Journal of Institution of Engineers India Series C](#), Vol.99 (1), pp. 9-17, doi: 10.1007/s40032-016-0335-9.
15. Behcet R. “Performance and emission study of waste anchovy fish biodiesel in a diesel engine”. [Fuel Process Technol](#),92:1187-94,2011.
16. Usta N. “An experimental study on performance and exhaust emissions of a diesel engine fuelled with tobacco seed oil methyl ester”. [Energy Conversion & Management](#), Vol.46, pp.2373–2386, 2005.
17. A.M. Liaquat, H.H. Masjuki, M.A. Kalam, M. Varman, M.A. Hazrat, “Application of blend fuels in a diesel engine”, 2nd International Conference on Advances in Energy Engineering (ICAEE 2011), [Energy Procedia](#) 14, pp. 1124 – 1133, 2012.
18. Aydin H, Bayindir H. “Performance and emission analysis of cottonseed oil methyl ester in a diesel engine”. [Renew Energy](#), Vol.35, pp.588–592, 2010.
19. Verma PCM, Murlu Krishna MVS, Prabhakar Reddy C, “Investigation on biodiesel (Esterified jatropha carcus oil) diesel engines”. Proceedings of the 16th national conference on IC engines and combustions”. New Delhi:, Narosa Publishing House, pp. 159-162A, 2000.
20. Lin Y, Tsai C, Yang CR, Wu CHJ, Wu TY, Chang-Chien GP. “Effects on aerosol size distribution of polycyclic aromatic hydrocarbons from the heavy-duty diesel generator fueled with feedstock palm-biodiesel blends”. [Atmospheric Environment](#), Vol.42, pp.6679–6688, 2008.
21. Jaichandar S, Annamalai K. “Influences of re-entrant combustion chamber geometry on the performance of Pongamia biodiesel in a DI diesel engine”, [Energy](#), Vol.44 (1), pp. 633-640, 2012.

22. Pratiba BVV, Prasanthi G, "Influence of in cylinder air swirl on diesel engine performance and emission". *International Journal of Applied Engineering and Technology*, Vol.1, pp.113-118, 2011.
23. Jaichander S, Annamalai K, "Combined impact of injection pressure and combustion chamber geometry on the performance of a biodiesel fueled diesel engine". *Energy*, Vol.55, pp.330-339, 2013.
24. Mamilla VR, Mallikarjun MV, Rao GLN. "Effect of combustion chamber design on a DI diesel engine fuelled with *Jatropha* methyl esters blends with diesel". *Procedia Engineering*, Vol.64, pp.479–90, 2013.
25. Wickman DD, Yun H, Reitz RD. "Split-spray piston geometry optimized for HSDI diesel engine combustion". SAE technical paper, Vol.01-0348, 2003.
26. Bin Wang, Tie Li, LinlinGe, Hideyuki Ogawa, "Optimization of combustion chamber geometry for natural gas engines with diesel micro-pilot-induced ignition", *Energy Conversion and Management*, Vol. 122, pp. 552–563, 2016.
27. N Keerthi Kumar, T K Chandrashekar, N R Banapurmath, V S Yaliwal, "Effect of combustion geometry on combustion, performance and emission characteristics of CI engine using simarouba oil methyl ester", *IOP Conf. Series: Materials Science and Engineering* 376, 2018.



ICSEM 2016

Kinetic analysis of isothermal solid state process for synthesized potassium sodium niobate piezoelectric ceramics

Nandini R Nadar ^{a*}, Krishna M ^b

^{a*}^b R. V. College of Engineering, R& D centre, Department of Mechanical Engineering, Bangalore-560059, INDIA.

Solid state kinetic models were developed for predicting conversion fraction (α), reaction rate ($d\alpha/dt$), kinetic triplet (model $f(\alpha)$, frequency factor (A) and activation energy (E_a)) of $(K_{0.5}Na_{0.5})NbO_3$ ceramics using thermogravimetric analysis data obtained at constant temperature of 900°C. The integral reaction model $g(\alpha)$, were evaluated for experimental data and theoretical reaction models. Kinetics of solid state reaction of KNN ceramics was a homogenous nucleation process with one dimensional nuclei growth per particle at constant rate, 2D diffusion controlled reaction mechanism, particles with spherical/cubical shape based on Mapel, JMAEK nucleation, Jander Model and contracting volume model respectively.

© 2018 Elsevier Ltd. All rights reserved.

Selection and Peer-review under responsibility of INTERNATIONAL CONFERENCE ON SMART ENGINEERING MATERIALS (ICSEM 2016).

Keywords: KNN; solid state reaction; Kinetics analysis; Kinetic Triplet; Reaction model; Diffusion model; Nucleation model; Crystal imperfections.

1. Introduction

Presently, potassium sodium niobate (KNN) based lead free piezoelectric ceramic materials have high potential applications in emerging areas of micro-motors[1], energy harvesting devices[2], magneto-electrical sensor [3] etc., due to their high curie temperature (T_C)[4], piezoelectric and ferroelectric properties[5]. Solid state method is a convenient way to decompose the presence of carbonates and oxides in KNN piezoelectric materials with good control on particle morphology [6-7]. The KNN is a heterogeneous material with melting point of two alkali

* Corresponding author. Tel.: +91-958-892-2999; fax: +91-806-717-8011

E-mail address: nandini.nadar@gmail.com, krishnam@rvce.edu.in

elements close to normal calcination temperature in solid state route. Hence establishment of the calcination temperature may result in the formation of non-stoichiometric phases due to volatile nature of the alkaline elements, which hinders the densification and piezoelectric properties [8-10]. In this direction many researchers have investigated the influence of calcination parameters and alkali carbonates on phase transformation of KNN from orthorhombic to tetragonal crystal structure [11-13].

Many researchers have worked on kinetic (isothermal or non-isothermal) analysis of model-fitting and model-free (iso-conversional) methods [14-19] for amorphous, polymeric and pharmaceutical materials in the solid state route. Avrami models were used to achieve required reaction mechanism and to determine kinetics of $(\text{GeS}_2)_{0.3}(\text{Sb}_2\text{S}_3)_{0.7}$ glass, zirconia gel ZrO_2 [15] crystalline material, crystallographic transition[16], decomposition kinetics of the AlH_3 polymorphs, thiourea and thiourea oxides[17-18], hydrogen adsorption or desorption of MgH_2 with single walled carbon nano tubes (SWNT) and metallic catalyst[19], hydration of tricalcium and dicalcium silicate mixtures [20] and de-solvation of sulfa meter solvates [21] respectively. Thermal decomposition of AgMnO_4 crystals for polymorphic transformation was analyzed by kinetics models based on Maxwell-Boltzmann distribution of energy [22]. Acid-base type solid chemicals such as sulfonamide and ammonia adducts [23] showed that diffusion model plays a vital role when the crystal lattices of the reactants are separate. The dehydration process of calcium oxalate monohydrate followed geometrical contraction models [24]. Thermal oxidation of porous silicon [25] followed Mapel (First-order) Model. But as per authors knowledge no or few research is focused on solid state kinetic analysis to optimize the synthesis route of KNN piezoelectric materials to achieve $(\text{K}_{0.5}\text{Na}_{0.5})\text{NbO}_3$ system without non-stoichiometric phases for better piezoelectric properties.

The purpose of the work was to investigate solid state kinetics of KNN ceramic particles for the system $(\text{K}_{0.5}\text{Na}_{0.5})\text{NbO}_3$ isothermally by thermal gravimetric analysis. The isothermal reaction rate (da/dt), the kinetic triplet (A , E_a , $f(\alpha)$) and integral reaction model $g(\alpha)$ was determined by conversion fraction (α). The nucleation, geometrical contraction, diffusion, reaction-order models were studied to achieve completion of the isothermal reaction of KNN piezoelectric materials, without non-stoichiometric phases by model fitting method for better piezoelectric properties.

2. Experimentation

The potassium sodium niobate piezoelectric ceramics was synthesized by conventional solid state method [26]. The synthesized homogeneous KNN nano powders were subjected for thermo-gravimetric analysis to study isothermal solid state kinetics behind solid state route of KNN ceramics. Thermo-gravimetric measurements was done by using simultaneous thermogravimetry / differential thermal analyser, (DTG-60/60) Shimadzu, with an analytical measuring instrument to work in inert atmosphere ($50\text{ml min}^{-1} \text{N}_2$). Small sample (2.724mg) was placed in a platinum cell to reduce the phenomena of heat and mass transfer. A constant rate controlled thermal degradation curve was obtained to study the solid state kinetics of KNN ceramic powders. The measured parameters were transformed into a conversion fraction (α) to analyse the reaction mechanism of KNN piezoelectric ceramic powders.

3. Results and Discussions

3.1 Isothermal curves of KNN powder

The measured isothermal gravimetric data of KNN powder at 900°C for dwell time between 1-1000 min was transformed into conversion fraction (α) by using equation 1. m_0 , m_t , m_∞ is the initial mass, mass at time t , and final mass of KNN powder at 1000min. The obtained α values were plotted against the dwell time, from 1-1000 min. Isothermal curve (α vs. t) of synthesized KNN powder is depicted by Fig. 1(a). The parabolic nature of the graph indicates gradual increase in the mass fraction of the KNN powder as the reaction mechanism progress till 500min. Enhancement in the mass fraction during isothermal reaction is due to removal of moisture, decomposition of KNN powder from carbonates into bi-carbonates with the release of CO_2 gas. Further the mass fraction of the isothermal reaction from 500-1000 min was constant. This ensured that isothermal reaction mechanism of KNN powder at 900°C is completed. The reaction rate of the KNN powder at 900°C was evaluated by determining change in mass fraction to change in dwell time (da/dt) and was plotted against the conversion fraction as shown in

Fig 1(b). Here the reaction rate reduced gradually as the reaction progressed and almost zero towards the mass fraction value of 1 ensuring that, kinetic model of KNN ceramic powders can be grouped under deceleratory models.

$$\alpha = \frac{m_0 - m_t}{m_0 - m_\infty} \tag{1}$$

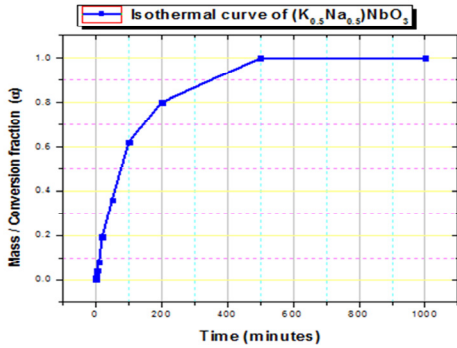


Fig. 1(a). Mass fraction(α) vs. time of synthesized $(K_{0.5}Na_{0.5})NbO_3$ ceramic

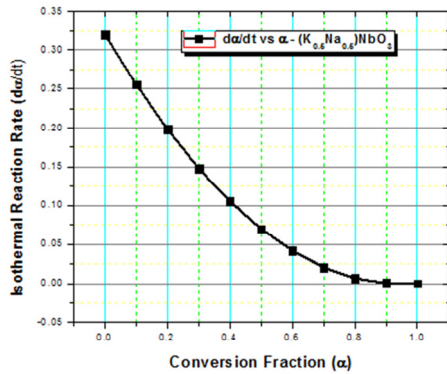


Fig. 1(b). Reaction rate vs. Mass fraction(α) of synthesized $(K_{0.5}Na_{0.5})NbO_3$ ceramic powder.

3.2 Order based models of KNN

The conversion fraction (α) and reaction rate (da/dt) computed from the measured parameter of isothermal gravimetric analysis was used to determine reaction model $f(\alpha)$ and integral reaction model $g(\alpha)$ of KNN particles. The experimental $f(\alpha)$ value was determined by equations 2,3 and $g(\alpha)$ by Eqs. 4,5 respectively. The frequency factor, activation energy, absolute temperature, gas constant, heating rate, reaction and integral reaction model is denoted by $A, E_a, T, R, \beta, f(\alpha)$ and $g(\alpha)$ respectively. The heating rate [β] is given by the equation dT/dt .

$$\frac{d\alpha}{dt} = A e^{-(E_a/RT)} f(\alpha) \tag{2}$$

$$g(\alpha) = A e^{-(E_a/RT)} f(\alpha) \tag{4}$$

$$\frac{d\alpha}{dt} = \frac{A}{\beta} e^{-(E_a/RT)} f(\alpha) \tag{3}$$

$$g(\alpha) = \frac{A}{\beta} \int_0^T e^{-(E_a/RT)} f(\alpha) \tag{5}$$

The theoretical first, second and third order reaction models were determined by the Eqs. 6- 8 using conversion fraction (α) values of KNN particles. The order of integral reaction models was evaluated by Eqs. 9-11. The reaction and integral models of KNN powder computed from measured parameters were mapped with derived order based models by model fitting method.

$$f(\alpha) = (1-\alpha), \quad 1st \text{ order} \tag{6}$$

$$g(\alpha) = (\ln|(1-\alpha)|), \quad 1st \text{ order} \tag{9}$$

$$f(\alpha) = (1-\alpha)^2, \quad 2nd \text{ order} \tag{7}$$

$$g(\alpha) = (1/(1-\alpha)) - 1, \quad 2nd \text{ order} \tag{10}$$

$$f(\alpha) = (1-\alpha)^3, \quad 3rd \text{ order} \tag{8}$$

$$g(\alpha) = (1/2)((1-\alpha)^{-2} - 1), \quad 3rd \text{ order} \tag{11}$$

In this regard, the plot of order based models of synthesized KNN nano-powders is indicated by Fig. 2a and 2b. In Fig. 2a, The $f(\alpha)$ vs. (α) for different order of the reaction was almost similar to homogenous kinetics. The nature of the graph ensured reaction rate (da/dt) and the mass fraction (α) were proportional to each other, raised to a particular power, called to be the reaction order. The evaluated reaction model $f(\alpha)$ of KNN experimentally was compared with derived models for different orders (1, 2 and 3). The nature of the experimental reaction model was similar to second order reaction at initial and final α values. The other consecutive α values of the experimental reaction model was fitting towards first order model. To confirm the reaction order of the synthesized KNN nano-powders, the graph of integral reaction models $g(\alpha)$ vs. mass fraction (α) for different order was plotted as shown in

Fig.2b. The experimental integral reaction model $g(\alpha)$ fitted exactly with the derived second order reaction model, ensuring that synthesized KNN powders in the system $(K_{0.5}Na_{0.5})NbO_3$ is the second order solid state reaction.

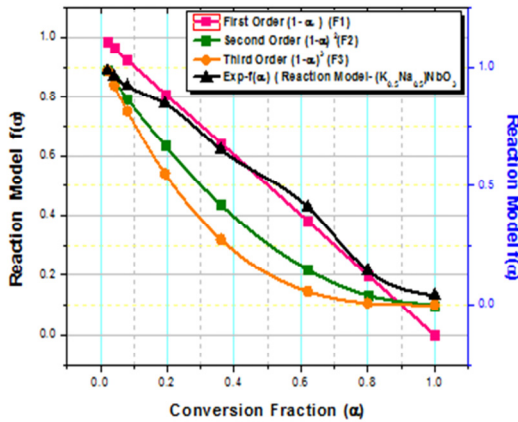


Fig. 2(a) Order based reaction models of synthesized $(K_{0.5}Na_{0.5})NbO_3$

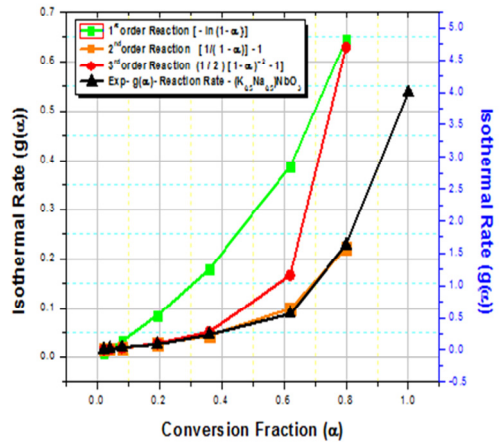


Fig.2(b) Integral reaction model of synthesized $(K_{0.5}Na_{0.5})NbO_3$

3.3 Activation Energy $[E_a]$ of KNN.

The activation energy $[E_a]$ of the synthesized KNN powders can be evaluated by the rate law as shown in Eq. 2 or 4, after evaluating $d\alpha/dt$, $f(\alpha)$ and $g(\alpha)$ values of KNN particles. Here A is the frequency factor, T is the absolute temperature, R is the gas constant, $f(\alpha)$ is the reaction model. The variation in activation energy for synthesized KNN nanoparticles by solid state reaction is indicated by Fig. 3. The uniqueness and variance in activation energy ensured that it is a complex reaction mechanism with two or more elementary steps in the mechanism. In such a case, change in activation energy will be observed as the reaction progress [29]. This indicates that during a reaction, reactivity changes due to formation of the required system $(K_{0.5}Na_{0.5})NbO_3$, and presence of crystal defect and intra crystalline strain. The reactivity of KNN solid state reaction is also affected by experimental variables, which changes the kinetics of reaction mechanism. The dependence of E on α in decreasing mode confirms that it is an endothermic reversible reaction which follows an irreversible reaction [30].

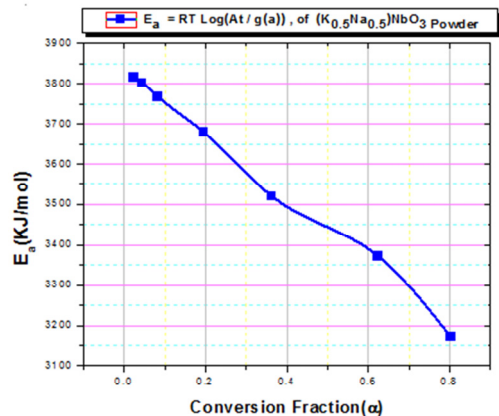


Fig. 3. Dependence of E on α for synthesized KNN powders

3.4 Kinetics of solid state reaction of KNN piezoelectric powders

3.4.1 Nucleation Model.

The kinetics behind solid state reaction of KNN particles can be divided into nucleation models, geometric contraction, and diffusion and reaction order based on its reaction mechanism. The nucleation based integral reaction expression were derived by Power law, Avrami, Mapel and JMAEK models from Eqs. 12 to 20 as shown below.

$$P2 = \alpha^{1/2} \quad (12) \quad A2 = [-(1-\alpha)]^{1/2} \quad (15) \quad B1 = \ln [\alpha/(1-\alpha)] + c^a \quad (18)$$

$$P3 = \alpha^{1/3} \quad (13) \quad A3 = [-\ln(1-\alpha)]^{1/2} \quad (16) \quad -\ln(1-\alpha) = kt \quad (19)$$

$$P4 = \alpha^{1/4} \quad (14) \quad A4 = [-\ln(1-\alpha)]^{1/4} \quad (17) \quad [-\ln(1-\alpha)]^{1/n} \quad (20)$$

The formation of the required system i.e.(K_{0.5}Na_{0.5})NbO₃ was achieved by decomposition [27] of the reactant with the release of CO₂ in the lattice of reactant (K₂CO₃, Na₂CO₃ and Nb₂O₅).The nucleation rate of the experimental value was comparatively higher than that of Avrami (Fig.4b)and power model (Fig.4a) which indicates problem of ingestion and overlap of nuclei [26].Prout-Tompkins (B1) model was not relevant to experimental g(α) values of KNN. The integral reaction rate of KNN powder mapped with the derived value of Mapel Nucleation model, ensured single nucleus per particle in the synthesized system of (K_{0.5}Na_{0.5})NbO₃ ceramic materials as shown in Fig4b. The nature of the diffusion controlled nucleation models (JMAEK) for n=1.5 was in agreement with reaction rate of KNN particles as indicating Fig. 4c. This JMAEK model ensured that it is a homogeneous nucleation with one dimensional nuclei growth at constant rate, considered under bulk mechanism [29].

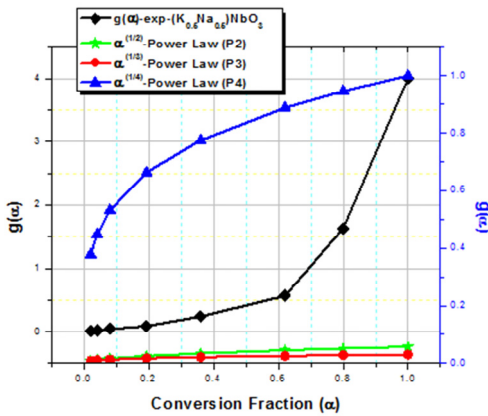


Fig. 4a. Power law models of synthesized (K_{0.5}Na_{0.5})NbO₃

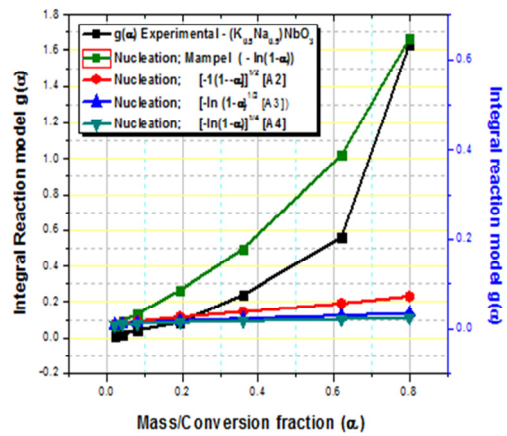


Fig. 4b. Avrami and Mapel models of synthesised (K_{0.5}Na_{0.5})NbO₃powders

3.4.2 Diffusion model of KNN powder

The experimental rate controlling process for the reaction mechanism of the KNN powder was analysed by diffusion models. In this regard 1-D,2-D,3-D and Brounshtein models were derived from α values of KNN particles, using below mentioned equations 21-24.

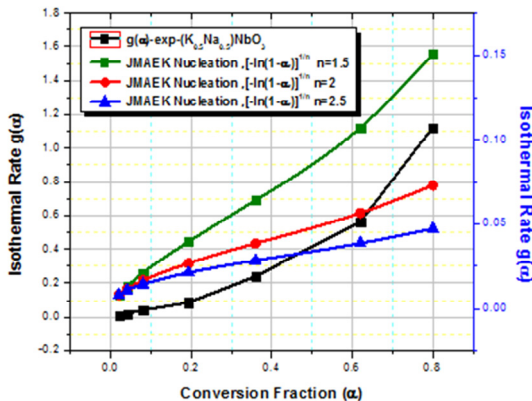


Fig. 4.(c)JMAEK nucleation models of (K_{0.5}Na_{0.5})NbO₃powders

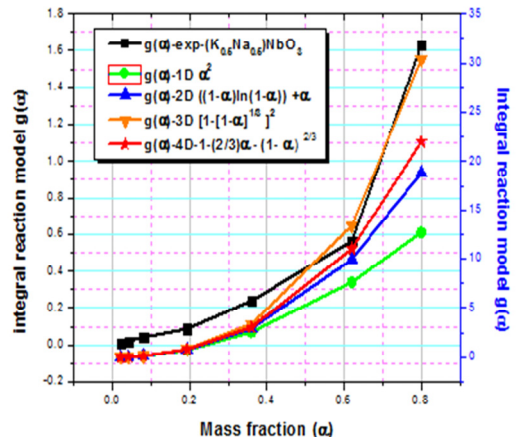


Fig. 5. Diffusion Models (a) 1D, 2D, 3D, D4- of (K_{0.5}Na_{0.5})NbO₃powders.

$$D1 = \alpha^2 \tag{21}$$

$$D3 = [1 - (1-\alpha)^{1/3}]^2 \tag{23}$$

$$D2 = ((1-\alpha)\ln(1-\alpha)) + \alpha \tag{22}$$

$$D4 = 1 - (2/3) \alpha - (1-\alpha)^{2/3} \tag{24}$$

The rate controlling process (Diffusion) for the solid state reaction of KNN powders is indicated by Fig.5. The experimental integral reaction expression $g(\alpha)$ of the KNN powders was mapped with the derived diffusion models for 1, 2, 3 and 4 dimensions models. The reaction model was not proportional to mass fraction values (α) conforming that, it is not 1D model. The Jander model(D3) which assumes spherical shape of the solid particle and Ginstling and Bounstein(D4) for low conversion values, didn't hold good for integral reaction rate models of KNN powders. The graphical shape of the experimental diffusion model maps with the 2D-Diffusion model. 2D-Diffusion model which was in agreement with the integral reaction rate of KNN ensured, that the synthesized KNN solid particles are in cylindrical shape with increased reaction zone at radial diffusion through a cylindrical shell. The product formation rate decreased proportionally as shown in Fig.1b, in diffusion controlled reactions with a barrier to the product layer [31]. Hence we can conclude that, solid state kinetics of KNN powder is a 2D-diffusion controlled reaction mechanism.

3.4.3 Geometrical contraction model of KNN powders

Contraction (Phase Boundary) models of synthesized KNN powders which assumes nucleation to occur quickly across the surface of the KNN crystal is indicated by Fig.6a and 6b. The reaction rate and integral reaction rate of the model was derived from Eqs. 25 - 26, using mass fraction (α) value, obtained from measured gravimetric data. The experimental integral reaction value $g(\alpha)$ of KNN particles was mapped with derived models of contracting area and volume as shown in Fig. 6. Since the reaction interface of KNN powder progress towards the centre in contraction models, the rate of degradation can be controlled. The graphical shape of reaction and integral reaction rate model at almost all α values, excluding few of KNN particles as shown in Fig.6a and 6b, was in match with contraction volume model [27]. This confirmed that, the KNN solid particles where spherical/cubical in shape.

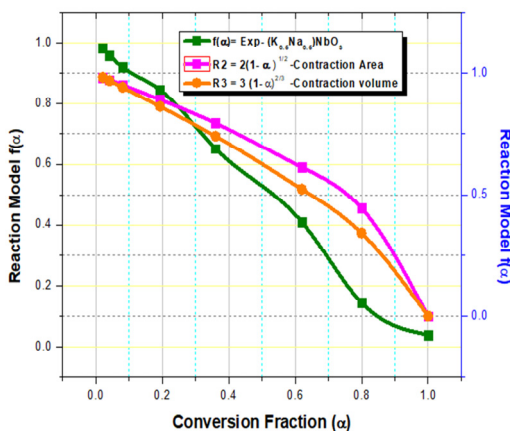


Fig. 6a. Geometrical contraction (R) reaction models $f(\alpha)$.

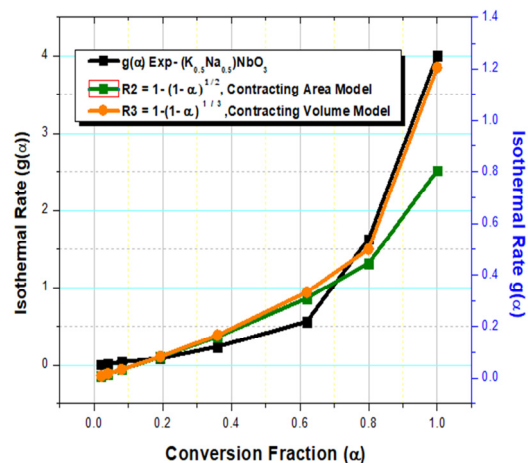


Fig. 6b. Geometrical contraction (R) Integral reaction models $g(\alpha)$.

$$R2 = 2(1-\alpha)^{1/2} \tag{25}$$

$$R2 = 1 - (1-\alpha)^{1/2} \tag{27}$$

$$R3 = 3(1-\alpha)^{2/3} \tag{26}$$

$$R3 = 1 - (1-\alpha)^{1/3} \tag{28}$$

4. Conclusion

The current work was focussed on isothermal kinetic analysis, to study the kinetics behind solid state reaction of potassium sodium niobate piezoelectric ceramics. Mass fraction (α) and reaction rate of KNN powder achieved completion of the solid state reaction at 900°C, 500min with a deceleratory reaction rate. The E_a values revealed that synthesized KNN powders were of complex endothermic reversible reaction followed with irreversible reaction. Order based model concluded that reaction mechanism of KNN is the second order solid state reaction. The Mapel and JMAEK nucleation model revealed that $(K_{0.5}Na_{0.5})NbO_3$ ceramic materials is an constant rate homogenous nucleation with one dimensional growth of single nucleus per particle. Jander Model conclude that, solid state kinetics of KNN powder is a 2D-diffusion controlled reaction mechanism. Geometrically contacting volume model ensured that the synthesized KNN solid particles were spherical/cubical in shape.

In summary, the theoretical based experimental approach helped to analyze the kinetics behind reaction mechanism of calcined KNN nanopowders through various derived solid state models. Solid state kinetics tool helped in achieving completion of the reaction mechanism successfully without non-stoichiometric phases, thereby leading to betterment of piezoelectric properties.

References

- [1]. Kim H, Tadesse Y, Priya S, In: Priya S, Inman DJ (eds). Piezoelectric energy harvesting, energy harvesting technologies. Springer, New York, 2009, p. 3–39.
- [2]. Priya S, Advances in energy harvesting using low profile piezoelectric transducers, J Electroceram, 2007,19,pp167–184.
- [3]. Hollenstein E, Damjanovic D, Setter N. Temperature stability of the piezoelectric properties of Li-modified KNN ceramics. J. Eur Ceram Soc 27,2007,13(15),p.4093–4097.
- [4]. Park S-E, Shrout TR. Ultrahigh strain and piezoelectric behaviour in relaxor based ferroelectric single crystals. J Appl Phys 1997, 82(4),p1804–1811.
- [5]. Herklotz A et al. Electrical characterization of PMN–28%PT(001) crystals used as thin film substrates. J Appl Phys 2010,108(9).p.094-101.
- [6]. Ahn C W et al. Effect of elemental diffusion on temperature coefficient of piezoelectric properties in KNN-based lead-free composites. J Mater Sci Lett,(2010), 45(14).p.3961–3965.
- [7]. Bomlai P et al. Effect of calcination conditions and excess alkali carbonate on the phase formation and particle morphology of $(Na_{0.5}K_{0.5})NbO_3$ powders. J Am Ceram Soc 2007, 90(5),p.1650–1655.
- [8]. J. L. Zhang, X. J. Zong, Y. Gao, Y. L. Qing, M. L. Zhao, C. L. Wang. Recent study progresses of $(K, Na)NbO_3$ -based lead-free piezoelectric ceramics., J. of Optoelectronics and advanced mate 2010, 12(9), p. 1921 - 1925.
- [9]. E.K.Akdogan, K.Kerman, M.Abazari, A.Safari Origin of high piezoelectric activity in ferroelectric $(K_{0.44}Na_{0.52}Li_{0.04})-(Nb_{0.84}Ta_{0.1}Sb_{0.06})O_3$ ceramics. Applied Physics Letters 2008,92(11),p.2908.
- [10]. J. Fu, R. Z. Zuo, X.H.Wang, L.T.Li, Phase transition and domain variation contributions to piezoelectric properties of alkaline niobate based lead-free systems. J.Mater. Sci. 21 ,2010 ,p.519-522.
- [11]. Bomlai P et al. Effect of calcination conditions and excess alkali carbonate on the phase formation and particle morphology of $Na_{0.5}K_{0.5}NbO_3$ powders. J Am Ceram Soc .2007,90(5),p.1650–1655
- [12]. Skidmore TA, Milne SJ. Phase development during mixed-oxide processing of $a[(Na_{0.5}K_{0.5})NbO_3]_1 \cdot x[LiTaO_3]_x$ powder. J Mater Res 2007, 22(08):2265–2272 .
- [13]. Wang Y et al. Compositional Inhomogeneity in Li- and Ta-Modified $(K, Na)NbO_3$ Ceramics. J. Am Ceram. Soc., 2007,90(11),p.3485–3489.
- [14]. L.A.Perez-Maqueds, J.M.Criado, P, E, Sanchez-Jimenez, Combined kinetic analysis of solid state reactions: A powerful tool for the simultaneous determination of Kinetic parameters and the kinetic model without previous assumptions on the reaction mechanism., J.Phys.Chem.A, 2006, 110,p.12456-12462.
- [15]. Jeri Malek. Kinetic analysis of crystallization process in amorphous materials, thermo chimica acta.,2000, 335,p 239-253.
- [16]. Burnham, A.K., Weese, R.K., Weeks. A distributed activation energy model of thermodynamically inhibited nucleation and growth reactions and its application to the β - δ phase transition of HMX. B.L.J. Phys. Chem. B. 2004,108,p.19432-19441.

- [17]. Jason Graetz, J. J. Reilly, Decomposition Kinetics of the AlH₃ 3 Polymorphs, *The Journal of Physical Chemistry B*, 2006,109(47),p.22181-5.
- [18]. Wang,S. Gao, Q.Y, Wang. Thermodynamic analysis of decomposition of thiourea and thiourea oxides. *J.C. J.Phys.Chem.B*,2005,109,p.17281.
- [19]. Wu C, Wang P, Yao X, Liu C, Chen D, Lu GQ, Cheng H, Effects of SWNT and metallic catalyst on hydrogen absorption/desorption performance of MgH₂. *J Phys Chem. B*. 2005 ,109(47),p.22217-21.
- [20]. Peterson,V.K., Neumann,D.A, Livingston,R.A. Hydration of tricalcium and dicalcium silicate mixtures studied using quasielastic neutron scattering. *J. Phys. Chem. B* .,2005,109, p.14449.
- [21]. Khawam, A, Flanagan, D.R. Complementary use of model-free and modelistic methods in the analysis of solid-state kinetics. *J.Phys.Chem.B*.2005, 109, p.10073
- [22]. Peter J. Skrdla , Rebecca T. Robertson., Semi-empirical Equations for Modelling Solid-State Kinetics Based on a Maxwell–Boltzmann Distribution of Activation Energies: Applications to a Polymorphic Transformation under Crystallization Slurry Conditions and to the Thermal Decomposition of AgMnO₄ Crystals. *J. Phys. Chem. B*2005, 109 (21), p.10611–10619.
- [23]. Wyandt, C.M, Flanagan, D.R. Solid-state non-isothermal kinetics of sulfonamide-ammonia adduct desolvation. *Thermochim. Acta* 1992, 109, p. 379.
- [24]. J.E. House Jr., Randal W. Eveland. Kinetic Studies on the Dehydration of Calcium Oxalate Monohydrate. *J. Solid state Chem*,1993,105(1) p.136-142.
- [25]. Joakim Riikonen, Mikko Salomaki, Jessica van Wonderen, Marianna Kemell, Wujun Xu, Ossi Korhonen, Mikko Ritala, Fraser MacMillan, Jarno Salonen, Vesa-Pekka Lehto. Surface Chemistry, Reactivity, and Pore Structure of Porous Silicon Oxidized by Various Methods.*J.ACS.pub*.2012, 28 (28), p.10573–10583.
- [26]. Carniti, P, Gervasini, A, Bennici, S. Experimental and modelization approach in the study of acid-site energy distribution by base desorption. Part I: modified silica surfaces. *J. Phys. Chem. B* 2005,109,p15-28.
- [27]. Sestak,J.Berggren, G.study of the kinetics of the mechanism of solid state reactions at increasing temperatures., *Thermochim. Acta* 1971, 3, 1.
- [28]. Haibo Yang, Ying Lin, Jianfeng Zhu, Fen Wang, An efficient approach for direct synthesis of (K_{0.5}Na_{0.5})NbO₃ powders. *Powder Technology* ,2009,196,p.233-236.
- [29]. L.A.Perez-Maqueda,J.M.Criado,J.Malek, Combined kinetic analysis for crystallization kinetics of non-crystalline solids. *J.Non-Crystalline Solids* ,2003,320,p.84-91.
- [30]. Sergey vyazovkin ,Wolfgang linert, Kinetic analysis of reversible thermal decomposition of solids. *Int.J.Chem.Kinetics* 1995,27(1),p73-84.
- [31]. Chirsty M.Wyandt, Douglas R. Flanagan, Solid -state non isothermal kinetics of sulphonamide-ammonia adduct desolvation. *Thermochimica Acta*, 1992, 196(2),p379-389.



INTERNATIONAL JOURNAL OF ADVANCE RESEARCH, IDEAS AND INNOVATIONS IN TECHNOLOGY

ISSN: 2454-132X

Impact factor: 4.295

(Volume 5, Issue 2)

Available online at: www.ijariit.com

Outcome Based Education, need for the hour- NBA

S. Nithya Poornima

nithyapmech@bmsit.in

BMS Institute of Technology and Management, Bengaluru, Karnataka

ABSTRACT

Outcome-Based Education (OBE) model is being adopted at a fast pace at Engineering colleges in India at the moment. It is considered as a giant leap forward to improve technical education in India and help Indian Engineers compete with their global counterparts. Outcome Based Education (OBE) is an important demonstration Tool for student-centered instruction that focuses on measuring student performance through outcomes. Outcomes include Engineering Knowledge, Problem Analysis, Ethic, Individual and Team Work, Communication etc... It enables the students to perpetuate these outcomes as they perceive over the years of engineering. The students are evaluated for all the required parameters (Outcomes) during the course of the program. The attainment, defined by the NBA, gives a substantial opportunity for Tier-II students to bridge this gap of employability. In this present paper, a case study is developed through CO-PO mapping and attainment for Mechanical Engineering Students of Tier-II. The formulated rubrics assessment is indicative of a continuous improvement strategy that can be easily adaptable by faculty and students across engineering streams.

Keywords— CO-PO Mapping, Outcomes, Rubrics, Attainment

1. INTRODUCTION

The traditional way of teaching was where the teacher instructs the students and the students generally take down the notes without even logical thinking. The important thing regarding teaching in the traditional method is that topic is written on the blackboard and students take down notes from the blackboard as a result at the end of the day the students memorize the same and appear for the examination with the at most intention to pass the Examination. With the recent advancement, there is no point in adhering to the Traditional method as the completion towards has increased enormously.

The programme should be also responsible for preparing the students to compete with the fast moving technology and standards that enable them with more job oriented opportunities with the decision-making skills. This outcome-based education enables the students to possess certain strong traits such as leadership skills, communications skills and working teams. The optimum method for teaching is to integrate both traditional and modern teaching methods for effective teaching

2. METHODOLOGY

Course outcomes outline the content that covers the entire content of the syllabus that has to be delivered. These outcomes are broken into different levels to enhance learning. Here the course outcomes of the subject Mechatronics and microprocessor is considered as an example for showing the OBE activity.

Course outcomes for the subject Mechatronics and microprocessor (10ME65):

2.1 Formulating Course Outcomes (CO)

- CO1: Outline the concept Measurement and control systems their elements and functions and describe the mechatronics based system and Microprocessor based controllers.
- CO2: Interpret and Compute the Principle of working of various types of sensors and transducers and their applications.
- CO3: Analyze the principles of Electrical systems, Mechanical switches, solid-state switches, solenoids, DC & AC motors, Stepper motors, amplifiers, protection, multiplexers
- CO4: Discuss the concepts of Evolution and describe the Organization of Microprocessors and basic concepts of programming of microprocessors

2.2 Mapping of CO with PO

Table 1: Mapping of CO with PO

	PO1	PO2	PO3	PO4	PO5	PO6	PO7	PO8	PO9	PO10	PO11	PO12
CO1	2	2	1									
CO2	3	2	3		3				3	3		
CO3	2	2	1									
CO4		1										
Average	2.33	1.75	1.66									

The course coordinator has to Map to course outcomes to program outcomes. It enables them to identify the curricular gap in the course. The content beyond the syllabus is planned delivered to the students through teaching, arranging guest lectures with demo and hands-on which is highlighted in the table in blue colour. Program level CO-PO matrix for all the courses including first-year courses will be done by the program coordinator [6]

2.3 CO-PO Mapping explanation

The table shows weight given by the course coordinator for different Program outcome

Table 2: CO-PO Mapping explanation

	PO-1	PO-2	PO-3
CO1	Co1 is mapped with po1 with a value of 2 as it enables students to apply basic fundamental knowledge of measurements. The students should have strong fundamentals of basics	Co1 is mapped with po2 with a value of 2 as it enables students to apply knowledge appropriate selection, specification, installation, maintenance mechatronics system	Co1 is mapped with po1 with a value of 1 as it enables students to incorporate the ideas in project-based learning i.e. to develop small models for society
CO2	Co2 is mapped with po1 with a value of 3 as it enables students to apply basic fundamental knowledge of basic electronic components. The students should have strong fundamentals of basics	Co2 is mapped with po2 with a value of 3 as it enables students to apply knowledge appropriate selection, specification, installation, maintenance sensors and transducers	Co2 is mapped with po1 with a value of 3 as it enables students to incorporate the ideas in project-based learning i.e. to develop small models for society and sensors are an important component of any mechatronics system
CO3	Co3 is mapped with po1 with a value of 2 as it enables students to apply basic fundamental knowledge of measurements. The students should have strong fundamentals of basics	Co3 is mapped with po2 with a value of 2 as it enables students to apply knowledge appropriate selection, specification, installation, maintenance of dc motors ac motors switches and stepper motors	Co3 is mapped with po1 with a value of 1 as it enables students to incorporate the ideas in project-based learning i.e. to develop small models for society
CO4		Co4 is mapped with po2 with a value of 1 as it enables students to apply knowledge of the basic working of a microprocessor and needs in installation, maintenance mechatronics system	

2.4 Mapping the Gap

To map the gap of peer to peer learning i.e PO 9, modern tool usage i.e. PO5 and combination i.e PO 10, the course coordinator organised a Hands-on “Advances in Mechatronics” by Mr Venugopal, Managing director of Vijay Automation for the sixth semester students on 3/3/17 as shown in figure 1. The speaker enhanced knowledge of the students on the various application of sensors and encoders through videos and kit to map PO 5. This practical demonstration and hands-on i.e PO 4 and PO 5 helped students to understand the subject in a better perspective. The advantages and applications of relays, sensors and encoders were highlighted to students.[7]



Fig. 1: Mr. Venugopal explaining key components of Mechatronics

2.5 Assessment and attainment

Students have to appear for internal examinations as per Visvesvaraya Technological University norms. All internal tests are conducted in the dates in adherence to the academic calendar. Three tests are scheduled every semester and an average of the best two tests will be considered for finalizing the internal marks. A centralized process is used for conduction of tests. The course coordinator sets the question paper following the Blooms Taxonomy. The Module coordinator checks the question paper for quality and Blooms taxonomy levels. Then the Programme Assessment committee asses for the levels of learning and for their CO/PO mapping. Approved papers are sent to the internal exam coordinator for the conduction of the test. Table 1 shows the details of the batch, course and course code, semester and course coordinator details and the attainment of students with respect to Course outcomes attained in three different tests.

And the attainment level is taken as follows:

- Attainment level 1: 50% of students scoring more than 60% marks
- Attainment level 2: 55% of students scoring more than 60% marks
- Attainment level 3: 60% of students scoring more than 60% marks

Further to show that the OBE has enhance the students learning perspective I have considered the previous batch students to show that 2014 have performed well in their assessment when compared to the students in 2013 batch Table 2 shows the details of the batch, course and course code, semester and course coordinator details and the attainment of students with respect to Course outcomes attained in three different test [1][2]

Table 1 shows the details of the 2014 batch, course and course code, semester and course coordinator details and the attainment of students with respect to Course outcomes attained in three different tests

Table 1: Details of the 2014 batch

Batch (Year)	2014			
Course Name	Mechatronics and Microprocessor			
Course Code	10ME65			
Semester	VI			
Name of the Faculty	Nithya Poornima			
Percentage of students scoring > 60% of Marks (For internal assessment)				
	CO1	CO2	CO3	CO4
Number of Students Scored above 60% of Marks	32.00	28.00	37.00	44.00
Number of Students attempted the test	44.00	45.00	48.00	71.00
% Of students	72.73	62.22	77.08	61.97
Attainment Level	3	2	3	3

Table 2 shows the details of the 2013 batch, course and course code, semester and course coordinator details and the attainment of students with respect to Course outcomes attained in three different tests

Table 2: Details of the 2013 batch

Batch (Year)	2013			
Course Name	Mechatronics			
Course Code	10ME65			
Semester	VI			
Name of the Faculty	Nithya Poornima			
Percentage of students scoring > 60% of Marks (For internal assessment)				
	CO1	CO2	CO3	CO4
Number of Students Scored above 60% of Marks	48.00	25.00	29.00	35.00
Number of Students attempted the test	71.00	71.00	71.00	71.00
% Of students	67.61	35.211	40.845	49.30
Attainment Level	2			1

Table 3: shows students comparison of 2013 and 2014 batch

Batch	2014	2013	2014	2013	2014	2013	2014	2013
Course outcomes	CO1	CO1	CO2	CO2	CO3	CO3	CO4	CO4
Number of students scored above 60% of marks	32	48	28	25	37	29	44	35
Number of Students attempted the test	44	71	45	71	48	71	71	71
% of students	72.73	67.61	62.22	35.211	77.08	40.845	61.97	49.3
Attainment level	3	2	2		3		3	1

Table 3 shows the comparison of students' performance of 2013 and 2014 batch. The course was delivered by the same course coordinator, but the response by the students in the performance in the test is observed in the table. The course coordinator did not conduct any OBE activities for the 2013 batch, by the end of the semester and analysis was made considering the test marks. The result showed that they were only showing average performance. But when the same coordinator delivered the classes for 2014 batch with OBE activities have shown enormous interest in the subject and definitely, the attainment levels have improved

drastically. This table 3 shows the comparison of students' performance of 2013 and 2014 batch for the same syllabus. and the graph for the same is shown below in figure 2.

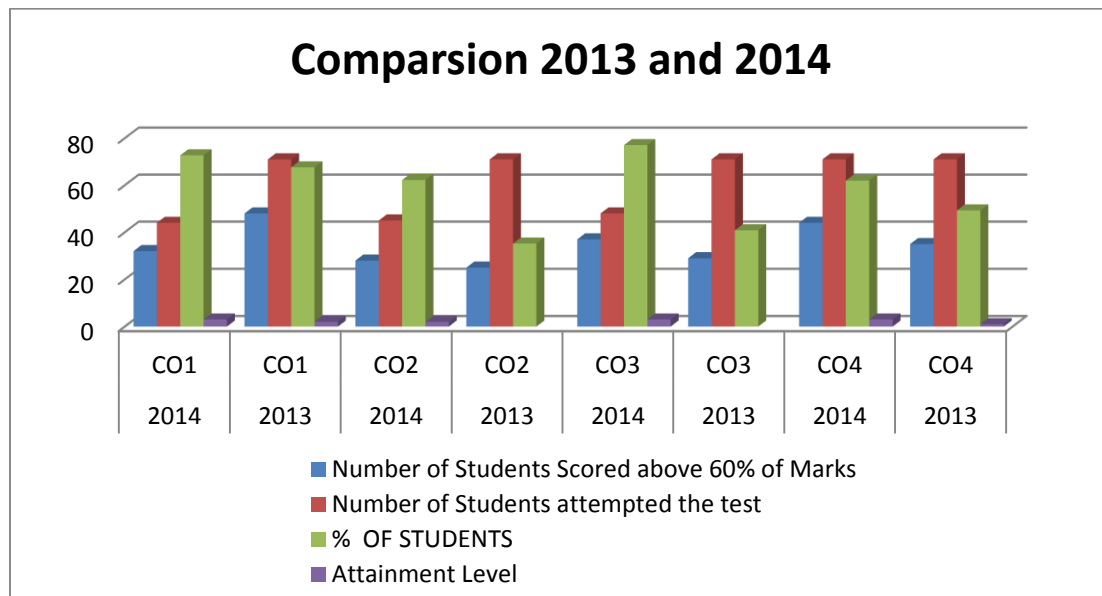


Fig. 2: Comparison of 2013 and 2014 batch

3. CONCLUSION

To achieve this new vision, teaching and learning for students need to change with professional learning opportunities. Learning and teaching in a traditional way needs to change so as to reform the technical education that has emphasized the need for all students to learn significant disciplinary core ideas, coupled with scientific and engineering practices with case studies Demonstration and hands on. Outcome-based education does offer many powerful ideas, such as a commitment to learning for all students, possibilities for authentic assessment, and interest in an integrated curriculum. This has motivated a great interest in students in understanding and perceiving concepts in a better way

4. REFERENCES

- [1] <http://www.nba.com/news/nba-register-and-nbaguide>.
- [2] <http://www.nbaind.org/files/obe-and-nbaaccreditation.pdf>
- [3] Kavitha, A, Immanuel Arokia James, K, Harish, KA., and Rajamani. V., "An Empirical Study
- [4] Assessment and Attainment Method of Course Outcome and Programme Outcome for NBA
- [5] Tier II Accreditation in Engineering Colleges through Outcome-Based Education (OBE)", Special issue on Green Computing and Networking in International Journal of Pure Applied Mathematics, Academic Publications Ltd., Bulgaria, Vol 117, No 22, pp. 25-28, Dec" 2017, pISSN 1311-8080.
- [6] Surendar Rawat, Shruti Karkare, "An Empirical Study on Assessment of CO attainment for a Diploma Course", IJECET, vol 6, no.2, pp. 06-12, 2015.
- [7] Surendar Rawat, Shruti Karkare, "An Empirical study on Assessment of PO Attainment for a Diploma program", IJARET, vol 6, no 11, pp. 50-58, 2015.
- [8] Geeta Deswal, Kumar Gaurav, Ashwani Dhingra, Priyanka Kriplani, Bhawna Chopra and Rameshwar Dass, "Assessment Method for Course Outcomes and Program Outcome", vol 2, no3, pp.58-68, Academica Editores: ActaVelit, 2016.
- [9] Zamri Mohamed, Mohd YusofTaib, M.S. Reza, "Assessment Method for Course Outcome and Program Outcome in Outcome Based Education (OBE)", Proc. Of Malaysian Technical Universities Conference on Engineering and Technology, 2010.
- [10] PritiKudal, Vishakha Pawar, Deepika Thakare, Bhakti Nandurdikar, "A Tool for Course Outcome Attainment", International Journal of Technical Research and Applications, vol 5, no 1, pp: 38-42, 2017.
- [11] Bhimasen Soragaon and Mahesh K S, "Measuring Attainment of Course Outcomes and Program Outcomes – A Simplified Approach as per Self-Assessment Report- June 2015", IOSR Journal of Research & Method in Education, vol 6, no 4, pp: 13-18,2016.
- [12] Abhishek Koshti, Durvesh Kadole, Navnath Kamble, Pushkar Gadgil, Laxmi Bewoor, "Knowledge Based Tool for PO Attainment", Special issue on Int. Journal of Research in Advent Technology, pp: 122-126, 2016.
- [13] Dr. Rita Jain, Dr. A. A. Ansari, "A Simplified approach to measure Course Outcomes and Program Outcomes for Accreditation of Engineering Institutes, Int. Journal of Electrical and Electronics Engineers".

APPENDIX

CO: Course Outcomes
 PO: Program Outcomes
 NBA: National Board of accreditation

See discussions, stats, and author profiles for this publication at: <https://www.researchgate.net/publication/330411207>

Heat Transfer Enhancement in a High Power LED Using Heat Sink with Liquid Pockets

Article in *Journal of scientific and industrial research* · October 2018

CITATIONS

0

READS

53

5 authors, including:



Sangmesh Bm

BMS Institute of Technology and Management

9 PUBLICATIONS 1 CITATION

SEE PROFILE

Some of the authors of this publication are also working on these related projects:



Heat Transfer Enhancement in a High Power LED using Heat Sink with Liquid Pockets [View project](#)

Short Communication

Heat Transfer Enhancement in a High Power LED Using Heat Sink with Liquid Pockets

B Sangmesh^{1,2*}, K Gopalakrishna¹, S H Manjunath³, M N Kumar¹ and G V kumar¹,

¹Centre for Incubation, Innovation, Research and Consultancy, Jyothy Institute of Technology, Bangalore, Karnataka, India

²Visvesvaraya Technological University, Jnana Sangama, Belagavi, Karnataka, India

³School of Mechanical Engineering, Reva University, Bangalore, Karnataka, India

*Received 20 June 2017; revised 16 May 2018;
accepted 23 April 2018*

This study presents an experimental investigation on two types of heat sinks, a novel Heat sink with liquid pockets (HSLP) and the other one being conventional heat sink. The heat transfer characteristics of the HSLP were investigated experimentally using passive cooling method. For this purpose, an experimental setup was built by drilling longitudinal holes in the base of heat sink. The holes were filled with De-ionized (DI) water to enhance heat transfer in high-power LED COBs. The junction temperature of the LED was measured, to measure increased heat transfer. The thermal performance of aluminium heat sink with liquid pockets was studied with parameters such as fill ratio, influence of liquid cooling and orientation effect. The performance of the HSLP was found to be better than conventional heat sink of same geometry due to its lower thermal resistance. The HSLP performs better than the conventional heat sink for 15° orientation, 100 vol. % with De-ionized water. Fluid channels filled with liquid in the heat sink have a noticeable effect on heat removal rate.

Keywords: De-ionized Water, HSLP, LED, Heat Sink

Introduction

Thermal management of LED module is a key design parameter as increase in temperature directly affects its life span. The maximum light output, quality, reliability and the life span of LEDs are all closely related to the junction temperature¹. Thus, thermal management has become a key reliability factor for LED modules for which various solutions are being proposed². Different cooling methods can be used to reduce the temperature of LED: a simple one being the use of heat sink. Heat sinks are essential for dissipation of heat and various types of heat sinks are employed

either active or passive in nature. Hongjun³ conducted an experimental investigation by introducing copper heat sink which was directly bonded with the alumina substrate by Zn-Al filler with an ultrasonic-assisted bonding method. Abouali⁴ presented a numerical investigation on rectangular and arc shape grooves employing micro channel in the heat sink. The results depict that the arc grooves to be better in comparison with rectangular grooves. R Thanigaivelan⁵ employed three different materials for fabrication of micro fin array. The result indicated improvement in the overall thermal resistance for copper micro fin array.

Experimental methodology

From the literature it is found that numerous studies have been undertaken on fin geometries, forced convection and heat sink with micro channels. However studies on heat sink with liquid as a means of passive cooling has not been reported in the literature. Thus, the present investigation involves experimental study of the heat transfer characteristics of a heat sink with liquid pockets (HSLP) filled with De-ionized water as the coolant and subjected to natural convection. The performance of the HSLP is compared with the conventional heat sink without the liquid pockets. This study explores the use of passive cooling using De-ionized water as the coolant for removal of heat and evaluates its performance with that obtained using conventional heat sink. In the current investigation heat sinks with liquid pockets (HSLP), fins parallel and rectangular in nature with multiple holes in the base were fabricated. The holes were filled with De-ionized water for effective heat dissipation at the LED junction. The fabricated novel HSLP was used for cooling high-power LED COBs.

The aluminium heat sinks of dimension 200mm×120 mm × 20mm have aluminum rectangular fins for a length of 100mm. The fluid pockets were filled with De-ionized water for different fill ratios. The typical aluminum heat sink used in the current study to suit the actual street light application The LEDs chosen for this study were 100 W COB LEDs and fixed to a MCPCB substrate located on the HSLP. The current and voltage were set so as to result in a constant power input of 100W (CREE Make- X lamp XP-G). A

*Author for Correspondence
E-mail: sangmesh.sangu293@gmail.com

Thermal interface material was used to establish good surface contact between the LED and the heat sink. The hotspots were identified with the use of infrared thermal camera and a thermocouple was located at the hotspot where the LED experienced maximum temperature. T-Type thermocouples were used to measure the junction temperature. A data acquisition system (TRACER make) with a resolution of 10^{-5} °C was used to map the junction temperature of the LED with a sampling rate of 1/s. De-ionized water was used in the pockets of the HSLP and the heat transfer rate was determined for different liquid fill ratios of 25%, 50%, 75%, and 100%. The effect of different orientations (tilt angle) of the LED in line with the street light was also studied. The experiments were conducted for both steady state and transient conditions for a period of 90min. Steady state was attained at the end of 60 minutes of experimentation. Figure 1 shows the experimental setup of the current study. Comparison of the HSLP performance was undertaken with a conventional heat sink of same geometry. Variation of temperature as a function of power input has been recorded. All experiments were conducted under open environment condition to match with practical application of the prototype and the data presented are the average of five tests each.

Results and Discussion

Based on the magnitude of heat dissipation, a novel cooling HSLP system was proposed. The HSLP was designed in such a way that, the circulation of De-ionized water in the HSLP takes place due rise in temperature, capillary and gravity effect. De-ionized water is employed as the coolant inside the liquid pockets to enhance heat removal from the LED junction. In this work the liquid pockets were filled with De-ionized water in vol. % basis for different fill ratios. The heat dissipation capability of liquid pockets was determined for different orientations to study the influence of gravity. The experiments were conducted for 90 minutes to study both steady and transient heat transfer.

Effect of orientation on junction temperature

The LED COBs were placed on the HSLP and positioned at varying tilt angle to determine the influence of gravity effect on heat transfer rate. The heat transfer characteristics in terms of gravity

effect for four different orientations were analyzed. It was observed that the junction temperature increases with increase in power supplied for time duration of 60 min and then reached the steady state. It is evident from the Figure 2 that there is a reduction in junction temperature for an inclination of 15° in comparison to other orientations. The De-ionized water in the liquid pockets which is in contact with heated surface tends to flow upwards against gravity due to reduction in density affected by rise in temperature. The inclination of the heat sink facilitated the reverse flow as the fluid gets condensed because of fins provided in the heat sink. It is clearly seen from the Figure 2 that 15° to the horizontal is the optimum orientation. Higher inclinations tend to restrict the upward flow against gravity leading to decrease in the heat transfer rate. However at 0° the circulation might not be as positive as it is at 15° due to an air surface above the entire water surface.

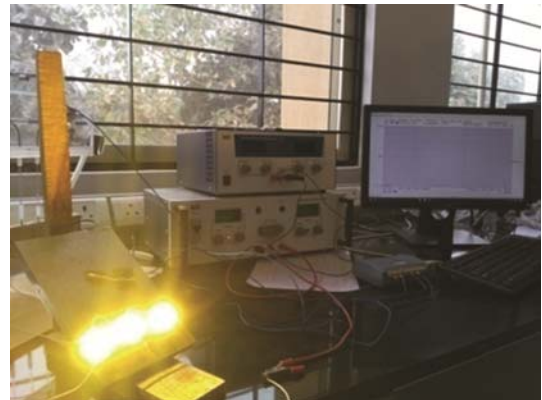


Fig. 1 — Experimental Setup

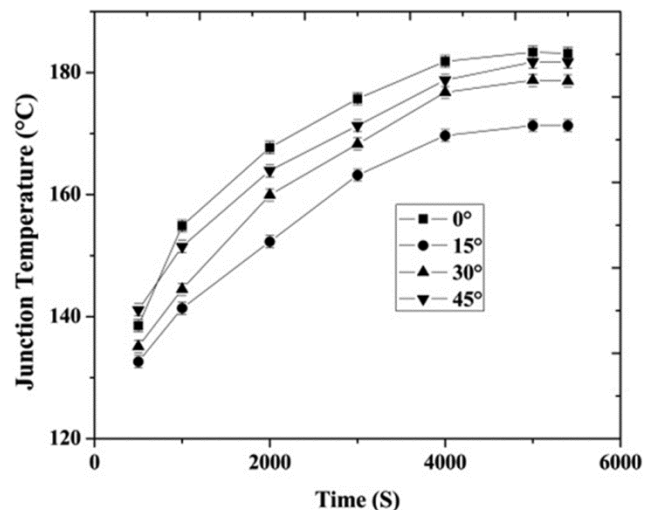


Fig. 2 — Influence of orientation effect on junction temperature

Effect of fill ratio on junction temperature

Here we report the effect of varying fill ratio on heat dissipation as shown in Figure 3. Liquid cooling was used to enhance the overall performance of the system. The heat sink with De-ionized water was tested for different fill ratios of 25%, 50%, 75%, and 100%. The results revealed a positive effect for 100% fill ratio of fluid compared to other fill ratios. When the volume of liquid increases the heat dissipation from the junction increased because of its ability to conduct heat. The measured data indicated that the junction temperature of LED decreased with increasing rate of fluid. This observation proposes that higher vol. % of liquid results in faster heat dissipation. Hence liquid cooling can be employed for cooling LED.

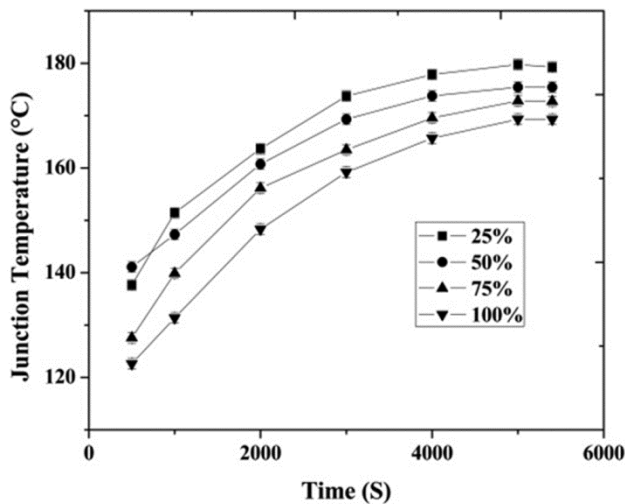


Fig. 3 — Variation of Temperature for different fill ratio

Table 1 — Variation of junction temperature with time for different heat sinks

Time in Sec	Junction Temperature in °C	
	Conventional Heat Sink	HSLP
500	159.35	122.62
1000	167.73	131.38
2000	176.06	148.30
3000	181.50	159.20
4000	185.56	165.70
5000	187.47	169.31
5400	187.80	169.30

Table 2 — Thermal resistance of the HSLP

% Volume of fluid	Thermal Resistance in °C/W
0.25	1.47462
0.5	1.43642
0.75	1.40917
1.0	1.37501

Effect of fluid on junction temperature

Under the same operating conditions, HSLP gave better thermal performance than that of the conventional heat sink as shown in Table 1. This may be attributed to the large thermo physical property of cooling fluids resulting in lower junction temperature. The De-ionized water normally has very high adhesion properties. The stagnant layer of water conducts the heat for the liquid to continue with convective heat transfer. Variation in density of water due to heating and cooling cycles would also support rapid heat transfer. Based on the results obtained in this study, De-ionized may be used as heat transfer fluid for passive heat transfer in electronic device cooling applications.

Overall thermal resistance

Thermal resistance of liquid cooling system was analyzed to predict thermal behavior of the heat sink with liquid pockets. The study revealed that for a HSLP, improved performance was obtained by adapting liquid cooling using De-ionized water as the coolant in comparison with conventional heat sink. Reduction in thermal resistance reduces the junction temperature. The results depict that the increase in the volume of fluid results in decrease in the overall thermal resistance and an increase in the thermal dissipation as shown in Table 2.

Conclusions

In this study, thermal performance of a novel heat sink HSLP for passive heat transfer characteristics is presented. The heat transfer characteristics of HSLP is evaluated in terms of liquid pockets, fill ratio and orientation. De-ionized water was used as the heat transfer fluid for cooling in the liquid pockets to enhance heat removal from the LED junction. The junction temperature reported by HSLP with 100 vol. % and 15° orientation is less than the conventional heat sink by atleast 20%. The physics behind such behavior would be the variation in density coupled with gravity and the properties of the heat transfer fluid. Larger the volume of liquid used in HSLP faster is the heat dissipation. The addition of liquid cooling will enhance the heat conduction & convection because of uniform heat distribution across the liquid pocket. Based on the experiments and results it may be concluded that, water pockets in heat sink can be employed for LED cooling applications.

References

- 1 Narendran N, Gu Y., Freyssinier J.P., Yu H. & Deng L., Solid State Lighting Failure Analysis of White LED, *J crys gro*, **268** (2004), 449-456.
- 2 Sangmesh, Gopalakrishna Keshava Narayana, Manjunath Shiraganhalli Honnaiah, Krishna Venkatesh & Keertishekar Mysore Siddalingappa, Thermal Performance of Heat Sink with Fluid Pockets for High Power Light Emitting Diode, *Int J Auto and Mech Eng*, **14**(4) (2017) 4846-4862.
- 3 Hongjun Ji, Xiao Cheng, Hao Chen, Mingyu Li & Qingtao Li, Direct Bonding of Alumina Substrate with Copper Heat Sink in Air Assisted by Ultrasonic Vibrations for High Power LED Devices, *4th Int Conf on Electro Pack Tech*, (2013) 1158-1161.
- 4 Abouali O & Baghernezhad N, Numerical Investigation of Heat Transfer Enhancement in a Microchannel with Grooved Surfaces, *J Heat Trans*, **132** (8) (2010).
- 5 R Thanigaivelan, D Deepa, T Mythili and R M Arunachalam, Experimental Investigation of Natural Convective Heat Transfer around Micro-Fin array, *J Sci Ind Res* **76** (2017) 501-505.



Mechanical and Wear behaviour of Al6061 reinforced with Graphite and TiC Hybrid MMC's

Gowrishankar T P, Manjunatha L H & Sangmesh B

To cite this article: Gowrishankar T P, Manjunatha L H & Sangmesh B (2019): Mechanical and Wear behaviour of Al6061 reinforced with Graphite and TiC Hybrid MMC's, Materials Research Innovations, DOI: [10.1080/14328917.2019.1628497](https://doi.org/10.1080/14328917.2019.1628497)

To link to this article: <https://doi.org/10.1080/14328917.2019.1628497>



Published online: 11 Jun 2019.



Submit your article to this journal [↗](#)



Article views: 15




View related articles [↗](#)



View Crossmark data [↗](#)



Mechanical and Wear behaviour of Al6061 reinforced with Graphite and TiC Hybrid MMC's

Gowrishankar T P ^a, Manjunatha L H^b and Sangmesh B^c

^aDepartment of Mechanical Engineering, R L Jalappa Institute of Technology, Doddaballapur, Karnataka, India; ^bSchool of Mechanical Engineering, Reva University, Bangalore, Karnataka, India; ^cDepartment of Mechanical Engineering, BMS Institute of Technology & Management, Bangalore, Karnataka, India

ABSTRACT

Aluminium (Al6061) with Graphite (Gr) and Titanium Carbide (TiC) particles of different configurations have been prepared using stir casting method. The development of aluminium with Gr and TiC composites has been confirmed with Energy Dispersive Spectrometer (EDS) tests. Scanning Electron Microscope (SEM) study has been performed to identify the configuration of the composite material. In the current work, an attempt is made to study the mechanical and tribological behaviour of Al6061 reinforced with 5wt% Gr for different fraction of TiC hybrid composites. The addition of Gr was maintained constant and equal to 5 wt.% throughout the experiment. TiC was varied from 0% to 8 wt. % in a step of 2%. The effect of addition of Gr and TiC on microstructure, micro hardness, tensile strength, wear resistance were investigated. The results showed that aluminium reinforced with Gr and TiC exhibited better mechanical and tribological properties of composites.

ARTICLE HISTORY

Received 15 March 2019
Accepted 30 May 2019

KEYWORDS

Al6061; TiC; stir casting; SEM

Introduction

Particle-reinforced aluminium metal matrix composites are nowadays replaced by the conventional materials in several fields of engineering because of its low density, light weight, high strength and good wear resistance properties [1]. Aluminium, copper, magnesium, titanium, zinc and their alloys are the commonly used matrices for the development of MMCs. The type, shape, size and weight fraction of the reinforcement are the factors influencing the properties of these MMCs [2]. There are several series of aluminium alloys are available and Al6061 is one among them, which is a popular choice for developing MMCs due to their machinability, corrosion resistance, good weldability and other favourable mechanical and tribological properties. The most popular reinforcement with Al6061 includes ceramic particles like Zirconia, alumina, silicon carbide, Gr etc that would result in enhancement of mechanical properties of composites. These particulates increase the strength and tribological properties of Al6061 [3]. There are different manufacturing techniques to develop MMCs such as powder metallurgy, vacuum casting, stir casting, squeeze casting, compo casting etc. to accomplish composites with different reinforcement. Among them, the stir casting technique is the most popular casting technique widely used in the industry due to its ease and low cost method compared to others [4,5]. Some of the study reports that there is an enhancement in hardness and tensile strength of the composites by adding titanium carbide (TiC) as reinforcement. Gr is good reinforcing agent to enhance the strength of the composites by reducing the weight of the composites as it has less density [6–9]. Due to its low CTE and wear resistant property, Gr is used in many applications including piston, cylinders, brake discs etc.

A very few investigations have been carried out by using Gr and TiC particulates as a reinforcement to Al6061 material,

therefore, the present investigation focused on addition of Gr and TiC particulates as a reinforcement to Al6061 material with the use of stir casting method. Hence, in present work an attempt is made to develop a hybrid MMC with Gr and TiC composition and tested for their mechanical properties. Al6061 is added with 5 wt.% of Gr and 0–8 wt.% TiC in a step of 2 wt.%, and its mechanical properties were examined.

Methods and materials

The hybrid MMCs containing Al6061, 5 wt.% of Gr and TiC (0–8 wt.%) was prepared with the help of stir casting method. The prepared composite material was machined in CNC to carryout different tests. The prepared composite was examined for microstructure study to identify the distribution of reinforcement particles in matrix alloy. Mechanical properties such as hardness, tensile tests were evaluated. In addition, Scanning Electron Microscope (SEM) Energy Dispersive Spectrometer (EDS) tests have been performed to identify the configuration of the composite. The tests results were compared with the matrix alloy of Al6061 to validate the experimentation. In this work, Al6061 was selected as a matrix material, and its chemical composition is shown in Table 1. Gr particles of size 35–45 μm and TiC particulates of size 45–55 μm were used as reinforcement. The Gr of 5wt% composition was maintained same throughout the experimentation whereas TiC is varied from 0 wt.% to 8 wt.% in a step of 2 wt.%.

Initially, a known quantity of aluminium alloy rods was placed into the Gr crucible and was melted at 850°C in an electric furnace. A stirring process was performed to obtain uniform distribution of reinforcement materials. A fine vortex is created by using a mechanical stirrer by stirring a melt for 10 min [10]. The mixture of Gr and TiC was preheated to 700°C in a separate furnace to increase the wettability. The preheated

Table 1. Chemical composition of Al6061.

Elements	Si	Fe	Cu	Mn	Zn	Ti	Mg	Cr	Al
Percentage	0.58	0.106	0.275	0.0014	0.25	0.13	1.15	0.201	Balance

Table 2. Composites of different composition used in present work.

Sample A	Al6061
Sample B	Al6061 + 5% Gr
Sample C	Al6061 + 5% Gr+2%TiC
Sample D	Al6061 + 5% Gr+4%TiC
Sample E	Al6061 + 5% Gr+6%TiC
Sample F	Al6061 + 5% Gr+8%TiC

mixture of Gr and TiC was poured into a furnace containing molten metal of Al6061. A constant feed rate was maintained while adding the material. The stirring action was performed with the help of electric stirrer at a speed of 450 rpm. The molten metal was taken out from the crucible and poured into a mould cavity to solidify at atmospheric temperature. The process of fabrication was repeated for different weight fraction of TiC (2,4,6 and 8wt%) in the hybrid MMCs. The different configurations of composites are shown in Table 2.

Testing of composites

The machining of composite material was performed to prepare the sample specimens to study the micro structural, mechanical properties. Composites with different specifications were machined as per the requirement of test rig. Microstructure study was performed using Scanning electron microscopy (SEM) (Model: Hitachi-Su) to examine the distribution of reinforcement particles in composites material. A conventional metallographic procedure was adopted to polish the specimens for the microstructural study. Keller's reagent was used to etch the polished surfaces. Micro-hardness of the composites was examined using Micro Vicker's hardness tester for a load of 500 gm and a dwell period of 15 seconds.

Ultimate Tensile Strength (UTS) and Yield strength was measured using electronic tensometer (ER-3 Model) having a maximum capacity of 20KN. The tensile and yield strength of the specimens was measured as per the ASTM E8 standards. The specimens were tested for wear study using computerised pin on disc apparatus as shown in Figure 1.

Wear rate and coefficient of friction is measured for three different loads (20N, 40N, 60N) and speeds (100, 150, 200 rpm) at constant sliding distance of 1000 m by loading a stationary pin of 30 mm length and 8 mm diameter in size against a rotating steel disc under ASTM G99-05 standard. Figure 2 shows the specimens used for current research.

**Figure 1.** Wear Test machine and SEM apparatus.**Figure 2.** Specimens used for Hardness, Tensile and Wear test.

Results and discussions

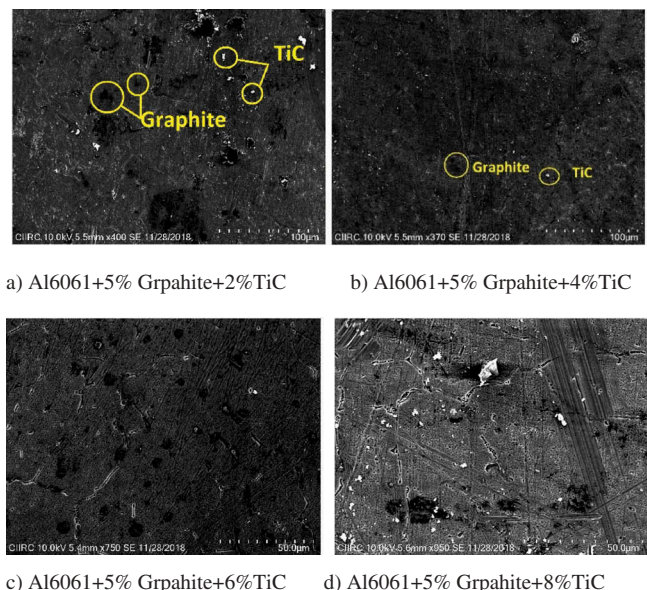
Microstructure study

In present work, an Al6061 reinforced with micro size Gr and varying TiC particles were used in the MMCs. A morphological study was carried out to analyse the distribution of reinforcement material by using SEM. Figure 3 shows the microphotographs of Al/5%Gr with 2 wt.%, 4 wt.%, 6 wt.% and 8 wt.% TiC, respectively. Figure 3 (a-d) reveals proper distribution of Gr and TiC particulates in Al6061 matrix. A homogeneous distribution of reinforced materials is observed in the SEM images. The distribution of particles may have obtained due to Vortex effect caused while stir casting. Also, Mg element present in the Al6061 alloy influences the uniform distribution of Gr particulates in matrix material [11].

Figure 4 shows EDS spectrum of hybrid composites to identify the presence of elements in the hybrid composites. The graphite and TiC in the form of C and Ti elements were seen in the EDS spectrum along with the high intensity peak of Al6061. This authenticated that the proposed composite includes all elements anticipated in the study.

Hardness measurements

The hardness test was measured with the help of Vicker hardness test. Figure 5 shows the variation of hardness with the addition of Gr and TiC to the matrix alloy. An addition of Gr into the matrix alloy would result in reduction in the hardness by significant amount in comparison with matrix alloy due to soft and slippery nature of Gr. Being a soft dispersoid, Gr does not contribute for the enhancement of hardness [12,13]. Being efficient solid lubricant Gr eases the

**Figure 3.** (a-d): Micrographs of Al6061 reinforced with graphite and TiC hybrid Metal Matrix Composites.

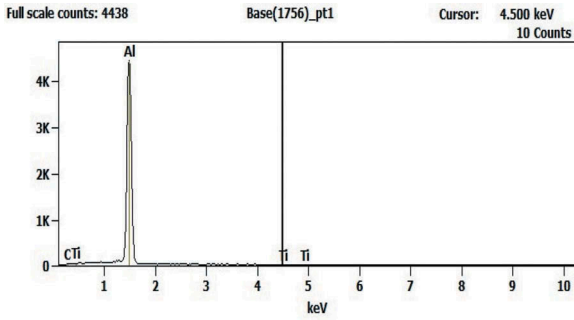


Figure 4. EDS Spectrum of composites.

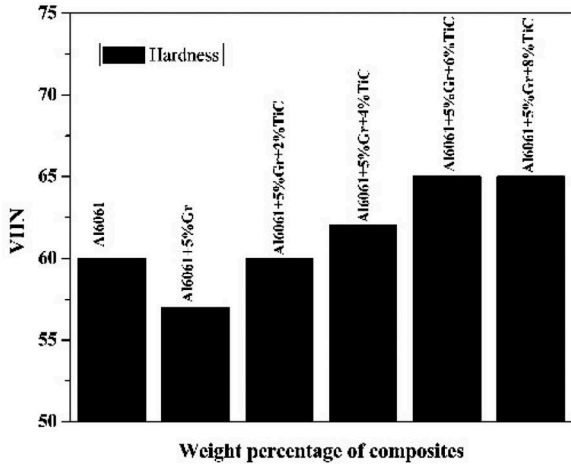


Figure 5. Variation of hardness with the addition of graphite and TiC to Al6061.

movement of grains along the slip planes, portrait the material more easily deformable under the indenter of the hardness tester. An enhanced hardness is observed when TiC is prefixed with the base alloy along with Gr. Hardness of the specimens increased with the addition of TiC from 2 wt.% to 8 wt.%. This is because the TiC particulates are hard in nature which improves the hardness of the composites, same trend was also observed in [14,15]. Good bonding and interface between matrix alloy and reinforcement materials results in increased hardness of composites. However, a negligible enhancement in the hardness is observed between 6 to 8 wt.% of TiC particles into the MMCs. This indicated that the enhancement of hardness at higher weight fraction of TiC particles is negligible and also previous studies shows that diminishing of hardness for higher weight fractions of TiC due to agglomeration [16].

Table 3 represents the mechanical properties such as microhardness, UTS and yield strength of tested specimens obtained for various combinations of Al6061/Gr/TiC composites.

Tensile strength

The specimens were tested for Ultimate tensile strength (UTS) and yield strength using electronic tensometer. Figure 6 shows the variation of UTS and yield strength with the addition of Gr and TiC particulates. The results are compared with the matrix alloy. The addition of 5 wt.% Gr to Al6061 enhances the UTS and yield strength of the

Table 3. Mechanical properties of composites for various combinations of Al6061, Gr and TiC.

Composite Specimen	VHN	Yield Strength (Mpa)	UTS (Mpa)
Al6061	60	87.24	133
Al6061 + 5%Gr	57	93.19	147
Al6061 + 5%Gr+2%TiC	60	93.92	164
Al6061 + 5%Gr+4%TiC	62	115.19	183
Al6061 + 5%Gr+6%TiC	65	101.13	141
Al6061 + 5%Gr+8%TiC	65	91.53	130

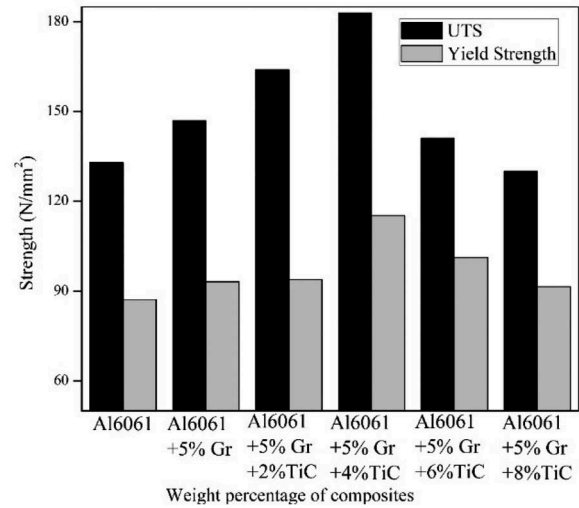


Figure 6. UTS and Yield strength of composites with the addition of graphite and TiC to Al6061.

alloy. This may be due to the presence of Gr which act as a barrier to dislocation in microstructure. This type of results is also reported by [6,7]. UTS and Yield strength of composites increases with the addition of TiC particulates to Al/5%Gr up to 4 wt.%. UTS and yield strength of the composites increase upto 37.5% and 32%, respectively, for the addition of 4 wt.% TiC to Al/5%Gr, and this is due to hard TiC particles share strength to the soft aluminium matrix and results in better resistance against applied tensile load [7,15]. A negative trend in the strength is produced for increasing wt% of TiC, and this tends to decrease the strength of the composites after 4 wt.%. This may be due to brittle nature of reinforcing particles, and this plays a vital role in decreasing the strength of composites. Increasing wt.% of TiC after 4% negatively affects and decreases the strength of composites.

The fractured surfaces are studied through SEM and shown in Figure 7 (a-f) of different specimens. The investigation of fractured surface conducted on fracture toughness specimens shows a dimpled fracture surface and larger voids for the unreinforced alloy in Figure 7 (a). Therefore, unreinforced alloy undergoes severe plastic deformation that indicates ductile fracture of specimen. Fracture topographies of reinforced surfaces are shown in 7 (b-f) reveals smaller dimples can be observed due to presence of Gr and TiC. Also, regions of clustered particles for reinforcement of 4 wt.% of TiC was observed results in reduction in fracture toughness of composites. Higher percentage of TiC composites shows more cleavage and coarse dimples results in brittle fracture failure. This confirms the uniform distribution of reinforcement material

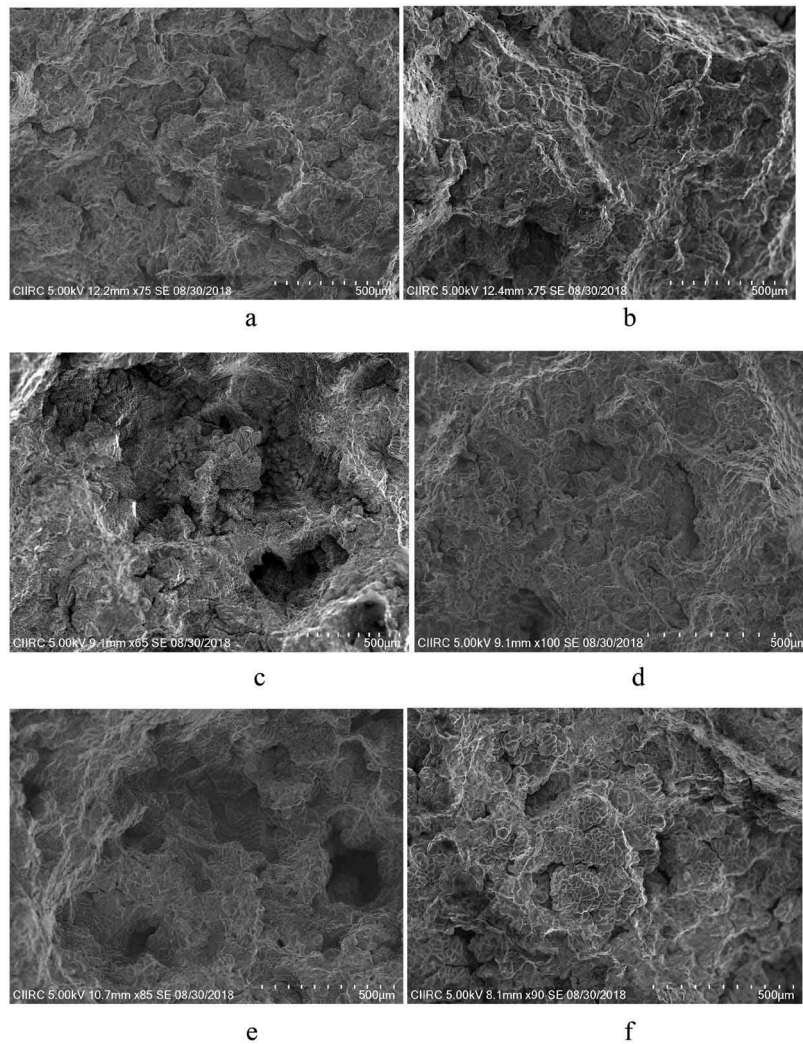


Figure 7. Tensile fractographs of the specimens (a) Al6061, (b) Al/5%Gr, (c) Al/5%Gr+2%TiC, (d) Al/5%Gr+4%TiC, (e) Al/5%Gr+6%TiC, (f) Al/5%Gr+8%TiC.

throughout matrix and a good bonding between matrix and reinforcement. This results in improved mechanical properties of composites [17,18].

Wear behaviour

Effect of load and percentage reinforcement on Wear rate

Wear rate of the specimens were measured for different load condition, sliding speeds and constant sliding speed of 1000m at room temperature. Figure 8 shows the variation of wear rate of composites for different loads of 20N, 40N and 60N. It can be seen from the result that volume loss of the matrix metal Al6061 is more compared to reinforced composites. The reduced wear rate is obtained due to the addition of Gr and hard ceramic TiC particulates. Addition of Gr forms a stable and ridiculous tiny layer on the tribo surfaces and therefore reduces the wear rate of composites. Also, it indicated that load is proportional to wear rate, as increase in load tend to increase the wear rate. Volume loss of the composites increased up to an average of 55% for a load of 60N from 20N. With the increase in load, Gr and TiC particulates squeeze out of the composites results in rupture of the surface layer. Wear resistance of the composites increased due to the incorporation of hard TiC particles and lubricating action of Gr particulates. An enhanced wear resistance is obtained upto 60%

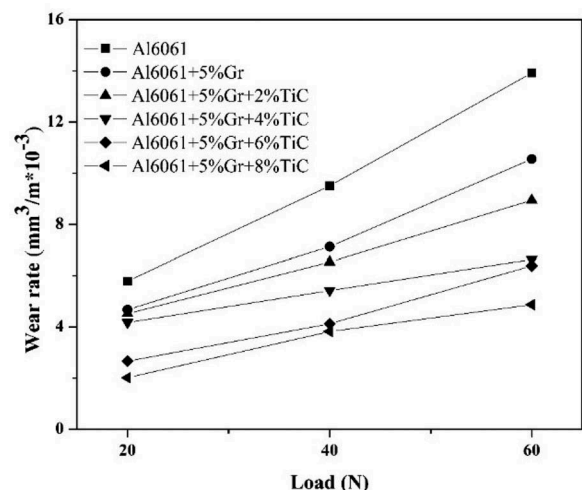


Figure 8. Effect of load on wear rate.

compared to unreinforced Al6061 alloy. The results of same kind is observed in [3,19,20].

Effect of sliding speed and percentage reinforcement on Wear rate

Wear rate of the composites was determined for different sliding speeds of 100, 150 and 200 rpm at a constant load of 40N and at constant sliding distance of 1000 m. Figure 9

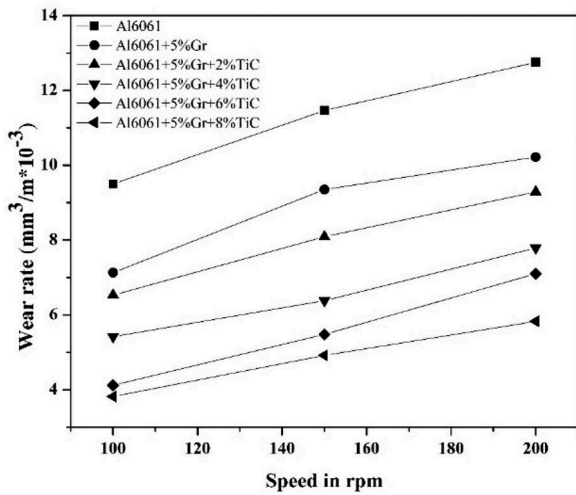


Figure 9. Effect of Sliding speed on Wear rate.

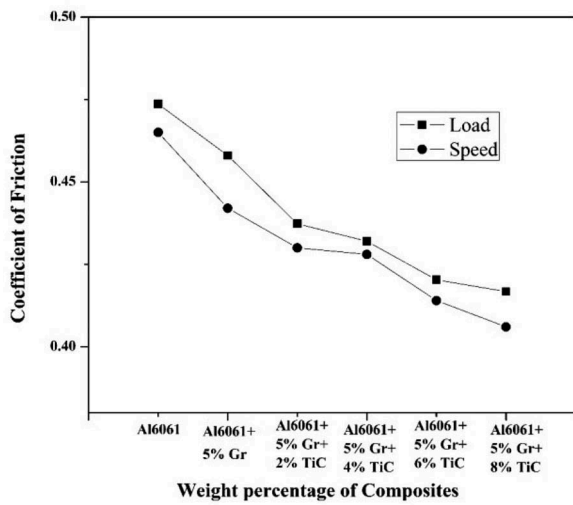


Figure 10. Coefficient of friction at different sliding speeds.

shows that the wear resistance of the composites increases with the inclusion of Gr and TiC particles. Wear rate of unreinforced alloy is more compared to reinforced composites. From the Figure 9 it is seen that the wear rate is increased for increase in sliding speed. This behaviour was in similar line with [3,21-22]. Wear rate increased upto an average of 30% from sliding speed of 100 rpm to 200rpm. Due to higher velocities, temperature of sliding surface increases and hence Gr and TiC particles squeeze out of the surface layer, and it is evident that sliding speed is proportional to wear rate. Therefore, with the increase in sliding speed material destroy rapidly due to frictional heat developed between rubbing surfaces. This shows that the wear resistance increases with the addition of Gr and hard TiC particles up to 60%.

Effect of load and speed on coefficient of friction

Figure 10 shows the average coefficient friction of composites at different loads and speeds. It is clearly shown that addition of Gr and TiC reduces the coefficient of friction for different load and speeds. Coefficient of friction of hybrid composites exhibits lower coefficient of friction compared to unreinforced Al6061 alloy irrespective of load and speed conditions. High rate of COF was observed for Al6061 alloy and low COF was observed for reinforced composites for all varying loads and speeds. Reduction in coefficient of friction by the addition of Gr is because of lubricating action of Gr on the surface of the composite forming a thin layer on the rubbing surface and minimises the metal-to-metal contact. This shows that the presence of Gr in the composite acts as a lubricant on the surface. Hence, it has been proved that tribological properties of the composites enhances with the addition of Gr and TiC. This type of trend was also observed in [15,23-25].

Figure 11(a-d) shows the SEM micrographs of worn out surfaces of composites under a load of 20N and sliding speed

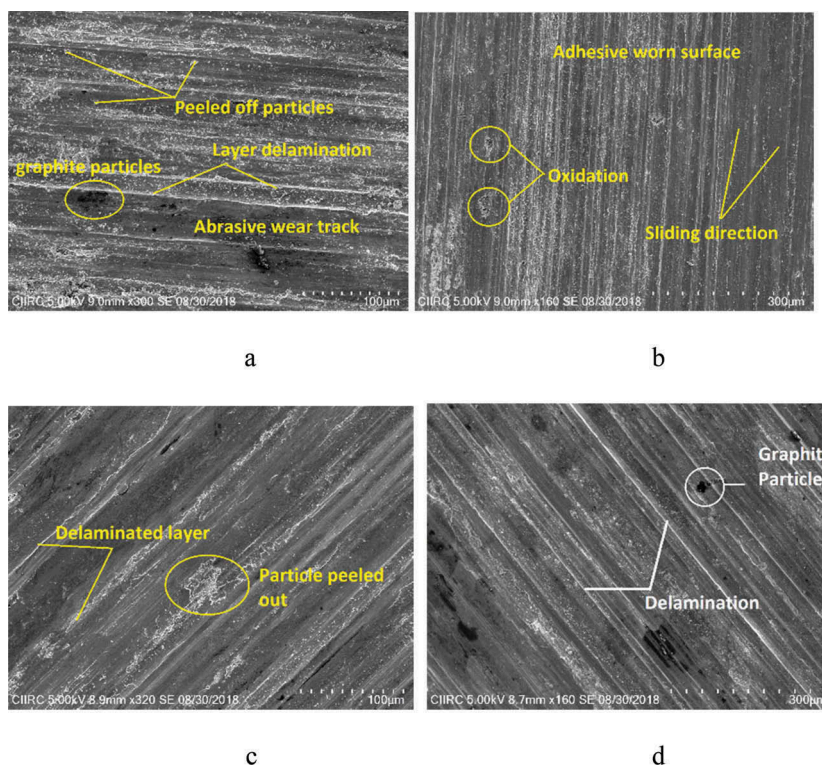


Figure 11. SEM worn out micrographs of a) Al+5%Gr+2%TiC b) Al+5%Gr+4%TiC c) Al+5%Gr+6%TiC d) Al+5%Gr+8%TiC at 20N and 100 rpm.

of 100 rpm. The oxide film and lubricating layer was formed between disc and the pin surfaces, which reduces the wear rate of the specimens. Grooves and scratches formed over the surface of the specimens were observed in all specimens, and particles were peeled off from the surface because of plastic deformation. This confirms the adhesive wear on the surfaces, also observed the same in [20,22]. Due to friction abrasion, delamination, and oxidation occurs on the surface of the specimens and particles squeeze out from the surface layer. It is evident that wear resistance of the composites increased due to the presence of Gr and hard ceramic TiC particles in the matrix material. An improved mechanical property are seen because of the presence of Gr element, which act as a lubricant agent thus improvise the properties of the material.

Conclusion

- (1) An attempt is made to study the mechanical properties of Al6061 reinforced with Gr and TiC particulates fabricated with the use of stir casting approach. Composites were prepared by addition of constant amount of Gr and different fraction rate of TiC to the aluminium alloy. Investigation of microstructure showed a uniform distribution of reinforcement particles to Al6061.
- (2) It is observed that addition of Gr alone into aluminium alloy reduces the hardness of the composite whereas an increased hardness of the composite is seen with the addition of TiC particles (2,4,6 and 8 wt.%) to Al/5%Gr.
- (3) UTS and Yield strength of composites increased upto 37.5 and 32%, respectively, for addition of 4 wt.% of TiC to Al/5%Gr and thereafter decreased due to increase in brittleness of AMCs. The fractography outcomes reveal that the increase in weight percentage of Gr and TiC particulates changes the mode of failure from ductile to brittle.
- (4) Wear resistance of the composites increased with the addition of Gr and TiC particulates into the matrix upto 60% as compared to Al6061 alloy for different test conditions. Coefficient of friction of composites decreases with the addition of Gr and TiC into Al6061 alloy irrespective of all loads and speeds. Worn out surfaces was studied using SEM and reveals that abrasion, delamination, and oxidation occur on the surface of the specimens and therefore particles squeeze out from the surface layer.

Disclosure statement

No potential conflict of interest was reported by the authors.

Notes on contributors

Gowrishankar T P is a Research scholar in VTU Belagavi. He completed his bachelors in Mechanical Engineering from KIT Tiptur and masters from SSIT Tumkur. He is currently working as a Assistant Professor in Department of Mechanical Engineering, R L Jalappa Institute of Technology, Doddaballapur. His areas of interest are heat transfer, material science.

Dr. Manjunatha L H is a professor in REVA University, Bangalore. He completed his bachelors in Mechanical Engineering from Adichunchanagiri Institute of Technology, Chikkamagaluru masters from BMS College of Engineering, Bangalore and Ph.D from VTU

Belagavi. He has more than 20 years of teaching experience. His area of interest are Composite materials, Design Engineering.

Dr. Sangmesh B is a Assistant Professor in BMS Institute of Technology, Bangalore. He completed his bachelors in Mechanical Engineering from KIT Tiptur masters from Jain University and Ph.D from VTU Belagavi. His areas of interest are heat transfer, nanotechnology, material science.

ORCID

Gowrishankar T P  <http://orcid.org/0000-0001-9432-3836>

References

- [1] Shorowordi KM, Laoui T, Haseeb ASMA, et al. Microstructure and interface characteristics of B4C, SiC and Al₂O₃ reinforced Al matrix composites: a comparative study. *J Process Technol.* 2003;142:738–743.
- [2] Michael Rajan HB, Dinaharan I, Rambalan S, et al. Influence of friction stir processing on microstructure and properties of AA7075/TiB₂ in situ composite. *J Alloys Compd.* 2016;657:250–260.
- [3] Umanath K, Palanikumar K, Selvamani ST. Analysis of dry sliding wear behavior of Al6061- SiC -al₂O₃ hybrid metal matrix composites. *Compos Part B.* 2013;53:159–168.
- [4] Mohanavel V, Rajan K, Ravichandran M. Synthesis, characterization and properties of stir cast AA6351 aluminium nitride (AlN) composites. *J Mater Res.* 2016;31(2):3824–3831.
- [5] Manjunatha LH, Dinesh P. Development and study on microstructure, hardness and wear properties of as cast, heat treated and extruded cnt- reinforced with 6061al metal matrix composites. *Int J Mech Eng Technol.* 2012;3:583–598.
- [6] Madeva Nagara VA, Kori SA. Microstructure and mechanical properties of Al6061-graphite composites fabricated by stir-casting process. *Appl Mech Mater.* 2015;308–314.
- [7] Harti J, Prasad TB, Nagara M, et al. Hardness and Tensile behavior of Al2219-TiC metal matrix composites. *J Mech Eng Autom.* 2016;6(5A):8–12.
- [8] Sharma SC, Seah KHW, Girish BM. Corrosion characteristics of ZA-27 graphite particulate composites. *Corros Sci.* 1997;39(1):1–7.
- [9] Wei JN, Cheng HF, Zhang YF, et al. Effects of macroscopic graphite particulates on the damping behavior of commercially pure aluminum. *Mat Sci Eng.* 2002;A325:444–453.
- [10] Hashim JLL, Hashmi MSJ. Metal matrix composites: production by the stir casting method. *J Mater Process Technol.* 1999;92-93:1–7.
- [11] Liu Z, Guoyin Z, Luo H, et al. Influence of Mg addition on graphite particle distribution in the Al alloy matrix composites. *J Mater Sci.* 2010;26(3):244–250.
- [12] Sharma SC, Seah KHW, Satish BM, et al. Effect of short glass fibers on the mechanical properties of cast ZA-27 alloy composites. *Mater Des.* 1996;17:245–250.
- [13] Sharma P, Paliwal K, Garg RK, et al. A study on wear behaviour of Al/6101/graphite composites. *J Asia Ceram Soc.* 2017.
- [14] Basavaraja P, Nagara M, Vidyashankar S, et al. Evaluation of Mechanical properties of Al2219-SiC-Graphite reinforced hybrid Composites. *Int J Appl Eng Res.* 2015
- [15] Kumar A, Gautam RK, Tyagi R. Dry sliding wear characteristics of in situ synthesized Al-TiC composites. *Compos Interfaces.* 2016.
- [16] Ramakoteswara V, Ramanaiah N, Sarcar MMM. Dry sliding wear behaviour of TiC-AA7075 Metal Matrix Composite. *Int J Appl Sci Eng.* 2016;14,1:27–37.
- [17] Suresh S, Shenbaga Vinayaga Moorthi N, Vittivel SC, et al. Effect of Graphite addition on mechanical behavior of Al6061/TiB₂ hybrid composite using acoustic emission. *Mat Sci Eng A.* 2014;612:16–27.
- [18] Kataiah GS, Girish DP. The mechanical properties & fractography of aluminium 6061 – tiO₂ composites. *Int J Pharm Stud Res.* 2010;1:17–25.
- [19] Baradeswaran A, Elaya Perumal A. Effect of graphite on mechanical and tribological properties of AA7075 Composites. *Tribol Trans.* 2015;58:1–6.

- [20] Kumar M, Megalingam Murugan A. Tribological characterization of Al6061/alumina/graphite/redmud hybrid composite for brake rotor application. *Part Sci Technol.* 2017;1–48.
- [21] Seah KHW, Sharma SC, Girish BM. Mechanical properties of cast ZA-27/Graphite particulate composites. *Mater Des.* 1995;16(5, 277);271-275.
- [22] Jeyasimman D, Gurnathan K, Narayanasamy R. Dry sliding wear behavior of AA6061 -MWCNT nanocomposites prepared by mechanical alloying. *IOSR J Mech Civil Eng.* 2016;46–53.
- [23] Santhosh Kumar BM, Girish DP. Friction and wear behaviour of tungsten carbide and E glass fibre reinforced Al7075 based hybrid composites. *IOP Conf Series Mat Sci Eng.* 2018;390;1-6.
- [24] Rao RN, Das S, Mondal DP, et al. Dry sliding wear behavior of cast high strength aluminium alloy (Al-zn-mg) and hard particle composites. *Wear.* 2009;267.;1688-1695.
- [25] Leng JF, Xing ZH, Huo DJ, et al. Effect of graphite particles on machinability of SiC/Gr/Al composites. *Mater Res Innovations.* 2015;19.

See discussions, stats, and author profiles for this publication at: <https://www.researchgate.net/publication/328248077>

Experimental investigation on HSFP using MWCNT based nanofluids for high power light emitting diodes

Article · September 2018

DOI: 10.15282/jmes.12.3.2018.7.0338

CITATIONS

0

READS

41

7 authors, including:



Sangmesh Bm

BMS Institute of Technology and Management

9 PUBLICATIONS 1 CITATION

[SEE PROFILE](#)



Kumaran Kadirgama

Universiti Malaysia Pahang

375 PUBLICATIONS 4,559 CITATIONS

[SEE PROFILE](#)



S. Mahendran

Universiti Malaysia Pahang

46 PUBLICATIONS 264 CITATIONS

[SEE PROFILE](#)

Some of the authors of this publication are also working on these related projects:



Numerical Study on Turbulent Forced Convective Heat Transfer Using Nanofluids TiO₂ in an Automotive Cooling System [View project](#)



Floating Solar [View project](#)

Experimental investigation on HSFP using MWCNT based nanofluids for high power light emitting diodes

**Sangmesh B^{1,2*}, Gopalakrishna K.¹, Manjunath S.H.², Kathyayini N.¹, K. Kadirgama^{3*},
M. Samykan^{3*}, G.C. Vijayakumar¹**

¹ Centre for Incubation, Innovation, Research and Consultancy, Jyothy Institute of Technology, Bangalore, Karnataka, India

²Research Scholar, VTU, Belagavi, Karnataka, India

*Email: sangmesh.sangu293@gmail.com

Phone: +91 9964311824; Fax: +91 448797660

² School of Mechanical Engineering, Reva University, Bangalore, Karnataka, India

³ Faculty of Mechanical Engineering, Universiti Malaysia Pahang, 26600 Pekan, Pahang, Malaysia

*Email: kumaran@ump.edu.my; mahendran@ump.edu.my

ABSTRACT

LEDs, of late, have received attention as the next generation lighting system for enhanced luminous efficiency and higher lifespan. However, the thermal management of the LEDs is the crucial parameter to be countered for global acceptance as a revolutionary illumination source. This paper reports the experimental investigation of natural convective heat transfer of high power LED COBs using MWCNT and MWCNT-CuO nanofluids mixed with de-ionized water. The study uses MWCNT based nanofluids as a route to enhance the heat transfer of high power LEDs by the passive cooling technique. This study presents an innovative cooling device integrated with numerous fluid pockets, called the HSFP, to achieve the enhanced thermal performance of heat sinks for applications in high intensity LED lights. Nanofluids of various concentrations were formulated and their heat transfer performance evaluated using a series of experiments and compared with liquid cooling and a conventional heat sink. The experimental finding reveals 20–30% lowered thermal resistance using the new HSFP (nanofluids). Thus, the HSFP found to effectively dissipates the heat in high-power LED COBs using nanofluids as the cooling medium compared to the conventional heat sink.

Keywords: HSFP; Heat Sink with fluid pockets; Thermal management of LEDs; Nanofluids.

INTRODUCTION

Being ten (10) times more efficient than incandescent lights, LEDs are increasingly penetrating in domestic applications. Their increased reliability, coupled with long operating life, renders them as an obvious choice for next-generation lighting systems. However, most of the power supplied to them converts to heat. The increased input power further cause's degradation of luminance efficiency and lifespan since higher heat is generated. Therefore, it is essential to have a proper heat dissipation module to ensure proper operation. Hence, thermal management of LEDs is the crucial parameter to enhance their lifespan and luminance effect. Active or preferably passive cooling with air can be the predominant choice for LED lighting systems. A proposed design must have a meager thermal resistance between the junction and the heat sink base which relies on conduction heat transfer [1]. Tisha Dixit, et al. [2] studied the miniaturization of the heat sink and found that characteristics such as compactness, small size and lesser weight attracted widespread attention.

Yiwei Wang, et al. [3] studied a new flat plate heat pipe with a micro-fins cast on the condensation surface. It was found to be more effective for heat dissipation of high-power LED COBs than the traditional new flat plate heat pipe. Z. Lin et al. [4] developed a plate oscillating heat pipe heat sink for LED cooling. They found that when a plate OHP was used in an LED heat sink, it led to a significant decrease in the temperature of the LED through a natural convection process. Whereas, the thermophysical properties and heat transfer performance have been carried out by Patrice Estell et al. [5]. Hamed Khajeh Arzani, et al. [6, 7] studied MWCNT-ASP (aspartic acid) with water for different weight fractions experimentally.

Their results showed a significant increase in heat transfer rate. M. Hemmat Esfe et al. [8] studied the thermo-physical properties of nanofluids and concluded that thermal conductivity increases with an increase in temperature. Meanwhile, W.S. Sarsam et al. [9] revealed that aqueous colloidal dispersions of β -alanine-MWCNTs are promising alternative working fluids for enhanced thermal performance. B. Munkhbayar et al. [10] performed an investigation on the enhancement of thermal conductivity of silver nanoparticle with multi-walled carbon nanotubes. They reported that grinding has significantly improved the dispersion stability and thermal conductivity of MWCNT. S. Jyothirmayee Aravind et al. [11] reported that no surfactant, good fluidity, long-term stability, and high thermal conductivity would enable f-MWCNT nanofluids to be used as advanced coolants in thermal management applications. Sh. M. Vanaki et al. [12] observed that nanofluids have the ability to significantly enhance heat transfer rate of conventional heat transfer fluids as a result of the dispersed highly conductive nanoparticles in the base liquid. Mohammadali Baghbanzadeh et al. [13] studied the effect of hybrid silica nanosphere/MWCNT on the thermal conductivity of distilled water.

Their results showed that the effective thermal conductivity of nanofluid was obtained by increasing the concentration of nanoparticles. K. Kouloulis et al. [14] performed an experimental study on natural convection of $\text{Al}_2\text{O}_3\text{-H}_2\text{O}$. They found that the convective heat transfer is enhanced when the applied heat flux increases and the induced flow becomes more turbulent. Zeinali Heriset al. [15] studied $\text{Al}_2\text{O}_3/\text{water}$ nanofluid heat transfer in laminar flow. Experimental investigations depict that heat transfer coefficient increases by increasing the volume fraction of nanoparticles in the nanofluid. Literature shows enhancement in the thermal conductivity, viscosity, and heat transfer through the use of nanofluids which increases with increasing volume of nanoparticles [16,17]. Y. Ding et al. [18] observed that enhanced convective heat transfer was obtained in comparison with pure water. It was also reported that the enhancement depends on the flow condition, concentration and the pH level. In another study of Cu-Ti [19] with Vol.% of MWCNTs, it was reported that linear and small coefficient of thermal expansion was obtained for low concentrations of multiwall carbon nanotubes. In an experimental investigation by Majid Zarringhalam et al. [20] who studied the effect of volume fraction on heat transfer coefficient. They reported that heat transfer coefficient of nanofluids was higher than that of base fluid. It was also observed that the heat transfer coefficient and Nusselt number of nanofluids increases with increasing nanoparticles volume fraction.

The experimental study by Saednia et al. [21] on CuO nanofluid for different concentrations, flowing inside a circular tube, showed that heat transfer coefficient increases with increasing nanoparticle concentration. Ali Hassan et al. [22] observed that enhancement of convective heat transfer coefficient of ethylene glycol (EG) base cuprous oxide (Cu_2O) nanofluids was higher than for the base fluid. Hooman Yarmand et al. [23] prepared a hybrid nanofluid mixture of graphene nanoplatelet (GNP) and Platinum (Pt) nanofluids. Experimental results revealed that nanofluids have a higher heat transfer capability compared with the base liquid, and the improved heat transfer coefficient is dependent on Reynold number, and the weight concentration of the nanocomposite. Hong Seok Jo et al. [24] fabricated an innovative fractal-like Cu_2O surface on a NiCr wire to identify the effects of wettability on pool boiling performance. Their results revealed that hydrophobic texturing is desirable for electronics cooling. R. Ellahi et al. [25] studied the nanolayer effects on SWCNTs and MWCNTs with natural convection. They observed that the

velocity decreased by increasing the volume fraction of nanotubes. S. Zeinali Heriset al. [26] has studied Al_2O_3 /water nanofluid heat transfer in laminar flow. Their investigations depicted that heat transfer coefficient increased with an increase in the volume fraction of nanoparticles in nanofluid. I.D. Garbadeen et al. [27] performed experimental investigations on nanofluids consisting of multi-walled carbon nanotubes with water as the base fluid. Their results indicated that natural convection yielded a maximum enhancement in heat transfer performance of 45% at a volume concentration of 0.1%.

This research supports the idea that nanofluids with effective thermal conductivity are higher than the thermal conductivity of the base fluid. Hina Muryam et al. [28] compared gold and silver nanoparticles with de-ionized water by studying their characteristics of convective heat transfer. They concluded that gold/DIW based nanofluids exhibit better convective heat transfer than silver/DIW based nanofluids. Till date, a number of experiments work has been carried out on forced convection. As noted from the literature, most of these studies involve flow rate, volume fraction and thermal conductivity rather than the heat transfer characteristics of nanofluids. A large number of studies have also been undertaken in improving the thermal conductivity of the nanofluids. Therefore, an attempt is made in the present study to fill this space with a focus on natural convection. Heat dissipation capabilities of nanofluids have been carried out and verified by natural convective heat transfer experiments for both steady state and transient conditions. An experimental setup was designed and fabricated for this purpose and applied to cool high-power LEDs. The junction temperature of the LEDs was measured to investigate enhanced heat transfer. The thermal resistance was analyzed to understand the cooling potential of nanofluids and liquid cooling better.

METHODS AND MATERIALS

Materials

In this work, a heat sink with fluid pockets (HSFP) was developed with parallel rectangular fins and multiple holes at the base. The novel HSFP was designed, fabricated and applied to cool high-power LED COBs. The holes were filled with nanofluids for effective heat dissipation from the LED junction. The main objective of the study was to investigate the influence of nanoparticles suspended in the base fluid on the heat transfer characteristic of nanofluids. MWCNT and MWCNT-Copper oxide (CuO-MWCNT) nanofluids with de-ionized water of various concentrations were used in the test. Due to their unique thermal properties, carbon nanotubes (MWCNTs) and MWCNT-CuO have been used as additives to increase thermal conductivity and other thermal properties of the nanofluids. The fluid pockets were filled with nanofluids along with the base fluid in wt% basis for different volume fraction. Measurement of heat transfer performance of MWCNT/DI water and MWCNT-CuO/DI watered nanofluids with nanoparticle concentration in the range of 0.2 to 0.8 wt% was tested and compared with liquid cooling and the conventional heat sink. Tests were done using stable nanofluids under natural convection condition for both steady state and transient conditions. The composite nanofluid has an equal volume of carbon nanotubes and copper in the base fluid. The nanofluids circulate within the fluid pockets by thermal energy and gravity force. Typical dimensions of the heat sink are shown in Figure 1. The aluminum heat sink was designed to suit actual street light applications. The heat sink was designed for a length of 200mm, the width of 120mm, the base of 10mm height, and a fin height of 10mm with a hole of diameter 6mm drilled across the length to fill liquid with nanoparticles into it. The fins were maintained for half the length in order to achieve condensation of heat transfer fluids [29,30].

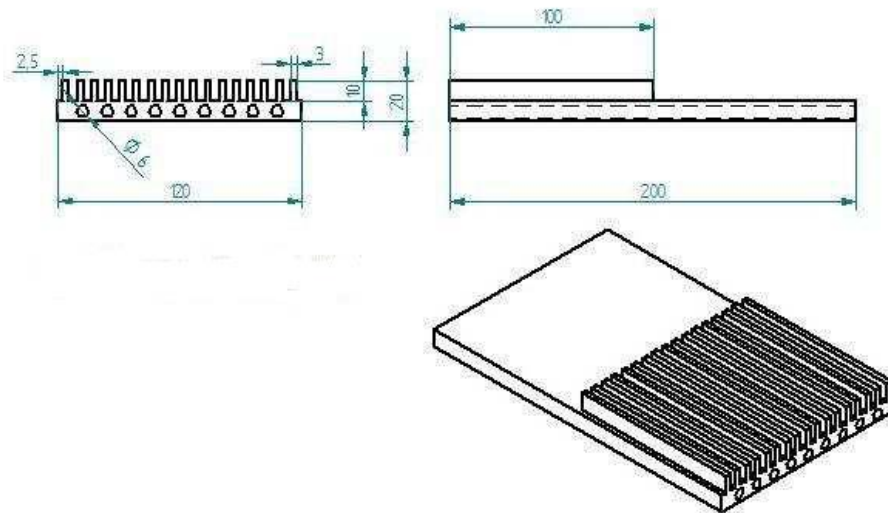


Figure 1. Heat Sink with fluid pockets and half-length fins

The LED setup chosen in this study has 3sets of COB LEDs of each having 40W (CREE Make- X lamp XP-G) with the wattage of 120 W. A thermal interface material was used to establish proper surface contact to avoid air gap. The data acquisition system (TRACER make) has a resolution of 10^{-5} ° C to measure the junction temperature of the LED. The sampling rate was 1/s. The thermocouple positions were diagnosed with the use of an infrared thermal image camera. Recognized hotspots over the MCPCB were placed with T type thermocouples to measure the junction temperature. Five trials were conducted for each test condition for repeatability of the measurements and to avoid uncertainties in the course of experimentation. Validation of the setup was done with the conventional heat sink of same configurations excluding fluid pockets. The test duration was 100 min. Steady state was attained around 60 minutes of the experiment. The constant power input was 120 W. Two different nanofluids such as MWCNT and CuO-MWCNT were used with different solid volume fractions of suspended nanoparticles. The test results were compared with liquid cooling and conventional heat sink. Figure 2 shows the experimental setup used in this study.

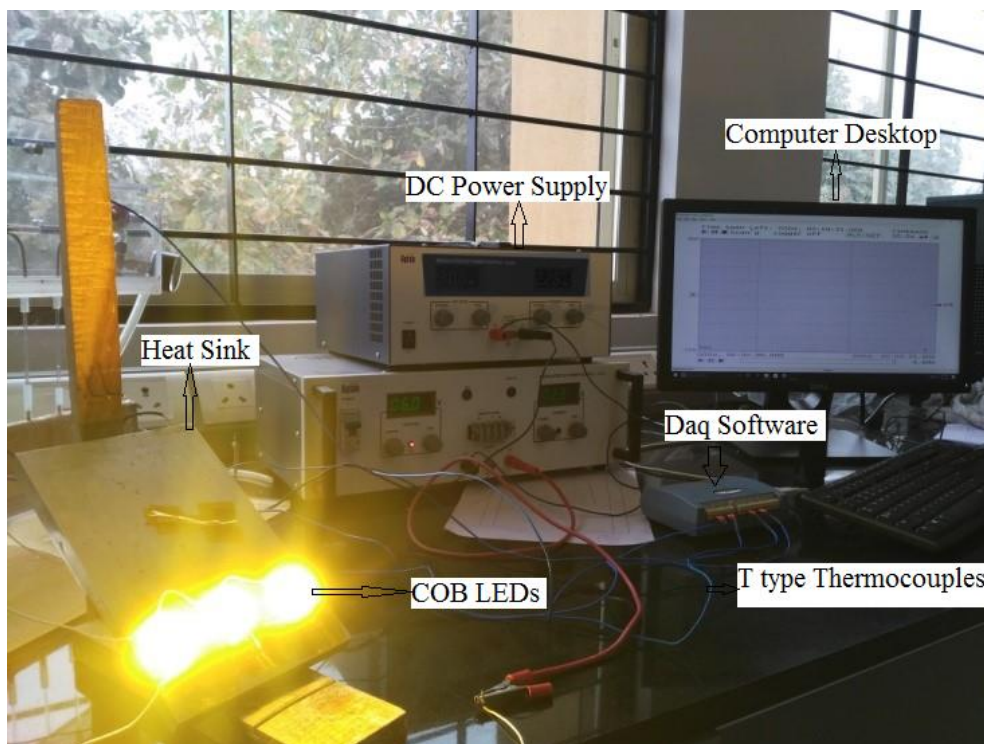


Figure 2. Experimental Setup of the present study

Preparation and Characterization of Nanofluids

MWCNTs were acquired from Reinste Nano Endeavors Private Ltd. Also concentrated H_2SO_4 , concentrated HNO_3 and Cu, and Na_2SO_3 were gotten from Merck. The crude MWCNTs and copper oxide were sonicated for 4 hours at $80^\circ C$ of an ultrasonic shower with a (v/v, 3:1) blend of concentrated H_2SO_4 and HNO_3 to present oxygen containing useful gatherings on the crude MWCNT surface and it was sifted and washed over till the washing demonstrated no acidity.

The clean MWCNTs were dried in the stove at $80^\circ C$ for 24 hours and the process was repeated for copper oxide. The MWCNT and CuO/MWCNT catalysts were described utilizing a wide range of systematic analytical techniques, including X - ray diffraction (XRD), scanning electron microscopy with energy dispersive X-ray spectroscopy (SEM-EDS).

These investigations were led to build up a better understanding of the physico - chemical properties of these catalysts. In order to investigate the morphology and the chemical composition of the materials, SEM-EDS analysis was also carried out to evaluate the elemental composition of nanofluids. The morphology of MWCNT and CuO-MWCNT samples was analyzed using SU 3500N emission scanning electron microscopy (SEM) operating at 10 kV. Figures 3a and 3b show the SEM images of MWCNT and CuO-MWCNT respectively. From the SEM image of MWCNTs (Figure 3a), a tubular network is observed.

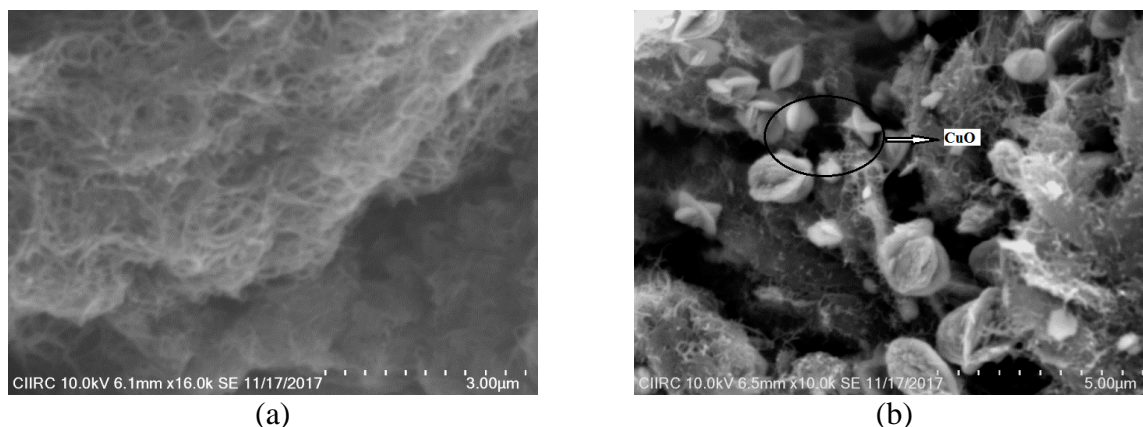


Figure 3. SEM image of (a) MWCNT and (b) CuO-MWCNT

In case of CuO-MWCNTs, the formed CuO flakes appear to have agglomerated to form of flower-like morphology within the MWCNTs network. EDS spectra indicate the presence of Cu, C and O in the case of CuO-MWCNTs and only C and O in the case of MWCNTs as shown in Figure 4a and 4b.

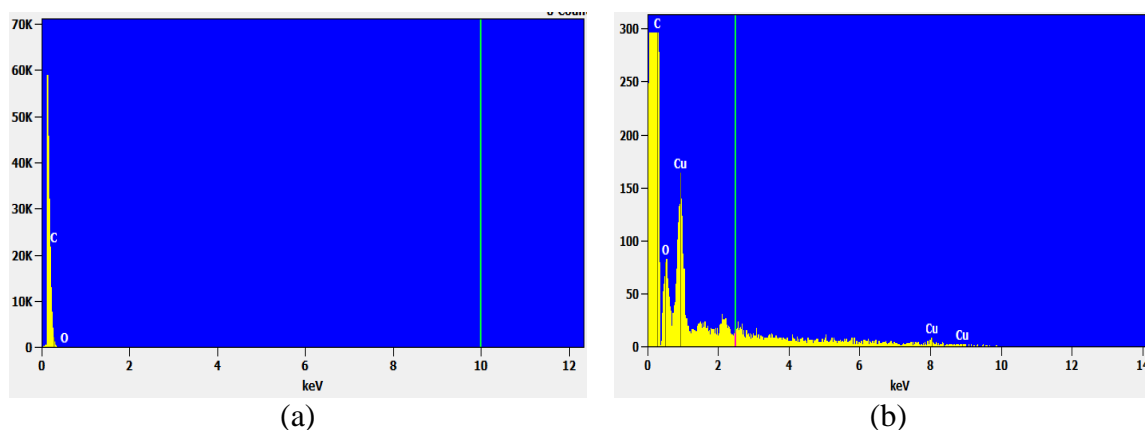


Figure 4. EDS spectra of (a) MWCNT and (b) CuO-MWCNT

Figures 5a and 5b show the P-XRD patterns of MWCNT and CuO-MWCNT respectively. Bruker D2 Phaser XRD system was used to get X-ray diffraction (XRD) patterns. The P-XRD patterns of MWCNT exhibit two sharp peaks at 2θ values 26° and 42° corresponding to (002) and (100) hkl planes respectively [30]. While the P-XRD patterns of CuO-MWCNT exhibit peaks at $2\theta = 32.51^\circ, 35.53^\circ, 38.5^\circ, 46.28^\circ, 48.76^\circ, 53.58^\circ, 58.31^\circ, 61.58^\circ, 66.24^\circ$ and 68.08° corresponding to different hkl planes of monoclinic phase of CuO [31, 32]. It is noticed that the intensity of the peak at 26° corresponding to (002) plane of MWCNT is less in CuO-MWCNT compared to other peaks. These might be due to the low MWCNT content.

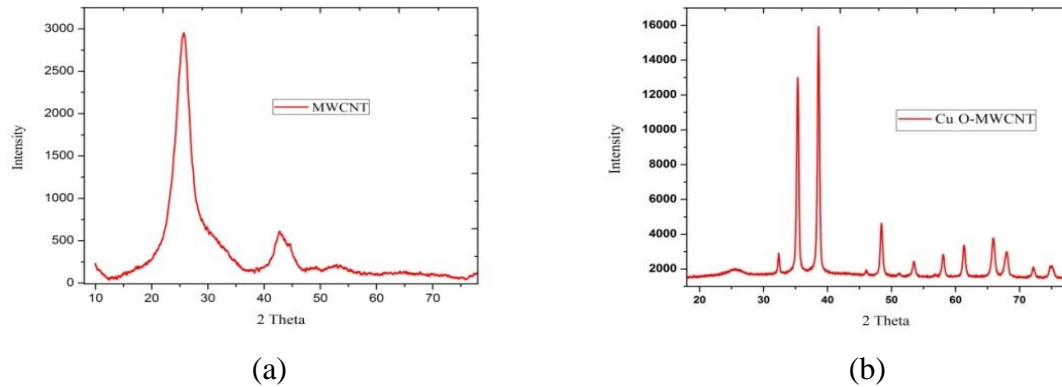


Figure 5. XRD spectra of (a) MWCNT and (b) CuO-MWCNT

RESULTS AND DISCUSSION

Effect of Liquid Cooling for Enhanced Heat Transfer

The experiment was done using de-ionized water as the cooling fluid for 100% fill ratio to investigate the thermal enhancement of LED with liquid as the cooling medium. Results were compared with the conventional heat sink to determine the influence of liquid cooling for enhanced heat transfer. The junction temperature of the LED with heat sink, in the presence of liquid exhibits, was in agreement as presented in Figure 6. It evidently depicts that minimized junction temperature is obtained with the use of liquid cooling in the heat sink compared to the conventional heat sink. Fluid pockets in the heat sink efficiently strengthen the convective heat transfer. It demonstrates that conventional cooling technique reduces the junction temperature but requires time to dissipate it to the atmosphere. The junction temperature of the LED increased rapidly without cooling fluids and attained 210 °C [33, 34].

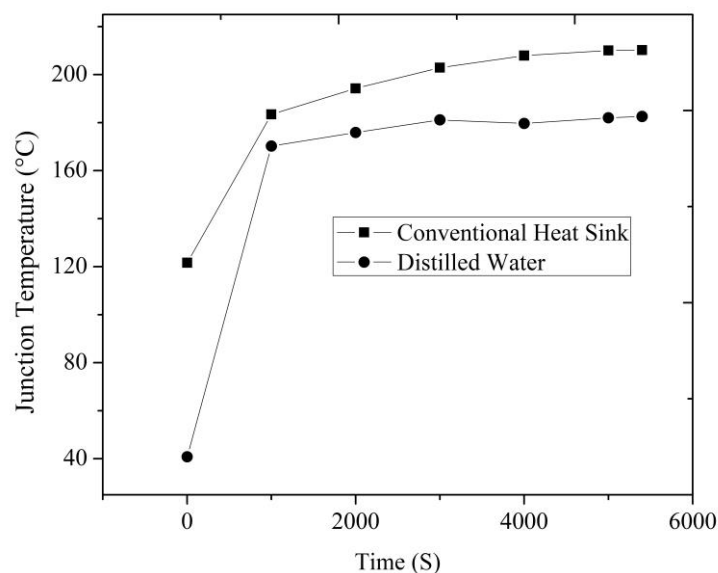


Figure 6. Variation of operating temperature for De-ionized water and conventional heat sink

Influence of Nanoparticle Volume Fraction on Heat Transfer

In this section, thermal characterization of nanofluid in terms of reduction in junction temperature of LED is examined experimentally. The effect of volume fraction on heat transfer characterization of MWCNT/De-ionized water and CuO-MWCNT/De-ionized water nanofluids was studied in terms of reduced LED junction temperature. Various suspensions of MWCNT and CuO-MWCNT were tested at a volume fraction of 0.2, 0.4, 0.6 and 0.8 wt%. The variation of the junction temperature of LED versus time for different volume fractions of MWCNT and CuO are depicted in Figure 7 and 8. It is evident that the heat dissipation enhances with an increase in volume fraction due to its high thermal conductivity. The thermal conductivity of nanofluids is higher than that of base fluid and there may exist an optimum concentration that maximizes the heat transfer. These corroborate the finding of various authors that thermal conductivity increases with increase in the concentration of nanoparticles. The enhancement of thermal dissipation at a low volume fraction of nanofluid is relatively small. However, with increasing volume fraction of nanoparticles, the enhancement of thermal dissipation due to its ability to extract heat from the junction temperature is significant [35-38]. Also, it can be seen that the reduced junction temperature is an increasing function of volume fraction. However, there is a negligible difference between 0.6 and 0.8 wt% of total volume which may be because of increase in particles tending to clog up fluid pocket channels.

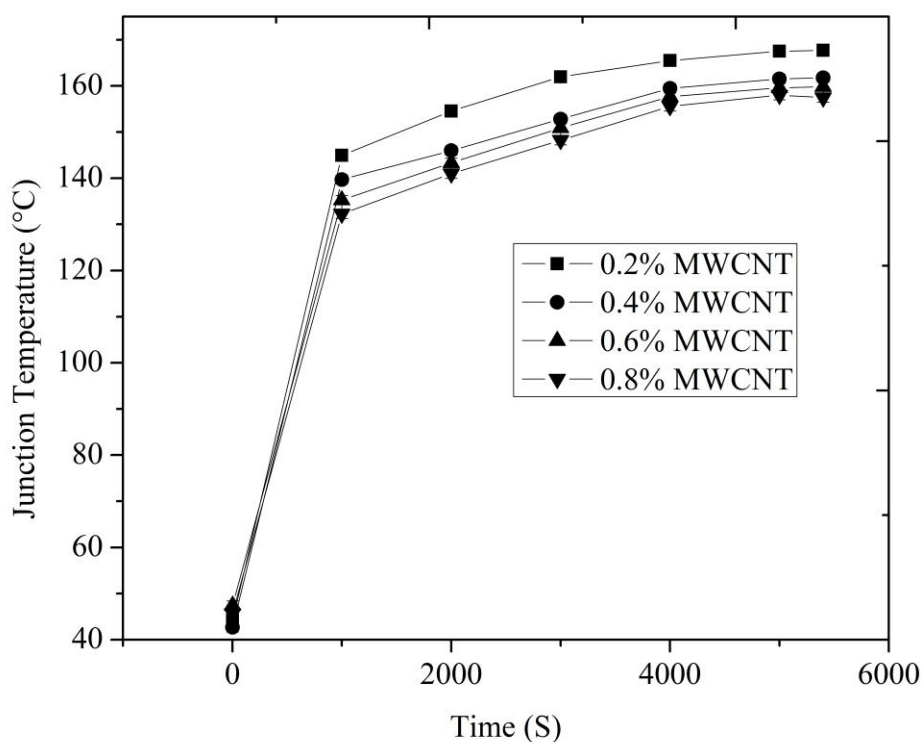


Figure 7. Junction temperature of LED of MWCNT for different volume fraction

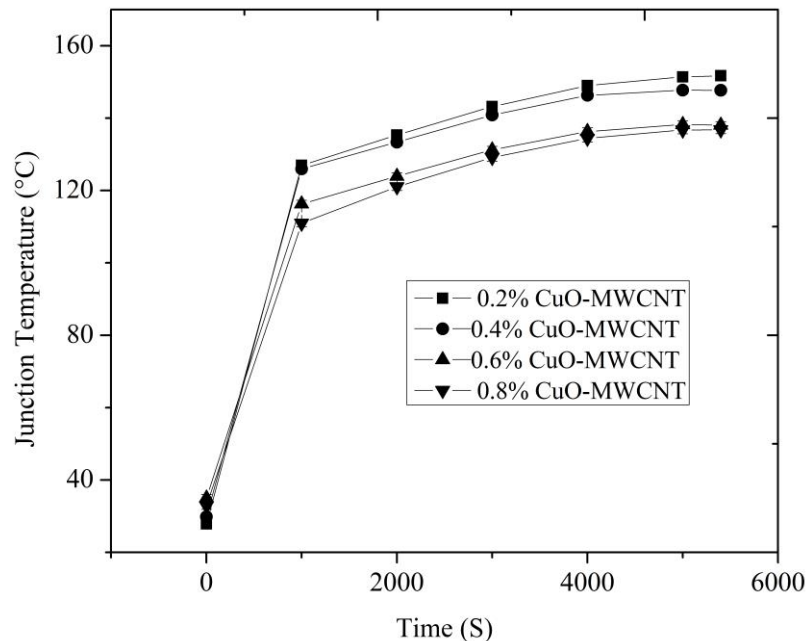


Figure 8. Junction temperature of LED of CuO-MWCNT for different volume fraction

Effect of Nanofluids on Natural Convection

Natural convection is a passive cooling technique and therefore can be used in many heat transfer applications to improve heat transfer rate without any additional power. Nanofluids evolved over the years due to the limitation of the conventional heat transfer fluids to facilitate higher cooling rates. The use of nanofluids through natural convection mode further enhances the performance and compactness of heat transfer devices. In this study, the HSFP was designed and operated in such a way that the circulation of nanofluids may happen naturally due to rise in junction temperature of LED and return on its own due to the gravity effect. This mechanism tends to achieve a better circulation of fluid within the circular tubes of HSFP. This continued circulation of fluid in the HSFP improved the heat dissipation quickly as compared to the conventional heat sink. The added MWCNT nanofluid with water further enhanced the dissipation due to increase in thermal conductivity; the use of higher thermal conductivity material reduced the thermal resistance significantly. Overall results show that the existing model HSFP for heat dissipation of LED COB is valid for both single and composite nanofluids. It is evident from Figure 9 that there is an enhanced heat transfer rate when composite nanofluids are used due to added nanoparticles of copper. Copper in the MWCNT increases the thermal conductivity of the nanofluid which results in improved heat transfer. The results depict that both single and composite nanofluids are in good agreement. The composite nanofluid exhibited pronounced heat transfer followed by MWCNT nanofluid and liquid cooling using distilled water. The junction temperature increased rapidly and prolonged over a period when the conventional heat sink is used. Passive cooling with distilled water was found to be comparatively good. Liquid cooling is an effective tool where heat dissipation is necessary. Thus, the HSFP proves to be an alternative low-cost device that can be effectively used for cooling of LEDs.

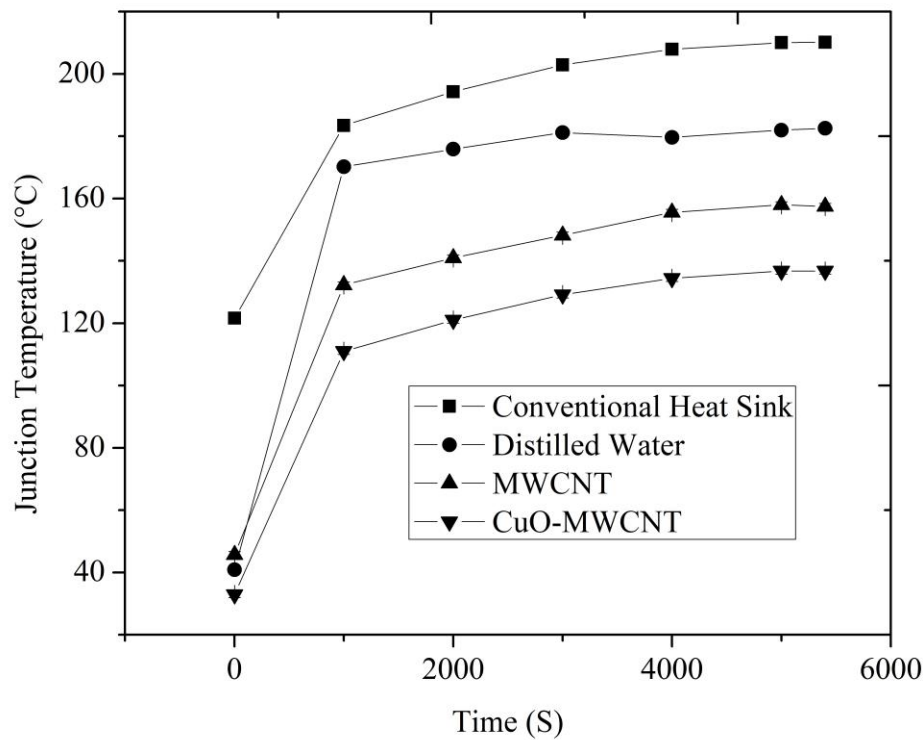


Figure 9. Effect of nanofluids on junction temperature of LED

Thermal Resistance of the Nanofluids

Thermal resistance analysis was performed to evaluate the efficacy of these nanofluids used as heat transfer fluids. The heat transfer characteristics of the heat sink for various nanofluids were evaluated by the thermal resistance. The overall thermal resistance of LED COB as the ratio of the difference in junction temperature and ambient to the maximum heat load applied to the LED COB was considered as shown in Eq. 1.

It is evident from Figure 10 that thermal resistance increases with increase in junction temperature; it is worthy to note that it reduces with increase in volume fraction of nanoparticles. From the literature, it is observed that the increased nanoparticles volume fraction increases the thermal conductivity of the coolant. Therefore, increase in the thermal conductivity increases the convective heat transfer coefficient which, in turn, reduces the convective thermal resistance and, therefore, the overall thermal resistance of the CuO-MWCNT was found to be higher than the MWCNT nanofluid.

$$R = \frac{T_j - T_a}{Q} \quad (1)$$

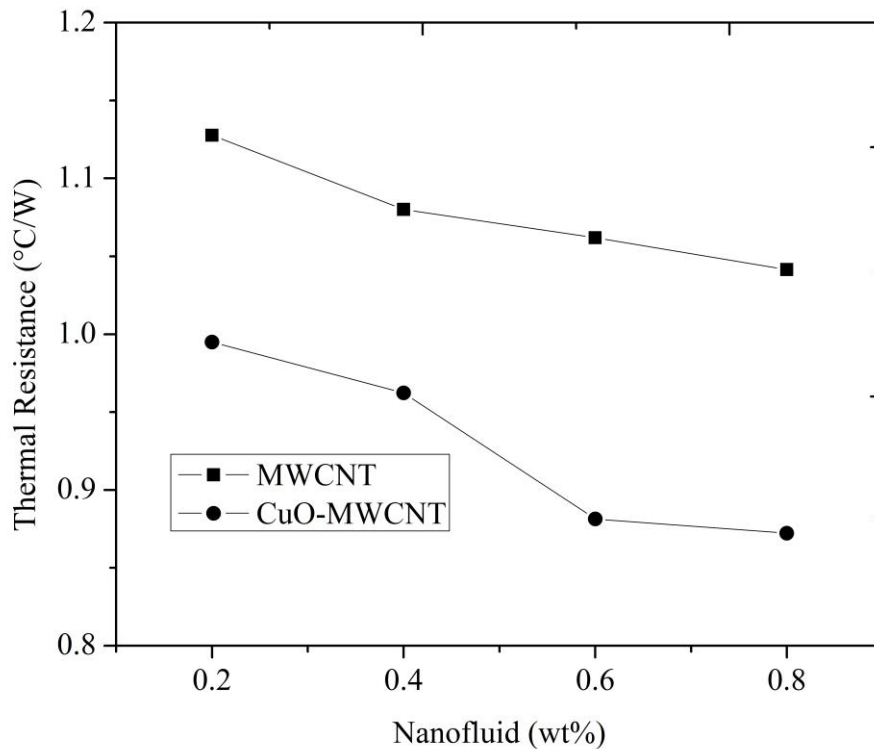


Figure 10. Thermal resistance for varying fill ratio for MWCNT and CuO-MWCNT nanofluids

CONCLUSIONS

In this work, natural convective heat transfer characterization for MWCNT based nanofluids flowing in fluid pockets within the base of the heat sink was studied. Heat transfer performance studies on natural convection using MWCNT based nanofluids for different concentrations in the range of 0.2 to 0.8 wt% of the total volume were performed and validated using liquid cooling and a conventional heat sink. The heat transfer effectiveness of the nanofluids was measured in terms of the reduced junction temperature of the LEDs and thermal resistance of the nanofluids. Experimental results demonstrated that the thermal resistance of the LED COB cooling system is reduced by 15% when using the novel HSFP model with de-ionized water as the heat transfer fluid. The effect of varying nanofluid concentrations with the base fluid enhanced heat transfer in the range of 29%. The combined effect of MWCNT and CuO-MWCNT further reduced the thermal resistance by 41%. Finding also discloses that between 0.6 and 0.8 wt%, there was no significant change in the result. However, a decline in heat transfer performance was seen especially for conventional heat sinks.

A maximum heat transfer enhancement of 35% occurred for 0.6-0.8 wt% volume concentration and there was a negligible difference for further increase in concentration which may be due to clogging up and restricted motion of the fluid. The results of this study are believed to be attributed by the use of MWCNT based nanofluids with buoyancy-driven heat transfer mechanism as a useful technique for enhancing the performance of high power LED particularly street light applications without the aid of external power. From the converged experimental results, it is worthy to note that the feature of HSFP providing longitudinal fluid pockets filled with MWCNT based nanofluids as the cooling agent is significantly useful for the high-power LED package as against the conventional heat sink. Thus, it can be concluded that the use of nanofluids in natural convection mode demonstrated a significant enhancement in their heat transfer performance when used for high

power LED since they maintained very low junction temperature. However, the volume fraction range of nanoparticles would require more in-depth experimental studies. Therefore, experimental studies are very crucial for understanding the thermophysical behavior of nanofluids.

ACKNOWLEDGEMENTS

The authors would like to thank the Centre for Incubation, Innovation, Research and Consultancy, Jyothy Institute of Technology for the laboratory and financial assistance provided.

REFERENCES

- [1] Mehmet A, Charles B, Stanton W, and James P. Thermal management of LEDs: Package to System. Conference on Solid State Lighting, Proc. of SPIE. 2004; 5187: 0277-786X/04/15.
- [2] Tisha D, Indranil G. Review of micro and mini channel heat sinks and heat exchangers for single phase fluids. Renewable and Sustainable Energy Reviews. 2015;4:1298-1311.
- [3] Yiwei W, Jiwen C, Fangming J, Wenjiong C. Heat dissipation of high-power light emitting diode chip on board by a novel flat plate heat pipe. Applied Thermal Engineering. 2017;123:19-28.
- [4] Zirong L, Shuangfeng W, Jiepeng H, Yanxin H, Jinjian C, Winston Z, Eton L. Heat transfer characteristics and LED heat sink application of aluminum plate oscillating heat pipes. Applied Thermal Engineering. 2011;31:2221-2229.
- [5] Patrice E, Salma H, Thierry M. Thermo physical properties and heat transfer performance of carbon nanotubes water-based nanofluids. Journal of Thermal Analysis and Calorimetry, Springer-Verlag; Springer (Kluwer Academic Publishers). 2017;3:2075-2081.
- [6] Hamed KA, Ahmad A, Kazi SN, Chew BT, Badarudin A. Experimental investigation of thermophysical properties and heat transfer rate of covalently functionalized MWCNT in an annular heat exchanger. International Communications in Heat and Mass Transfer. 2016;75:67-77.
- [7] Hessam T, Jorge LA, Ehsan ML. Enhanced thermophysical properties of multiwalled carbon nanotubes based nanofluids. Part 2: Experimental verification. 2017;10: 117.
- [8] Mohammad HE, Seyfolah S, Wei MY, Masoud A, Nima S. Study on thermal conductivity of water-based nanofluids with hybrid suspensions of CNTs/Al₂O₃ nanoparticles. J Therm Anal Calorim. 2016;124:455-460.
- [9] Wail SS, Ahmad A, Kazi SN, Badarudin A. Stability and thermo physical properties of non-covalently functionalized graphene nano platelets nanofluids. Energy Conversion and Management. 2016;116:101-111.
- [10] Munkhbayar B, Md RT, Jinseong J, Hanshik C, Hyomin J. Surfactant-free dispersion of silver nanoparticles into MWCNT-aqueous nanofluids prepared by one-step technique and their thermal characteristics. Ceramics International. 2013;39:6415-6425.
- [11] Aravind SSJ, Tessy TB, Sabareesh RK, Sumitesh D, Ramaprabhu S. Investigation of structural stability, dispersion, viscosity, and conductive heat transfer properties of functionalized carbon nanotube based nanofluids. J. Phys. Chem. 2011;115:6737-16744.
- [12] Vanaki SM, Ganesan P, Mohammed HA. Numerical study of convective heat transfer of fluids: A Review. Renewable and Sustainable Energy Reviews. 2016;54:1212-1239.
- [13] Mohammadali B, Alimorad R, Davood R, Roghayeh L, Azadeh A. Synthesis of spherical silica/multiwall carbon nanotubes hybrid nanostructures and investigation of thermal conductivity of related nanofluids. Thermochemica Acta. 2012;549:87-94.

- [14] Kouloulias K, Sergis A, Hardalupas Y. Sedimentation in nanofluids during a natural convection experiment. *International Journal of Heat and Mass Transfer*. 2016;101:1193–1203.
- [15] Zeinali H, Esfahany MN, Etemad SG. Experimental investigation of convective heat transfer of Al₂O₃/water nanofluid in circular tube. *International Journal of Heat and Fluid Flow*. 2007;28; 203-210.
- [16] Gianluca P, Samuel P, Mihir S. Nanofluids and their properties. *Applied Mechanics Reviews*. 2011;64:031002-1.
- [17] Murshed SMS, Leong KC, Yang C. Thermophysical and electrokinetic properties of nanofluids – A critical review. *Applied Thermal Engineering*. 2008;28:2109-2125.
- [18] Yulong D, Hajar A, Dongsheng W, Richard AW. Heat transfer of aqueous suspensions of carbon nanotubes (CNT nanofluids). *International Journal of Heat and Mass Transfer*. 2006;49:240–250.
- [19] Smail H, Ahmed J, Revo S, Ivanenko K, Youcef J, Avramenko T. Thermal analysis of copper-titanium multiwall carbon nanotube composites. *Nanoscale Research Letters*. 2017;12:251.
- [20] Majid Z, Arash K, Davood T. Experimental study of the effect of solid volume fraction and Reynolds number on heat transfer coefficient and pressure drop of CuO–Water nanofluid. *Experimental Thermal and Fluid Science*. 2016;76:342-351.
- [21] Saeedinia M, Akhavan-Behabadi MA, Razi P. Thermal and rheological characteristics of CuO–Base oil nanofluid flow inside a circular tube. *International Communications in Heat and Mass Transfer*. 2012;39:152-159.
- [22] Ali H, Naveed R, Asim U, Ayyaz A, Hina M. Enhancement of convective heat transfer coefficient of ethyleneglycol base cuprous oxide (Cu₂O) nanofluids. *Heat and Mass Transfer*. 2018;54:325-332.
- [23] Hooman Y, Nurin WMZ, Samira G, Seyed F, Seyed S, Abdullah AAAA, Mohamad AA, Mahidzal D, Kazie SN. Convective heat transfer enhancement with graphene nanoplatelet/platinum hybrid nanofluid. *International Communications in Heat and Mass Transfer*. 2017;88:120–125.
- [24] Hong SJ, Seongpil A, Hyun GP, Min-Woo K, Salem S. Al-Deyab, James SC, Jeehoon C, Sam SY. Enhancement of critical heat flux and superheat through controlled wettability of cuprous-oxide fractal-like nanotextured surfaces in pool boiling. *International Journal of Heat and Mass Transfer*. 2017;107:105–111.
- [25] Ellahi R, Hassan M, Zeesha A. Study of natural convection mhd nanofluid by means of single and multiwalled carbon nanotubes suspended in a salt water solution. *IEEE Transactionson Nanotechnology*. 2015;14:726-734.
- [26] Heris SZ, Esfahany MN, Etemad SG. Experimental investigation of convective heat transfer of Al₂O₃/water nanofluid in circular tube. *International Journal of Heat and Fluid Flow*. 2007;28:203–210.
- [27] Garbadeen ID, Sharifpur M, Slabber JM, Meyer JP. Experimental study on natural convection of MWCNT-water nanofluids in a square enclosure. *International Communications in Heat and Mass Transfer*. 2017;88:1-8.
- [28] Muryam H, Ramzan N, Umer A, Awan GH, Ali Hassan. Comparative study of convective heat transfer characteristics of nanofluids. *Heat Mass Transfer*. 2017;53:2309-2316.
- [29] Bailin F, Pei Z, Ganghan H, Jun WY. Research on properties of fluid pressure drop for electric vehicle igpt pin fin heat sink. *International Journal of Engineering, Transaction A:Basics*. 2015; 28:627-633.
- [30] Monaheng LM, Lebea NN, Soraya PM, Edward NN, Sabelo DM. Chitosan-based nanocomposites for de-nitrification of water. *Physics and Chemistry of the Earth*. 2017;100:1-13.

- [31] Manyasree D, Kiran MP, Ravikumar R. CuO nanoparticles: Synthesis, Characterization and their bactericidal efficacy. *Int J App Pharm.* 2017;9:71-74.
- [32] Prachi K, Surapaneni M, Swati C, Padmavathy N. Understanding the pathway of antibacterial activity of copper oxides nanoparticles, electronic supplementary material (esi) for rsc advances. *The Royal Society of Chemistry.* 2015;5:12293-12299.
- [33] Sangmesh, Gopalakrishna KN, Manjunath SH, Krishna V, Keertishekar MS. Thermal performance of heat sink with fluid pockets for high power light emitting diode, *International Journal of Automotive and Mechanical Engineering.* 2017;14(4): 4846-4862.
- [34] Lv L, Li J, Zhou G. A robust pulsating heat pipe cooler for integrated high power LED chips. *Heat and Mass Transfer.* 2017;53:3305-13.
- [35] Abidin SZ, Mohamad IS, Hashim BAY, Abdullah N, Hafiz MIM, Masripan NAB, Abdullah A. Investigation of thermal characteristics of CNF-based nanofluids for electronic cooling applications. *Journal of Mechanical Engineering and Sciences.* 2016;10(3):2336-2349.
- [36] Kou HS, Lee JJ, Chen CW. Optimum thermal analysis of a heat sink with various fin cross-sections by adjusting fin length and cross-section. *Heat Transfer Engineering.* 2008; 29:537-45.
- [37] Hussein AM, Bakar RA, Kadirgama K, Sharma KV. Experimental measurements of nanofluids thermal properties. *International Journal of Automotive and Mechanical Engineering.* 2013;7:850-63.
- [38] Abdul Hamid K, Azmi WH, Mamat R, Usri NA, Najafi G. Effect of temperature on heat transfer coefficient of titanium dioxide in ethylene glycol-based nanofluid. *Journal of Mechanical Engineering and Sciences.* 2015;8:1367-75.

Performance studies on cryogenic treated carbide cutting tool for turning of AISI304 steel

Nagraj Patil^{1,2*}, Gopalakrishna K³, Sangmesh B³, K Sudhakar⁴, G C Vijaykumar³

¹Department of Mechanical Engineering, School of Engineering and Technology,
Jain University, Bangalore 562112, Karnataka, India

²Research scholar, Visvesvaraya Technology University, Belagavi 590018, Karnataka, India

*Email: nagrajpatil81@gmail.com

Mobile: +91 9590785153; Fax: +9180-27577199

³Centre for Incubation, Innovation, Research and Consultancy (CIIRC),
Jyothy Institute of Technology, Bangalore 560082, Karnataka, India

⁴Faculty of Mechanical Engineering, Universiti Malaysia Pahang 26600 Pahang, Malaysia

ABSTRACT

This paper attempts to compare and contrast cryogenic treated and untreated carbide cutting tool in turning operation of AISI304 steel. Machining parameters, namely cutting speed, feed rate and depth of cut are optimized for cryogenic treated tools. Tool life of the insert was determined based on the tests performed such as hardness, surface roughness and maximum wear. A design of experiments (DOE) and an analysis of variance (ANOVA) have been incorporated in the study. The objective of the paper is to determine the effects of each parameter on the surface roughness and tool wear. Material characterization was carried out using scanning electron microscope (SEM) and the maximum wear was estimated using optical microscope before and after the cryogenic treatment. The experimental results showed that cryogenic treated cutting tools significantly reduction in surface roughness, improves resistance to wear than untreated one. A confirmation test was performed between experimental and optimum values and the results are found to be in good agreement.

Keywords: Cryogenic treatment; tool wear; surface roughness; Taguchi method; ANOVA.

INTRODUCTION

The main challenge in machining is to achieve high accuracy in terms of dimensional accuracy of surface roughness and less tool wear. The lower thermal conductivity, high strength, high ductility made Austenitic AISI304 stainless steels harder material, which lead to difficulty in machining. A high impact surface and tool wear were normally experienced during machining of AISI304 materials because of their high strength and high ductility. However, a superior surface is the most essential parameter to decide the nature of the product and is precision to enhance, wear protection, and weariness quality, of fabricated items. Deep cryogenic treatment is normally preferred in the machining to improve their microstructure properties of the material, which convert retained austenite to martensite as the martensite is the hardest phase in the iron carbon diagram. The presence of martensite phase in the material improves the hardness property. The deep cryogenic treatment involves a low-temperature treatment process around -176°C using liquid nitrogen; it enhances the wear resistance, surface roughness of the cutting tool. Selection of the optimum cutting parameters by using various optimization techniques can avoid to improper selection of the cutting parameters. This causes high manufacturing cost and poor quality of the machined part.

Hence it is essential to use a systematic tool for optimization of cutting parameters. Taguchi L9 method is the most effective tool used for optimization.

Literatures also reported that few mechanical and physical properties of the cutting tool material can be improved after cryogenic treatment. Sreerama Reddy et al. [1] analyzed the effect of low-temperature treatment on carbide tool insert and untreated insert on the C-45 work piece. It was observed that the flank wear and surface roughness were found to be better in low-temperature treatment carbide insert. Whereas Khan et al. [2] performed an investigation on commercially available titanium grade 2 with cryogenically treated carbide tool insert and untreated tool in a dry cutting environment. The author analyzed the experimental results using Taguchi method L9 orthogonal array and it was found that cryogenically treated insert resist more wear compared to the untreated. Also studied by Akhbarizadeh et al. [3] carried out an experiment for different cryogenic treatment methods such as shallow and deep cryogenic treatment. The results revealed that the deep cryogenic method was performed better in comparison with shallow cryogenic treatment. An increase in percentage of carbide and their homogenous distribution due to cryogenic treatment was studied by Amini et al. [4]. The result indicated an improvement in the hardness and tool wear for optimum holding time. Likewise, Bordin et al. [5] was performed experimentation on applied cryogenic treatment for tungsten carbide insert. It was observed that cryogenic cooling reduces the adhesive wear in comparison with dry machining. Likewise, Das et al. [6] investigated the performance of deep cryogenic treatment and compared their results with conventional heat treatment on AISI2 steel. In another work the use of cryogenic treatment for cutting tool significantly improves tool wear by Dhananchezian et al. [7] studied the effect of liquid nitrogen on rake face turning of Ti-6Al-4V alloy. The result showed that the cryogenic cooling reduces the cutting temperature by 61- 66% surface roughness by 36% and flank wear by 33%. In this regard Ozbek et al. [8] studied the improvement in coated cryogenic treatment insert in comparison with the uncoated insert in turning of AISI 304 steel. It was found that cryogenically treated insert exhibits superior in wear resistant compare to the uncoated. Similarly, Ozbek et al. [9] performed a test on different soaking time of cryo-treatment for tool wear in turning austenite stainless steel. The study revealed a positive wear resistant for 24hrs soaking time. It was also observed that increase in hardness and improved microstructure in carbide insert. Yong et al. [10] studied on the cryogenic treatment of tungsten carbide. It was found that cryogenic treatment tool performs better in intermittent machining than continuous. In another work, Seah et al [11] investigated on different condition of treatment of carbide insets. The authors found, improved tool life and wear resistance for cryogenic treatment insert even at higher cutting speed. It was also observed that over all resistance to chipping. Recently, Cryogenic treatment performance was reported by Vadivel et al. [12] investigated on coated cryogenic treated and untreated insert. This result showed coated carbide insert significantly exhibited better results in comparison with untreated insert.

Apart from cryogenic some of the researchers studied on optimization of cutting parameter by using Taguchi technique in this regard, Mahdavinejad et al. [13] adopted a design of experiment for finding the optimum value of tool wear and surface roughness of turning AISI304 stainless steel, using Analysis of Variance. In the study it was analyzed that the most affecting parameter for tool wear is the cutting speed and for surface roughness is the feed rate. In another work Taguchi method of the L9 orthogonal array was studied by Whereas Sitki Akıncıoğlu et al [14] used to optimize the cryogenic treated tool insert in turn of Haste alloy on surface roughness. The results demonstrated that the feed rate contribution was 87.64% and the results revealed that shallow cryogenic treatment and deep cryogenic process improved the tool wear resistance. Applied Taguchi method by Zerti1 et al. [15] found the effect of cutting parameters under optimum cutting condition in their study. Analysis of variance was used to evaluate the affecting parameter. The study concluded that feed rate was most significant parameter for surface roughness. In another study by E. Daniel Kirby et al. [16] on Taguchi method, it was found that an enhanced tool life and increase in resistance to tool wear was obtained for cryogenic treatment. Likewise, performed an optimization technique on machining parameters by Hascalık et al. [17] using a taguchi orthogonal

array method. The results revealed that feed rate and cutting speed are the most predominant factor for surface roughness and at tool life. In an experiment conducted by Ramazan Cakiroglu et al. [18] it was found that feed rate is the main affecting parameter for surface roughness and speed was found to be the most affecting parameter for tool wear. In their study, experimental results were found to be in line with design of experiment.

Many researchers have conducted experiment on cryogenic treatment process to improve the properties of carbide insert in this regard, Thakur et al. [19] performed experiment on cryogenic treatment for tungsten carbide inserts subjected to different post treatments. The experimental results indicated a remarkable change in all post-treatment analysis. Similarly, Gill et al. [20] reported that low temperature treated tungsten carbide insert performance was found to be good in wet turning condition under different machining conditions and exhibited increase in the tool life in interrupted machining. Similarly, investigated on machining AISI304 stainless steel by Kaladhar et al. [21] on popularly used grade due to their low heat conductivity and high built-up edge formation. The author employed Taguchi methods with a two-layer chemical vapor deposition (CVD) coated tool insert. It was found that cutting speed is the most significant factor for surface roughness and flank wear. Ciftci et al. [22] analyzed the influence austenitic stainless steels by using coated cemented carbide tools under different cutting speed. The results showed that the cutting speed affect the surface roughness of the machined parts. Cryo-processing cooling investigation by Reitz et al. [23] exposed the material to extremely low temperatures to change their mechanical and physical properties. It was observed that reducing the amount of retained austenite; this improves on wear resistance, dimensional stability, electrical and thermal conductivity, and hardness. Da Silva et al. [24] performed a cryogenic treatment on high steel tool to indicated micro structural changes in the material that can impact tool life and productivity significantly. It was found that tool life changes from 92% to 81.7% when utilizing the cryogenically treated HSS tool in the industry. Dhar et al. [28] investigated on minimization of cutting. The results revealed that the reduction in tool wear and surface roughness by minimum quality lubricant and it was observed that reduction in tool chip temperature and work-tool interface. From the literature, it was found that most of the studies are restricted to the studies of cryogenic treated carbide cutting tool in terms of optimization of cutting parameters such as tool wear, surface roughness and hardness. However, the available results in the literature related to wear, surface roughness and optimization of cutting parameters were not providing detailed results. Thus, the present study is aimed at investigating the performance of a cryogenic treated carbide cutting tool for different cutting parameters. The test results were validated with Taguchi technique. In addition, a confirmation test was performed to validate the experimental results.

EXPERIMENTAL DETAILS

Experimental Methodology

The Machining work carried on AISI304 Steel work piece having a specification of 30mm diameter, length 150mm and having chemical composition of 0.085% C, 18% Cr, 66.34% Fe, 2% Mn, 8% Ni, 0.045% P, 0.035S, 1% Si. The length / diameter proportion was considered during the experimentation in order to meet the ISO 3685. In the course of experimentation, a total of 9 work piece were utilized to predict the tool life. The machining operation of the cutting tool insert was performed using CNC lathe (ACE jobber CNC Lathe) having a maximum speed of 4000rpm, maximum turning diameter 290mm, length 400mm and chuck size 200mm. The machining experiments were performed for different cutting speed, depth of cut, and feed rate. The cutting speed was done for 100m/min, 120m/min, 140m/min and depth of cut was done for 0.5mm, 1.0mm and 1.5mm. While feed rate 0.1mm/rev, 0.15mm/rev and 0.2mm/rev. Material characterization of the carbide inserts were examined by using scanning electron microscope (SEM) combined with micro hardness analyzer. Hardness test was conducted for both cryogenic treated and untreated

inserts by using Vickers hardness testing machine with a load of 50Kgf impressed on the tool insert. With a dwell time, 15sec and the average of the hardness were evaluated. The improved surface structure due to cryogenic treatment was measured with the use of surface measuring instrument SJ210 average value were evaluated. The flank wear caused due to rubbing action between cutting tool and workpiece was measured in the experiment. The maximum flank wear test of the insert was measured at a time step of 5 min as per ISO 3685 of 1993[25-26].

In the present work, examined the cryogenic treatment of a tungsten carbide cutting tool and compared their results with untreated carbide cutting tool. An optimization test was carried out using Taguchi L9 array. A Minitab Statistical 16 Software trial version was used for Taguchi Design. Various mechanical tests were performed for both cryogenic treated and untreated insert for comparison. In the process of cryogenic, the temperature was lowered from ambient conditions to -176°C in the beginning at a rate of -1°C /min and was soaked maintaining the same temperature for 36 hours. The temperature was brought back to its ambient conditions at a rate of -1°C /min. The experiment was carried out for various parameters such as cutting speed, feed rate, and depth of cut. In the current experimental set up, PVD coated tungsten carbide insert of ISO standard TNMG160408GS PC8110 was used. The cutting tool insert thickness was 4.76mm, 0.8mm nose of triangular shape was used for machining.

Design of Experiments

The optimization of the experimental results was performed by using Taguchi approach with the L9 orthogonal array to optimize the cutting parameters and to determine the optimal level of process parameters for optimizing the quality of surface finish and tool wear of AISI304 material. In this three different cutting levels were considered for each parameter as shown in Table 1. The Table 2 demonstrates the response table for tool wear and surface roughness.

Table 1. Selection of cutting parameters for different levels.

Parameters	Level-1	Level-2	Level-3
Cutting speed, (m/min)	100	120	140
Depth of Cut, (mm)	0.5	1	1.5
Feed, (mm/rev)	0.1	0.15	0.2

Table 2. Response Table for different cutting parameter obtained from Taguchi L9.

Test No.	Cutting Speed, (m/min)	Depth of Cut,(mm)	Feed, (mm/rev)	Flank wear,(mm)	Surface Roughness, (microns)
1	100	0.5	0.10	0.217	2.123
2	100	1.0	0.15	0.17	1.11
3	100	1.5	0.20	0.26	2.59
4	120	0.5	0.15	0.33	0.79
5	120	1.0	0.20	0.51	2.312
6	120	1.5	0.10	0.60	1.75
7	140	0.5	0.20	0.34	1.54
8	140	1.0	0.10	0.61	0.902
9	140	1.5	0.15	0.52	1.12
				Avg. Tool Wear = 0.395	Avg. surface roughness = 1.581

RESULTS AND DISCUSSION

Flank Wear Study

The flank wear produced during the experimental operation on stainless steel AISI304 was observed in terms of tool wear for coated and uncoated cutting tool insert frequently for varying time. In the present wear study, it was observed that the tool wear was occurred due to various factors that include rubbing action between the cutting tool and work piece, enormous amount of heat generation at the tool tip and excessive generation of chips during machining operation. These factors cause a premature failure of the cutting tool. The flank wear growth during the machining operation was observed for three different speed rates. The flank wear enhanced was noticed for increase in speed. Figures 1, 2 and 3 shows wear resistance, at different cutting speed, having the constant depth of cut and feed rate for cryogenic treated and untreated inserts. From the graph shown in Figure 1 at a cutting of speed of 100m/min, depth of cut 0.5mm& feed rate 0.1mm rev/min the treated insert resists maximum wear than untreated inserts. As cutting speed increase, the wear resistant was found to be more in cryogenic treated compared to untreated insert as demonstrated in the Figures 1,2 and 3. The presence of coating layer over the cutting tool, resist initial wear due to machining operation because of improved surface roughness and strengthen the surface resistance. Hence the initial wear produced for both were seen to be slow and increased rapidly with time. This is due to the presence of coating layer over the cutting tool. Wear tests were conducted for all three cutting speed, cryogenic insert resist wear more effectively due to enhanced thermal and other mechanical properties, Hence, enhance tool life was observed for cryogenic treated inserts than untreated insert. However, an increased wear was noticed for the untreated cutting tool for all the three different cutting speed. The gain in hardness and improved surface roughness due to cryogenic treatment upgrade the tool life of the cutting tool up to some extent.

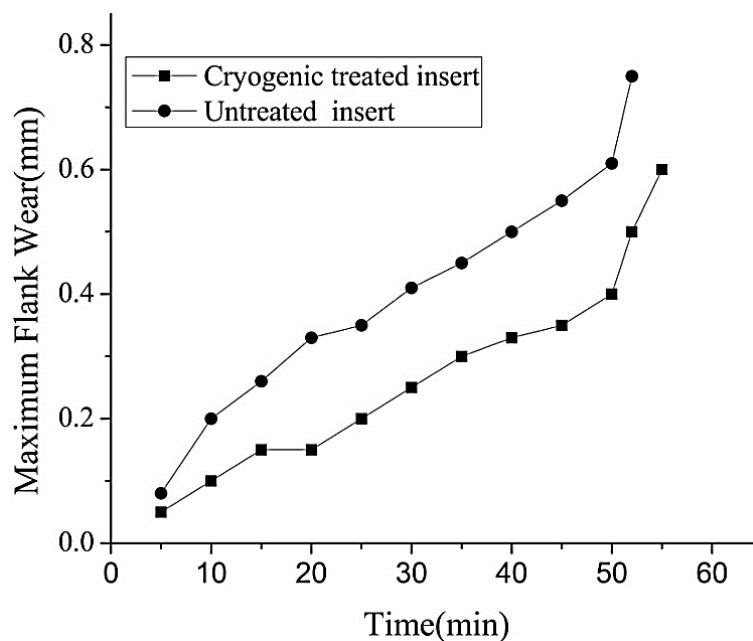


Figure 1. Maximum Flank wear vs. Machining time for 100m/min cutting speed.

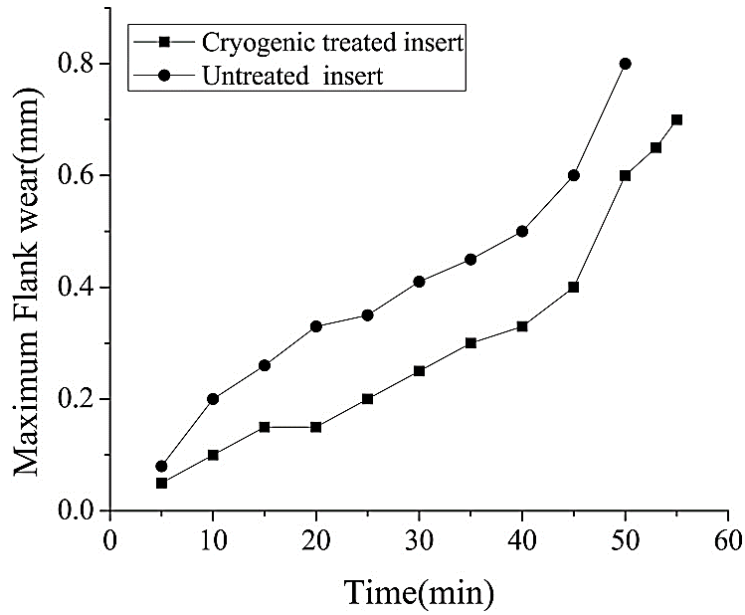


Figure 2. Maximum Flank wear vs. Machining time for 120m/min cutting speed.

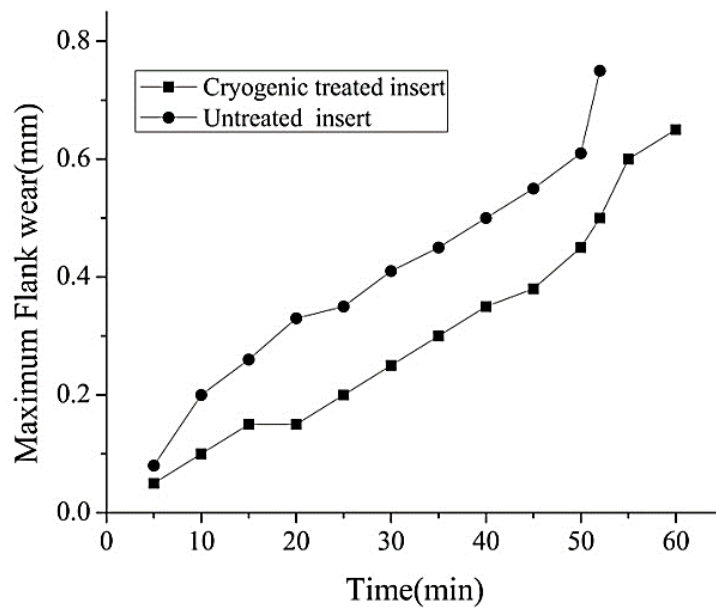


Figure 3. Maximum Flank wear vs. Machining time for 140m/min cutting speed

An enhanced tool life was noticed in terms of tool wear due to cryogenic treatment of tungsten carbide cutting tool. The cryogenically treated cutting tool performs better under discontinuous machining condition at higher cutting speed. The results also demonstrate that an improved wear resistance of cryogenic treated insert was found in comparison with untreated tool insert under deep cryogenic treatment for different holding times on machining AISI 304 steel. The Table 3 reveals a tool life (min) for cryogenic treated tool insert and untreated tool insert.

Table 3. Tool life for different cutting speed for both cryogenic treated and untreated cutting tool.

Machining Condition	Tool life for different cutting speed (min)		
	100 (m/min)	120 (m/min)	140 (m/min)
Cryogenic treated cutting tool	55	49	46
Untreated cutting tool	50	44	40

Microscopic Study of Tool Wear

The Figure 4 and Figure 5 showed the variety of normal flank wears at each exploratory run for cryogenic treated and untreated cutting tool inserts. It is observed that the utilization of a cryogenic treated cutting insert helps in reducing the flank wear strikingly. The flank wear was noticed minimum in the range of cutting speed (100-140m/min), depth of cut (0.5mm), and feed rate (0.1mm/rev) in the present investigation. The SEM images demonstrate a minimum wear in case of cryogenic treated cutting insert, however untreated insert observed to be more in correlation with the cryogenic treated cutting tool insert.

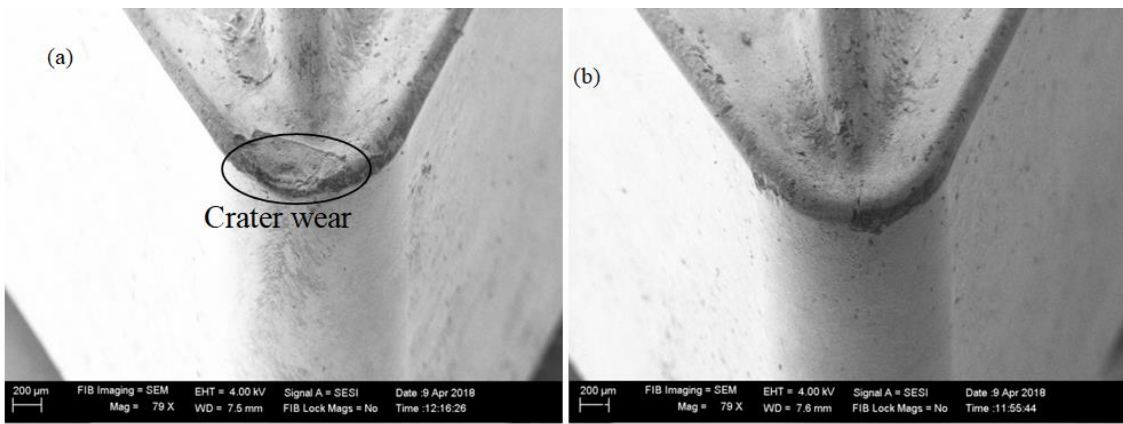


Figure 4. Microscopic image of wear observed at cutting speed 140m/min, depth of cut 0.5mm and feed rate 0.1mm/rev for(a) untreated cutting tool insert and (b) cryogenic treated cutting tool insert.

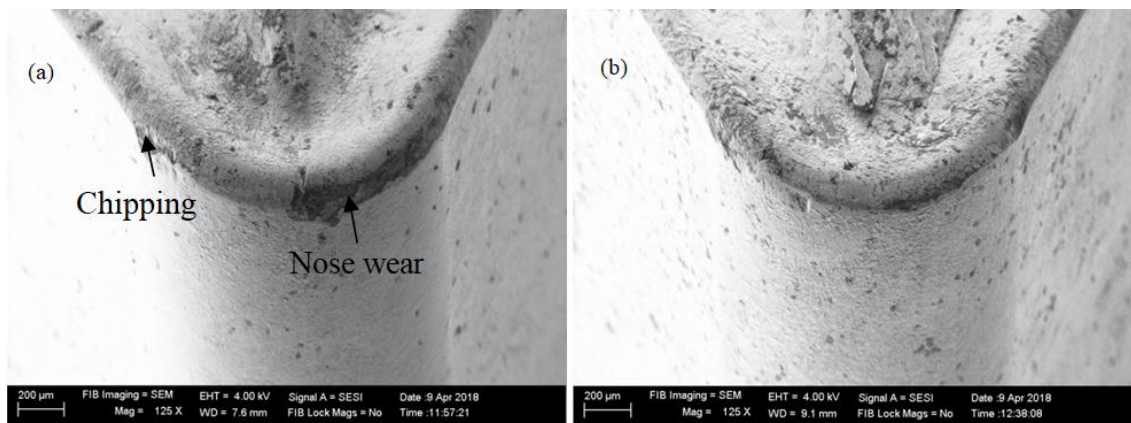


Figure 5. Microscopic image of wear observed at cutting speed 100m/min, depth of cut 0.5mm and feed rate 0.1mm/rev for(a) untreated cutting tool insert and (b) cryogenic treated cutting tool insert.

The use of cryogenic treated cutting tool insert was found to be better at higher cutting speed of 140m/min for machining AISI 304 material. This is due to the reduction in flank and crater wear at incredible extent. From the figure, it is seen that the crater wear is significantly reduced in case of

for cryogenic treated cutting tools. The width of crater wear was found to be less for cryogenic treated cutting tool than the untreated one as shown in Figure 4a and 4b. The crater wear on the rake surface and significant impacts were missing (Figure 4b) for higher cutting speeds in comparison with untreated cutting tool. The fracture and chipping are found to be seen less in the case of cryogenic treated cutting tool. Minimized built-up edges were observed due to cryogenic treatment even at higher cutting speed.

Morphological Study of Cryogenic Treated and Untreated Insert

The SEM microstructure analysis was carried out for both cryogenic treated and untreated insert as shown in Figure 6a and Figure 6b. The analysis was conducted according to the ASTM B6572003 standard method [26]. The general phases were observed in Tungsten carbide α phase indicates tungsten carbide, β phase indicated Cobalt binder, γ phase indicates Carbides of cubic lattice and Eta η phase multiple carbides tungsten. The increased concentration of carbide particle was seen. The enhanced Eta η -phase was obtained due to long exposure of the insert to a lower temperature. The similar micro structure phases were obtained in [1, 2]. From the SEM image, an increase in the eta phase is observed in Figure 6a. The increase in eta phase improves wear resistance because of the densely packed carbides in the structure due to longer exposure of the cutting tool to a lower temperature [9].

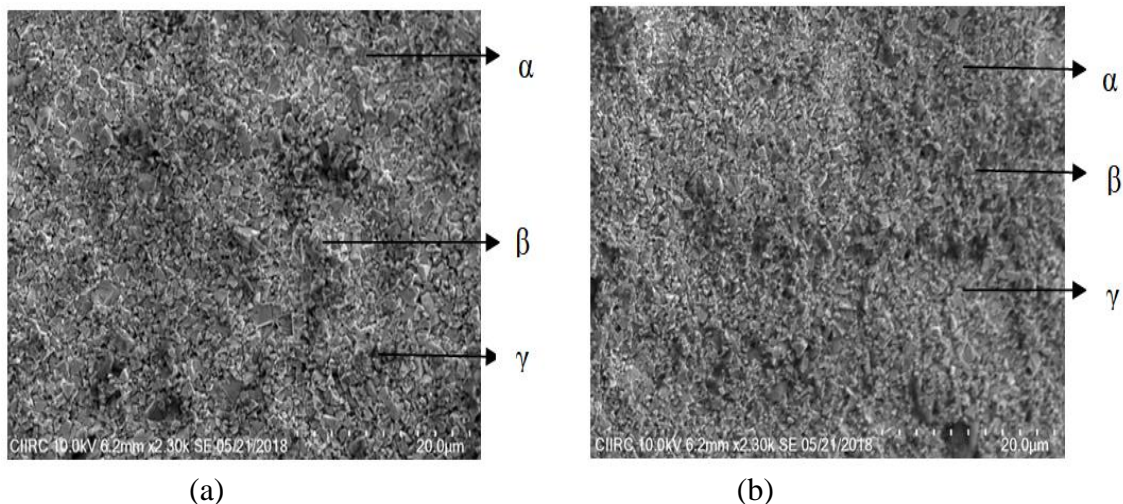


Figure 6. SEM image (a) Cryogenic cutting tool insert (b) Untreated cutting tool insert.

Hardness Test

In the present work, Vickers hardness test of the carbide cutting tool was analyzed. The effect of cryogenic treatment on carbide tool inserts was examined and compared their results with untreated cutting tool as shown in Figure 7. An increase in hardness rate is obtained due to improved micro structural and phase change of a material. The cutting tools which were cryogenically treated demonstrated further increment in hardness because of the higher chromium carbide rate. The enhanced hardness was seen for deep cryogenically treated tungsten carbide tool due to increase in the Eta phase, the carbon percentage increases the hardness over the surface of the insert. The Eta phase was found multiple carbides results in increase in hardness. The growth in the hardness was seen to be approximately 4% after cryogenic treatment. The improved hardness of the cryogenic treated insert was observed due to cobalt densification by [1].

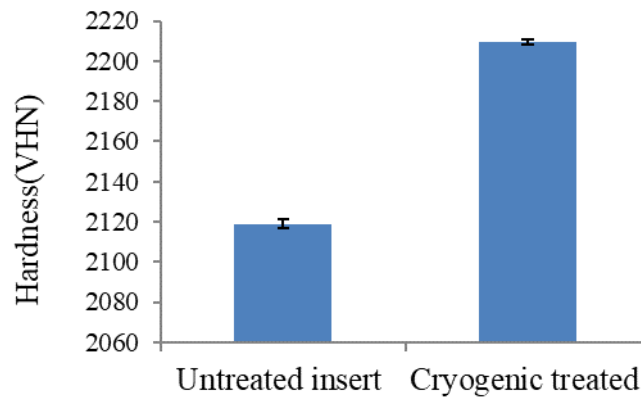


Figure 7. Hardness values at cryogenic treated and untreated insert.

Surface Roughness

Surface roughness is an important parameter to decide the quality of the machined parts and life of the cutting tool. The irregularity of machined surface is output of the machining process including the selection of cutting tool, feed rate and depth of cut and also depend on different coolant were in decrease the cutting temperature. The Figure 8 shows the surface roughness of cryogenic treated and untreated cutting tool for different cutting speed of machining time 10min. An increase in the cutting speed decrease in surface roughness is observed. Also it was noticed that cryogenic treatment inserts show lower surface roughness in comparison with untreated insert. Reddy et al [1] claimed due to increase in the thermal conductivity in the cryogenic treated surface roughness reduces. Dhar [27] also reported cryogenic cooling reduces the surface roughness.

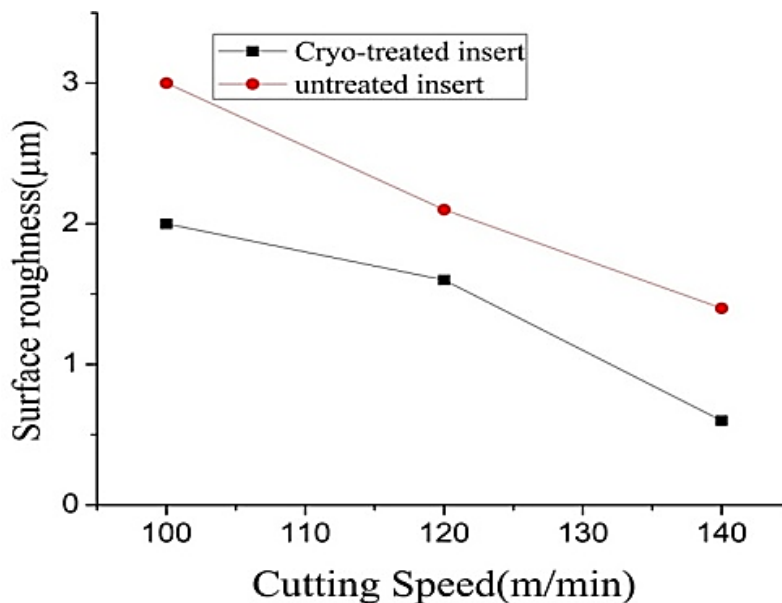


Figure 8. Variation of surface roughness for different cutting speed.

ANOVA for Tool Wear

In this present work ANOVA method was deployed in order to find out the essential factor which affects the performance measures. The Table 4 demonstrates that the cutting speed is the most significant affecting parameter among others in terms of tool wear. A maximum contribution for the tool failure is obtained for cutting speed and a minimize contribution was obtained for feed rate. The Table 5 demonstrates that the feed rate is the most significant affecting parameter among others

in terms of surface roughness. The analysis was conducted for the significance level of $\alpha=0.05$ i.e. for a confidence level of 95% if the p-value less than 0.05 are considered.

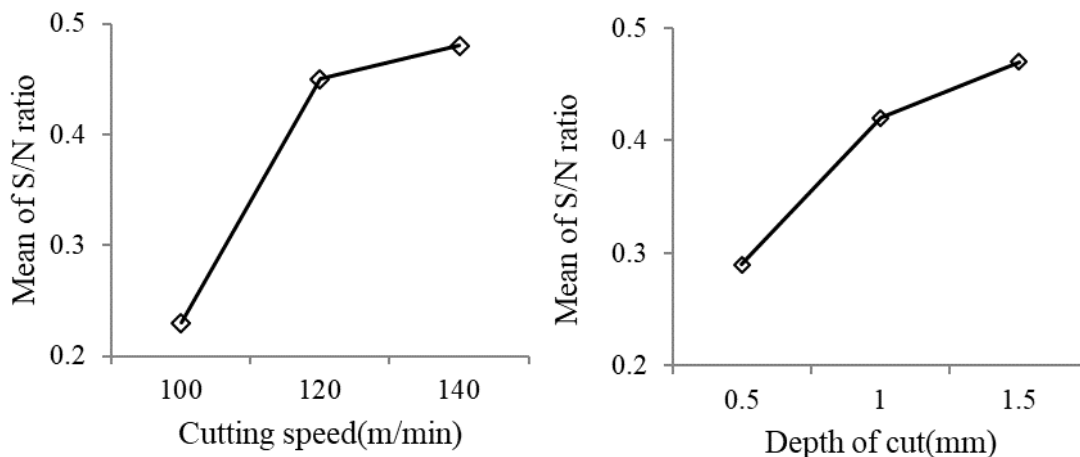
Table 4. Analysis of variance for tool wear (ANOVA).

Source	DOF	Seq.SS	MS	F	P	% Contribution
Cutting speed	2	0.145231	0.072615	44.95	0.022	65.52
Depth of cut	2	0.045951	0.022975	14.22	0.066	20.72
Feed rate	2	0.030471	0.015235	9.43	0.096	13.74
Residual Error	2	0.003231	0.001615			
Total	8	0.224884				

DOF-Degrees of freedom, Seq.SS-Sequential sum of squares, MS-Mean sum of Squares

Main Effect Graphs for Tool Wear and Surface Roughness

The ANOVA analysis was made with the help of the MINITAB16 statistical tool to study the cutting parameters (cutting speed, depth of cut and feed rate) and the main effect plots on tool wear and surface roughness were analyzed as shown in Figures 7 and 8 respectively. The main effect graphs showed the variation of individual response with the three cutting parameters. In the main effect graphs x-axis indicates the value of cutting parameters at three levels and the y-axis indicates the response value. The main effect graphs were used for finding the optimum levels of tool wear and surface roughness. Figure 9 shows the main effect graphs for tool wear as tool wear increase with increase with cutting speed; on the other hand, increase in the feed rate will decrease in tool wear. However, increase in depth of cut there is an increase in tool wear. Maximum tool wear shown at the 1.5mm depth of cut. Similarly, from Figure 10 as cutting speed increase surface roughness decrease on the other hand increase in feed rate will increase in the surface roughness. From Figure 9 optimum value of tool wear Cutting speed of 110 m/min [level 1] Depth of cut 0.5 mm [level 1] Feed rate of 0.15 mm/rev [level 2] From Figure 10 low value of surface roughness was obtained at Cutting speed of 140m/min [level 3] Depth of cut 1.0 mm [level 2] Feed rate of 0.15 mm/rev [level2].



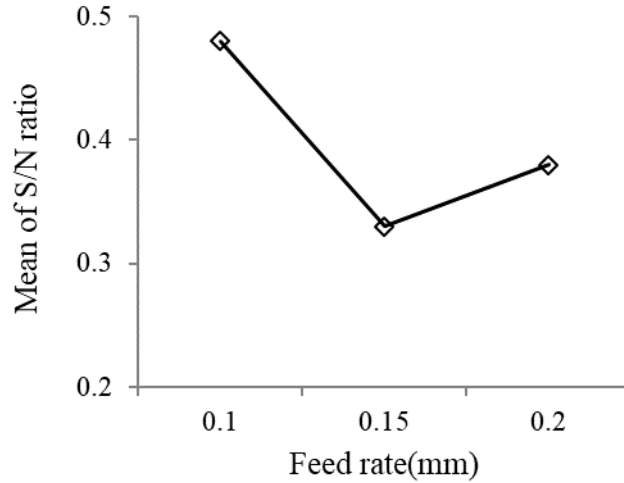


Figure 9. Main effect plot for tool wear.

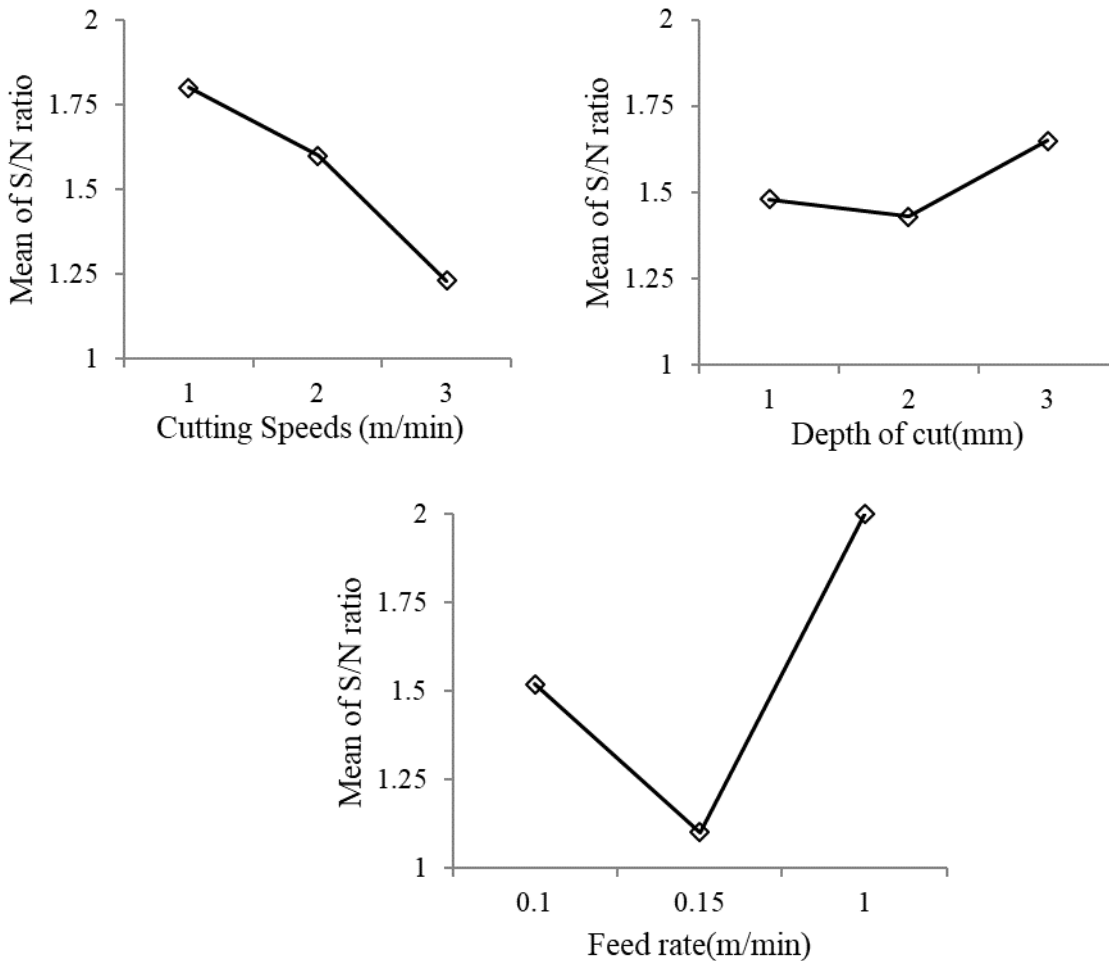


Figure 10. Main effect plot for surface roughness.

Optimal Design

An optimization of the tool wear and surface roughness is adopted in the present study considering from mean response value from Table 2. The predicted values for surface roughness and tool wear were evaluated by using the optimum levels of cutting speed, feed rate and depth of cut for surface roughness and tool wear.

Tool wear for cutting speed and depth of cut is given by equation Equation (1).

$$\mu_{\text{Tool Wear}} = V_1 + D_1 - \text{Avg}_{\text{Tw}} \quad (1)$$

The values of V_1 and D_1 were taken from Table 5 and average tool wear was considered to be 0.395 from the Table 2.

$$\mu_{\text{Tool Wear}} = 0.1157$$

Confidence interval (CI) for tool wear was calculated using Equation (2).

$$CI = \frac{\sqrt{F_{95\%, 1, \text{DOF error}} \times V_{\text{error}}}}{\eta_{\text{eff}}} \quad (2)$$

When η_{eff} is calculated using equation Equation (3).

$$\begin{aligned} \eta_{\text{eff}} &= \frac{\text{Number of trials}}{1 + \text{DOF associated to that level}} \\ &= \frac{9}{1+2+2} = 1.8 \end{aligned} \quad (3)$$

From F-Table $F_{95\% 1,4}=7.71$

From Table 4 we have, $V_{\text{error}}=0.001615$

$$CI = \frac{\sqrt{7.71 \times 0.001615}}{1.8} = 0.083$$

The predicted optimal range of tool wears at 95% confidence level is given by Equation (4).

$$\begin{aligned} 0.1157 - 0.083 &\leq \mu_{\text{Tool Wear}} \leq 0.1157 + 0.083 \\ 0.0327 &\leq \mu_{\text{Tool Wear}} \leq 0.1987 \end{aligned} \quad (4)$$

Surface roughness of cutting speed and feed rate is given by Equation (5)

$$\mu_{\text{Sa}} = V_3 + F.R_2 - \text{Avg}_{\text{SR}} \quad (5)$$

The values of V_3 and $F.R_2$ were taken from Table 6 and average surface roughness was considered to be 1.581 from the Table 2.

$$\mu_{\text{Sa}} = 1.187 + 1.007 - 1.581 = 0.613$$

Confidence interval (CI) for surface roughness was calculated using- Equation (6).

$$CI = \frac{\sqrt{F_{95\%, 1, \text{DOF error}} \times V_{\text{error}}}}{\eta_{\text{eff}}} \quad (6)$$

When η_{eff} is calculated using Equation (7)

$$\begin{aligned} \text{Where } \eta_{\text{eff}} &= \frac{\text{Number of trials}}{1 + \text{DOF associated to that level}} \\ &= \frac{9}{1+2+2} = 1.8 \end{aligned} \quad (7)$$

F95% 1,4=7.71(From F-table), $V_{error}=0.1649$ (from Table 5)

$$CI = \sqrt{\frac{7.71 \times 0.1649}{1.8}} = 0.840$$

The predicted optimal range of surface roughness at 95% confidence level is given by Equation (8).

$$\begin{aligned} 0.613-0.840 \leq \mu_{Sa} \leq 0.613+0.840 \\ -0.227 \leq \mu_{Sa} \leq 1.453 \end{aligned} \tag{8}$$

Table 5. Means response table for tool wear.

Level	Cutting speed(V)	Dept of cut(D)	Feed rate(FR)
1	0.2157	0.2957	0.4757
2	0.4800	0.4300	0.3400
3	0.4900	0.4600	0.3700
Delta	0.2743	0.1643	0.1357
Rank	1	2	3

Table 6. Means response table for surface roughness.

Level	Cutting speed(V)	Dept of cut(D)	Feed rate(FR)
1	1.941	1.484	1.592
2	1.617	1.441	1.007
3	1.187	1.820	2.147
Delta	0.754	0.379	1.141
Rank	2	3	1

Where SR_{opt} and TW_{opt} denote the predicted value of surface roughness and the tool wear in optimum condition respectively. As per the Equations (9) & (10), it was calculated that optimum value of $SR_{opt} = 0.473 \mu m$ and $TW_{opt} = 0.0614 mm$.

$$TW_{opt} = (V1 - Avg_{TW}) + (D1 - Avg_{TW}) + (FR2 - Avg_{TW}) + Avg_{TW} \tag{9}$$

$$SR_{opt} = (V3 - Avg_{SR}) + (D2 - Avg_{SR}) + (FR2 - Avg_{SR}) + Avg_{SR} \tag{10}$$

Confirmation Test

Confirmation test was carried out using the optimum surface roughness levels (3, 2, 2) and tool wear (1,1,2) selected. Among various experimental parameters, the experimental value of surface roughness value is $0.421 \mu m$ and optimum roughness values using the Taguchi technique were calculated by estimating $0.473 \mu m$. While for the tool wear is $0.0560 mm$ obtained from the experimental data. The tool wear values using the Taguchi method were calculated by estimating $0.0614 \mu m$. The results demonstrate an error of 8.79% and 10.9% error between experimental value and predicted value for wear and surface roughness respectively. Hence the the predicted and the experimental surface roughness values were found to be in good agreement. The confirmation test results showed optimization correctly.

CONCLUSION

This research paper compared and discussed on the investigation of cryogenic treated cutting tool insert and untreated cutting tool insert. The following conclusions were drawn based on the experiments and statistical study.

1. The tool wear resistance was more effective in cryogenically treated tungsten carbide inserts due to enhanced thermal and other mechanical properties, which results in enhancing the tool life of the cutting inserts up to some extent for all the three cutting speed tested. An increased wear was noticed in the untreated cutting tool as compared with Cryogenic treated one. It was observed from the results that the utilization of a cryogenically treated cutting tool insert helps in decreasing the flank wear strikingly.
2. The enhanced in the Eta phase, the carbon percentage increased. The improved hardness on the top surface of the insert, the Eta phase indicates multiple carbides. Hence the gain in hardness and improved surface roughness was achieved which upgrade the tool life. The growth in the hardness approximately 4% after Cryogenic treatment.
3. The surface roughness diminishes with increase in cutting speed. With cryogenic treated embeds in correlation with untreated tool at all cutting rates.
4. The design of experiment in the current study proposed optimum levels for cutting parameters. The errors between predicted and experimental results were found to be 8.79% for tool wear and 10.9% for surface roughness.

REFERENCES

- [1] Sreerama Reddy TV, Sornakumar T, Venkatarama Reddy M, Venkatram R. Machining performance of low temperature treated P-30 tungsten carbide cutting tool inserts. *Cryogenics*. 2008;48:458–461.
- [2] Khan A, Maity K. Comparative study of some machinability aspects in turning of pure titanium with untreated and cryogenically treated carbide inserts. *Journal of Manufacturing Processes*. 2017;28:272–284.
- [3] Akhbarizadeh A, Shafyei A, Golozar MA. Effects of cryogenic treatment on wear behavior of D6 tool steel. *Materials and Design*. 2009;30:3259–3264.
- [4] Amini K, Nategh S, Shafyei A. Influence of different cryotreatments on tribological behavior of 80CrMo12 5 cold work tool steel. *Materials and Design*. 2010;31:4666–4675.
- [5] Bordin A, Bruschi S, Ghiotti A, Bariani PF. Analysis of tool wear in cryogenic machining of additive manufactured Ti6Al4V alloy. *Wear*. 2015;328-329:89–99.
- [6] Das D, Dutta AK, Ray KK. Correlation of microstructure with wear behaviour of deep cryogenically treated AISI D2 steel. *Wear*. 2009; 267:1371–1380.
- [7] Dhananchezian, Pradeep Kumar M. Cryogenic turning of the Ti–6Al–4V alloy with modified cutting tool inserts. *Cryogenics*. 2011;51:34–40.
- [8] Özbek NA, Çiçek A, Gülesinc M, Özbek O. Effect of cutting conditions on wear performance of cryogenically treated tungsten carbide inserts in dry turning of stainless steel. *Tribology International* 2015.
- [9] Özbek NA, Çiçek A, Gülesin M, Özbek O. Investigation of the effects of cryogenic treatment applied at different holding times to cemented carbide inserts on tool wear. *International Journal of Machine Tools & Manufacture*. 2014;86:34–43.
- [10] Yong AYL, Seah KHW, Rahman M. Performance evaluation of cryogenically treated tungsten carbide tools in turning. *International Journal of Machine Tools & Manufacture*. 2006;46:2051–2056.

- [11] Seah KH., Rahman M. Yong KH, Performance evaluation of cryogenically treated tungsten carbide cutting tool inserts, Proceedings of the Institution of Mechanical Engineers. Part B: Journal of Engineering Manufacture. (2003); 217:29:29-43.
- [12] Vadivel K. Rudramoorthy R. Performance analysis of cryogenically treated coated carbide inserts. *Int J Adv Manuf Technol.* (2009);42:222–232.
- [13] Mahdavinejadand RA, Saeedy S. Investigation of the influential parameters of machining of AISI 304 stainless steel. *Indian Academy of Sciences.* 2011;36: 963–970.
- [14] Akıncıoğlu, Gökkaya H, Uygur İ. The effects of cryogenic-treated carbide tools on tool wear and surface roughness of turning of Hastelloy C22 based on Taguchi method. *Int J Adv Manuf Technol.* 2016;82:303-314.
- [15] Rashid WB, Goel S, Davim JP, Joshi SN. Parametric design optimization of hard turning of AISI 4340 steel (69 HRC). *Int J Adv Manuf Technol.* 2016;82:451–462.
- [16] Kirby ED, Zhang Z. Joseph C. Chen. Chen J. Optimizing surface finish in a turning operation using the Taguch parameter design method. *Int J Adv Manuf Technol.* 2006;30:1021–1029.
- [17] Haşcalık A, Çaydaş U. Optimization of turning parameters for surface roughness and tool life based on the Taguchi method. *Int J Adv Manuf Technol.* 2008;38:896–903.
- [18] Cakıroğlu R, Acır A. Optimization of cutting parameters on drill bit temperature in drilling by Taguchi method. *Measurement.* 2013;46:3525–3531.
- [19] Thakur D, Ramamoorthy B, Vijayaraghavan L. Influence of different post treatments on tungsten carbide–cobalt inserts. *Materials Letters.*2008; 62:4403–4406.
- [20] Gill SS, Singh R, Singh H, Singh J. Wear behaviour of cryogenically treated tungsten carbide inserts under dry and wet turning conditions. *International Journal of Machine Tools & Manufacture.* 2009;49:256–260.
- [21] Kaladhar M, Subbaiah KV, Rao CHS. Optimization of surface roughness and tool flank wear in turning of AISI 304 austenitic stainless steel with CVD coated tool. *Journal of Engineering Science and Technology.*2013;8:165 – 176.
- [22] Ciftci I. Machining of austenitic stainless steels using CVD multi-layer coated cemented carbide tools. *Tribology International.* (2006);39:565–569.
- [23] Reitz W, Pendray J. cryoprocessing of materials. A review of current status. *Materials and Manufacturing Processes.* 2001;16:829–840.
- [24] Da Silva FJ, Franco SD, Machado ÁR, Ezugwu EO, Souza AM. Performance of cryogenically treated HSS tools. *Wear.* 2006;261:674–685.
- [25] ISO 3685-1993(E). Tool life testing with single point turning tools; 1993.
- [26] Standard method for metallographic determination of microstructure in cemented tungsten carbides, B 657, Annual book of ASTM standards. ASTM International. 2003;02.05:386–91.
- [27] Singh R, Singh B. Comparison of cryo treatment effect on machining characteristics of titanium in electric discharge machining. *International Journal of Automotive and Mechanical Engineering.* 2011;3:239-248.
- [28] Dhar NR, Kamruzzaman M and Ahmed M. Effect of minimum quantity lubrication on tool wear and surface roughness in turning AISI-4340 steel. *Journal of Materials Processing Technology.* 2006;172:299-304.

Thermal management of vehicle radiator by nanocellulose with one-dimensional analysis

Cite as: AIP Conference Proceedings 2059, 020043 (2019); <https://doi.org/10.1063/1.5085986>
Published Online: 11 January 2019

F. Benedict, K. Kadirgama, D. Ramasamy, M. M. Noor, M. Asok Raj Kumar, M. M. Rahman, Z. Ghazali, and B. Sagmesh



View Online



Export Citation

ARTICLES YOU MAY BE INTERESTED IN

[An experimental investigation on the combustion and performance of an HCCI-DI engine](#)
AIP Conference Proceedings 2059, 020010 (2019); <https://doi.org/10.1063/1.5085953>

[An experimental study of the performance and emission characteristics of a compression ignition \(CI\) engine fueled with palm oil based biodiesel](#)
AIP Conference Proceedings 2059, 020036 (2019); <https://doi.org/10.1063/1.5085979>

[Influence of TDSI/LUTAH fuel booster on the performance and emissions of diesel engine](#)
AIP Conference Proceedings 2059, 020042 (2019); <https://doi.org/10.1063/1.5085985>

AIP | Conference Proceedings

Get **30% off** all
print proceedings!

Enter Promotion Code **PDF30** at checkout



Thermal Management of Vehicle Radiator by Nanocellulose with One-Dimensional Analysis

F. Benedict¹, K. Kadirgama^{1, a)}, D. Ramasamy¹, M.M. Noor¹, M. Asok Raj Kumar²,
M.M. Rahman¹, Z. Ghazali¹, B. Sagmesh³

¹Faculty of Mechanical Engineering, University Malaysia Pahang (UMP),
26600, Pekan Pahang, Malaysia.

²Gnanamani College of Technology, Namakkal_637018, India

³Centre for incubation, Innovation, Research, and consultancy, Jyothy Institute of
Technology, Bangalore, India

^{a)}Corresponding author: kumaran@ump.edu.my

Abstract. This paper is about the nanocellulose with water and Ethylene Glycol for car radiator application. The research is conducted in order to prove that addition of nanocellulose from plant with varying concentration provides a better heat transfer efficiency compared to usage of distilled water as radiator coolant. The objective of the research is to analysis the performance of vehicle radiator using one-dimensional analysis based on collaboration of nanocellulose with readily available coolants which is Ethylene Glycol. The scopes of the research are the nanoparticles used in the experiment is nanocellulose between ranges of size 40-80 nm. The tested concentration of the cellulose nanofluids are as of 0.5%. Based on the nanocellulose properties, the performance characteristics of a radiator running with water and Ethylene Glycol were investigated using the one-dimensional numerical analysis method of one dimensional software. Radiator model was drawn and the results of the analysis is compared. The radiator model was developed corresponding to a real model of radiator. The radiator was simulated to study the characteristic of radiator performance when the radiator is operating with nanocellulose. The simulation results showed that the temperature decreases with the increasing in volume concentration. Furthermore, the heat transfer coefficient and effectiveness increases with increasing in percentage of nanocellulose.

INTRODUCTION

A radiator is a heat exchanger which absorb heat from a hot coolant that passes through it and directs the collected heat to the air that blown in by the fan. It is made of many tubes which are mounted in parallel arrangement where the coolant will flow from the inlet to the outlet. Heat is extracted from the tubes by the fins on the radiator surface and transfer it to the air that flows in through the radiator. The amount of heat extraction depends highly on the difference between temperature of the fluid that runs through the radiator and tubes (Yadav & Singh, 2011). Thermal conductivity is defined as ability of a material to conduct heat. It is illustrated as the rate of heat transfer through a unit thickness of the material per unit area per unit temperature difference (Fadhilah, Hidayah, Hilwa, Faizah, & Marhamah, 2013). Major improvement in cooling capabilities of conventional heat transfer fluids have come to halt although numbers of research and development effort were done to improve the heat transfer efficiency (Natarajan, 2018; Sparrow, 2018). This is mainly due to the low thermal conductivity properties of those fluids. It is a known fact that metal in solid state have larger thermal conductivities than fluids at room temperature. The thermal conductivity of metals which are in liquid form is considerable better than that of non-metallic liquids. Thus, thermal conductivities of fluids that comprise suspended solid metallic particles are expected to be considerably enhanced when compared with conventional heat transfer fluids (Eastman, Choi, Li, Yu, & Thompson, 2001). Thermal conductivity of nanofluids differs with the particle size, shape of the particle, and type of nanoparticles. For an instance, non-metallic (oxide) nanoparticles were found out to have lower thermal

conductivity compared to a nanofluid with metallic nanoparticles. Nanofluid with smaller particles size possess greater thermal conductivity and the thermal conductivity increases as the size of nanoparticle gets smaller. Furthermore, the shape of the particle also affects the thermal conductivity of the respective nanofluid. Nanofluid containing cylindrical shaped nanoparticles exhibit greater thermal conductivity compared to nanofluid having nanoparticles with spherical shape (Pramuanjaroenkij, Tongkratoke, & Kakaç, 2018). The effectiveness of radiator is the major parameter to evaluate the efficiency of radiator. Besides, the energy crises of recent time have required to improve the heat transfer rates and at the same time the need to make the radiator to be more efficient and smaller (Leong, Saidur, Kazi, & Mamun, 2010). The spiral design of (Alleving, Unger, Skold, Petersson, & Max, 2004), revealed that the heat transfer is enhanced compared to the other heat transfer. Some study to increase the effectiveness of radiator is by adding the nanoparticles in the coolant so that it will enhance the heat transfer rate of radiator. Based on theory of heat exchanger, the radiator performance can be calculated and determined by The Effectiveness-NTU Method (ϵ -NTU) (Jaber & Webb, 1989). The radiator simulation software was developed from the Gamma Technologies, Inc and can be integrated with other simulation software packages such as Computational Fluid Dynamic, Matlab and Fortran. Gamma Technologies software allows to modelling and do simulation of different systems in transportation and automotive (Naraki, Peyghambarzadeh, Hashemabadi, & Vermahmoudi, 2013). One-Dimensional simulation software expresses the flow in the component of the radiator model and these entire components are linked together to produce a whole system of the radiator (Kandlikar & Shah, 1989). In addition, the simulation result will be analysed by the pre-processor with the properties of the radiator model defined by the user, and all the calculation of involve during the analysis will be shown in the post processing result. The attribute related in the One-Dimensional simulation software are implying several equation and correlation in order to perform the analysis for the radiator cycle starting from radiator inlet and radiator outlet.

METHODOLOGY

The preparation of nanocellulose coolant is carried out at Advanced Automotive Liquid Lab (A2LL) of Faculty of Mechanical Engineering University Malaysia Pahang. There are few criteria that need to be finalized before the preparation of the nanocellulose which are concentration volume, required volume of nanofluid and amount of cellulose to be mix with the nanofluid. During normal operation of a radiator in an automotive engine, the radiator cooling fluid is prepared with mixture of water and Ethylene Glycol with certain percentage which comprises the total volume of the radiator. For an instance, assuming the volume of the radiator is 1 litre, and the mixing ratio is set to be 50:50. Thus, the mixture of the cooling fluid in the radiator will be 500ml of water (50%) and 500ml of Ethylene Glycol (50%). As proposed in this research, the volume of the radiator used is 4 litre and the agreed mixing ratio is 60:40 whereby 60% of total volume of radiator will be Ethylene Glycol while the rest 40% will be water. The purpose of this study is to perform one-dimensional modelling of a radiator for different concentration of nanocellulose. The concentration that been used in this project is 0.5% of nanocellulose. The simulation done by using a one-dimensional cooling system 1D under hood code developed by Gamma Technology for the purpose of radiator modelling. It is the market leading radiator simulation software, used by every major heat exchange manufacturer for the design and development of their radiators. It is designed for steady state and transient simulation an applicable to many types of heat exchange. The most important step in this one-dimensional simulation study is to collect the engine component data corresponding to the real engine model that is Perodua Myvi 1.3 as shown in Table 1.

TABLE 1. Engine specification for Perodua Myvi 1.3 standard G-manual

Column Header Goes Here	Column Header Goes Here
Engine type	K3-VE
Valve mechanism	DOHC,16V with DVVT
Total displacement (cc)	1298
Fuel tank capacity (Litres)	40
Maximum output/torque (Kw/rpm)/(Nm/rpm)	

The data for radiator specifications is measured and the result of the data is tabulated as shown in Table 2. Figure 1 illustrates the width and height of radiator that been measured according to real model test rig. All the radiator component parameter will be defined into the one-dimensional simulation software library.

TABLE 2. Radiator specifications

Attribute	Unit	Object value
Heat exchanger height	mm	435
Heat exchanger width	mm	350
Total heat exchanger depth	mm	39
Inlet connection diameter (Master Fluid)	mm	35
Outlet connection diameter (Master Fluid)	mm	35
Heat exchanger material properties object	mm	Aluminum

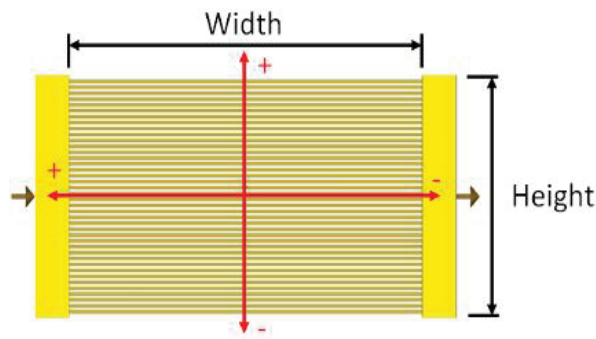


FIGURE 1. Dimension of radiator

The modelling format in the one-dimensional radiator simulation software uses an object-oriented structure. This structure is composed of a three-level hierarchy that includes templates, objects, and parts. Templates are provided which contain the unfilled attributes needed by the models within the program. The templates are made into objects, and when component and connection objects are placed on the project map, they become parts and acquire their values from their parent objects. These parts may call reference objects such as radiator dimension, nanoparticles properties, and heat transfer objects. During the course of building the radiator model, many reference objects will be used, and most are automatically imported into the project at the time they are needed. The first step in building the radiator model is to import the necessary templates from the Template Library. The template library contains all of the available templates that can be used for radiator modelling. Some of these templates need to be copied into the project before they can be used to create objects and parts. The Libraries tab in the lower-left corner or the Template Library icon from the 'Home' menu of the ribbon toolbar is clicked, thus placing the software template library on the left side of the screen. The one-dimensional simulation software demonstrates a basic vehicle cooling system running at a steady-state operating point. The heat rejected from the engine to the coolant is applied directly as a source heat term to the coolant using the 'HeatAddition' template. This heat rejection is looked up as a function of engine speed and load, which are both model inputs. The coolant is circulated by a pump that is represented by a performance map. The model also includes a thermostat valve with a bypass, a radiator, and an expansion tank, along with the associated pipe network. The air side of the cooling system is represented by a very simple "1-D" underhood model that includes a ram air velocity boundary condition and a fan. The fan rotates at a speed independent of the engine and is represented by a performance map. The engine speed and load (and therefore heat transfer rate to the coolant) are constant in the example. Because the purpose of the model is a steady-state prediction, the system is initialized at a coolant temperature and pressure assumed to be close to the final result. The thermal wall solver is also set to "steady" in Run Setup. These settings minimize the convergence time required to achieve steady state. In this model, the cooling system model is modelling the piping system. The piping system has a few components, attributes, and conditions. Figure 2 shows the schematic diagram of cabin heat.

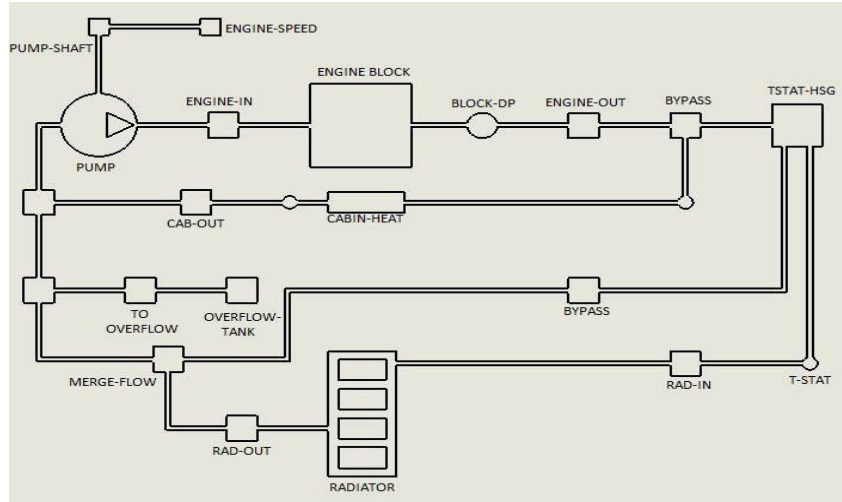


FIGURE 2. Schematic Diagram of Cooling System with the Cabin Heat

Attributes in radiator templates are width, length and height of radiator as shown in table 3. For the purpose of this study, 1 bar of absolute pressure is set as the pressure attribute. The temperature is set to 350K. Initial fluid compositions is based on the ASHRAE data at the temperature of 350K for the thermal conductivity and viscosity as shown in table 3.3. In this model, the composition of coolant is very important since it will be used to determine the amount of heat transfer and effectiveness of the radiator. The template of ‘HxMaster’ is the main template that can change the type and properties of coolant. In addition, the composition of 50W+50EG in template “coolant_int_low” can be change to another composition as needed to get 0.5%, of nanocellulose. Table 3 below shows the basic properties of composition 60% of water + 40% of EG.

TABLE 3. Properties of Composition 60%W+40%EG

Attribute	Unit	Object value
Minimum Valid Temperature	K	238.15
Maximum Valid Temperature	K	398.15
Minimum Valid Pressure	bar	0.0060
Maximum Valid Pressure	bar	2
Density at (Pref, Tref)	kg/m ³	1071.11
Minimum Valid Temperature	K	238.15

In case setup template, the case setup was created with different parameter for the radiator before it can run and develop result. The case level is named so that it will be easy to edit the parameter. The case setup is set up to 10 case with different engine speed. The engine speed is started from 500 rpm and ended with 5000 rpm with the increment of 500 rpm for each case. Table 4 indicated all the parameter and engine speed that used in this model.

TABLE 4. Parameter in case setup

Parameter	Unit	Case 1	Case 2	Case 3	Case 4	Case 5
Engine-speed	RPM	500	1000	1500	2000	2500
BMEP-Engine	10	10	10	10	10	10
Fan speed	RPM	1200	1200	1200	1200	1200
Coolant pressure low	bar	1.3	1.3	1.3	1.3	1.3
Coolant pressure high	bar	2.6	2.6	2.6	2.6	2.6

Parameter	Unit	Case 1	Case 2	Case 3	Case 4	Case 5
Engine-speed	RPM	3000	3500	4000	4500	5000
BMEP-Engine	10	10	10	10	10	10
Fan speed	RPM	1200	1200	1200	1200	1200
Coolant pressure low	bar	1.3	1.3	1.3	1.3	1.3
Coolant pressure high	bar	2.6	2.6	2.6	2.6	2.6

RESULT AND DISCUSSION

The variation of average total temperature with the engine speed for 60% EG+40%water , by adding 0.5% nanocellulose is shown in Figure 3. It was observed that the average total temperature for 60%W+40%EG is higher at the beginning of the engine speed which is 500 rpm. The graph indicates that, the adding of nanoparticles into the simulation will decrease the average total temperature. It can be seen when added 0.5% of nanocellulose the temperature is decrease from 101.397oC for 60% water+40%EG to 101.091oC. Furthermore, the grap will be on stable temperature that is on 2000 rpm(Farrell, Wert, & Webb, 1991). However, the higher addition of nanoparticles, will give a result to more effective the radiator since the total temperature will decreases. In short, at the beginning of engine speed that is 500 rpm, the temperature for 60%water+40%EG, 0.5% nanoparticles 101.091oC respectively(Ali, El-Leathy, & Al-Sofyany, 2014). Is it well known that the percentage of nanocellulose affects the average temperature of the radiator.

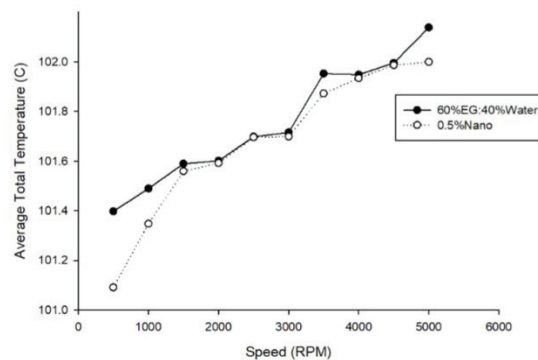


FIGURE 3. Total Temperature Comparison at Radiator Inlet

Figure 4 below shows the variation of data on speed of engine with the average total temperature at radiator outlet. Moreover, Figure 4 indicates the graph of total temperature for 60% EG+40% water, by adding 0.5% nanoparticles against speed. If compared with Figure 3, it shows that the temperature at the inlet of radiator is decrease. It is about 1°C of temperature is decrease for every data in the simulation. It is about 0.05% temperature decreases for 0.5% of nanocellulose and 60% water+40%EG (Naraki et al., 2013).

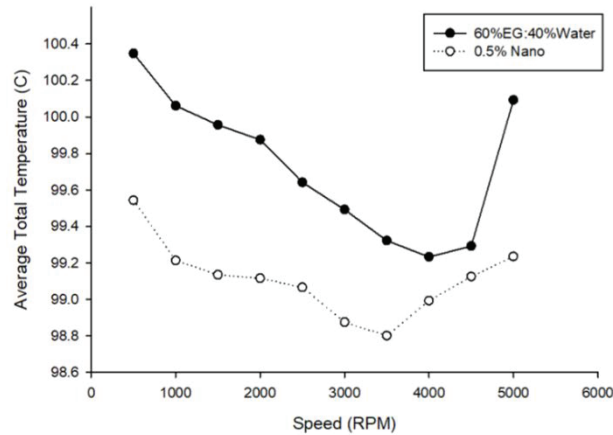


FIGURE 4. Total Temperature Comparison at Radiator Inlet

The effect of Ethylene Glycol and water on heat transfer for various speeds is shown in Figure 5. It can be seen that at low speed, the heat transfer coefficient increases as the engine speed increases, reaches the maximum and then, as the engine speed increases further, the heat transfer coefficient is remain the same. The heat transfer remain the same because the radiator reaches its limit when transferring the heat at the higher speed (Fadhilah et al., 2013; Natarajan, 2018). It is clear that, the higher the speed, the heat transfer coefficient will increase. The maximum heat transfer coefficient recorded for 60% Water+40% EG are 1624.8517 W/m².K at engine speed of 2000 rpm (Ali et al., 2014; Jaber & Webb, 1989). The heat transfer flattens at 1500 rpm and rpm indicating the best heat transfer regions starts 2000 rpm to 5000 rpm. For 0.5% of TiO₂ the heat transfer coefficient is 1640.0101 W/m².K are recorded at speed of 2500 rpm. It shows that the percentage of the heat transfer is increase about 0.4% from 60% Water+40% EG to 0.5% nanocellulose.

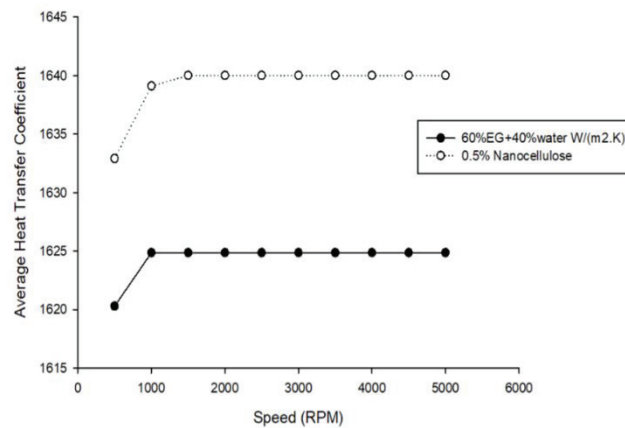


FIGURE 5. Average heat transfer coefficient

The effect of engine speed variation on overall effectiveness for 60%W+40%EG and 0.5% of nanocellulose is shown in Figure 6. The effectiveness increases the engine operating with 0.5% of nanocellulose compared to 60%EG+40%water. The Figure 6 shows that the maximum effectiveness of 0.5% of nanocellulose and 60%W+40%EG is 0.689% and 0.691% when the engine is operating at engine speed of 4000 RPM (Alleving et al., 2004; Leong et al., 2010). The increasing of effectiveness when the engine is operating with 0.5% of n compared to 60%EG+40%W was about 0.03%. This situation is due to lower percentage of nanocellulose. The higher the percentage of nanocellulose the effectiveness of radiator also increases and will achieved its stable range that is on speed or 1500 RPM (Leong et al., 2010; Yadav & Singh, 2011). At the speed of 1500 rpm, the

graph is constant because the radiator has reach its maximum value of heat transfer. Figure 6 below indicated the result of effectiveness of 60%EG+40%W and 0.5% nanocellulose.

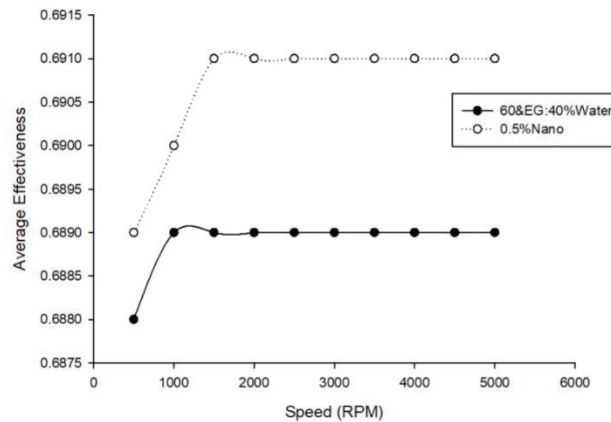


FIGURE 6. Average Effectiveness of 60%W+40%EG and 0.5% Nanocellulose

CONCLUSION

- It was found that the effectiveness of radiator for 0.5% nanocellulose was higher than the other percentage of nanocellulose and 60%W+40%EG. The addition of nanoparticles influenced the effectiveness of radiator. This is because the different concentration has different density and specific heat that can increase the effectiveness of radiator.
- Nanoparticles are more efficient than normal coolant in term of its temperature, heat transfer and effectiveness for the different speed of engine.

ACKNOWLEDGMENT

The authors would like to thank UMP and FKM in the following grants, RDU160306 and RDU151311

REFERENCES

1. B. R. Jackson and T. Pitman, U.S. Patent No. 6,345,224 (8 July 2004) Ali, M., El-Leathy, A., & Al-Sofyany, Z. (2014). The effect of nanofluid concentration on the cooling system of vehicles radiator. *Advances in Mechanical Engineering*, 6, 962510.
2. Alleving, P., Unger, A., Skold, J., Petersson, M., & Max, E. (2004). System for determining the effectiveness of a catalytic coating on a radiator in a motor vehicle: Google Patents.
3. Eastman, J. A., Choi, S., Li, S., Yu, W., & Thompson, L. (2001). Anomalously increased effective thermal conductivities of ethylene glycol-based nanofluids containing copper nanoparticles. *Applied physics letters*, 78(6), 718-720.
4. Fadhilah, S., Hidayah, I., Hilwa, M., Faizah, H., & Marhamah, R. (2013). Thermophysical properties of Copper/Water nanofluid for automotive cooling system—Mathematical modeling. *Journal of Mechanical Engineering and Technology (JMET)*, 5(2).
5. Farrell, P., Wert, K., & Webb, R. (1991). Heat transfer and friction characteristics of turbulator radiator tubes. *SAE transactions*, 218-230.
6. Jaber, H., & Webb, R. (1989). Design of cooling towers by the effectiveness-NTU method. *Journal of Heat Transfer*, 111(4), 837-843.
7. Kandlikar, S., & Shah, R. (1989). Multipass plate heat exchangers—effectiveness-NTU results and guidelines for selecting pass arrangements. *Journal of Heat Transfer*, 111(2), 300-313.

8. Leong, K., Saidur, R., Kazi, S., & Mamun, A. (2010). Performance investigation of an automotive car radiator operated with nanofluid-based coolants (nanofluid as a coolant in a radiator). *Applied Thermal Engineering*, 30(17-18), 2685-2692.
9. Naraki, M., Peyghambarzadeh, S., Hashemabadi, S., & Vermahmoudi, Y. (2013). Parametric study of overall heat transfer coefficient of CuO/water nanofluids in a car radiator. *International Journal of Thermal Sciences*, 66, 82-90.
10. Natarajan, P. (2018). HEAT TRANSFER ANALYSIS IN LIGHT PASSENGER CAR RADIATOR WITH VARIOUS GEOMETRICAL CONFIGURATIONS. *HEAT TRANSFER*, 5(06).
11. Pramuanjaroenkij, A., Tongkratoke, A., & Kakaç, S. (2018). Numerical Study of Mixing Thermal Conductivity Models for Nanofluid Heat Transfer Enhancement. *Journal of Engineering Physics and Thermophysics*, 91(1), 104-114.
12. Sparrow, E. M. (2018). *Radiation heat transfer*: Routledge.
13. Yadav, J., & Singh, B. R. (2011). Study on performance evaluation of automotive radiator. *S-JPSET*, 2(2), 47-56.

Nanocellulose as heat transfer liquid in heat exchanger

Cite as: AIP Conference Proceedings **2059**, 020044 (2019); <https://doi.org/10.1063/1.5085987>
Published Online: 11 January 2019

F. Benedict, K. Kadirgama, D. Ramasamy, M. M. Noor, M. Samykano, M. M. Rahman, Z. Ghazali, and B. Sagmesh



View Online



Export Citation

ARTICLES YOU MAY BE INTERESTED IN

[Cobalt nanowires: Advancing into future nanomaterial](#)

AIP Conference Proceedings **2059**, 020006 (2019); <https://doi.org/10.1063/1.5085949>

[3D printing: Overview of PLA progress](#)

AIP Conference Proceedings **2059**, 020015 (2019); <https://doi.org/10.1063/1.5085958>

[Air flow distribution measurement of the vehicle cooling system test rig](#)

AIP Conference Proceedings **2059**, 020002 (2019); <https://doi.org/10.1063/1.5085945>

AIP | Conference Proceedings

Get **30% off** all
print proceedings!

Enter Promotion Code **PDF30** at checkout



Nanocellulose as Heat Transfer Liquid in Heat Exchanger

F.Benedict¹, K.Kadirgama^{1, a)}, D.Ramasamy¹, M.M.Noor¹, M.Samykano¹,
M.M.Rahman¹, Z.Ghazali¹, B.Sagmesh²

¹Faculty of Mechanical Engineering, University Malaysia Pahang (UMP),
26600, Pekan Pahang, Malaysia.

²Centre for incubation, Innovation, Research, and consultancy, Jyothy Institute of
Technology, Bangalore, India

^{a)}Corresponding author: kumaran@ump.edu.my

Abstract. This Nanocellulose with water and Ethylene Glycol addition to coolant for car radiator application has benefits of improving efficiency of the radiator. Improved efficiency leads to more compact design of the radiator and increases the durability of the engine. The research is conducted to prove that addition of nanocellulose originating from plant base with varying concentration provides a better heat transfer efficiency compared to usage of distilled water as radiator coolant. The tested concentration of the cellulose nanofluids are as of 0.1%, 0.5%, 0.9%, and 1.3%. The experiment is carried out by running the radiator test rig with distilled water as radiator coolant. This is done so that the result obtained through experimental analysis of distilled water is a benchmark for the comparison of heat transfer efficiency. The thermal coefficient test indicates that all the cellulose nanofluid with varying concentration possess better heat conducting properties compared to Ethylene Glycol. Furthermore, this proves that cellulose nanofluids can transfer the absorbed heat from the radiator to the surrounding air much faster compared to conventional Ethylene Glycol. Experimental analysis shows that cellulose nanofluids have higher specific heat capacity compared to distilled water. Thus, cellulose nanofluids can absorb and store more heat compared to distilled water. Heat transfer coefficient result supports that application of cellulose nanofluids as car radiator coolant leads to increase in thermal absorption enhancement. However, as the concentration of cellulose nanofluid increase from 0.1% to 1.3% and so on, the heat transfer coefficient decreases rapidly. This is because formation of sediments of cellulose nanoparticles causes inactive involvement in heat transfer process but the sediments do not clog in the flat tubes or trigger erosion on the internal wall of car radiator. It can be concluded that application of cellulose nanoparticles integrated with Ethylene Glycol as coolant in car radiator is acceptable and provides better heat transfer efficiency.

INTRODUCTION

Coolant can be characterized as a liquid that forestalls overheating of a device by coursing through it to accumulate extreme undesirable heat delivered by the device. The gathered heat will be exchanged to another device that will misuse or scatter it. A coolant with high heat limit, minimal effort, low consistency and is synthetically dormant whereby it doesn't cause or advances consumption of the cooling framework is considered as a perfect coolant. A coolant is regularly synthetically joined with a high boiling point fluid to shape a compound liquid. This compounded liquid capacity as a radiator fluid operator against to a great degree cold conditions and additionally tackles the issue of overheating due to hot weather. A coolant with generally high boiling temperature can cool faster as the engine gets more hotter. Amid an operation of an internal combustion engine, about third of heat energy created are considered as undesirable heat that winds up in the cooling system. An engine is kept from getting harmed when the radiator coolant lifts the boiling point of the water which permits it to transmit more heat away from the engine (Efeovbokhan & Ohiozua, 2013). A radiator is a heat exchanger, which absorb heat from a hot coolant that goes through it and guides the gathered heat to the air that passed up the fan. It is made of many tubes which are mounted in parallel course of action where the coolant will flow from inlet to the outlet. Heat is separated from the tubes by the fins on the radiator surface and exchange it to the air that streams in through the radiator. The deeply exceeding on the distinction between temperature of the liquid that goes through the radiator and tubes

depends of the amount heat (Yadav & Singh, 2011). Generally radiator is comprised of three primary bits, for example, inlet tank, outlet tank and core. Core principally comprise of two arrangements of section which are set of tubes and sets of fins. Tubes will be the stream section for the coolant while air will stream between the fins. Heat is transferred to the fins by the tube that obtained it from the hot coolant. Air that flows between the fins will eventually pick up and brings the heat away. (Amrutkar & Patil, 2013). Ability of a material to conduct heat is known as thermal conductivity. It is illustrated as the rate of heat transfer through a unit thickness of the material per unit area per unit temperature difference (Cengel et al., 2013). Numbers of research and development effort were done to improve the heat transfer efficiency. Nevertheless, major refinement in cooling capabilities of conventional heat transfer fluids have come to halt. This is mainly due to the low thermal conductivity properties of those fluids. Metal in solid state have larger thermal conductivities than fluids at room temperature. The thermal conductivity of metals which are in liquid form is preferred compared to non-metallic liquids. Thus, thermal conductivities of fluids that encompass suspended solid metallic particles are expected to be considerably enhanced when compared with conventional heat transfer fluids (Choi & Eastman, 1995). The study about nanoparticles mixture ratio in hybrid / composite nanofluids is very limited but several researchers have put interest in this study. (Afrand, Toghraie, & Ruhani, 2016) used 50:50 ratios of Fe₃O₄-Ag water based hybrid / composite nanofluids prepared at different solid volume fractions to study the effect of temperature and concentration of nanoparticles on the rheological behaviour. He evaluated the viscosity at temperature between 25°C to 50°C. It is observed that viscosity the Fe₃O₄-Ag water based hybrid / composite nanofluids is decreasing as temperature increased. The study reported that the hybrid/composite nanofluids contains less than 0.3% solid volume fraction possess Newtonian behaviour while others exhibit non-Newtonian behaviour. Similar discovery is reported by (Bahrami, Akbari, Karimipour, & Afrand, 2016) when he prepared equal ratio (50:50) iron (Fe) and copper oxide (CuO) water/ethylene glycol based hybrid/composite nanofluids at different solid volume (Hayat, Hussain, Muhammad, & Alsaedi, 2016) investigate the entropy generation of 0.1% graphene-alumina hybrid/composite nanofluids. The sample was prepared was at same ratio (1:1) that are dispersed in water as base fluid. However, the study revealed the nanofluids compare to alumina water based single nanofluids and graphene-alumina water based hybrid/composite nanofluids. (Allahyar, Hormozi, & ZareNezhad, 2016) conduct a research on thermal performance of a coil heat exchanger using the mixture of 97.5% alumina and 2.5% Ag prepared at 0.1% to 0.4% concentration. It is reported that the maximum heat transfer is observed at 0.4% concentration of hybrid/composite nanofluids. (Esfe, Saedodin, Wongwises, & Toghraie, 2015) also prepared ratio 50:50 by volume Ag-MgO water hybrid nanofluids at concentration 0.0%, 0.005%, 0.01%, 0.015%, and 0.02%. The hybrid nanofluids is reported stable at all concentration for several days. (Kumar, Vasu, & Gopal, 2016) and Huang et al. (2016) prepared 50:50 Cu-Zn hybrid nanofluids and 1:2.5 Al₂O₃-MWCNT hybrid nanofluids was observed stable for two weeks before sedimentation visible. This section will describe the preparation method of hybrid/composite nanofluids. Two main methods to prepare the hybrid/composite, one-step method and two-step method will be discussed deeper in the next section. One-step method or also known as single method is usually used in small scale production while two-step method is more suitable to be used in the mass production. One-step method is a process where the production of nanoparticles and dispersion of nanoparticles in conventional base fluid are combined in single step. Physical Vapor Deposition (PVD) method is used to produce the nanoparticles. One-method not only good for small scale production, it is also help to minimize the agglomeration of nanoparticles. However, this method only compatible with low vapor pressure fluid. The second method used to prepare the hybrid/composite nanofluid is two-step method. (Manna, 2012) reported that this method is suitable to prepare the oxide nanofluid but less suitable to prepare metallic nanofluid. However, (Wang & Mujumdar, 2007) stated that two-step method can be used to prepare almost every kind nanofluids. This method involves the production of nanomaterials in the base fluid like water, ethylene glycol or oil. The fluid is now need to be stirred using magnetic stirrer to ensure to solution mixes well then the Hybrid/Composite nanofluid will be subjected to sonication process to enhance its stability. Both magnetic stirrer and sonicator are commonly used by the researcher like Hamid et al. (2016) and (Azmi, Hamid, Usri, Mamat, & Mohamad, 2016).

METHODOLOGY

The nanocellulose coolant is prepared in Advanced Automotive Liquid Lab (A2LL) of Faculty of Mechanical Engineering University Malaysia Pahang. Some criteria is finalized beforehand such as the concentration volume, required volume of nanofluid and amount of cellulose to be mix with the nanofluid. The radiator cooling fluid is prepared with mixture of water and Ethylene Glycol with certain percentage that is composed of the total volume of the radiator during standard procedure of a radiator in an automotive engine. For example, if the volume of the

radiator is 1 litre, and the mixing ratio is set to be 60:40, then the mixture of the cooling fluid in the radiator will be 600ml of water (60%) and 400ml of Ethylene Glycol (40%). Figure 1 shows the schematic diagram of the radiator test rig design. A 24V DC power supply is the main source of power for the pump and heater. The radiator test rig is a closed loop system in which the water from the tank is redirected back to the tank and complete the cycle using a 24V DC water pump. K-Type thermocouples are fixed at four points on the radiator wall to measure the surface temperature of the radiator. A 12V cooling fan is attached to the radiator to function as a normal radiator fan which is similar to the readily available automobile radiator. Heat produced from an automobile system during its routine is imitated by a 1kW heater.

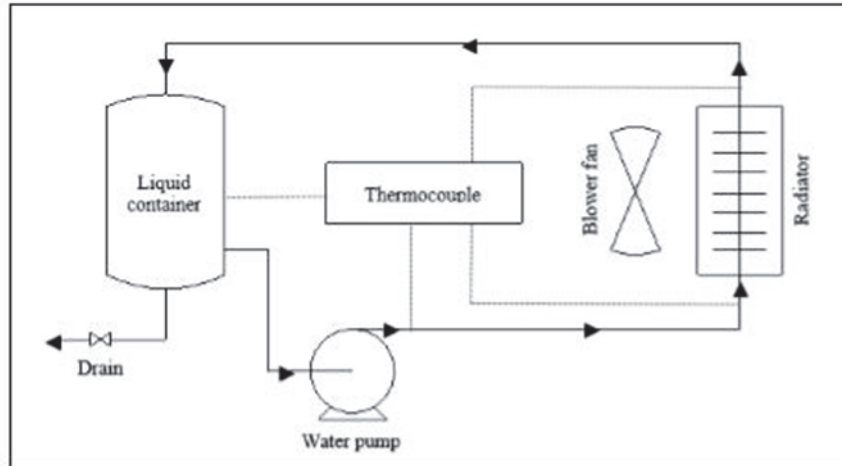


FIGURE 1. Schematic diagram of radiator test rig

RESULTS AND DISCUSSION

The nanoparticles used for this research is Al_2O_3 /CNC dispersed in a base mixture fluid with different ratios of water to ethylene glycol (40:60). The approximation of the nanoparticles size was checked using a Field Emission Scanning Electron Microscope (FESEM). As shown in Figure 2, the nanoparticles have an average size of 13nm with a spherical shape as the primary shape of the nanoparticle. (Hatami & Okhovati, 2014) also found that their nanoparticle were in spherical shape although they were in different sizes. No cluster particles were observed through the Figure 2. (Meriläinen et al., 2013) found that the smaller sized and smooth particles with a spherical shape were the best in enhancing heat transfer while keeping the pressure effect moderately.

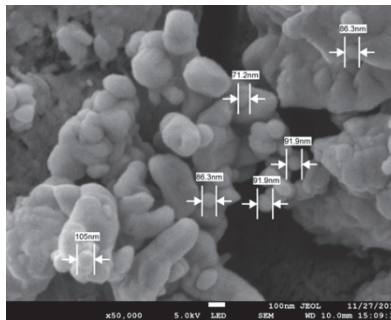


FIGURE 2. FESEM image of Al_2O_3 /CNC nanoparticles

The reliability of the experiment system was evaluated using the 60:40 ratio (EG:W) base mixture as the working fluid. The experiment heat transfer coefficient was dignified for base fluid as a benchmark and the evaluated Nusselt Number. The preliminary results of the experiment is shown in Figure 3 using 60:40 (EG: W) as the base fluid. The graph shows that the average deviation of the experiment data was up to 11% compared to the theoretical value from the literature. However, the most fir equation that have the smallest average

deviation, AD of 3.4% with the experiment data is (Dittus & Boelter, 1930). The experimental setup was also in good term with ((Notter & Sleicher, 1972) where AD is 4.7%. The flow rate of the nanofluid is varies by adjusting the operating voltage of the pump. The data for flow rate of the nanofluid has been recorded using the flow meter which was connected to PLX-DAQ software as shown in Figure 4. The flow rate of the coolant or working fluid in the radiator cooling system increase the rate of heat transfer also is increases (Ramachandran, Hussein, et al., 2017). This is because at higher flow rate the more scrubbing action will occur at the surface of the radiator flat tubes, thus more heat energy will be transferred from coolant to radiator flat tube by the mean of conduction (Ramachandran, Kadirgama, Ramasamy, Azmi, & Tarlochan, 2017). Nevertheless, there is limit of the flow rate of the coolant is applicable in car cooling system. As the flow rate exceed the limit of the flow rate, the aeration or erosion on the radiator flat tube and foaming of coolant inside the system will likely to happen which is to be avoided (Ramachandran, Kadirgama, et al., 2017). For the consideration of engineering application, it is essential to investigate the temperature drop of nanofluids in addition to the heat transfer enhancement features. The effect of thermal gradient for temperature drop system or also knows as temperature loss along the radiator fins was included additional investigation. This is because at higher flow rate the more scrubbing action will occur at the surface of the radiator flat tubes, thus more heat energy will be transferred from coolant to radiator flat tube by the mean of conduction. Other than that, there is limit of flow rate of the coolant is applicable in car cooling system. As the flow rate exceed the limit of the flow rate, the aeration or erosion on the radiator flat tube and foaming of coolant inside the system will likely to happen which is needed to be avoided. This is because it can reduce the efficiency of the radiator.

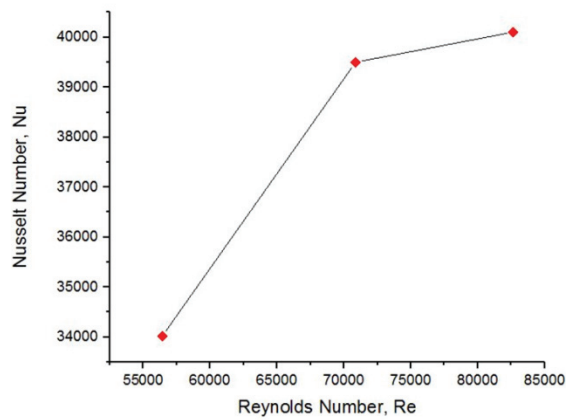


FIGURE 3. validation of experiments

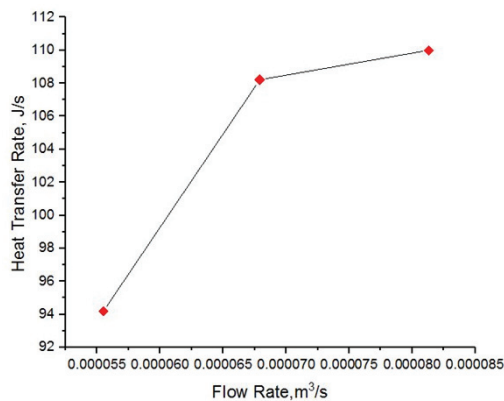


FIGURE 4. Relationship between flow rate and rate of heat transfer

Using thermal infrared camera, the heat distribution of fluid inside the radiator was captured. The temperature range is from 30°C to 70°C where it is the optimum temperature of the radiator test rig. Figure 5 (a) until (e) shows the thermal imaging of base fluids which is distilled water and Ethylene Glycol is circulating the radiator.

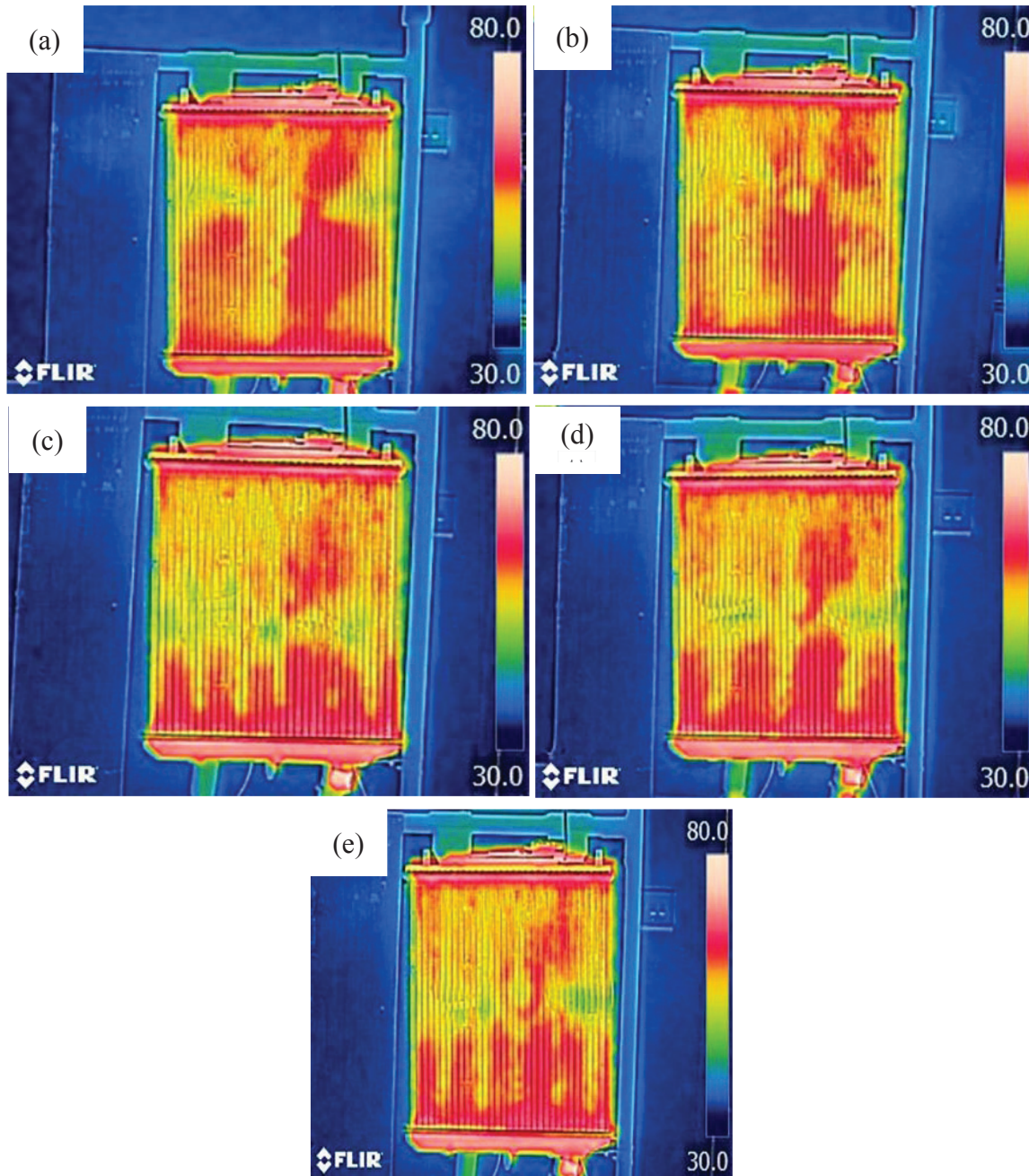


FIGURE 5. (a)-(e): Thermal imaging of base fluids in radiator

After conducting the test for base fluids, nanofluid of volume concentration 0.5% at ratio 60:40 (EG: W) was poured in the tank and later run in the test rig to get the thermal image of the fluid inside the radiator. The same range used for nanofluid is same as base fluid which is from 30°C to 80°C. From Figure 6 (a) until (e) the images show the colour of yellowish or green at the radiator which means the nanofluid absorbs more heats as

its running in the test rig. Compared to the base fluids, nanofluids absorbs more heat and it is enhancing better than the base fluid

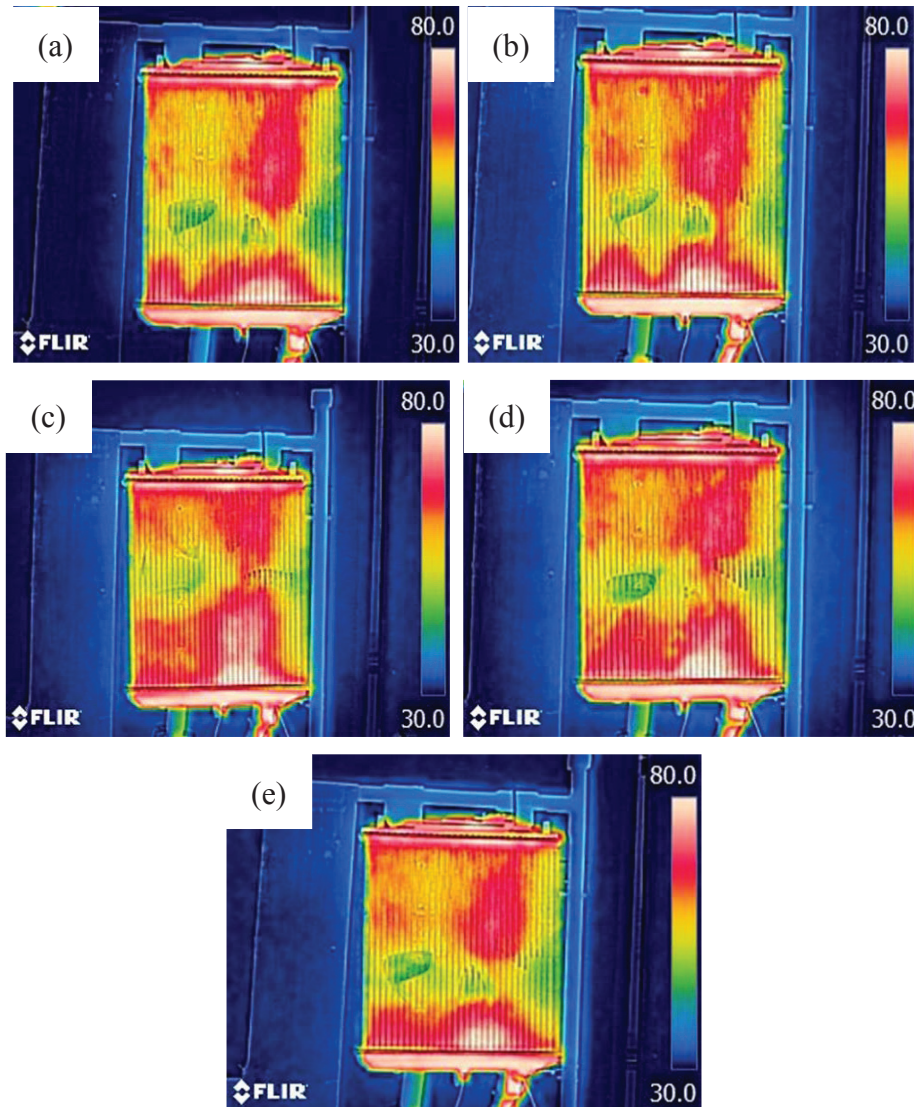


FIGURE 6. (a) – (e): Thermal imaging of nanofluid in radiator

The experimental study of forced convection heat transfer evaluates the heat transfer coefficient of fluids according to their operating condition. Through heat transfer coefficient evaluation, the ability of the fluid as a thermal fluid for transferring heat out from the system are understood based on established literature that evaluated single phase fluid condition. However, the characteristics and thermal ability of nanofluids are yet to be understood. A mixture of water-ethylene glycol had been used as coolant especially for extreme temperature in Alaska (Kulkarni et al.,2008). The coolant mixture, known as heat transfer fluid, is utilized heat without changing state (ASHRAE, 2005). The chief ability of water-ethylene glycol mixture is to lower the freezing point of water and their low volatility is one of the main reasons they are suitable for different condition as thermal fluid. However, their thermal ability is lower compared to solid substance. Hence, proposition of using nanoparticles suspended in the base mixture is one of the alternative to enhance their thermal ability. On the other hand, the ratio 60:40(EG:W) by volume percentage of water-ethylene glycol mixture are the standard ratios used in engineering practice following ASTM standard (2015). An earlier paper by (Sundar, Singh, &

Sousa, 2013) investigate thermal conductivity of magnetic FeO₃O₄ nanoparticles dispersed in 50:50 (W:EG) by the weight. The continuation studies in 60:40 (EG:W) by weight were presented by (Sundar et al., 2013) and Sundar et al., (2014). The results indicated that the increment of volume of volume percentage of ethylene glycol in the mixture decreased the thermal conductivity enhancement. However, the studies left a gap for experimental convection heat transfer using nanofluids in different base mixture. There are limited studies on convection heat transfer conducted using Al₂O₃/CNC nanoparticles dispersed in different base mixture fluids. Therefore, this section deliberates on determination of convection heat transfer coefficients of Al₂O₃/CNC nanofluids for different base mixture at concentration of 0.1%, 0.5%, and 0.9% and working temperature of 30, 50, 70°C. Al₂O₃/CNC nanofluids dispersed in 40:60(EG:W) base mixture fluid with volume concentration of 0.1%, 0.5% and 0.9% with Reynolds numbers are discussed in this section. The plotted graph in Figure 7 shows the convective heat transfer of 13nm Al₂O₃ dispersed in 40:60 volume ratio of water-ethylene glycol mixture under different working temperature. The increment of the heat transfer coefficient was obtained by suspending nanoparticles at higher volume concentration for each working temperature. It was observed from the figures that the enhancements in heat transfer coefficient compared to 40:60 (W:EG) base mixture fluid at different Reynolds numbers almost identical for all volume concentration of nanofluids. From the Figures 8, it was seen the maximum enhancement in the heat transfer coefficient was obtained for nanofluids with volume concentration of 0.9%. Based on the figures for Al₂O₃/CNC nanofluids in 40:60(W:EG) base mixture fluid, the highest enhancement of heat transfer coefficient was found for a working temperature of 70°C at all volume concentration with an average enhancement of the heat transfer coefficient of 16.9% compared to the base fluids.

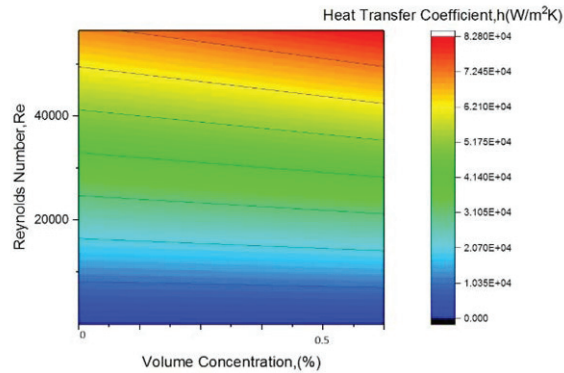


FIGURE 7. Effect of volume concentration on heat transfer coefficient within working temperature of 70 °C

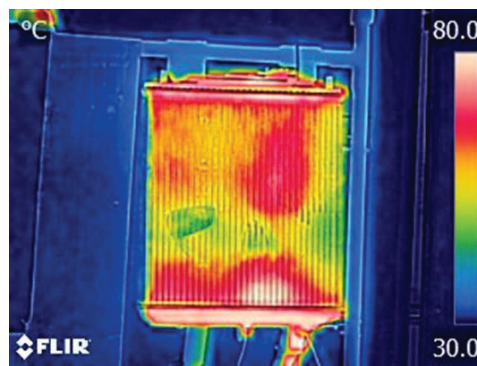


FIGURE 8. Distribution of heat transfer coefficient with Reynolds Number at the same volume concentration.

CONCLUSION

The maximum enhancement compared to base fluid W/EG can be found at volume concentration 0.9% at temperature of 70°C. While for the dynamic viscosity, the increase in temperature affect the viscosity in an opposite

way from the thermal conductivity. It is found the viscosity is exponentially decreased when temperature increased. The minimum viscosity of Al₂O₃/CNC composite nanofluids can be found at volume concentration of 0.1% which appear to temperature of 70C. The enhancement of viscosity compared to base fluid W/EG is increasing with temperature which make the enhancement of viscosity also a temperature dependent like thermal conductivity. Minimum enhancement is preferable for viscosity and was recorded at volume concentration 0.1% at the temperature 70C, the viscosity of the composite nanofluids is enhancement which is the maximum enhancement observed in the experiment. Both density and specific heat of Al₂O₃/CNC composite nanofluids is estimated using mixture relation equation. The equation shows that the percentage volume concentration of each Al₂O₃ or CNS of the Al₂O₃/CNC does not affect the density and specific heat of the composite nanofluids. The density of the composite nanofluids is observed decreasing as temperature increases, while the specific heat is increased.

ACKNOWLEDGMENT

The authors would like to thank UMP and FKM in the following grants, RDU160306 and RDU151311

REFERENCES

1. Afrand, M., Toghraie, D., & Ruhani, B. (2016). Effects of temperature and nanoparticles concentration on rheological behavior of Fe₃O₄-Ag/EG hybrid nanofluid: an experimental study. *Experimental Thermal and Fluid Science*, 77, 38-44.
2. Allahyar, H., Hormozi, F., & ZareNezhad, B. (2016). Experimental investigation on the thermal performance of a coiled heat exchanger using a new hybrid nanofluid. *Experimental Thermal and Fluid Science*, 76, 324-329.
3. Amrutkar, P. S., & Patil, S. R. (2013). Automotive radiator performance—Review. *International Journal of Engineering and Advanced Technology*, 2(3), 563-565.
4. ASHRAE, A. (2005). Handbook of fundamentals. *American Society of Heating Refrigerating and Air Conditioning Engineers, Atlanta, GA*.
5. Azmi, W., Hamid, K. A., Usri, N., Mamat, R., & Mohamad, M. (2016). Heat transfer and friction factor of water and ethylene glycol mixture based TiO₂ and Al₂O₃ nanofluids under turbulent flow. *International Communications in Heat and Mass Transfer*, 76, 24-32.
6. Bahrami, M., Akbari, M., Karimipour, A., & Afrand, M. (2016). An experimental study on rheological behavior of hybrid nanofluids made of iron and copper oxide in a binary mixture of water and ethylene glycol: non-Newtonian behavior. *Experimental Thermal and Fluid Science*, 79, 231-237.
7. Choi, S. U., & Eastman, J. A. (1995). *Enhancing thermal conductivity of fluids with nanoparticles*. Retrieved from
8. Dittus, F., & Boelter, L. (1930). Publications on Engineering, vol. 2. *University of California at Berkeley, Berkeley, CA*, 443-461.
9. Efevbokhan, V. E., & Ohiozua, O. N. (2013). Comparison of the cooling effects of a locally formulated car radiator coolant with water and a commercial coolant. *The International Journal of Engineering and Science*, 2(1), 254-262.
10. Esfe, M. H., Saedodin, S., Wongwises, S., & Toghraie, D. (2015). An experimental study on the effect of diameter on thermal conductivity and dynamic viscosity of Fe/water nanofluids. *Journal of Thermal Analysis and Calorimetry*, 119(3), 1817-1824.
11. Hatami, F., & Okhovati, F. (2014). Analysis of turbulent flow of nanofluids in a pipe. *European Online Journal of Natural and Social Sciences*, 3(3 (s)), 72.
12. Hayat, T., Hussain, Z., Muhammad, T., & Alsaedi, A. (2016). Effects of homogeneous and heterogeneous reactions in flow of nanofluids over a nonlinear stretching surface with variable surface thickness. *Journal of Molecular Liquids*, 221, 1121-1127.
13. Kumar, M. S., Vasu, V., & Gopal, A. V. (2016). Thermal conductivity and rheological studies for Cu-Zn hybrid nanofluids with various basefluids. *Journal of the Taiwan Institute of Chemical Engineers*, 66, 321-327.
14. Manna, I. (2012). Synthesis, characterization and application of nanofluid—an overview. *Journal of the Indian Institute of Science*, 89(1), 21-33.

15. Meriläinen, A., Seppälä, A., Saari, K., Seitsonen, J., Ruokolainen, J., Puisto, S., . . . Ala-Nissila, T. (2013). Influence of particle size and shape on turbulent heat transfer characteristics and pressure losses in water-based nanofluids. *International Journal of Heat and Mass Transfer*, *61*, 439-448.
16. Notter, R., & Sleicher, C. (1972). A solution to the turbulent Graetz problem—III Fully developed and entry region heat transfer rates. *Chemical Engineering Science*, *27*(11), 2073-2093.
17. Ramachandran, K., Hussein, A., Kadirgama, K., Ramasamy, D., Azmi, W., Tarlochan, F., & Kadirgama, G. (2017). Thermophysical properties measurement of nano cellulose in ethylene glycol/water. *Applied Thermal Engineering*, *123*, 1158-1165.
18. Ramachandran, K., Kadirgama, K., Ramasamy, D., Azmi, W., & Tarlochan, F. (2017). Investigation on effective thermal conductivity and relative viscosity of cellulose nanocrystal as a nanofluidic thermal transport through a combined experimental–Statistical approach by using Response Surface Methodology. *Applied Thermal Engineering*, *122*, 473-483.
19. Sundar, L. S., Singh, M. K., & Sousa, A. C. (2013). Thermal conductivity of ethylene glycol and water mixture based Fe₃O₄ nanofluid. *International Communications in Heat and Mass Transfer*, *49*, 17-24.
20. Wang, X.-Q., & Mujumdar, A. S. (2007). Heat transfer characteristics of nanofluids: a review. *International Journal of Thermal Sciences*, *46*(1), 1-19.
21. Yadav, J., & Singh, B. R. (2011). Study on performance evaluation of automotive radiator. *S-JPSET*, *2*(2), 47-56.

Effect of Cryogenic treatment on Tool Wear, Chip Thickness of Uncoated Carbide Insert during Machining with AISI304 Stainless Steel

Nagraj Patil, Gopalakrishna K, Sangmesh B,

Abstract: *The cutting tool in the manufacturing industry is a key factor. The fulfilment of machining operation mainly depends on the tool material to improve the cutting life of the tool during machining with austenite stainless steel, however the austenite stainless steel difficult to machine and less amount of heat dissipation during machining in order to overcome. The aim of the investigation is to apply; the cryogenic treatment (CT) to the tungsten carbide insert, besides no study has been claimed on the chip thickness (tc), tool wear of machining with AISI 304. The machining test was conducted by three different speed and unchanged feed rate and depth of cut. The maximum flank wear was measured by using digital microscope also measured the chip thickness for both insert. The experimental results found that to reach the maximum flank wear for CT insert in all three speed was less in comparison with untreated insert (UT), chip thickness was also less in case of CT insert, built up edge were clearly observed in the UT insert, over all CT insert performed more desirable in compared with UT. The improvement in the microstructure properties of the CT insert owing to development of Eta (η) phase carbide and homogenous distribution in the tungsten carbide material, SEM and XRD tests are confirmed these results.*

Key words: Flank wear, CT, Chip thickness

I. INTRODUCTION

Tool life is most important for machining economics. If a work material creates more rapid tool wear, the life of the tool will reduce. Machining cost will involve increased cost of the tools and greater production time lost during tool changes. The machining operation results in higher heat generation leads to reduction in tool life, surface properties of the machined parts and growth of tool wear [1]. By keeping all these difficulties the machining industries are continually making an effort for finding new material and new cooling technique that gives the better tool life. In recent days, there has been an increase in CT application for different types of cutting tool the CT technique enhances the tool performances, such as reduction in cutting temperature, improved wear

Revised Manuscript Received on July 10, 2019.

Nagraj patil, Department of Mechanical Engineering, School of Engineering and Technology, Jain Deemed-to-be University Bangalore - 562112, Karnataka, India

Research Scholar, Visvesvaraya Technology University, Belagavi - 590018, Karnataka, India

Gopalakrishna K, Centre for Incubation Innovation Research and Consultancy, Jyothy Institute of Technology, Bangalore - 560082, Karnataka, India

Sangmesh B, Department of Mechanical Engineering, BMS institute of Technology and Management, Avalahalli, Yelahanka, Bangalore-560064, Karnataka, India

resistance and surface quality. Previous researchers have worked on CT technique to improve its properties of carbide insert in this regard, K H W Seah et al [3] investigated on six different types of cutting insert, found that CT and cold-treated insert showed elevated wear resistance in contrast with UT. Similarly, Hejia Zhang et al [4] analyzed the consequence of deep CT on different percentage of cobalt (Co) in tungsten carbide insert; the cryogenic effect was more on the low cobalt carbide insert than the high percentage of cobalt. In another study, Simranpreet Singh Gill et al [5] reported that the CT enhances the life of the coated tungsten carbide insert in comparison with UT, and they have recommended that the TiAlN coated insert is not suitable for deep CT. A.Y.L. Yong et al [5] reported that improvement of tool lives of cryogenically treated tool in comparison with untreated tool during intermittent machining. Likewise, Nursel Altan Özbek et al [6] investigated the CT on carbide insert at different holding temperature. The experimental results were observed that for a holding time of 24 hours the wear resistance was best in comparison with other holding times. This improvement was verified through hardness test and XRD analysis. Similarly, Hui-Bo He et al [7] conducted a study on different machining parameters that influences on the cutting temperature during machining with AISI 304. The experimental results revealed that cutting temperature increase with increase with speed also investigated the optimal parameters for cutting temperature. In another study, N.R. Dhar et al [8] claimed the cryogenic cooling method showed significant improvement in the tool life in comparison with other conventional. It was reported that the precooled cryogenic method enhance the tool life in comparison with other method. However more detailed research attempt on the fundamental of the cryogenic machining of the carbide insert on stainless steel are still required. Besides, due to not having enough considerable experimentation, the precise response of the AISI 304 steel in terms of growth of flank wear, chip thickness, is not clearly available in the previous literature survey. Accordingly, the aim of this investigation is to assess the performance of CT insert.

II. INVESTIGATIONAL METHOD

Commercial available AISI 304 stainless rod having a dimension of 40mm diameter and 300mm length was used as workpiece material for turning operation performed in the CNC machine. The length to diameter proportion was considered for the experiment to meet the ISO 3685 standard. Seco CNMG 120408 Grade MF3 029 uncoated carbide insert and DCLNR 2525 M12 tool holder were

Effect of Cryogenic treatment on Tool Wear, Chip Thickness of Uncoated Carbide Insert during Machining with AISI304 Stainless Steel

considered for the machining tests. The uncoated carbide insert were cryogenically treated at a temperature -176°C for 24hr. after the CT the inserts temperate at a 200°C for 2hr to minimize internal stresses produced during CT Figure 1 shows the CT process. In order to evaluate the performance of cryogenically treated in comparison with UT, in terms of progress of tool wear, chip thickness.

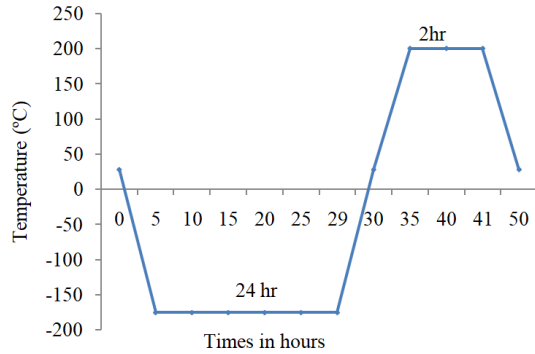


Figure 1. CT process

The entire machining test was conducted on CNC lathe, at different speed of (100.52m/min, 125.66/min, and 150.79/min), at a feed rate of 0.14mm/rev and depth of cut 0.5mm were kept constant. The machining test was carried out to measure the flank and crater wear of CT and UT insert, machining test was interrupted at every 4min interval of time, to study the development in the flank and crater wear. However, flank wear was obtained at higher cutting speed. The greatest amount of flank was evaluated using digital microscope (Dinocapture 2.0 Model: AM3113T, Magnification Range: 20X-250X). The tool life was measured according to the ISO 3685-1993 standard [9]. The EDX test was performed to identify the weight percentage of different elements adhered on the tool during machining. The chip thickness of the CT and UT was measured by using digital microscope. Figure 2 shows the experimental set for machining test.



Figure 2 Experimental set for machining test

III. RESULT AND DISCUSSION

3.1 Material Characterization with the use of SEM and EDX

Figure 3a and 3b shows the microstructure of CT and UT. It was clearly seen from the SEM images, generally four different phases were observed alpha (α), beta (β), and gamma (γ) phases were observed alpha phase contains tungsten

carbide, beta phase contains cobalt binder, and gamma phase contains multiple carbides. From the SEM images it's clearly depicts the presence of dark gray which indicates the presence of Eta (η) phase carbide and precipitation of cobalt binder, the presence of Eta (η) phase carbide provides a greater wear resistance compared with UT. Similarly the presence of Eta (η) phase carbide was also observed in the previous researchers [13].

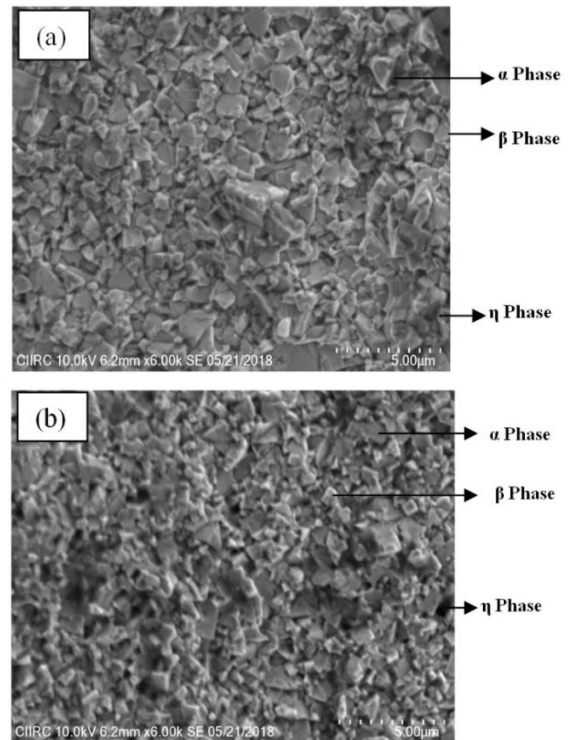


Figure 3. SEM images of carbide insert before and after deep CT (a) CT (b) UT

Figure 4a and 4b showed the EDX analysis for both CT and UT. The EDX test was conducted before and after CT, it was confirmed from the EDX test the CT insert showed in the concentration of cobalt (Co) and carbide (C) particles and decrease in the tungsten (W) in comparison with UT insert. The reduction in the tungsten carbide components (alpha phase) which is more stable form and in turn increase wear resistance. The weight % of the CT insert is excessive than the UT it was clearly indicated in the Figures. The increase in the percentage of C and Co leads to development of Eta (η) phase carbide which is hard in nature, which in turn growth in the wear resistance of the insert. Previous researcher also claimed that the precipitation of Eta (η) phase carbide was observed in the CT insert [5].

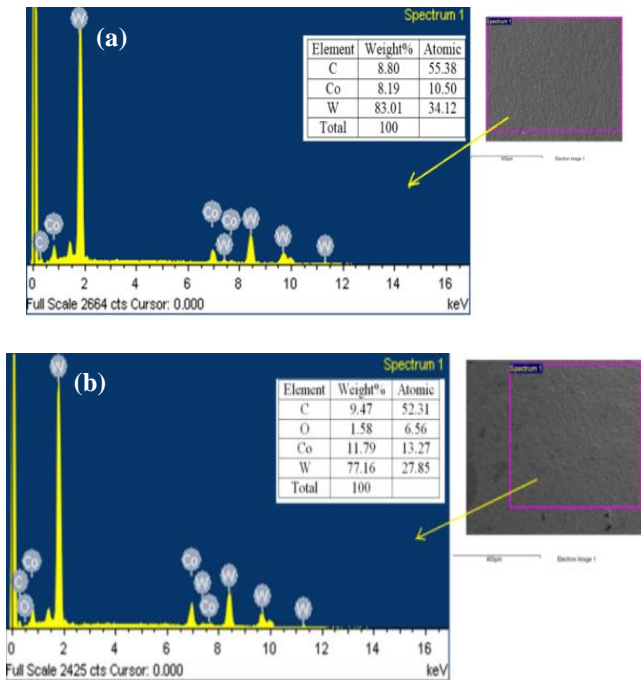


Figure 4b. EDX analysis (a) UT (b) CT inserts

3.2 XRD Analysis

The Figure 5a and 5b showed the X-ray diffraction (XRD) spectra of both CT and UT, XRD study was conducted to inspect the structural changes in the both CT and UT. After CT the transformation of phase takes place from austenite to martensite which leads to the generation of the Eta (η) phase carbide. Nearly at 28° the peak were observed for the CT insert. Some other researcher also confirmed that the CT, increase the cobalt binder and Condensation of Eta (η) phase carbide [6].

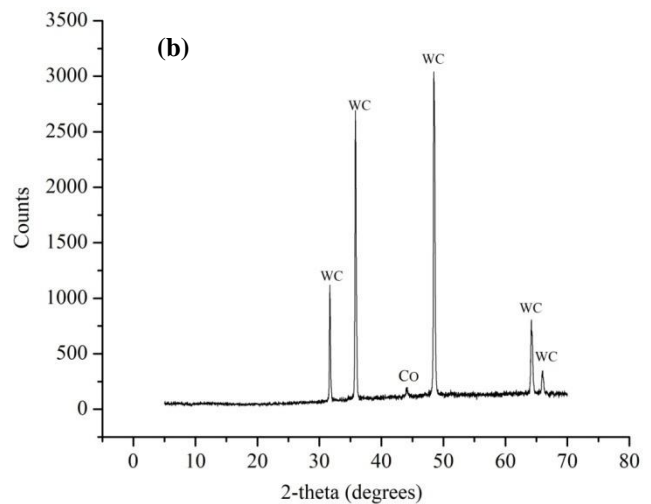
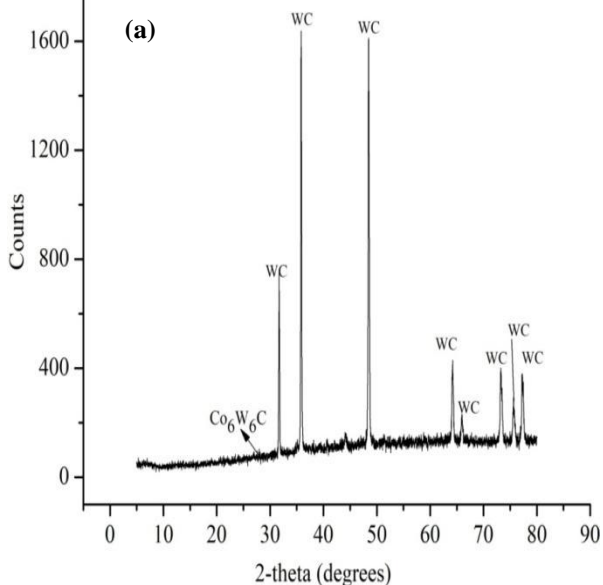


Figure 5 XRD profile (a) CT (b) UT inserts

3.3 Cryogenic treatment effect on tool wear

3.3.1 Flank wear

The development of wear of CT and UT insert over machining time during machining with all speed shown in Figure 6 and 7, respectively. From figures, it shows clearly the development of flank Wear were divided into three regions, initial region where the sharpness of the cutting edge is quickly broken down and a limited size of wear is established, further increase in the cutting time the wear rate becomes uniform, finally the rapid growth in the wear observed at larger speed [10]. The wear is mainly caused due to adhesion, adhesion wear caused due machined surface and tool flank area. In this investigation the progress of maximum flank wear (V_{Bmax}) of both CT insert and UT at feed rate of 0.14mm/rev and a speed of 100.52, 125.66 and 150.79m/min shown in Figure 6 and 7 respectively

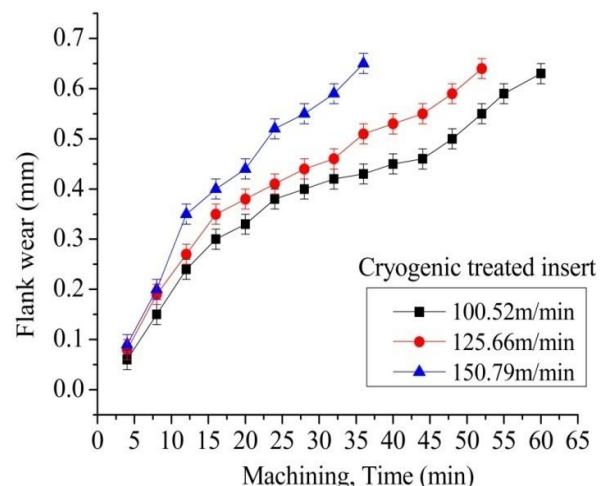


Figure 6: Flank wear (V_{Bmax}) vs machining time of the CTinsert

Effect of Cryogenic treatment on Tool Wear, Chip Thickness of Uncoated Carbide Insert during Machining with AISI304 Stainless Steel

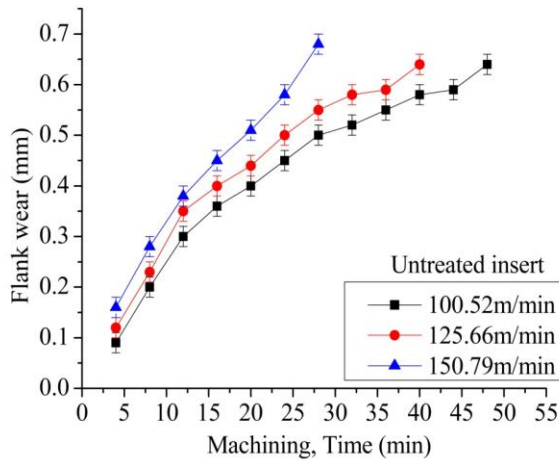


Figure 7: Flank wear (VBmax) vs machining time of the UT

The machining were carried out up to the tool reaches its tool life criteria ($V_{Bmax}=0.6mm$) by considering constant feed and depth of cut. Initially the flank wears growth very rapidly at all speed. However, at all speed the CT insert performed better in comparison with UT. The tool life of the cryogenically treated and UT were shown in the Table 1 the treated insert showed longer tool life in comparison with UT insert under dry machining conditions. The growth of the flank wear were measure by using digital microscope at every 4 minute of equal internal of time, the UT reached maximum flank wear very early in comparison with UT. The CT insert improved its mechanical properties due to transformation austenite phase to martensite phase which leads increase its wear resistance properties it was also claimed by the other researcher [11].

Table 1 Tool life Comparison between two inserts ($V_{Bmax}=0.6mm$)

Cutting speed (m/min)	Cutting insert	Machining Time (Min)
100.52	CT	48
	UT	39
125.66	CT	30
	UT	25
150.79	CT	24
	UT	22

Under some conditions, usually at relative lower speed, during machining the friction was generated, this friction is so significant that the chip fragments adhere on the tool face. The presence of this chip fragments material further increases the friction and this friction leads to building up of layer of chip material. The consequence pile of material is introduced as built up edge. In this study machining test were conducted to recognize the adhesion wear for both CT and UT with speed of 100.52m/min, feed rate of 0.14m/min. Figure 8(a) shows the EDX spectra of CT insert, the foreign particle are 9.48%Fe, and 3.70%Cr were adhered on the tool. Similarly the Figure 9(b) shows the EDX test on tool surface area 16.80Fe%, 4.57Cr% was observed. However, it was noted

that the CT insert showed less % of workpiece components on its tool rake surface. This was achieved attributable to boost its mechanical properties and enhanced thermal conductivity of the insert the similar result was also claimed by Bhatt et al [12].

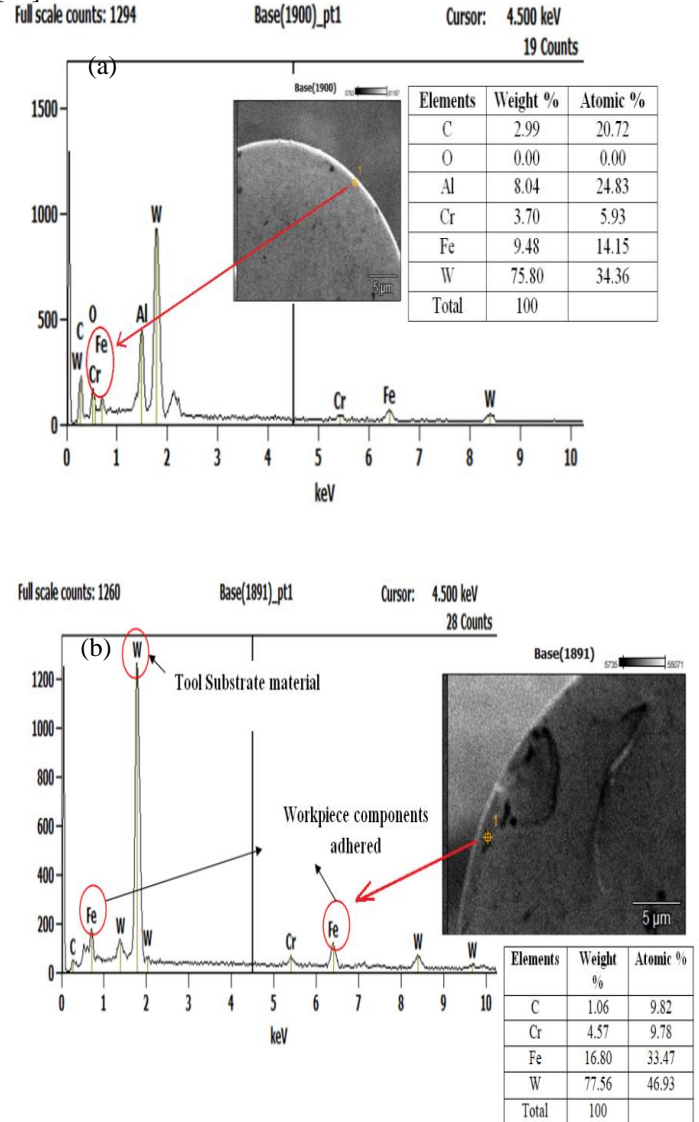


Figure 8: Shows the EDX spectra at a speed of 100.52m/min, feed rate of 0.14mm/rev (a) CT (b) UT insert

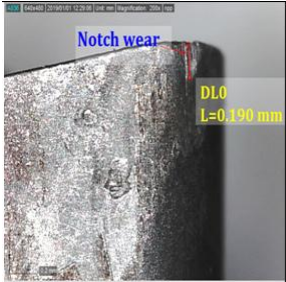
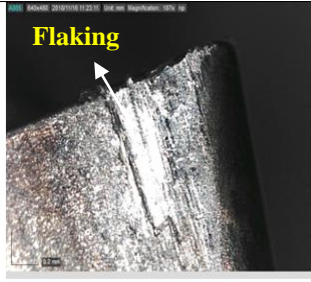
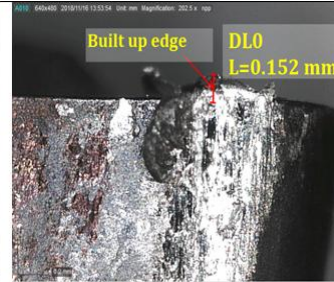
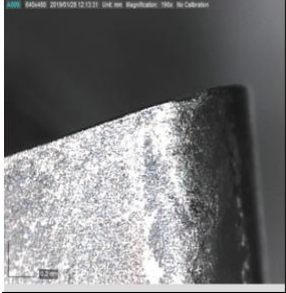

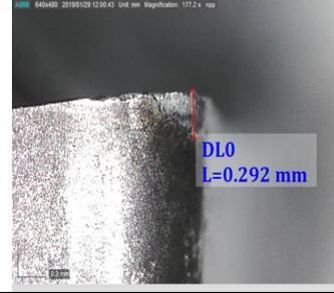
Untreated inset			
CTinsert			
	100.52m/min (10min)	125.66m/min (10min)	150.79m/min (10min)

Figure 9 Growth of flank wear at different cutting speed

Wear land of both CT and untreated inset were shown in the Figure 9. The flank wears and of both cutting insert for all speed were compared at constant machining period of 10min. The both cutting tool were machined at all three speed. It was observed notch wear 0.190mm in UT however, in the CT insert the cutting edges were protected at a speed of 100.52m/min, further increase in the speed from 100.52m/min to 125.66m/min flaking were observed on the UT in other hand the cryogenic insert showed less flank wear (0.136mm). At higher speed 150.79m/min the built up edge were observe for the UT, in this contrasts the CT insert shows no built up edge. Over all it was conclude that the cryogenic insert showed more desirable performance in comparison with UT. This was also supported by EDX test the UT showed a greater percentage of workpiece components on the tool rake of the cutting insert, the CT insert improved its microstructure properties after treatment attributable to formation of Eta phase carbide, this was also supported by XRD and EDX test.

3.4 Crater wear

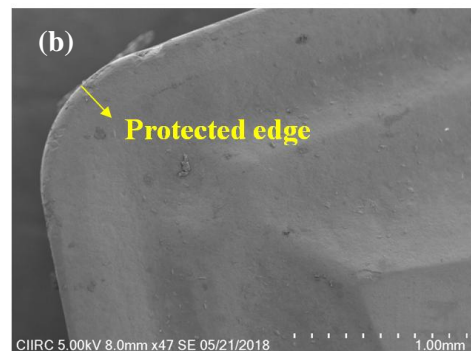
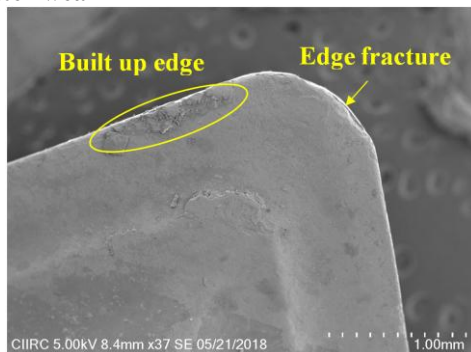


Figure 10 SEM image at a speed of 100.52m/min (a) UT (b) CT insert

The SEM images of the both CT and UT were shown in the Figure 10. In metal cutting operation highest temperature occur along the tool rake surface; sometimes this temperature can be of order 1000°C. Mainly in the carbide insert solid-state diffusion at this temperature can cause rapid wear. Usually the crater wear formed on the rake surface of the tool, this factor determines the cutting tool life. In this study carbide insert were CT the SEM images shows the machining operation at a speed 100.52m/min it from Figure 11(b) it was observed that there is no built up edge were seen on the tool of the insert the cryogenic insert prevented the built up edge in comparison with UT. The CT insert showed enhanced wear resistance due to development of Eta (η) phase particles and densification of cobalt binder (Co) [13].

3.5 Chip thickness

The microscopic images of the chip thickness of the CT insert and UT were shown in the Figure 11. It was confirmed that average tool chip thickness decreases with increase in the speed though the average t_c for both tool decreases with increase in the speed. At a lower speed 100.52m/min it was observed that chip thickness of the CT insert (0.685mm) was less in comparison with UT (0.849mm). Further increase in the speed the CT insert showed less t_c in comparison with UT, Figure 12 Clearly shows that for all three different speed the CT insert showed lesser amount of t_c the lesser t_c caused by increase in the heat dissipation capacity of the carbide insert which leads to the lesser heat generation during machining which enhance the wear resistance properties.

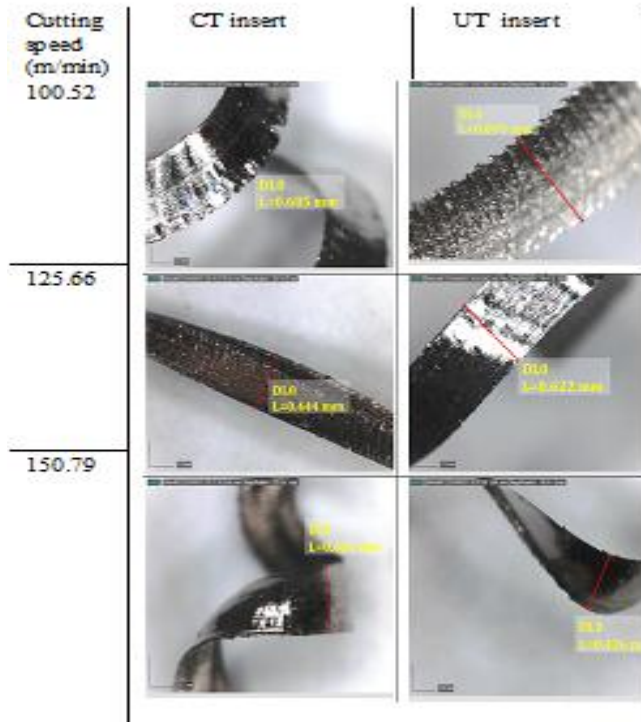


Figure 11 chip thickness variation with different cutting speed

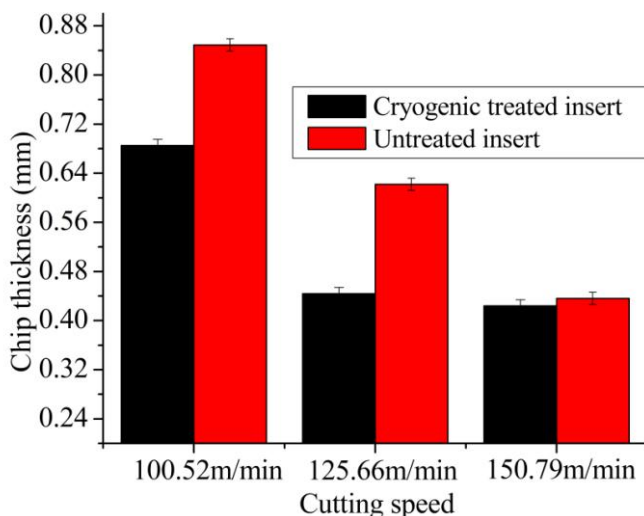


Figure 12 Cutting speed Vs chip thickness

CONCLUSION

CT applied for uncoated tungsten carbide of machining with AISI 304 under dry machining conditions the following conclusion was drawn.

1. The CT carbide insert shows the generation of Eta (η) phase carbide and homogenous distribution in the tungsten carbide substrate in comparison with UT which was confirmed from EDX and XRD test.
2. The maximum flank wear was more for UT in comparison with CT insert
3. Built up edge were observed on the rake face of the UT it was confirmed from the EDX test and microscopic test.
4. SEM images indicated the CT insert showed improved wear resistance.
5. The t_c of the CT insert was less in all cutting speed in comparison with UT.

REFERENCES

1. Kwong J. Axinte DA. & Withers PJ. The sensitivity of Ni-based superalloy to hole making operations: Influence of process parameters on subsurface damage and residual stress. *J of Mater Process Technol*, 2009, Vol. 209, No. 8, pp. 3968–3977.
2. Seah KHW. Rahman M. & Yong KH. Performance evaluation of CT tungsten carbide cutting tool inserts. *Proceedings of the Institution of Mechanical Engineers, Part B: J of Engg Manuf*, 2003, Vol. 217, No.1, pp. 29–43.
3. Zhang H. Chen L. Sun J. Wang W. & Wang Q. An investigation of cobalt phase structure in WC–Co cemented carbides before and after deep CT. *Int J of Refractory Metals and Hard Materials*, 2015, Vol.51, pp. 201–206.
4. Gill SS. Singh J. Singh H. & Singh R. Investigation on wear behavior of CT TiAlN coated tungsten carbide inserts in turning. *Int J of Mach Tools and Manuf*, 2011, Vol. 51, No. 1, pp. 25–33
5. Yong AYL. Seah KHW. & Rahman M. Performance evaluation of CT tungsten carbide tools in turning. *Int J of Mach Tools and Manuf*, 2006, Vol. 46, No.15, pp. 2051–2056.
6. ÖzbekNA. Çiçek A. Gülesin M. & Özbek O. Investigation of the effects of CT applied at different holding times to cemented carbide inserts on tool wear. *Int J of Mach Tools and Manuf*, 2014, Vol. 86, pp. 34–43.
7. He, H.-B., Li, H.-Y., Yang, J., Zhang, X.-Y., Yue, Q.-B., Jiang, X., & Lyu, S. (2017). A study on major factors influencing dry cutting temperature of AISI 304 stainless steel. *Int J of Precision Engineering and Manuf*, 2017, Vol.18, No.10, pp. 1387–1392.
8. Dhar NR. & Kamruzzaman M. Cutting temperature, tool wear, surface roughness and dimensional deviation in turning AISI-4037 steel under cryogenic condition. *International Journal of Machine Tools and Manufacture*, 2004, Vol. 47, No.5, pp. 754–759.
9. ISO 3685-1993 (E). Tool life testing with single point turning tools; (1993).
10. Che Haron CH. Ginting A. & Goh JH. Wear of coated and uncoated carbides in turning tool steel. *J of Mater Process Technol*, 2001, Vol. 116, No. 1, pp. 49–54.
11. Birmingham MJ. Palanisamy S. Kent D. & Dargusch MS. A comparison of cryogenic and high pressure emulsion cooling technologies on tool life and chip morphology in Ti–6Al–4V cutting. *J of Mater Process Technol*, 2012, Vol. 212, No.4, pp. 752–765.
12. Musfirah AH. Ghani JA. & Haron CHC. Tool wear and surface integrity of inconel 718 in dry and cryogenic coolant at high cutting speed. *Wear*, 2017, Vol. 376-377, pp.125–133.
13. Chetan Ghosh S. & Rao PV. Performance evaluation of deep cryogenic processed carbide inserts during dry turning of Nimonic 90 aerospace grade alloy. *Tribology Int*, 2017, Vol. 115, pp. 397–408.



A Timoshenko like model for piezoelectric energy harvester with shear mode

Shreya Banerjee, Sitikantha Roy*

Department of Applied Mechanics, Indian Institute of Technology-Delhi, New Delhi 110016, India

ARTICLE INFO

Keywords:

Energy harvester
Piezoelectric
Shear mode
Flexural mode
Base excitation
Variational Asymptotic Method (VAM)

ABSTRACT

In the present study a fully coupled electromechanical Timoshenko beam theory is developed for modelling an energy harvester operating in d31 (flexural mode with correction due to shear deformation/rotary inertia) and relatively rare d15 (pure shear) mode. The model is developed based on Variational Asymptotic Method (VAM). VAM is a dimensional reduction methodology, which asymptotically approximates the original 3D electro-mechanical enthalpy into an equivalent 1D electromechanical enthalpy functional, using small parameters present in the system. Firstly, we develop a fully coupled Timoshenko cross sectional model, which provides us a single common platform to analyze both d15 and d31 mode energy harvester. The developed cross sectional model is represented by a 7×7 electromechanical stiffness matrix with an additional 1D electrical variable along with 6 1D mechanical degrees of freedom commonly present in Timoshenko type analysis. The cross-sectional model is general enough to accommodate harvesters made of multilayer, arbitrary shaped cross-section, anisotropic material operating in both pure shear as well as in flexure mode. The coupled cross sectional output is fed subsequently into a 1D beam problem for a complete solution.

1. Introduction

The research effort towards vibration based energy harvesting has drastically increased over the past couple of years. This increase is partly because of exponential growth in the usage of wireless electronic devices and the subsequent need for their remote powering. A very initial study on energy harvesting concept was performed by Williams and Yates [2] on electricity generation from mechanical vibration. Many reviews [3,4] subsequently have highlighted the advantage of piezoelectric material to power harvesting from the vibrational energy. Piezoelectric energy harvesters operating in flexural or transverse mode, which is also termed as d31 mode [1] are relatively common in the literature, while harvesters operating in d15 or pure shear mode are rare. The ultimate aim in designing an efficient harvester is to maximize the power output for a certain input load. Dielt et al. [5] was among the first to develop an energy harvester model using Timoshenko beam theory. A shear corrected Timoshenko like model is needed in two situations, first if the beam type harvester is a thick beam and shear deformation of the cross-section cannot be ignored and second, when the piezoelectric material is operating in shear or d15 mode. Recently certain interest has been focused on shear mode energy harvester to maximize the power output [6]. In shear mode or d15 mode of operation the polarization direction in the piezoelectric layer and the

applied electric field [6,7] are normal to each other. If PZT polarization is inclined to the applied field, both shear as well as the transverse modes get activated. The piezoelectric coupling coefficient (d15), in general is larger in magnitude than transverse (d31) coupling term [6]. So, it will be advantageous to develop a model which can capture both flexural as well as shear mode of an energy harvester. A comparative study between the shear (d15) mode and transverse (d31) mode energy harvester can give us an insight into the performance and different aspects of energy harvester modelling. Research on shear mode energy harvester has been limited because of complex fabrication and polling process [6,7]. Majidi et al. [9] studied an interesting concept of nanoribbons generating electricity from elastic deformation induced by sliding friction or mechanical vibration. It was one of the early attempts to model shear mode energy harvesting based on elastic rod theory. Single crystal of $0.71 \text{ Pb}(\text{Mg}_{1/3} \text{ Nb}_{2/3})\text{O}_3 - 0.29 \text{ PbTiO}_3$ were used to study energy harvesting based on shear mode by Ren et al. [10]. A shear mode energy harvesting from pressurized water flow has been developed in [11], where the flow energy was converted into electrical energy from oscillation of piezoelectric film. A single degree of freedom model was developed by Aladwani et al. [7] and Zhou et al. [12] to model the mechanics of shear mode harvester. Shear deformation and rotary inertia are the two extra corrections generally seen in a Timoshenko based model [13] as compared to a classical one.

* Corresponding author.

E-mail address: sroy@am.iitd.ac.in (S. Roy).

<https://doi.org/10.1016/j.compstruct.2018.07.117>

Received 11 December 2017; Received in revised form 18 July 2018; Accepted 30 July 2018

Available online 04 August 2018

0263-8223/ © 2018 Elsevier Ltd. All rights reserved.

Malakooti et al [6] developed an analytical model of a PZT sandwich harvester based on Timoshenko beam theory to predict the electric power output while operating in shear mode under base excitation. Shear mode harvester for low frequency vibration application was studied by Zeng et al [14]. Kulkarni et al. [15] studied torsional stresses which are induced by non-rotational vibrations in an energy harvesting device. A finite element model was presented as well as prototype was demonstrated to validate the proposed design. Thus, the torsion based harvester was proved to have greater potential in producing high power output. Also various configurations for shear mode harvester device were presented along with model to predict the power output under various environment [16]. An initial model of cantilevered piezoelectric energy harvesters was developed by Erturk and Inman in the year 2008 [17]. The error in the existing single degree of freedom system was observed and rectified with some correction factor in the study. Later Aladwani introduced model on energy harvester with a dynamic magnifier for base excitation [18]

The present study is based on a theory named as Variational Asymptotic Method (VAM) which was first introduced by Berdichevsky in late 1970s [19]. Earlier, the theory was successfully implemented to study passive composite structures [20–22]. An original three dimensional elasticity problem has been solved analytically for an isotropic prismatic beam using Variational Asymptotic Method [23]. Later Roy et al. [24,25] extended the theory to study actuation effect. In our previous work we have modelled sensor under static and dynamic load [26]. In that study we used a different approach i.e a recovery module to recover back the 3D electrical field variables (voltage, charge etc) to analyze a sensor. Fully coupled model at cross sectional level is a better and efficient way to model an energy harvester. Also the model should be able to connect to an external circuit. Most of the existing literatures in energy harvester modeling are based on Euler Bernoulli beam assumptions, which are fairly good to study transverse mode of operation, but not much work has been reported in the literature on harvester model based on shear mode of piezoelectricity. Shear mode based energy harvesters can only be studied through a Timoshenko model. Previously we have developed the classical model for an energy harvester and has also validated it with experimental results from literature [29]. In the present work we develop a fully coupled Timoshenko model which can be used to study both flexural as well as shear mode energy harvesters. In a previous work Roy et al. [27] developed a generalized Timoshenko model for an actuator using VAM. The model lacked an electrical field variable at the cross sectional level, which is needed to analyze a fully coupled model to design an energy harvester. Our present study initiates with modification of the previous Timoshenko model [27] and developing a full-fledged energy harvester model that is capable of capturing all the physics involved with both transverse and shear mode of a harvester. Voltage, power, current expressions were obtained for a certain base harmonic acceleration. A comparative study has been performed and interesting findings have been discussed.

2. Mathematical formulation

In this section we briefly describe the basic kinematics of a 3D beam, and its subsequent dimensional reduction, for detailed derivation readers are referred to Refs. [26,27]. Following a Lagrangian description, an arbitrary material point in the un-deformed reference state of a beam can be represented by a position vector as,

$$\hat{r}(x_1, x_2, x_3) = r(x_1) + x_\alpha b_\alpha \tag{1}$$

where, r defines the locus of reference line. After deformation the triad b_i undergoes rotational transformation to a new set of triad B_i . Suffix i varies from 1 to 3. Due to transverse shear deformation B_i does not remain tangent to the deformed beam reference line. For the purpose of simplifying derivation we introduce another set of intermediate triad T_i as shown in Fig. 1. T_i (for $i = 1$) by construction is tangent to

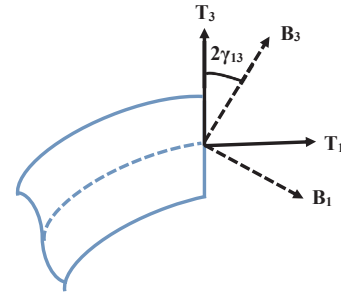


Fig. 1. Coordinate systems representing transverse shear deformation.

the deformed beam reference line. The relation between the two sets of triads B_i and T_i can be expressed by the small rotations associated with the shear deformations $(\gamma_{12}, \gamma_{13})$. Thus mathematically it can be expressed as,

$$\begin{Bmatrix} B_1 \\ B_2 \\ B_3 \end{Bmatrix} = \begin{bmatrix} 1 & -2\gamma_{12} & -2\gamma_{13} \\ 2\gamma_{12} & 1 & 0 \\ 2\gamma_{13} & 0 & 1 \end{bmatrix} \begin{Bmatrix} T_1 \\ T_2 \\ T_3 \end{Bmatrix} \tag{2}$$

The location of an arbitrary Lagrangian material point, with position vector \hat{r} is represented by \hat{R} after the deformation and is given by,

$$\hat{R}(x_1, x_2, x_3) = R(x_1) + x_\alpha T_\alpha(x_1) + \hat{w}_i(x_1, x_2, x_3) T_i(x_1) \tag{3}$$

where, R represents the position vector to a point on the reference line of the deformed beam and \hat{w}_i are the warping components expressed in T_i base system.

The expression for generalized strain and electric field for a Timoshenko model is [27],

$$\Gamma = \Gamma_h \hat{w} + \Gamma_\epsilon \epsilon_T + \Gamma_l \hat{w}' \tag{4}$$

where, $\Gamma_h, \Gamma_\epsilon, \Gamma_l$ are the operator matrices, and their explicit form can be found in Ref. [27], $\Gamma = [\Gamma_{11} \ 2\Gamma_{12} \ 2\Gamma_{13} \ \Gamma_{22} \ 2\Gamma_{23} \ \Gamma_{33} \ E_1 \ E_2 \ E_3]^T$, $\hat{w} = [\hat{w}_1 \ \hat{w}_2 \ \hat{w}_3 \ \tilde{\phi}]^T$ and $\epsilon_T = [\gamma_{11} \ \gamma_{12} \ \gamma_{13}]^T$ represent the 3D generalized strains, generalized warping field, and 1D mechanical strains respectively.

The 3D electromechanical enthalpy for linear piezoelectricity is given by,

$$2H = \left\langle \Gamma^T \begin{bmatrix} C^E - e \\ -e^T - k^s \end{bmatrix} \Gamma \right\rangle \tag{5}$$

Here C^E is of 6×6 dimension and contains the stiffness values of the material measured at constant electric field, e is of dimension 6×3 , and contains piezoelectric coupling coefficients and k^s is the 3×3 matrix of dielectric constants measured at constant strain condition.

2.1. Cross-sectional model

Problems involving any arbitrary cross section shape is solved using finite element based numerical solution technique. Thus the cross section is discretized using finite elements with four nodal variables, 3 of them are mechanical warpings and the fourth one is the electric potential-hereafter will be called as generalized warpings $\hat{w}_i \in (w_i, \phi)$,

$$\hat{w}(x_1, x_2, x_3) = S^u(x_2, x_3) V(x_1, t) \tag{6}$$

where, S^u is the shape function matrix and V represents a column matrix with discretized nodal variables. Substituting Eqs. (6) and (4) in Eq. (5) we obtain the discretized form corrected till second order of slenderness $\frac{h}{l}$ of the electromechanical enthalpy,

strain related to transverse shear deformation measures are zero, which mathematically means [19],

$$\begin{aligned} \bar{\gamma}_{11} &= \gamma_{11} \text{ and } 2\gamma_{1\alpha} = 0 \\ \bar{\kappa}_i &= \kappa_i \text{ and } 2\gamma_{1\alpha} = 0 \end{aligned} \tag{22}$$

thus, 1D strain measures defined in T_i and B_i basis follow a kinematical identity given as,

$$\varepsilon_T = \varepsilon_B + Q\gamma'_B \tag{23}$$

where,

$$Q = \begin{bmatrix} 0 & 0 \\ 0 & 0 \\ 0 & -1 \\ 1 & 0 \end{bmatrix} \tag{24}$$

$\varepsilon_B = [\gamma_{11} \kappa_1 \kappa_2 \kappa_3]^T$ are the classical strain measures and $\gamma_B = [2\gamma_{12} 2\gamma_{13}]^T$ are shear strains. These all strains are measured associated with Timoshenko model measured in B_i basis and ε_T are the 1D strains in T_i basis. Substituting Eq. (23) in Eq. (19) the electromechanical enthalpy can be expressed related to B_i basis, but such model involves derivatives of 1D strains which are not convenient for engineering applications. Thus the derivatives are eliminated and a generalized Timoshenko model has been constituted. The details of the derivation has been discussed in Appendix A.

The 1D coupled constitutive equations of a Timoshenko based energy harvester model which relates 1D generalized forces with its kinematical conjugates (1D generalized strains) as well as voltage,

$$F = \frac{\partial H_1}{\partial \varepsilon_B},$$

or,

$$F = S\varepsilon_B - \tilde{c}^a \phi \tag{25}$$

and,

$$q = \frac{\partial H_1}{\partial \phi}$$

or,

$$q = -\varepsilon_B^T \tilde{c}^a - c_p \dot{\phi} \tag{26}$$

where, S is the cross sectional stiffness of the electromechanical system, \tilde{c}^a represents the coupling coefficient and c_p is the capacitance per unit length of the structure. Eqs. (25) and (26) represents the coupled cross-sectional equations for the Timoshenko based energy harvester model.

The generalized Timoshenko constitutive model for an electro-mechanical energy harvester can be expressed in matrix form as,

$$\begin{bmatrix} F_1 \\ F_2 \\ F_3 \\ M_1 \\ M_2 \\ M_3 \\ q \end{bmatrix} = \begin{bmatrix} s_{11} & s_{12} & s_{13} & s_{14} & s_{15} & s_{16} & -\tilde{c}_{11} \\ s_{12} & s_{22} & s_{23} & s_{24} & s_{25} & s_{26} & -\tilde{c}_{12} \\ s_{13} & s_{23} & s_{33} & s_{34} & s_{35} & s_{36} & -\tilde{c}_{13} \\ s_{14} & s_{24} & s_{34} & s_{44} & s_{45} & s_{46} & -\tilde{c}_{14} \\ s_{15} & s_{25} & s_{35} & s_{45} & s_{55} & s_{56} & -\tilde{c}_{15} \\ s_{16} & s_{26} & s_{36} & s_{46} & s_{56} & s_{66} & -\tilde{c}_{16} \\ -\tilde{c}_{11} & -\tilde{c}_{12} & -\tilde{c}_{13} & -\tilde{c}_{14} & -\tilde{c}_{15} & -\tilde{c}_{16} & c_p \end{bmatrix} \begin{bmatrix} \gamma_{11} \\ \gamma_{12} \\ \gamma_{13} \\ \kappa_1 \\ \kappa_2 \\ \kappa_3 \\ \phi \end{bmatrix} \tag{27}$$

where $F_1, F_2, F_3, M_1, M_2, M_3$ are the equivalent force and moment terms over a cross section, $s_{11}, s_{22}, s_{33}, s_{44}, s_{55}, s_{66}$, are the axial, shear in 1–2 plane, shear in 1–3 plane, torsion, bending in 1–2 plane, bending in 1–3 plane stiffness terms and d denotes capacitance per unit length. All the off diagonal terms are the coupled stiffness and electro-mechanical coupling terms. $\gamma_{11}, \gamma_{12}, \gamma_{13}, \kappa_1, \kappa_2, \kappa_3$ are the strain terms and r represents the electric potential. Here r represents the three coordinate direction of a rectangular right hand coordinate system.

2.2. Short circuit and open circuit condition

Short or closed circuit condition is referred to when the external load or electrical resistance is very low. Open circuit condition prevails when external load or electrical resistance is very high. The two circuit conditions are important to study an energy harvester model, as they are important to know about the minimum and maximum operating range of a model. When we solve a free vibration problem for an energy harvester we get two different natural frequencies corresponding to the short circuit and closed circuit conditions.

2.2.1. Short circuit or closed circuit

The short circuit condition at the cross sectional level will be represented by the following equation,

$$\dot{q} = i = \frac{v}{R} = -\varepsilon_B^T \tilde{c}^a - c_p \dot{\phi} \tag{28}$$

Since, $R \rightarrow 0$ so the coupled cross sectional equation will be,

$$F = S\varepsilon_B \tag{29}$$

2.2.2. Open circuit

The open circuit condition at the cross sectional level can be represented as,

$$0 = -\varepsilon_B^T \tilde{c}^a - c_p \dot{\phi} \tag{30}$$

Integrating and substituting Eq. (30) in Eq. (25) and integrating it we get the corrected cross sectional stiffness for the open circuit condition as,

$$\bar{S} = S + \frac{\tilde{c}^a \cdot \tilde{c}^{aT}}{c_p} \tag{31}$$

Thus the coupled cross sectional equation for open circuit condition ($R \rightarrow \infty$) will be,

$$F = \bar{S}\varepsilon_B \tag{32}$$

$$0 = -\varepsilon_B^T \tilde{c}^a - c_p \dot{\phi} \tag{33}$$

2.3. 1D solution

For an electromechanical structure the Hamilton's principle can be expressed as,

$$\int_{t_1}^{t_2} [\delta(T - H_1) + \delta\bar{W}] dt = 0 \tag{34}$$

where, t_1 and t_2 define arbitrary time interval, T denotes kinetic energy, H_1 is the electromechanical enthalpy and $\delta\bar{W}$ is the virtual work due to the applied loads and electric charges. The bar over the virtual work term defines that it need not be variation of functions or functional.

For a two degree of freedom per node beam element as shown in Fig. 3 a cubic and quadratic shape functions are proposed for w and θ which can be exactly integrated and is immune to 'shear locking'. The discretized equation is given as

$$\begin{Bmatrix} w \\ \theta \end{Bmatrix} = \begin{bmatrix} N_w \\ N_\theta \end{bmatrix} \{\delta\} \tag{35}$$

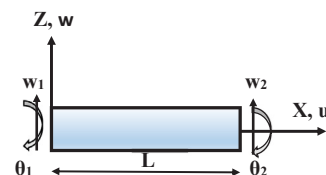


Fig. 3. 2-dof Timoshenko beam element.



Fig. 4. a. Shear mode energy harvester b. Transverse mode energy harvester.

Table 1
Geometry of cantilever beam type harvester.

Parameters	Shear mode harvester	Transverse mode harvester
Length (m)	0.1	0.1
Width (m)	0.025	0.025
PZT thickness, t_p (m)	0.002	0.001
Substrate thickness, t_s (m)	0.001	0.002

where,

$$\{\delta\}^T = \{w_1, \theta_1, w_2, \theta_2\} \quad (36)$$

The form of shape functions N_w and N_θ has been discussed in details in Appendix B.

The system level, discretized coupled dynamic equation of motion for a shear energy harvester can be derived from Hamilton's principle as,

$$M\{\ddot{\delta}\} + C\{\dot{\delta}\} + K\{\delta\} - \vartheta\phi(x, t) = -M\{\ddot{\delta}_{base}\} \quad (37)$$

and,

$$C_p\dot{\phi}(x, t) + \frac{\phi}{R} + \vartheta\{\delta_e\} = 0 \quad (38)$$

Eq. (37) is the global equation of motion where M , C and K are the global mass, damping and stiffness matrix of the harvester respectively. In Eq. (38), ϑ and C_p represent system coupling vector and total system capacitance. The damping for the present analysis is assumed to be proportional damping as,

$$C = \alpha M + \beta K \quad (39)$$

where α and β are the constant of proportionality.

The short circuit and open circuit natural frequencies are found by solving the simple eigen value problem from Eq. (37) and (38).

The eigenvalue problem associated with short circuit condition will be given by the following equation,

$$\det([K] - \omega^2[M]) = 0 \quad (40)$$

and for open circuit condition will be,

$$\det\left([K] - \omega^2[M] + \frac{[\vartheta][\vartheta]^T}{C_p}\right) = 0 \quad (41)$$

2.3.1. Steady state response for a harmonic base excitation

For a harmonic base excitation, $x_b = X_B e^{j\omega t}$ (X_B is the amplitude, ω is the excitation frequency and x_b the base displacement), it can be easily shown that the steady state voltage FRF can be expressed as,

$$V_{FRF} = \frac{-j\omega\left(\frac{1}{R} + j\omega C_p\right)^{-1}\vartheta^T\left[-\omega^2 M + j\omega C + K + j\omega\left(\frac{1}{R} + j\omega C_p\right)^{-1}\vartheta\vartheta^T\right]^{-1} M X_B}{X_B} \quad (42)$$

The point FRF for tip velocity is related to the velocity amplitude at the tip with respect to the inertial or fixed reference frame and normalized by gravitational acceleration (g),

$$w_{abs} = -\frac{j}{\omega}(1 + X_0) \quad (43)$$

where,

$$X_0 = \left[-M\omega^2 + Cj\omega + K + j\omega\left(j\omega C_p + \frac{1}{R}\right)^{-1}\vartheta\vartheta^T\right]^{-1} M\omega^2 X_B \quad (44)$$

Current FRF can be expressed as,

$$I_{FRF} = \frac{V_{FRF}}{R} \quad (45)$$

and, power FRF can be obtained as,

$$P_{FRF} = \frac{V_{FRF}^2}{R} \quad (46)$$

3. Results and discussions

In the present work a Timoshenko like beam model is developed for shear mode energy harvester using Variational Asymptotic Method. Shear mode energy harvester is modelled as a piezoelectric sandwich beam with piezoelectric as the core as shown in Fig. 4a. Table 1 lists the geometric parameters. A comparison study has been performed between shear and transverse mode energy harvester to analyze the outcome from the two models and to give us best possible conditions for improved energy conversion efficiency. The transverse mode energy harvester is also designed based on our developed Timoshenko model but with a bimorph configuration as shown in Fig. 4b. For both the configuration mass per unit length is kept constant. PZT 5H and a similar substrate alloy have been used for both shear and transverse mode harvester so that the effective dynamic properties remain the same. For the present study we have considered a proportional damping, which represents viscous resistance due to air or damping occurring from the environment. The damping ratio for both the shear and transverse mode is kept constant for the comparison study. The harvester model has been given a harmonic base excitation and has a cantilever boundary condition. The geometry considered for shear mode i.e PZT layer sandwiched in between by two substrate alloy layer will automatically excite the shear mode as the polarization is in the axial direction for the PZT layer as shown in the Fig. 4a. Also the transverse mode will be excited for the bimorph configuration as the polarization is in the transverse direction as shown in Fig. 4b. Both the configurations are having rectangular cross section having same mass and volume of material for both shear and transverse mode harvester.

3.1. Observations

First we have performed an eigen value analysis to get the correct modes from the developed model. In Fig. 5 we see the first three bending and rotational modes corresponding to first natural frequency. Our developed Timoshenko model is devoid of any shear locking problem since we have used independent cubic shape function for transverse displacement and quadratic shape function for rotation [28]. The details about the shape functions have been discussed in Appendix B.

The developed model predicts the voltage and power frequency response per base acceleration. An experimental validation of the classical transverse mode energy harvester model have already been discussed in our previous published work [29]. In Appendix C we have

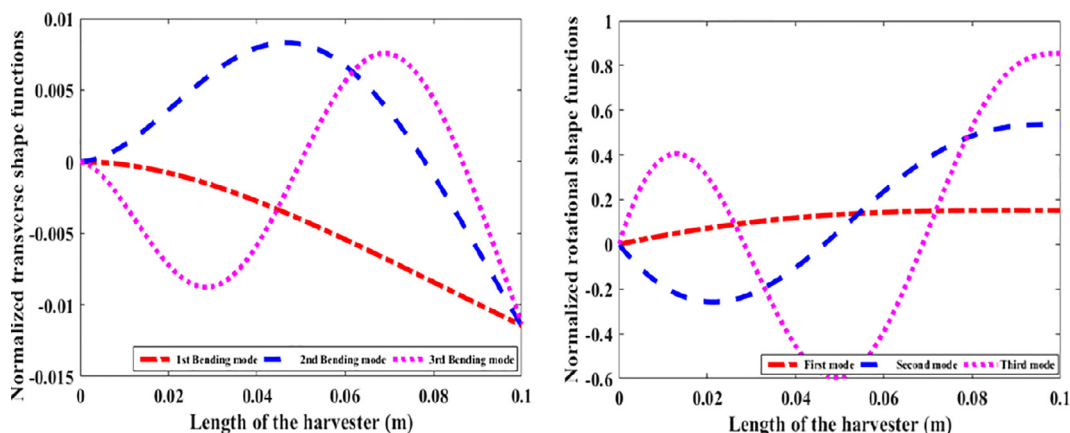


Fig. 5. First three transverse and rotational mode shapes of Timoshenko beam.

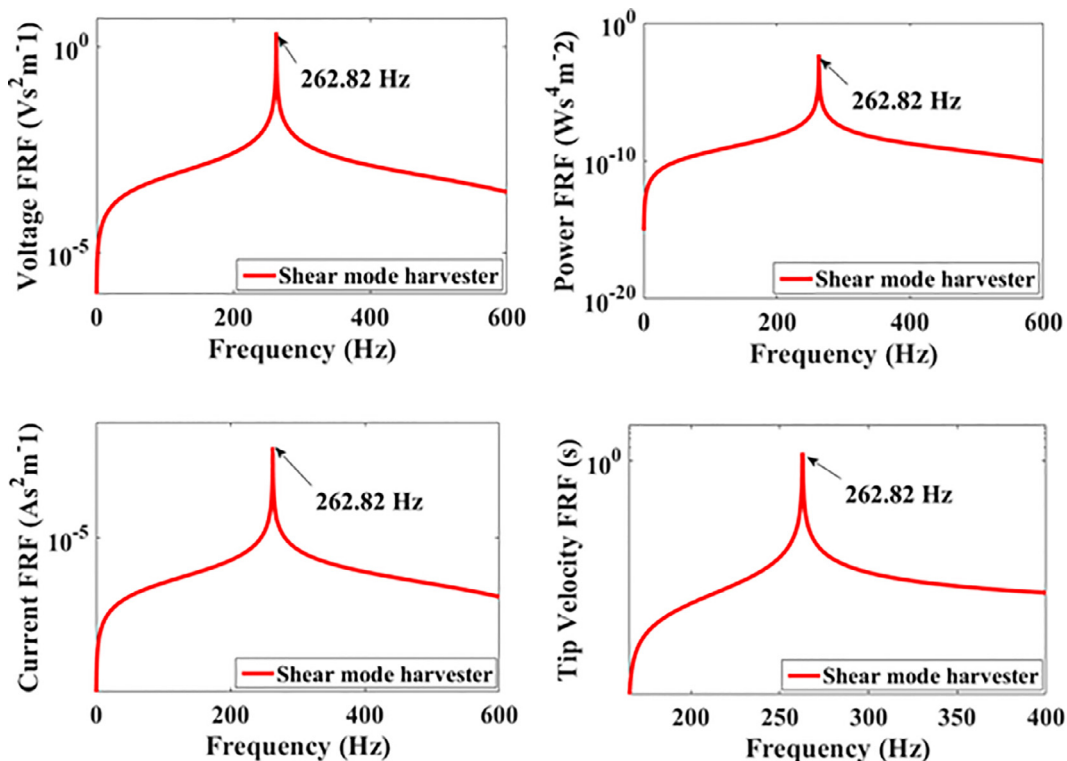


Fig. 6. Voltage, power, current and tip velocity FRF for shear mode piezoelectric energy harvester.

given a brief of the experimental validation of the harvester model operating in transverse mode. The experimental validation proves the accuracy and reliability of our model. Fig. 6 shows the voltage, power, current and tip velocity Frequency Response Function (FRF) for shear harvester excited at first resonance frequency. Voltage, power, current and tip velocity FRF with different load resistance excited at first and second resonance frequency has been shown in Figs. 7 and 8. With increase in load value voltage increases with a right side frequency shift. For current, with variation of load the frequency shift is in opposite direction i.e towards left for both the plots. Power variation with load is arbitrary and does not follow a proper pattern as voltage and current FRF. This happens as power is multiplication of current and voltage FRF.

A full spectrum of voltage, power, current and tip velocity FRF has been shown in Fig. 9. The model is also capable enough of capturing the effect of load resistance. The voltage generation increases with increase in load resistance, till an optimum frequency value then saturation

occurs as shown in the Fig. 10. The power follows a trend in which an optimum value of load reaches its peak value then it starts decreasing with increase in load value. The variation for tip velocity and current with load are shown in Fig. 10. Thus optimum designing of the resistance value for a particular harvester model can lead to maximum energy scavenging.

A detail study of resistance value to be used for any kind of energy harvester is very important. Fig. 11 shows the voltage, power, current and tip velocity comparison between shear and transverse mode energy harvester. It is quite clear from the plots that shear mode harvester generates more power than transverse mode. It has also been observed that the output power from both the model is highly dependent on damping ratio ξ . We have kept damping ratio ξ to be same for both the model. As all other influencing parameters are kept the same, the higher power output for shear harvester is because of higher value of electromechanical coefficient.

The Natural frequencies differ in short circuit and open circuit case

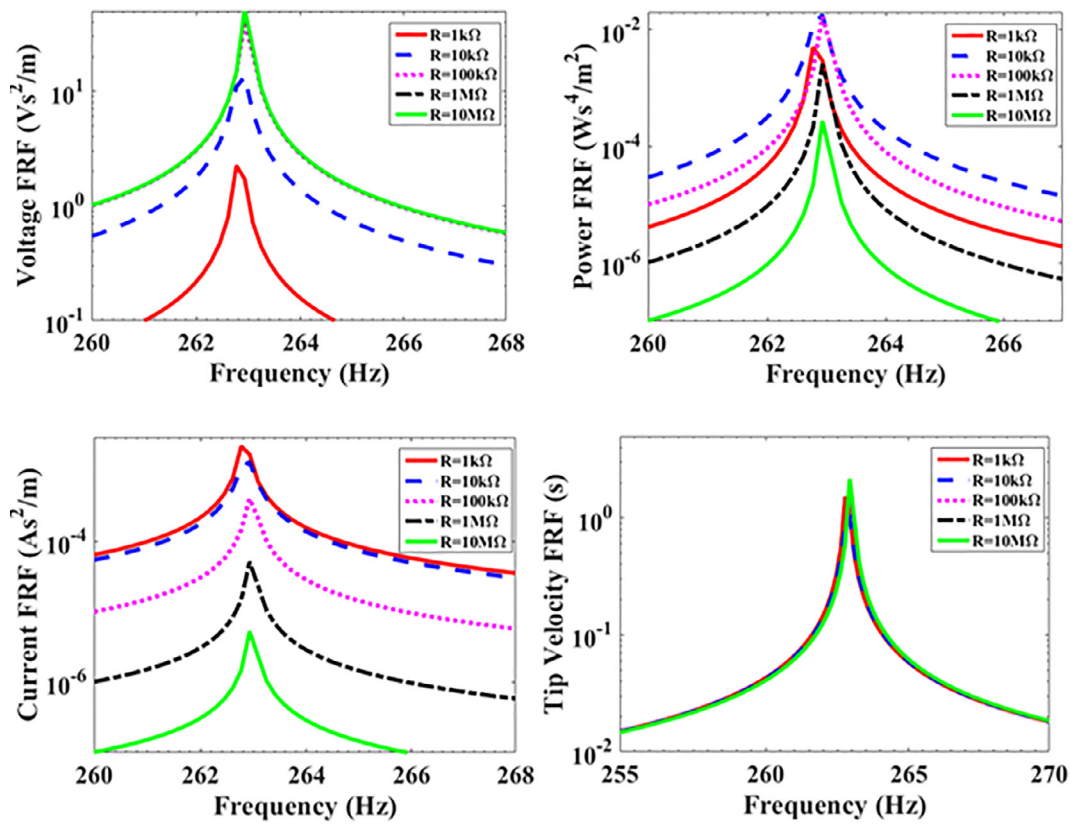


Fig. 7. Voltage, power, current and tip velocity FRF for 5 different values of load resistance excited at first resonance frequency for shear mode piezoelectric energy harvester.

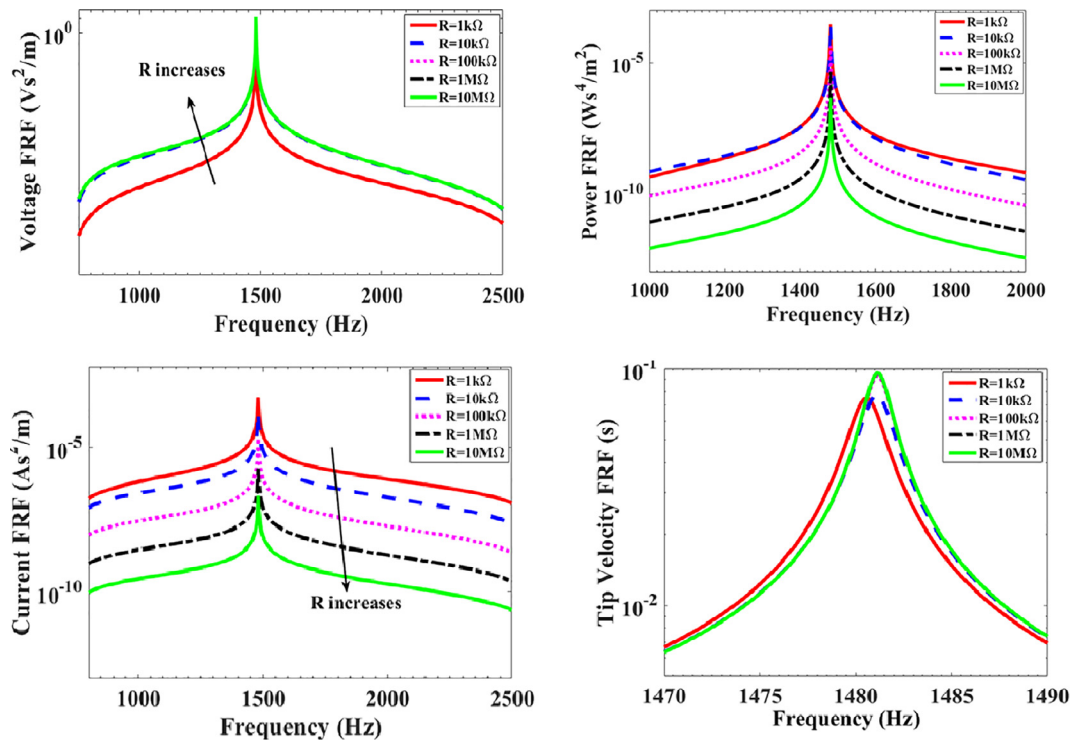


Fig. 8. Voltage, power, current and tip velocity FRF for 5 different values of load resistance excited at second resonance frequency for shear mode piezoelectric energy harvester.

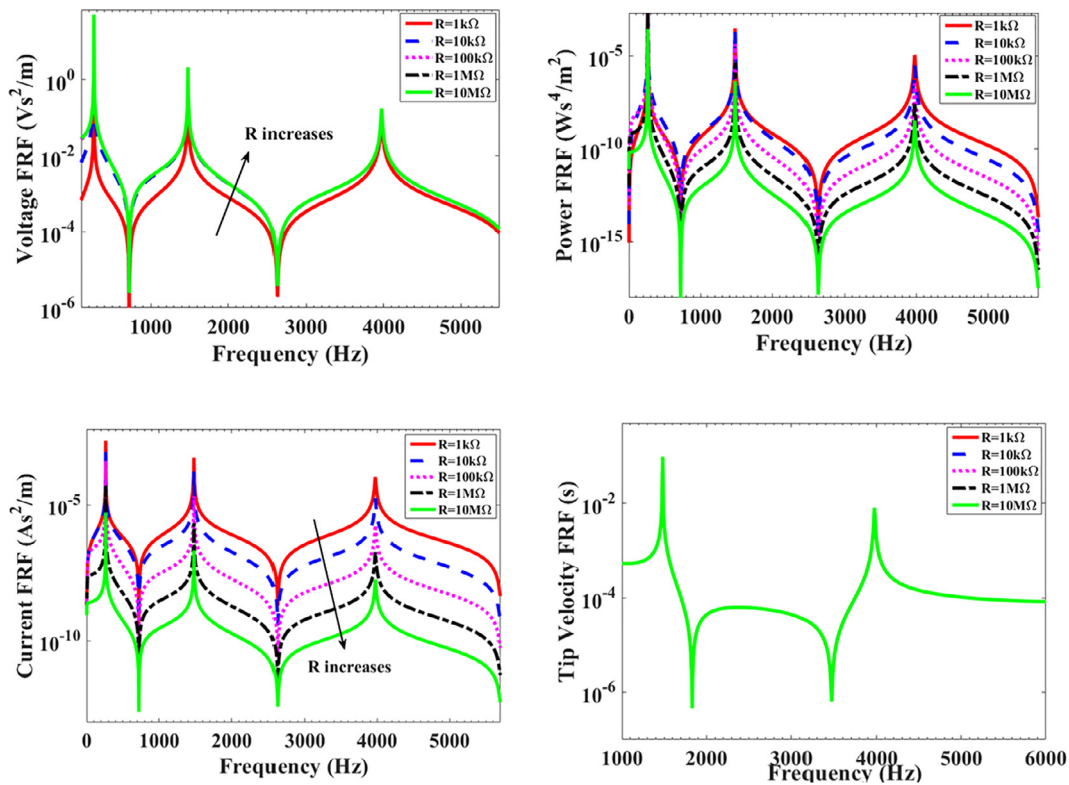


Fig. 9. Spectrum of voltage, power, current and tip velocity FRF for 5 different values of load resistance for shear mode piezoelectric energy harvester.

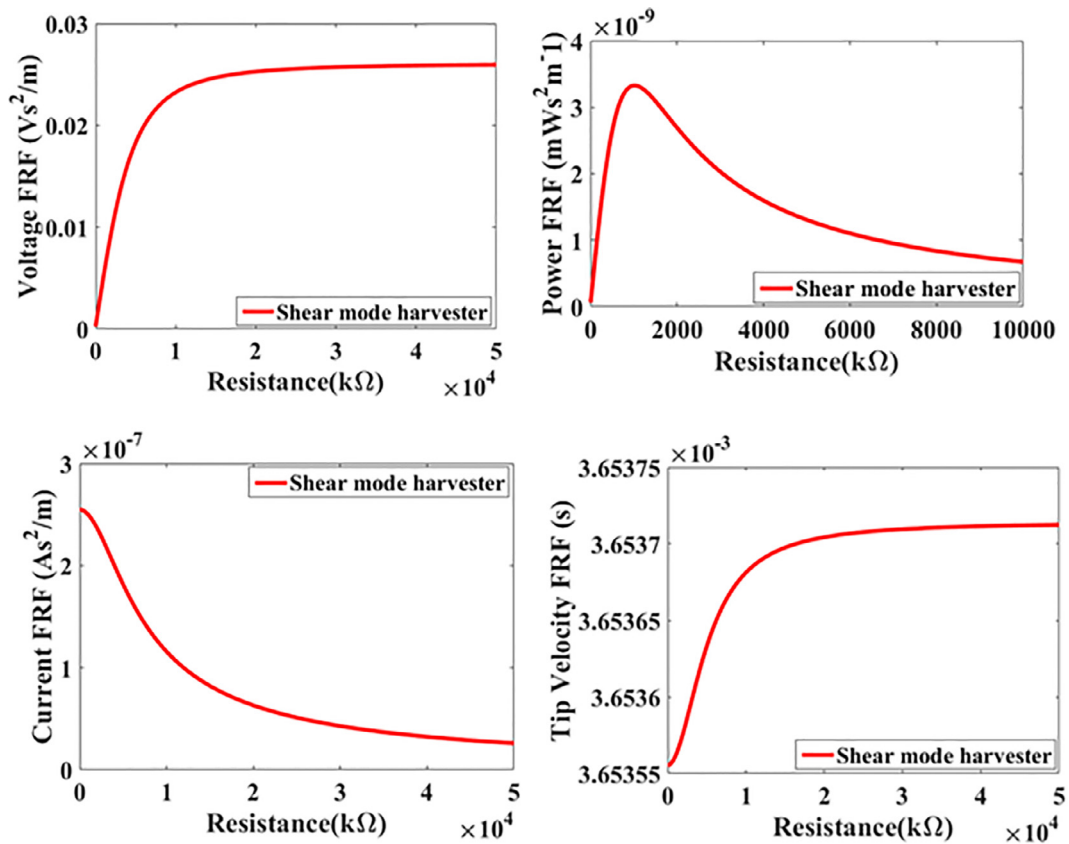


Fig. 10. Voltage, power, current and tip velocity FRF variation with load of a shear mode piezoelectric energy harvester.

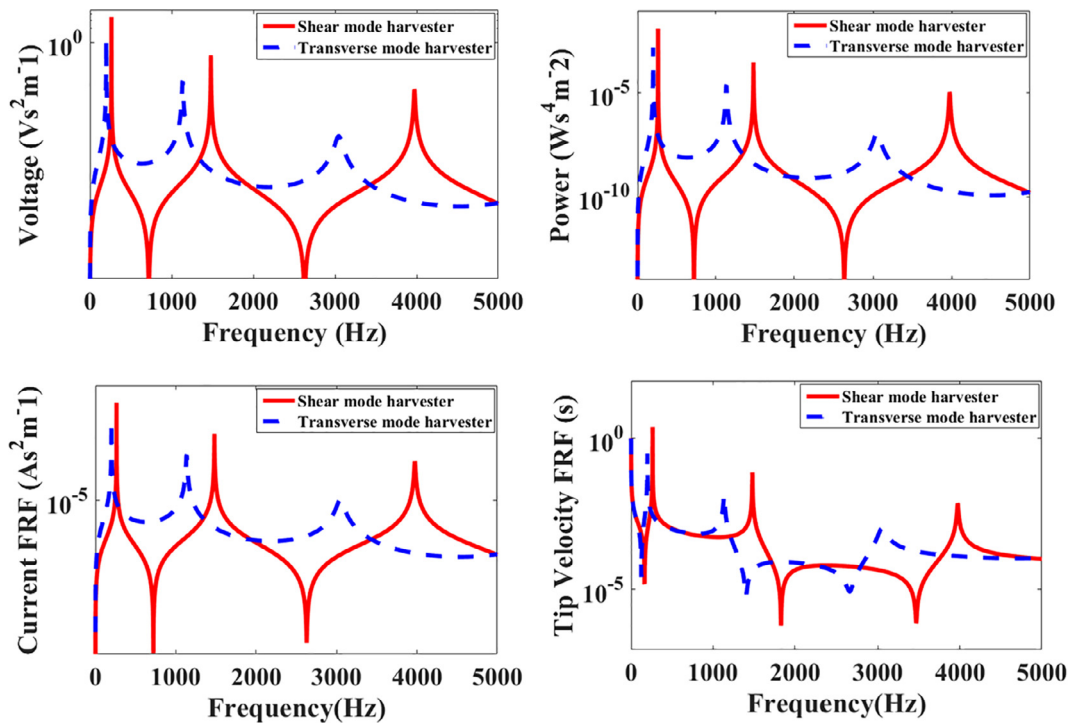


Fig. 11. Comparison of voltage, power, current and tip velocity FRF of shear and transverse mode piezoelectric energy harvester.

Table 2

First and second short circuit and open circuit natural frequency for shear and transverse mode energy harvester.

Frequency		Shear mode harvester	Transverse mode harvester
1st Natural frequency	SC Frequency	262.82 Hz	199.51 Hz
	OC Frequency	263.02 Hz	202.92 Hz
2nd Natural Frequency	SC Frequency	1480.50 Hz	1134.17 Hz
	OC Frequency	1486.23 Hz	1152.86 Hz

Table 3

Comparison between electrical and mechanical characteristics for shear and transverse mode energy harvester.

Equivalent structural and circuit parameters	Shear mode harvester	Transverse mode harvester
s_{33} (N)	0.12480654E+07	0.68899399E+06
s_{55} (Nm ²)	0.14616162E+02	0.86438215E+01
Electromechanical coupling (\tilde{e}_{13})	0.30780383E+00	0.00000000E+00
Electromechanical coupling (\tilde{e}_{15})	0.00000000E+00	-0.29762419E-03
Capacitance (C_p)	2.957e-07	1.003e-06

for both sandwich and bimorph beam as the stiffness is different for the two models. For shear mode energy harvester we can observe that there is not much frequency shift between first short and open circuit natural frequency. But the second short and open circuit natural frequency has larger frequency shift as compared to the first. Table 2 lists the first and second short and open circuit natural frequency for both shear and transverse harvester modelled through Timoshenko beam analysis.

The assumed geometry and based on the materials used transverse mode gives us a lower natural frequency as compared to the shear mode energy harvester. Table 3 lists the comparison between the electrical and mechanical parameters for shear and transverse harvester. An effective mathematical model is of large importance to visualize the

different parameters which are responsible for maximizing power generation for both shear as well as transverse mode energy harvester.

4. Conclusion

In an efficient design of an energy harvesting device the main goal is maximizing the output power. One of the important factors which determines the power output is the value of piezoelectric coupling coefficient. Large shear coefficient for most of the piezoceramics has motivated us for this present study. Firstly, a fully coupled Timoshenko model was developed mathematically based on a well-established theory named as Variational Asymptotic Method. Further it was used to model a shear as well as a transverse mode energy harvester. The model estimates the output voltage, power, current and tip velocity of a sandwich as well as bimorph beam operating in shear and transverse mode under base harmonic excitation. Effect of external electrical loads was studied as a parameter governing the harvester efficiency. The present study shows that shear mode harvester is more efficient as compared to the transverse mode energy harvester in terms of power output. Also the study on the effect of load resistance on the model shows that output power is sensitive to external electrical load. Determining the optimal value of load resistance is one of the major factors to enhance output power. Damping is also another crucial factor while comparing the output power for shear and transverse energy harvester. Complex polarization process is one of the major drawbacks for shear mode energy harvester model. Because of this reason the fabrication has been always very challenging. If this can be overcome then experimental studies can be performed which can strengthen our theoretical observations. There is a scope of future study of multilayer, anisotropic PZT harvester under the present modeling framework.

Acknowledgement

The first author would like to thank Ministry of Human Resource Development, Government of India (MHRD) for her PhD fellowship.

Appendix A

Timoshenko theory with second order asymptotical correction means it contains spatial derivatives of classical strain, also nonlinear terms will not affect the strain energy. So strain derivatives are eliminated in a generalized Timoshenko model and fitted into a much simpler quadratic form [27] of enthalpy which looks like,

$$2H_1 = \epsilon_B^T X \epsilon_B + 2\epsilon_B^T F \gamma_B + \gamma_B^T G \gamma_B - 2\epsilon_B^T E_1^a - 2\gamma_B^T E_2^a + c_p \phi^2 \tag{A.1}$$

Here $E_1^a = [\tilde{\epsilon}_{11} \ \tilde{\epsilon}_{14} \ \tilde{\epsilon}_{15} \ \tilde{\epsilon}_{16}]^T$ and $E_2^a = [\tilde{\epsilon}_{12} \ \tilde{\epsilon}_{13}]^T$

The expression in Eq. (A1) is derived from Eq. (19) which contains strain derivatives and 1D strains in **T** basis. To convert it into the above from in Eq. (A1) we use the following kinematic identity between 1D strain measures related to **T** and **B** bases as,

$$\epsilon_T = \epsilon_B + Q \gamma'_B$$

where,

$$Q = \begin{bmatrix} 0 & 0 \\ 0 & 0 \\ 0 & -1 \\ 1 & 0 \end{bmatrix} \tag{A.2}$$

and the expressions of the strain derivatives given by [27]

$$\begin{aligned} \epsilon'_B &= -N^{-1} Q F^T \epsilon_B - N^{-1} Q G \gamma_B \\ \gamma'_B &= G^{-1} F^T N^{-1} Q F^T \epsilon_B + G^{-1} F^T N^{-1} Q G \gamma_B \end{aligned} \tag{A.3}$$

and $\epsilon' = 0$

Substituting the above expressions back in Eq. (5.35) we can get the expressions of

$$\begin{aligned} X &= A + 2A Q G^{-1} F^T N^{-1} Q F^T - 2B N^{-1} Q F^T + F Q^T N^{-1} C N^{-1} Q F^T \\ F &= A Q G^{-1} F^T N^{-1} Q G - B N^{-1} Q G + F Q^T N^{-1} C N^{-1} Q G \\ G &= G^T Q^T N^{-1} C N^{-1} Q G \end{aligned} \tag{A.4}$$

Here, $N = X - F G^{-1} F^T$. The above equations are nonlinear in X, F and G and solved in an iterative manner numerically for a prismatic case [20,21,27], the expressions of E_1^a and E_2^a can be written as,

$$\begin{aligned} E_1^a &= -(\tilde{\epsilon}_\epsilon + F Q^T N^{-1} F G^{-1} Q^T \tilde{\epsilon}_\epsilon - F Q^T N^{-1} \tilde{\epsilon}'_\epsilon) \\ E_2^a &= -(G Q^T N^{-1} F G^{-1} Q^T \tilde{\epsilon}_\epsilon - G^T Q^T N^{-1} \tilde{\epsilon}'_\epsilon) \end{aligned} \tag{A.5}$$

where, $\tilde{\epsilon}_\epsilon, \tilde{\epsilon}'_\epsilon$, are defined earlier.

Appendix B

The polynomials which satisfies the homogeneous governing differential equations of a Timoshenko beam, are used as shape functions. Generally they are cubic and quadratic in degree and interdependent to each other, and interpolates two degrees of freedom w and ϕ [28]. The coefficients of the shape functions are determined by satisfying the following two constraints,

$$\frac{\partial}{\partial x} \left(\frac{\partial w}{\partial x} + \phi \right) = 0 \text{ and } \frac{\partial^2 \phi}{\partial x^2} - \frac{kGA}{EI} \left(\frac{\partial w}{\partial x} + \phi \right) = 0 \tag{B.1}$$

Thus the resulting explicit form of the shape functions are given as with ($\xi = x/L$)

$$[N_w]^T = \begin{bmatrix} \frac{1}{(1+\phi)} \{2\xi^3 - 3\xi^2 - \phi\xi + (1+\phi)\} \\ \frac{L}{(1+\phi)} \left\{ \xi^3 - \left(2 + \frac{\phi}{2}\right) \xi^2 + \left(1 + \frac{\phi}{2}\right) \xi \right\} \\ - \frac{1}{(1+\phi)} \{2\xi^3 - 3\xi^2 - \phi\xi\} \\ \frac{L}{(1+\phi)} \left\{ \xi^3 - \left(1 - \frac{\phi}{2}\right) \xi^2 - \frac{\phi}{2} \xi \right\} \end{bmatrix} \tag{B.2}$$

$$[N_\phi]^T = \begin{bmatrix} \frac{6}{(1+\phi)L} \{\xi^2 - \xi\} \\ \frac{1}{(1+\phi)} \{3\xi^2 - (4+\phi)\xi + (1+\phi)\} \\ - \frac{6}{(1+\phi)L} \{\xi^2 - \xi\} \\ \frac{1}{(1+\phi)} \{3\xi^2 - (2-\phi)\xi\} \end{bmatrix} \tag{B.3}$$

Here ϕ is the ratio of beam bending stiffness to shear stiffness and expressed as [8] $\phi = \frac{12}{L^2} \left(\frac{EI}{kGA} \right)$.

Appendix C

The classical energy harvester model based on the present theory VAM has been discussed in our previous work [29]. We have done an experimental validation of the model which we also present here to prove the accuracy and reliability of our mathematical model. As shear harvester

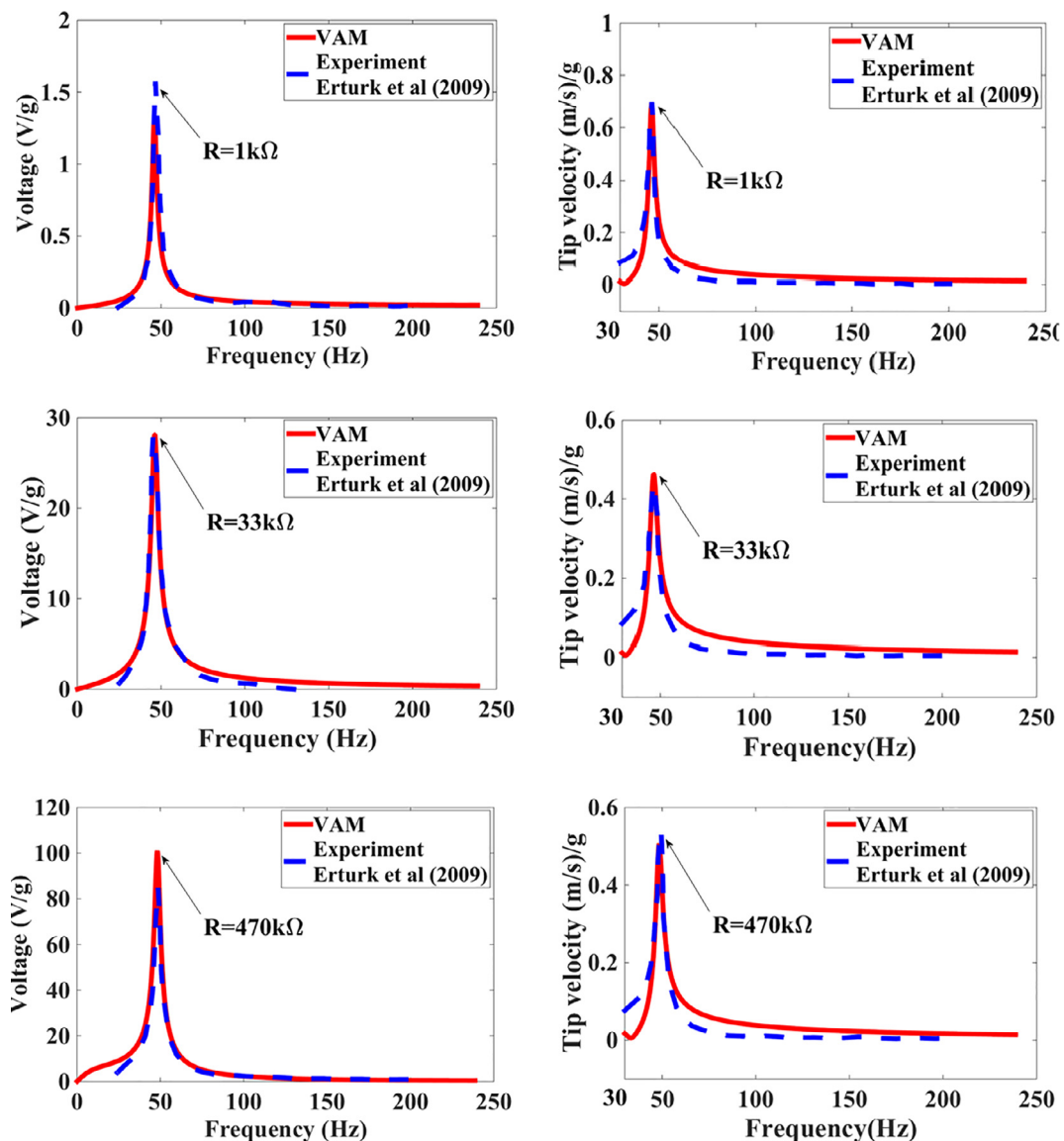


Fig. C1. VAM and experimental voltage and corresponding tip velocity FRF comparison for 1 k Ω , 33 k Ω and 470 k Ω load value [29].

is tough to design and fabricate so shear harvester based experimental results are scarce in literature. But as our model is experimentally validated for transverse harvester so we are very confident that our model can be equally reliable for shear harvester (Fig. C1).

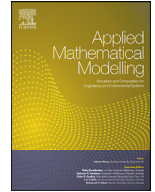
Appendix D. Supplementary data

Supplementary data associated with this article can be found, in the online version, at <https://doi.org/10.1016/j.compstruct.2018.07.117>.

References

- [1] Erturk A, Inman DJ. An experimentally validated bimorph cantilever model for piezoelectric energy harvesting from base excitations. *Smart Mater Struct* 2009;18(2):025009.
- [2] Williams CB, Yates RB. Analysis of a micro-electric generator for microsystems. *Sens Actuators, A* 1996;52(1–3):8–11.
- [3] Sodano HA, Inman DJ, Park G. A review of power harvesting from vibration using piezoelectric materials. *Shock Vibration Digest* 2004;36(3):197–206.
- [4] Anton SR, Sodano HA. A review of power harvesting using piezoelectric materials (2003–2006). *Smart Mater Struct* 2007;16(3):R1.
- [5] Dietl JM, Wickenheiser AM, Garcia E. A Timoshenko beam model for cantilevered piezoelectric energy harvesters. *Smart Mater Struct* 2010;19(5):055018.
- [6] Malakooti MH, Sodano HA. Piezoelectric energy harvesting through shear mode operation. *Smart Mater Struct* 2015;24(5):055005.
- [7] Aladwani A, Aldraihem O, Baz A. Single degree of freedom shear-mode piezoelectric energy harvester. *J Vib Acoust* 2013;135(5):051011.
- [8] Benjeddou A, Trindade MA, Ohayon R. A unified beam finite element model for extension and shear piezoelectric actuation mechanisms. *J Intell Mater Syst Struct* 1997;8(12):1012–25.
- [9] Majidi C, Haataja M, Srolovitz DJ. Analysis and design principles for shear-mode piezoelectric energy harvesting with ZnO nanoribbons. *Smart Mater Struct* 2010;19(5):055027.
- [10] Ren B, Or SW, Zhang Y, Zhang Q, Li X, Jiao J, Wang W, Liu DA, Zhao X, Luo H. Piezoelectric energy harvesting using shear mode 0.71 Pb(Mg_{1/3}Nb_{2/3})O₃-0.29PbTiO₃ single crystal cantilever. *Appl Phys Lett* 2010;96(8):083502.
- [11] Wang DA, Liu NZ. A shear mode piezoelectric energy harvester based on a pressurized water flow. *Sens Actuators, A* 2011;167(2):449–58.
- [12] Zhou L, Sun J, Zheng XJ, Deng SF, Zhao JH, Peng ST, et al. A model for the energy harvesting performance of shear mode piezoelectric cantilever. *Sens Actuators, A* 2012;30(179):185–92.
- [13] Timoshenko SP. LXVI. On the correction for shear of the differential equation for transverse vibrations of prismatic bars. *London Edinburgh Dublin Philos Mag J Sci* 1921;41(245):744–6.
- [14] Zeng Z, Ren B, Gai L, Zhao X, Luo H, Wang D. Shear-mode-based cantilever driving

- low-frequency piezoelectric energy harvester using 0.67 Pb (Mg_{1/3}Nb_{2/3}) O 3–0.33 PbTiO₃. *IEEE Trans Ultrason Ferroelectr Freq Control* 2016;63(8):1192–7.
- [15] Kulkarni V, Ben-Mrad R, Prasad SE, Nemana S. A shear-mode energy harvesting device based on torsional stresses. *IEEE/ASME Trans Mechatron* 2014;19(3):801–7.
- [16] Kulkarni V, Mrad BR, Prasad E, Nemana S. A shear-mode piezoceramic device for energy harvesting applications. In: *International Workshop Smart Materials, Structures and NDT in Aerospace Conference Canada*; 2011. p. 2–4.
- [17] Erturk A, Inman DJ. On mechanical modeling of cantilevered piezoelectric vibration energy harvesters. *J Intell Mater Syst Struct* 2008;19(11):1311–25.
- [18] Aladwani A, Arafa M, Aldraihem O, Baz A. Cantilevered piezoelectric energy harvester with a dynamic magnifier. *J Vib Acoust* 2012;134(3):031004.
- [19] Berdichevsky VL. Variational-asymptotic method of shell theory construction. *PMM* 1979;43(4):664–87.
- [20] Hodges DH. Nonlinear composite beam theory. *Prog Astronaut Aeronaut* 2006;213:304.
- [21] Yu W. Variational asymptotic modeling of composite dimensionally reducible structures; 2002.
- [22] Cesnik CE, Hodges DH. VABS: a new concept for composite rotor blade cross-sectional modeling. *J Am Helicopter Soc* 1997;42(1):27–38.
- [23] Yu W, Hodges DH. Elasticity solutions versus asymptotic sectional analysis of homogeneous, isotropic, prismatic beams. *J Appl Mech* 2004;71(1):15–23.
- [24] Roy S, Yu W, Han D. An asymptotically correct classical model for smart beams. *Int J Solids Struct* 2007;44(25):8424–39.
- [25] Roy S, Yu W. Dimensional reduction of a piezoelectric composite rod. *Eur J Mech-A/Solids* 2009;28(2):368–76.
- [26] Banerjee S, Roy S. Multiphysics analysis of an asymptotically correct piezoelectric sensor under static and dynamic load. *Int J Solids Struct* 2016;15(92):64–75.
- [27] Roy S, Yu W. A coupled Timoshenko model for smart slender structures. *Int J Solids Struct* 2009;46(13):2547–55.
- [28] Friedman Z, Kosmatka JB. An improved two-node Timoshenko beam finite element. *Comput Struct* 1993;47(3):473–81.
- [29] Banerjee S, Roy S. A dimensionally reduced order piezoelectric energy harvester model. *Energy* 2018;1:112–22.



An electromechanically coupled intrinsic, mixed variational formulation for geometrically nonlinear smart composite beam



P.M.G.B. Asdaque, Shreya Banerjee, Sitikantha Roy*

Department of Applied Mechanics, Indian Institute of Technology Delhi, Hauz Khas, New Delhi-110016, India

ARTICLE INFO

Article history:

Received 21 March 2018

Revised 6 August 2018

Accepted 29 August 2018

Available online 7 September 2018

Keywords:

Electromechanically coupled

Mixed formulation

Finite element analysis

Geometrical exact

Smart beams

ABSTRACT

The work presented in this article is the outcome of a combined strategy of a mathematical tool for 2D cross-sectional analysis, i.e., Variational Asymptotic Method (VAM) as well as the 1D exact beam analyzer, i.e., the intrinsic mixed variational formulation for modeling and analysis of Piezoelectric-laminated composite beams. This work talks about a novel approach of mixed variational formulation to analyze a two-way electromechanically coupled piezoelectric composite beam. In a classical intrinsic mixed variational approach for a passive structure, the 1D exact beam model deals only with mechanical degrees of freedom. In the present case, an extra 1D electrical degree of freedom has been incorporated. A computational code is developed based on the present theory to solve the two-way coupled electromechanical beam problem. In the present case, we have validated the static results for sensor application. Both linear and nonlinear results have been discussed. Results obtained are very promising and are helpful in building a platform where design, optimization and nonlinear analysis of composite ‘smart’ beams in a multibody framework can be done faster while maintaining acceptable accuracy.

© 2018 Published by Elsevier Inc.

1. Introduction

The possibility of achieving self-controllable and self-monitorable systems is the primary motto of applying active materials to civil and military structures and hence makes them smart. ‘Smart’ materials can sense the external stimuli of thermal, magnetic, electrical and mechanical nature and can behave accordingly. They can be categorized as actuators and sensors. Earlier William and Yates [1] proposed three sensing mechanisms viz. electrostatic, piezoelectric and electromagnetic, in which piezoelectric sensors are proved to be the most prominent. Discovered in 1880 by Pierre Curie, the piezoelectric material is one of those vastly used for sensing and actuation applications. A piezoelectric sensor operates based on the direct piezoelectric effect to produce electricity when external pressure, acceleration, strain, temperature or force is applied to it. The piezoelectric actuator experiences deformation when kept in the electrical field. Mechanical energy is converted into electrical energy by piezoelectric sensors and can be used to power other devices like self-powered electronic [2,3]. The accuracy of sensing will depend highly on how accurately we can model the electromechanical coupling.

One of the earliest mathematical models involving piezoelectric layer was of Robbins and Reddy [4], in which displacement based finite element was used to study the static and dynamic behavior of a piezoelectric actuator bonded with

* Corresponding author.

E-mail address: sroy@am.iitd.ac.in (S. Roy).

underlying passive beam structure. They proposed four different FEM models, two single layer and two multi-layer models that were derived from generalized laminated plate theory and it was vastly cited for actuation related validations. In the same year, Shen [5] developed a 1D beam theory to model and analyze the piezoelectric actuators and sensors. Another model was presented by Chee et al. [6] based on higher order displacement field and layer-wise linear electric potential. Timoshenko thick-beam theory was used. An analytical model for a multilayer piezoelectric laminated cantilever beam was proposed by Zhou et al. [7] for a micro-chemical sensor. The order of voltage output was in millivolts and hence is an appropriate alternative for micro-scale works like a system of position sensitive detection based on laser. An experimental study was done for different smart composite beams by Edery-Azulay and Abramovich [8], and various case studies were done. A finite element model derived from classical laminate theory with Euler–Bernoulli beam assumptions was presented by Bendary et al. [9] which was capable of accurately study the static and dynamic analysis when piezoelectric layers are either in patches or completely covers the structure. A refined theory was proposed by Beheshti-Aval and Lezgy-Nazargah [10] considering the normal transverse stress and the transverse flexibility effects, mainly for beams with soft-core or when the material properties change drastically through the depth of the beam. The higher order shear deformation theory was used to develop the finite element model by Elshafei and Alraies [11], where the displacement field accounts for the parabolic distribution of shear strains and nonlinearity of in-plane displacements across the thickness hence avoiding the involvement of the shear correction factor. Equations of motions were derived from the virtual displacement method. The model was validated for both segmented as well as the continuous piezoelectric layers either bonded or embedded in laminated beams. Two-noded elements with four mechanical degrees of freedom and additionally one electrical degree of freedom for each node was used. The electrical potential was treated as the function of length and thickness of the beam element. Piezoelectric fiber reinforced composite (PFRC) was examined for actuation and sensing cases by Kapuria and Yasin [12]. The mixed variational approach was applied to piezoelectric laminated composite structures by Maurini et al. [13], Benedetti and Milazzo [14], Legner et al. [15], etc. However, the final equations were complex. Fully coupled electromechanical, the Reissner-type mixed variational method was presented by Kapuria and Dhanesh [16] for actuation case in which problems related with free edge stresses were discussed.

A 3D beam problem can be decoupled into two successive steps. First step is a dimensional reduction over the cross-section and followed by a 1D beam analysis. Variational Asymptotic Method (VAM) is a widely popular cross-sectional analysis methodology. Berdichevsky [17] was the first to introduce VAM. The existence of small parameters and a governing functional is the essential requirements of VAM based analysis where the extremum leads to the correct solutions. For example, in our work, the slenderness of a sensor beam model is treated as the small parameter required. VAM is a proven mathematically rigorous tool for dimensional reduction and is said to make an asymptotical expansion of the energy functional based on one or more small inherent parameters. It is widely applied in the composite structural analysis. Validation results of 2D cross-sectional analysis tool, i.e., variational asymptotic beam sectional analysis (VABS II, 2004) which is based on VAM has been presented by Yu et al. [18]. The VAM methodology works well with slender structures, as it is convenient for dimensional reduction and hence splitting the original 3D problem into a 2D coupled cross-sectional analysis and a 1D beam analysis. Yu and Hodges [19] discussed the benefits of VAM based analysis, reproducing the same results as one obtains from 3D elasticity with very less computational cost. Recently, VAM is also applied to study the functionally graded cylinders [20]. Roy et al. [21] and Neto et al. [22] extended VAM to account for the incorporation of electro-mechanical effect in 2D cross-sectional analysis. The induced potential across the cross section was not approximated, rather calculated as an unknown. Recently, Banerjee and Roy [23] presented VAM as the platform to model and analyze a multiphysics problem of piezoelectric laminated composite cantilever sensor under static and dynamic load. Results were validated with past experimental work as well as with the 3D ABAQUS solutions. However, they only produced the recovery results for particular cross-sections of interest using the VABS II recovery tool. Also, geometric nonlinearity arising from large deflections and rotations was not discussed.

Danielson and Hodges [24] introduced new kinematical variable namely the local rotation in their 1D beam theory. The local rotation was defined as the change of orientation of material elements relative to the change of orientation of the beam reference triad. Hodges [25] presented a mixed variational theory based on exact intrinsic equations for the dynamics of moving beams. The kinematics of this work was based on his previous work [24]. The displacement/rotations, forces/moments and both linear and rotational momenta were considered as the independent variables in the final mixed variational approach. Yu and Blair [26] presented the extension of the mixed variational approach of Hodges [25] and developed a general purpose nonlinear analysis tool called geometrically exact beam theory (GEBT) for composite beams which generated nonlinear equations for the finite element analysis. Asdaque and Roy [27] incorporated actuation in beam modeling using intrinsic equations.

Recently, Sachdeva et al. [28] published the actuator and sensor model based on the mixed variational formulation of Hodges. However, they have not included any 1D electrical degrees of freedom in their beam analysis. For the actuator case, the actuating force is analyzed as the equivalent mechanical force. Sachdeva et al. [28], did not solve any electromechanically coupled 1D intrinsic beam equations. For the case of the sensor, their model is unable to output electrical variables without going through the computationally expensive recovery at the 3D level [23]. No validation was given for electrical output either. In the current work, we have overcome those limitations and developed an electromechanically coupled 1D mixed variational intrinsic beam theory.

There are many applications of piezoelectric type sensors reported in literature such as bitmap sensor [29], MEMS AC sensor based on silicon [30], energy harvesting via bending mode [31] and shear mode [32] and strain sensor [33]. Recently,

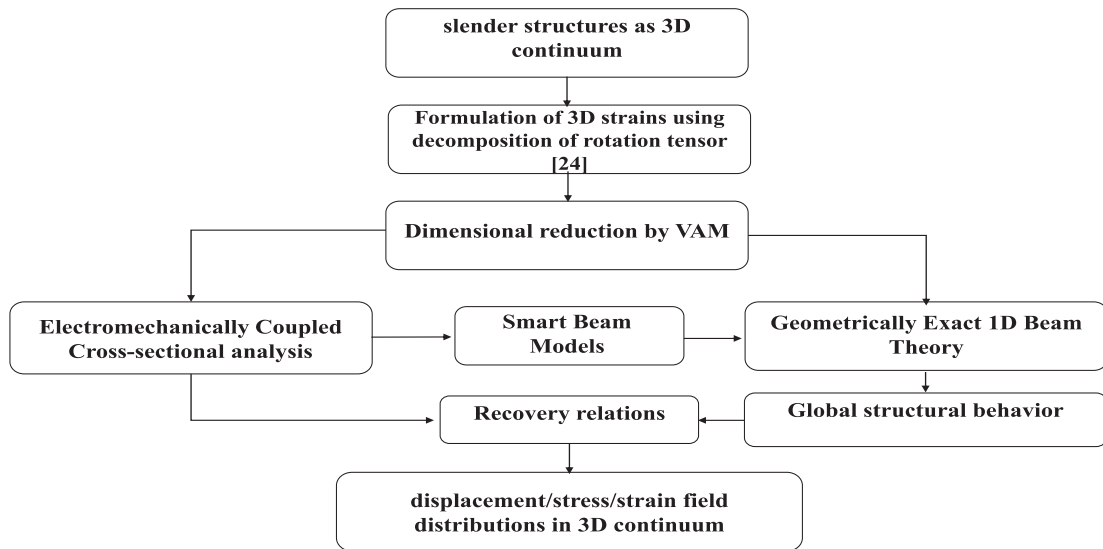


Fig. 1. Schematic of smart beam modeling.

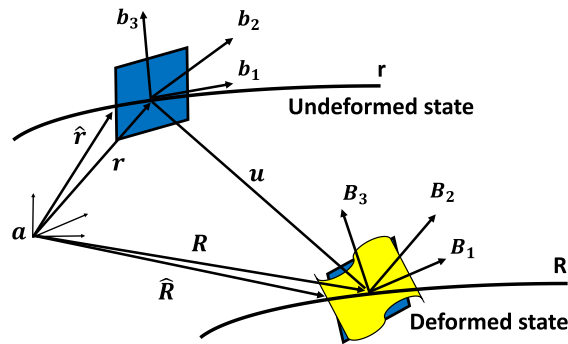


Fig. 2. The deformed and un-deformed configuration of a smart beam along the reference line.

promising applications in the biomechanical field, such as contracting muscle sensor [34], ceramic piezoelectric based frequency sensing circuit for low-level vibrations in medical works [35] and necklace type piezoelectric sensor monitoring eating habits to maintain a healthy lifestyle [36] were presented.

As discussed above, many models exist for analyzing smart structures. However, there is a need for fast computations in this modern era while maintaining the accuracy. In the present work, the electrical degrees of freedom has been additionally incorporated in 1D exact beam theory [25] based on an intrinsic formulation [37]. The updated mixed variational statement is derived for an electromechanical case which can capture geometrical nonlinearities. The fully coupled electro-mechanical, cross-sectional constitutive relations derived by Banerjee et al. [38] is used in the 1D mixed variational statement. The weak form of coupled mixed variational statement is implemented in a finite element code written in FORTRAN. A numerical example is taken into consideration, where cantilever boundary conditions are applied to a composite beam, and a point load is applied at the free end. The validation of the mathematically rigorous model for sensing both linear and non-linear exact beam model is another key contribution of the present study. The mechanical deflections and electrical potentials obtained are validated with the literature as well as the ABAQUS simulations and are found to be in good agreement with each other, validating the theory and proving the efficiency of the accompanying code. Also, the results obtained from non-linear beam analysis are discussed and validated with the ABAQUS simulations. Time consumption table is also presented, and the present algorithm is found to be much faster. Once ready, the plug-and-play sensor model, derived from the current code may be utilized for future applications like energy harvesting and higher harmonics imaging in atomic force microscopy (AFM), generating accurate results in real time (Fig. 1).

2. Geometrically exact smart beam formulation

Fig. 2 shows the deformed and the un-deformed state of a smart beam cross-section along the reference line. For consistency, three coordinate systems (a, b, B) are to be considered, where 'a' is the body-attached global reference frame,

'b' and 'B' are the un-deformed and deformed beam frame, respectively. In the absence of pre-twist and pre-curvature, 'a' and 'b' frame becomes the same. Electromechanical behavior of the slender beam laminated with piezoelectric layers will be analyzed. An electromechanical beam can be described by mechanical strain (Γ) and electrical field (E). We will not discuss the kinematics of 2D cross-sectional analysis and subsequent dimensional reduction of the smart beam which is detailed by Banerjee et al. [23,38]. Rather our main concern will be the 1D smart geometrically exact beam theory (SGEBT) formulation with extra degrees of freedom incorporating the electrical terms. Readers are referred to Appendix B for the important kinematical expressions. We will begin with the Hamiltonian which consists of electromechanical enthalpy Π^* . For simplicity, we will keep the terms same as presented in Hodges [37]. Subscripts a, b and B refer the respective frames and are mentioned whenever necessary, if nothing is explicitly mentioned, then it is assumed to be in the deformed frame. Extended Hamiltonian is given as [37],

$$\int_{t_1}^{t_2} \left[\delta \left(K - \Pi^* \right) + \delta \overline{W} \right] dt = \delta \overline{A} \tag{1}$$

where Π^* is the electromechanical enthalpy, K is the kinetic energy, $\delta \overline{W}$ is the virtual work equivalent and $\delta \overline{A}$ is the virtual action at t_1 and t_2 . Here, t_1 and t_2 are arbitrary fixed times. The spatial dimension can be reduced and replaced with a 1D model by using the fact that the axial dimension is larger than the other two. Hence, 3D functional can be expressed as an equivalent 1D functional. For the sake of continuity, we are listing down the important equations in the dimensional reduction process. A detail can be obtained in Refs. [21,26].

$$\int_{t_1}^{t_2} \left[\delta \left(K_{1D} + K^* - \Pi^* \right) + \delta \overline{W}_{1D} + \delta \overline{W}^* \right] dt = \delta \overline{A} \tag{2}$$

where K_{1D} , $\delta \overline{W}_{1D}$ and $\delta \overline{A}$ are expressed only as 1D unknown functional, while the terms with superscript '*' are still the functions of the 3D as well as the 1D unknown functions. By exploiting the small parameters in the slender structure, the variational statement in Eq. (2) can be asymptotically expanded and subsequently higher order terms can be neglected to construct 1D variational statement, symbolically expressed as

$$\int_{t_1}^{t_2} \int_0^l \left[\delta \left(K - \Pi \right) + \delta \overline{W} \right] dx_1 dt = \delta \overline{A} \tag{3}$$

where l is the length of the beam. K , Π and $\delta \overline{W}$ are 1D kinetic energy per unit length, electromechanical enthalpy per unit length and virtual work per unit length, respectively.

The terms in Eq. (3) can also be defined as

$$K = \frac{1}{2} \left\{ \begin{matrix} V_B \\ \Omega_B \end{matrix} \right\}^T I \left\{ \begin{matrix} V_B \\ \Omega_B \end{matrix} \right\}, \quad \Pi = \frac{1}{2} \left\{ \begin{matrix} \gamma \\ \kappa \\ \phi \end{matrix} \right\}^T S \left\{ \begin{matrix} \gamma \\ \kappa \\ \phi \end{matrix} \right\} \text{ and } \delta \overline{W} = \delta \overline{q}_B^T f_B + \delta \overline{\psi}_B^T m_B. \tag{4}$$

Here, ϕ is the 1D electrical variable, γ and κ are the column matrices containing 1D strains and curvatures [36]. I and S are mass and stiffness matrices, respectively. V_B and Ω_B are the linear and angular velocities of the particles of the beam reference axis in the deformed frame, respectively. Readers are referred to Appendix A for electromechanically coupled cross-sectional constitutive equations [38]. The constitutive relations are given as,

$$\left\{ \begin{matrix} P \\ H \end{matrix} \right\} = \left\{ \begin{matrix} \frac{\partial K}{\partial V} \\ \frac{\partial K}{\partial \Omega} \end{matrix} \right\} = I \left\{ \begin{matrix} V \\ \Omega \end{matrix} \right\} \text{ and } \left\{ \begin{matrix} F \\ M \\ Q \end{matrix} \right\} = \left\{ \begin{matrix} \frac{\partial \Pi}{\partial \gamma} \\ \frac{\partial \Pi}{\partial \kappa} \\ \frac{\partial \Pi}{\partial \phi} \end{matrix} \right\} = S \left\{ \begin{matrix} \gamma \\ \kappa \\ \phi \end{matrix} \right\}. \tag{5}$$

Internal forces can be defined from electromechanical enthalpy as follows,

$$\int_0^l \delta \Pi dx_1 = \int_0^l \left[\delta \gamma^T \left(\frac{\partial \Pi}{\partial \gamma} \right)^T + \delta \kappa^T \left(\frac{\partial \Pi}{\partial \kappa} \right)^T + \delta \phi^T \left(\frac{\partial \Pi}{\partial \phi} \right)^T \right] dx_1 \tag{6}$$

where F, M , and Q are the generalized internal forces, moments and electric charges, respectively, and defined as,

$$F = \left(\frac{\partial \Pi}{\partial \gamma} \right)^T, \quad M = \left(\frac{\partial \Pi}{\partial \kappa} \right)^T \text{ and } Q = \left(\frac{\partial \Pi}{\partial \phi} \right)^T. \tag{7}$$

Hence, the variation of electromechanical enthalpy can be written as,

$$\delta \Pi = \delta \gamma^T F + \delta \kappa^T M + \delta \phi^T Q. \tag{8}$$

Writing in terms of intrinsic variables $\delta \overline{q}$ and $\delta \overline{\psi}$ [37] (Appendix B: Eqs. (B.8)–(B.9) and (B.11)–(B.12)),

$$\delta \Pi = \left[\left(\delta \overline{q}' \right)^T - \delta \overline{q}^T \tilde{K} - \delta \overline{\psi}^T (\tilde{e}_1 + \tilde{\gamma}) \right] F$$

$$+ \left[(\overline{\delta\psi}')^T - \overline{\delta\psi}^T \tilde{K} \right] M + \delta\phi^T Q \tag{9}$$

Here, $(\tilde{*}) = -e_{ijk}(*), \sim$ is the tilde operator and e_{ijk} is the general permutation symbol. Inertial forces from Kinetic energy can be written as,

$$\int_0^l \delta K dx_1 = \int_0^l \left[\delta V^T \left(\frac{\partial K}{\partial V} \right)^T + \delta \Omega^T \left(\frac{\partial K}{\partial \Omega} \right)^T \right] dx_1 \tag{10}$$

Linear and angular momenta, P and H are conjugate to the generalized speeds V and Ω , and are introduced as

$$P = \left(\frac{\partial K}{\partial V} \right)^T = m(V - \tilde{\xi} \Omega) \tag{11}$$

$$H = \left(\frac{\partial K}{\partial \Omega} \right)^T = i\Omega + m\tilde{\xi} V \tag{12}$$

where ‘ m ’ is mass per unit length, $m\tilde{\xi}$ and i are first and second mass moments of inertia of beam cross-section, $A(x_1)$, respectively, and are defined as

$$m = \iint_{A(x_1)} \rho \sqrt{g} dx_2 dx_3 \tag{13}$$

$$m\tilde{\xi} = \iint_{A(x_1)} \rho \xi \sqrt{g} dx_2 dx_3 \tag{14}$$

$$i = \iint_{A(x_1)} \rho (\xi^T \xi \Delta - \xi \xi^T) \sqrt{g} dx_2 dx_3 \tag{15}$$

where

$$\xi = \begin{Bmatrix} 0 \\ x_2 \\ x_3 \end{Bmatrix} \tag{16}$$

And

$$\sqrt{g} = 1 - x_2 k_{b3} + x_3 k_{b2} > 0 \tag{17}$$

Readers are referred to [Appendix B](#) for further details of generalized speeds and their variations. Hence

$$\delta K = \delta V^T P + \delta \Omega^T H \tag{18}$$

Writing in terms of intrinsic variables, we get,

$$\delta K = \left(\overline{\delta q}^T - \overline{\delta q}^T \tilde{\Omega} - \overline{\delta\psi}^T \tilde{V} \right) P + \left(\overline{\delta\psi}^T - \overline{\delta\psi}^T \tilde{\Omega} \right) H \tag{19}$$

In the absence of external electrical loading, the virtual work equivalent is given as,

$$\overline{\delta W} = \int_0^l \left(\overline{\delta q}_B^T f_B + \overline{\delta\psi}_B^T m_B \right) dx_1 \tag{20}$$

The virtual action at the end of the time interval and the end of the beam and is given by

$$\overline{\delta A} = \int_0^l \left(\overline{\delta q}^T \hat{P} + \overline{\delta\psi}^T \hat{H} \right) \Big|_{t_1}^{t_2} dx_1 - \int_{t_1}^{t_2} \left(\overline{\delta q}^T \hat{F} + \overline{\delta\psi}^T \hat{M} \right) \Big|_0^l dt \tag{21}$$

Hence, the extended Hamiltonian can be written in terms of intrinsic variables $\overline{\delta q}$ and $\overline{\delta\psi}$,

$$\begin{aligned} & \int_{t_1}^{t_2} \int_0^l \left\{ \left(\overline{\delta q}^T - \overline{\delta q}^T \tilde{\Omega} - \overline{\delta\psi}^T \tilde{V} \right) P + \left(\overline{\delta\psi}^T - \overline{\delta\psi}^T \tilde{\Omega} \right) H \right. \\ & \quad \left. - \left[(\overline{\delta q}')^T - \overline{\delta q}^T \tilde{K} - \overline{\delta\psi}^T (\tilde{e}_1 + \tilde{\gamma}) \right] F - \left[(\overline{\delta\psi}')^T - \overline{\delta\psi}^T \tilde{K} \right] M - \delta\phi^T Q \right. \\ & \quad \left. + \overline{\delta q}^T f + \overline{\delta\psi}^T m \right\} dx_1 dt = \int_0^l \left(\overline{\delta q}^T \hat{P} + \overline{\delta\psi}^T \hat{H} \right) \Big|_{t_1}^{t_2} dx_1 - \int_{t_1}^{t_2} \left(\overline{\delta q}^T \hat{F} + \overline{\delta\psi}^T \hat{M} \right) \Big|_0^l dt \end{aligned} \tag{22}$$

3. Electromechanical mixed variational theory

Displacement-based finite element formulations include lengthy equations for general nonlinear behavior, which are further complicated with the involvement of the transcendental functions for orientation variables. A better way is to leave the force and moment strains, generalized linear and angular speeds, forces and moments, linear and angular momenta and charges and voltages as independent quantities, which can be achieved by adjoining constitutive and kinematical relations to weak Hamiltonian principle with Lagrange multipliers. Lagrange multiplier method is used, and the Lagrange multipliers will be identified to make the final statement as an electromechanical mixed variational statement, which has immense benefit especially in choosing shape functions, which are in simplest form when compared to displacement-based formulations. For further expressions, the direction cosine matrix is expressed as [37]

$$C = \frac{(1 - \frac{\theta^T \theta}{4})\Delta - \tilde{\theta} + \frac{\theta \theta^T}{2}}{1 + \frac{\theta^T \theta}{4}} \tag{23}$$

where a set of orientation variables, $\theta = [\theta_1 \theta_2 \theta_3]^T$ is chosen as the column matrix of Rodrigues parameters. Other rotation parameters can also be chosen. However, in this work, Rodrigues parameter will only be used. Inverse kinematical relations facilitate the integration by parts removing the terms in which they are differentiated. The inverse from strain-displacement and generalized speeds relation in Eqs. (B.3) and (B.10) is given by

$$u'_b = C^T(e_1 + \gamma) - e_1 - \tilde{\kappa}_b u_b \tag{24}$$

$$\dot{u}_b = C^T V - v_b - \tilde{\omega}_b u_b \tag{25}$$

where κ and Ω are also defined regarding orientation variables θ and the direction cosine matrix C by substituting Eq. (23) in Eqs. (B.5) and (B.11).

$$\kappa = \left(\frac{\Delta - \frac{\tilde{\theta}}{2}}{1 + \frac{\theta^T \theta}{4}} \right) \theta' + C \kappa_b - \kappa_b \tag{26}$$

$$\Omega = \left(\frac{\Delta - \frac{\tilde{\theta}}{2}}{1 + \frac{\theta^T \theta}{4}} \right) \dot{\theta} + C \omega_b \tag{27}$$

From Eq. (26), we obtain

$$\theta' = \left(\Delta + \frac{\tilde{\theta}}{2} + \frac{\theta \theta^T}{4} \right) (k + \kappa_b - C \kappa_b) \tag{28}$$

Also, from Eq. (27), we obtain

$$\dot{\theta} = \left(\Delta + \frac{\tilde{\theta}}{2} + \frac{\theta \theta^T}{4} \right) (\Omega - C \omega_b) \tag{29}$$

3.1. Electrical variables

Using the relation between electric field and electric potential which is given by

$$E = -\nabla \phi \tag{30}$$

Using Lagrange multipliers, we can combine the five kinematical constraints given in Eqs. (24), (25), (28), (29) and (30) with the variational equilibrium statement of Eq. (22) and convert it into a mixed variational statement given as,

$$\begin{aligned} & \int_{t_1}^{t_2} \int_0^l \left\{ \left(\overline{\delta q}^T - \overline{\delta q}^T \tilde{\Omega} - \overline{\delta \psi}^T \tilde{V} \right) P + \left(\overline{\delta \psi}^T - \overline{\delta \psi}^T \tilde{\Omega} \right) H \right. \\ & - \left[\left(\overline{\delta q} \right)^T - \overline{\delta q}^T \tilde{K} - \overline{\delta \psi}^T (\tilde{e}_1 + \tilde{\gamma}) \right] F - \left[\left(\overline{\delta \psi} \right)^T - \overline{\delta \psi}^T \tilde{K} \right] M - \delta \phi^T Q \\ & + \delta [\lambda_1^T (u' - C^T(e_1 + \gamma) + e_1 + \tilde{\kappa}u)] + \delta [\lambda_2^T (\dot{u} - C^T V + v + \tilde{\omega}u)] \\ & + \delta [\lambda_3^T (\theta' - \left(\Delta + \frac{\tilde{\theta}}{2} + \frac{\theta \theta^T}{4} \right) (k + \kappa - C \kappa))] + \delta [\lambda_4^T (\dot{\theta} - \left(\Delta + \frac{\tilde{\theta}}{2} + \frac{\theta \theta^T}{4} \right) (\Omega - C \omega))] \\ & \left. + \delta \left[\lambda_5^T \left(\phi + \int E dx_3 \right) \right] + \overline{\delta q}^T f + \overline{\delta \psi}^T m \right\} dx_1 dt \\ & = \int_0^l \left(\overline{\delta q}^T \hat{P} + \overline{\delta \psi}^T \hat{H} \right) \Big|_{t_1}^{t_2} dx_1 - \int_{t_1}^{t_2} \left(\overline{\delta q}^T \hat{F} + \overline{\delta \psi}^T \hat{M} \right) \Big|_0^l dt \end{aligned} \tag{31}$$

where $\lambda_1, \lambda_2, \lambda_3, \lambda_4$ and λ_5 are the Lagrange multipliers. The first four Lagrange multipliers were found as [37],

$$\lambda_1 = -C^T F, \lambda_2 = C^T P, \lambda_3 = -\left(\frac{\Delta - \frac{\tilde{\theta}}{2}}{1 + \frac{\theta^T \theta}{4}}\right)^T M \text{ and } \lambda_4 = \left(\frac{\Delta - \frac{\tilde{\theta}}{2}}{1 + \frac{\theta^T \theta}{4}}\right)^T H \tag{32}$$

Considering piezoelectric laminates are stacked in x_3 direction, i.e., in the thickness direction. Hence the electric field is developed only in x_3 direction. In Eq. (31), equating the coefficients of $\delta\varphi^T = 0$, we identified the fifth Lagrange multiplier as,

$$\lambda_5 = Q \tag{33}$$

Substituting all these Lagrange multiplier values in Eq. (31) we obtain

$$\begin{aligned} & \int_{t_1}^{t_2} \int_0^l \left\{ \left(\left(\overline{\delta q'} \right)^T - \overline{\delta q}^T \tilde{K} - \overline{\delta \psi}^T (\tilde{e}_1 + \tilde{\gamma}) \right) F \right\} + \left[\left(\overline{\delta \psi'} \right)^T - \overline{\delta \psi}^T \tilde{K} \right] M + \delta \phi^T Q \\ & - \left(\overline{\delta q}^T - \overline{\delta q}^T \tilde{\Omega} - \overline{\delta \psi}^T \tilde{V} \right) P - \left(\overline{\delta \psi}^T - \overline{\delta \psi}^T \tilde{\Omega} \right) H + \delta \gamma^T \left[\left(\frac{\partial \Pi}{\partial \gamma} \right)^T - F \right] + \delta \kappa^T \left[\left(\frac{\partial \Pi}{\partial \kappa} \right)^T - M \right] \\ & + \delta \phi^T \left[\left(\frac{\partial \Pi}{\partial \phi} \right)^T - Q \right] - \delta V^T \left[\mu \left(v - \tilde{\xi} \Omega \right) - P \right] - \delta \Omega^T \left[i \Omega + \mu \tilde{\xi} V - H \right] \\ & + \overline{\delta F}^T \left[e_1 + \tilde{k}_b u_b - C^T (e_1 + \gamma) \right] - \left(\overline{\delta F'} \right)^T u_b - \overline{\delta P}^T (v_b + \tilde{\omega}_b u_b - C^T V) + \overline{\delta P'}^T u_b \\ & + \overline{\delta M}^T \left(\Delta + \frac{1}{2} \tilde{\theta} + \frac{1}{4} \theta \theta^T \right) (C k_b - k_b - \kappa) - \left(\overline{\delta M'} \right)^T \theta - \overline{\delta H}^T \left(\Delta + \frac{1}{2} \tilde{\theta} + \frac{1}{4} \theta \theta^T \right) (C \omega_b - \Omega) \\ & + \overline{\delta H}^T \theta + \delta Q^T (\phi - \phi^c) - \overline{\delta q}^T f - \overline{\delta \psi}^T m \left. \right\} dx_1 dt \\ & = \int_0^l \left(\overline{\delta q}^T \hat{P} + \overline{\delta \psi}^T \hat{H} - \overline{\delta P}^T \hat{u}_b - \overline{\delta H}^T \hat{\theta} \right) \Big|_{t_1}^{t_2} dx_1 + \int_{t_1}^{t_2} \left(\overline{\delta q}^T \hat{F} + \overline{\delta \psi}^T \hat{M} - \overline{\delta F}^T \hat{u}_b - \overline{\delta M}^T \hat{\theta} \right) \Big|_0^l dt \end{aligned} \tag{34}$$

We can define the following variables for simpler representation as,

$$\overline{\delta F} = C^T \delta F_B, \overline{\delta M} = \left(\frac{\Delta - \frac{\tilde{\theta}}{2}}{1 + \frac{\theta^T \theta}{4}}\right)^T \delta M_B, \overline{\delta P} = C^T \delta P_B \text{ and } \overline{\delta H} = \left(\frac{\Delta - \frac{\tilde{\theta}}{2}}{1 + \frac{\theta^T \theta}{4}}\right)^T \delta H_B \tag{35}$$

Superscript 'c' in Eq. (34) stands for the values obtained from the constitutive relationship. Eq. (34) is the final coupled electromechanical mixed variational statement. One can also observe that the final variational statement is devoid of any rotational and displacement variables making it fully intrinsic.

Finite element equations (Appendix C) obtained from Eq. (34) are used for linear and non-linear analysis for smart beams. The obtained set of equations have been incorporated into a FORTRAN code. For a simple passive case, Eqs. (C.10) and (C.15) will vanish. Sensor beams with static loading for linear and non-linear analysis are considered in our work.

4. Results and discussions

In this section, the results obtained from the above theory will be compared with the literature. The cross-sectional analysis provides us the stiffness matrix and the coupling terms, as shown in Eq. (A.10).

4.1. Sensor model validation

A three-layer composite beam is analyzed as a benchmark example which was vastly studied in literature such as Robbins and Reddy [4], Saravanos and Heyliger [39], Roy et al. [21], Chee et al. [6], etc. The piezoelectric layer is kept on the top and is bonded to the substrate by an adhesive layer. The material properties and geometry of the different layers are provided in Table 1.

Input data contains all the information about the active nodes (where the potential is to be found and where the nodes are electrically grounded). For a Timoshenko like analysis, the cross-sectional analysis gives a 7×7 coupled matrix, which will act as the input for the smart GEBT developed here (Appendix A). The non-zero cross-sectional constants in the stiffness matrix and the coupling terms are presented in Table 2. Rest of the terms are zero or of lesser order close to zero.

For cross-sectional analysis, the cross-section of the three-layer composite beam is meshed with 100 eight-noded brick elements, ten elements along the width, six elements along the thickness of composite T300/934 and two elements each along the thickness of the adhesive and piezoelectric layer, as shown in Fig. 3. The material properties and mesh connectivity are fed as input for cross-sectional analysis, as detailed in Banerjee et al. [38].

Table 1
Material properties.

Parameters	T300/934	Adhesive	PZT-4
$E_{11} = E_{22}$ (GPa)	126.0	6.9	68.90
E_{33} (GPa)	7.9	6.9	48.30
Poisson's ratio, $\nu_{12} = \nu_{13} = \nu_{23}$	0.275	0.4	0.25
$G_{12} = G_{13} = G_{23}$ (GPa)	27.60	2.46	31.00
$e_{31} = e_{32}$ (Cm ⁻²)	0.00	0.00	-7.99
e_{33} (Cm ⁻²)	0.00	0.00	14.86
$e_{24} = e_{15}$ (Cm ⁻²)	0.00	0.00	15.37
g_{11} (F/m)	3.09×10^{-11}	5.43×10^{-9}	5.43×10^{-9}
g_{22} (F/m)	2.56×10^{-11}	5.43×10^{-9}	5.43×10^{-9}
g_{33} (F/m)	2.56×10^{-11}	5.32×10^{-9}	5.32×10^{-9}
Length, L (m)	0.1524	0.1524	0.1524
Thickness, h (m)	0.01524	0.000254	0.001524
Width, b (m)	0.0254	0.0254	0.0254
Density, ρ (kg/m ³)	1527	1662	7600

Table 2
Coefficients of the stiffness matrix.

Parameters	Values
S_{11} (N)	0.51487356×10^8
S_{22} (N)	0.98723265×10^7
S_{33} (N)	0.94229135×10^7
S_{44} (Nm ²)	0.66706688×10^3
S_{55} (Nm ²)	0.11454014×10^4
S_{66} (Nm ²)	0.27681120×10^4
$S_{15} = S_{51}$ (Nm)	-0.22380519×10^5
$S_{24} = S_{42}$ (Nm)	-0.14213994×10^4
f_1^a	-0.24299620
f_5^a	$-0.18811107 \times 10^{-2}$
c_p (F/m)	$1.921666667 \times 10^{-7}$

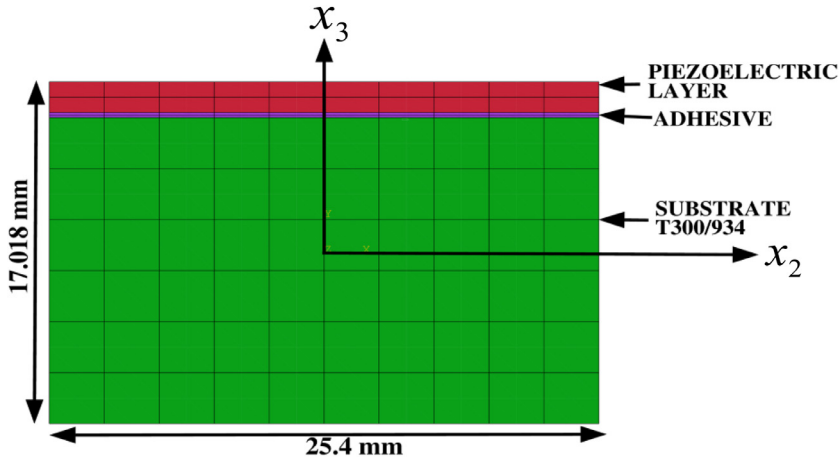


Fig. 3. The cross-sectional mesh of the piezoelectric laminated composite beam.

The electromechanically coupled stiffness matrix is then fed in smart GEBT to carry out the finite element procedure. The beam is meshed in ten finite elements along the length. A concentrated load of 1000 N is applied in an upward direction at the free end of the composite cantilever beam. On the piezoelectric layer, charges are generated due to electromechanical coupling resulting in a potential difference between the upper and the bottom, electrically grounded surface.

The exact intrinsic theory of Hodges has been extended to obtain, for the first time, the electric potential along the length of the smart beam. Results are found to be in good agreement with the results present in the literature [6,22,39] and are shown in Fig. 4. Also, the deflection curve of the midplane in x_3 direction is plotted along the length in Fig. 5 and compared with the literature proving the accuracy of our theory as well as the capability of capturing the accurate results regarding both, the mechanical variables as well as the electrical output.

The ultimate validation is from finite element analysis software, ABAQUS (Fig. 6). The material properties are given in Table 1. The piezoelectric structure is placed on the top while the adhesive layer is sandwiched between the piezoelectric

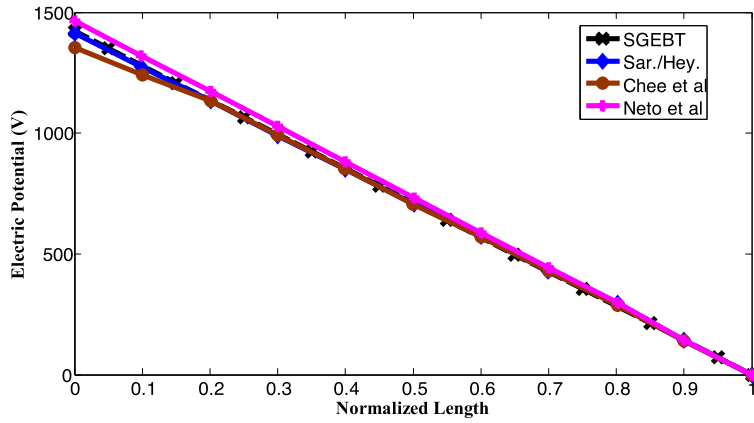


Fig. 4. Electric potential along the length compared to the literature.

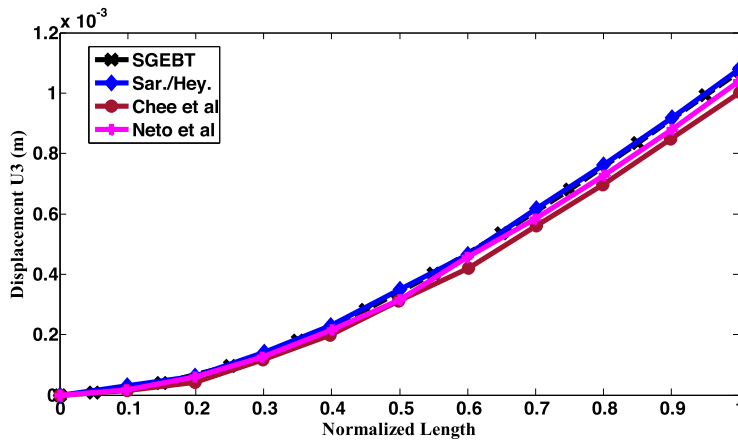


Fig. 5. Deflection plot of sensor composite beam.

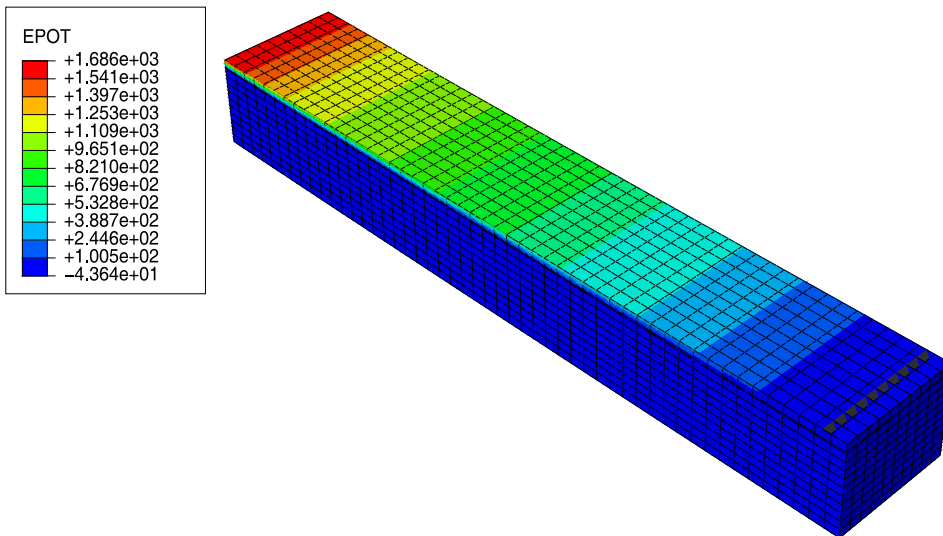


Fig. 6. Electric potential (EPOT) obtained from the electrodes mounted on the top surface of the piezoelectric layer.

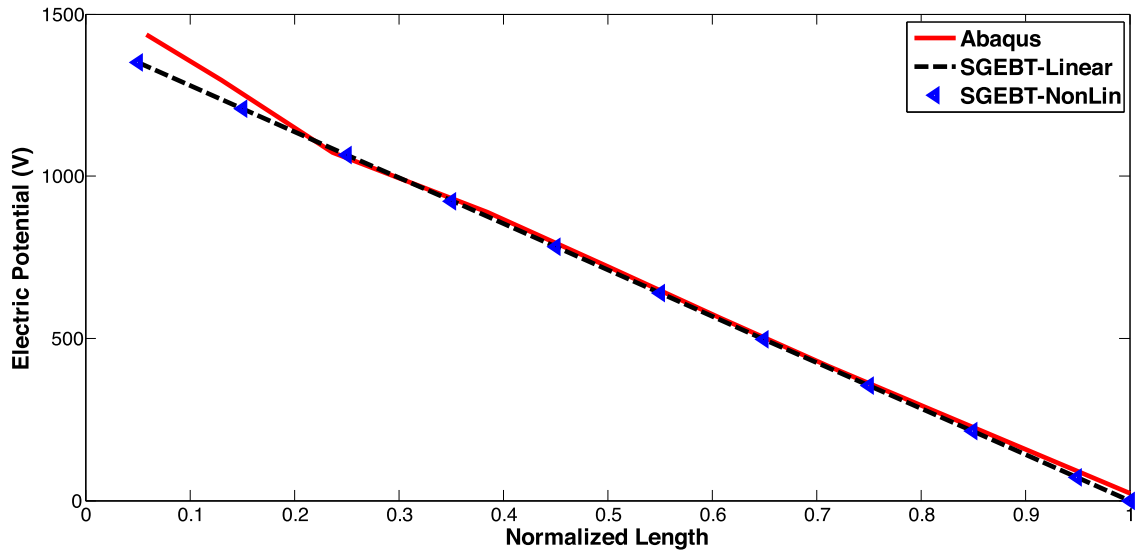


Fig. 7. Validation of electric potential along the length of the sensor beam from Abaqus simulation.

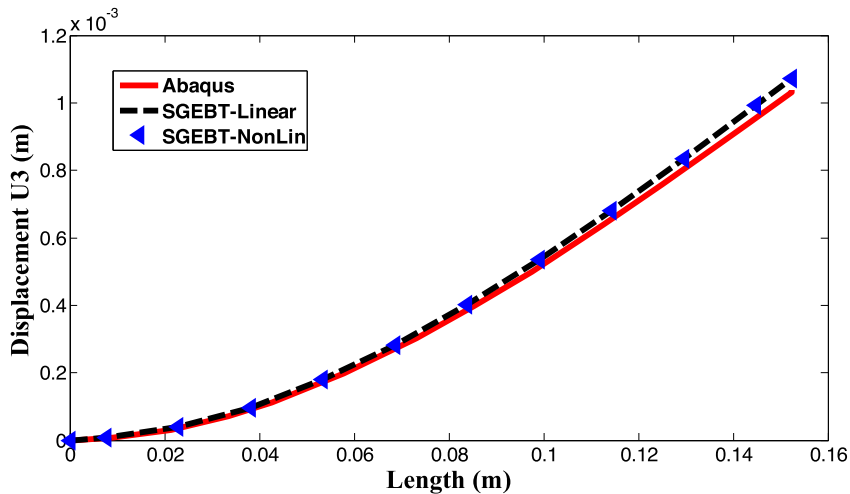


Fig. 8. Transverse deflection of the sensor beam.

laminate and the substrate material T300/934. For piezoelectric layer, 20-noded quadratic piezoelectric brick element (C3D20E), while for passive layers, i.e., adhesive and material T300/934, 20-noded quadratic brick element (C3D20) is assigned for meshing. Assembly is meshed with fifty elements along the length, while ten elements along the thickness of the substrate layer and one each along the thickness of adhesive and piezoelectric layers, respectively. Along the width, ten elements were placed uniformly.

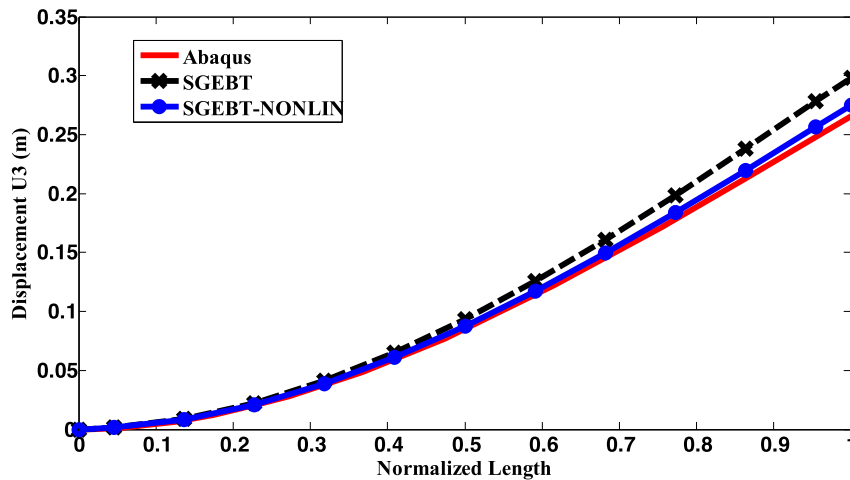
Tie constraint is applied for binding the piezoelectric bottom surface to the top surface of the adhesive and for binding the bottom surface of the adhesive to the top surface of the substrate material T300/934 to simulate perfect bonding. Mechanical boundary conditions are applied in which one end is encastered (no rotation, no translation) to simulate the fixed boundary of the cantilever composite beam. Also, the electrical boundary condition of zero voltage (electrically grounded) is provided to the nodes of the bottom surface of the piezoelectric layer. Load of 1000 N is applied at the center of the cross-section of the free end. Electrodes are placed on the top surface of the piezoelectric layer by the help of equation constraints, which help in simulating the equipotential surfaces from where the electric potential will be obtained. In post-processing, a path is drawn on the electrodes to obtain the electric potential along the length.

Also, transverse deflection of midplane is obtained. The results obtained from smart GEBT and Abaqus simulations are found to be in good agreement as observed from Figs. 7 and 8. In Fig. 7, a slight deviation of electric potential obtained from Abaqus simulation is observed at the fixed end of the cantilever, which may be attributed to the boundary effect. However, this deviation is only for a very small portion of the beam. The results obtained from the present method and

Table 3

Comparison of time consumption for the present model and Abaqus simulation.

Simulation	Time (s)
Abaqus simulation (without parallelization)	433.00
Abaqus simulation (parallelization: 8 processors)	145.00
Smart GEBT (linear)	0.70
Smart GEBT (non-linear)	1.50

**Fig. 9.** Nonlinearity effect on displacement increases with the increase of beam slenderness.**Table 4**

Comparison of time consumption for the present model and Abaqus simulation for increased slenderness.

Analysis	Time (s)
Abaqus simulation (parallelization: 8 processors)	152.00
Smart GEBT (linear)	0.73
Smart GEBT (non-linear)	2.00

the Abaqus software are compared and presented in [Tables 5 and 6 \(Appendix D\)](#). The 64-bit operating system we used for smart GEBT and Abaqus simulations have a processor of Intel® Xeon® CPU E3-1241 v3 @ 3.50GHz with 32 GB RAM and 3.50GHz frequency. Runtime for smart GEBT and Abaqus simulation are compared in [Table 3](#). It is observed that the time consumption for the smart GEBT is much lower than the Abaqus simulation, making the theory capable of simulating real-time operations like higher harmonics imaging in AFM, energy harvesting and sensing in wind turbines.

4.2. 'Smart' beam with increased slenderness

One can easily observe from [Figs. 7 and 8](#) that the nonlinearity effect is not distinguished for both the electric potential as well as the transverse displacement.

It is known that 1D exact beam theory can capture all types of geometric nonlinearities arising from large deformations and rotations while strains being very small. The length of the beam is increased to 1000 mm, keeping all other parameters like width, thickness and the material properties same as presented in [Table 1](#). The non-linear effect can be observed on displacement as well as electric potential, plotted in [Figs. 9 and 10](#), respectively. It is noted that for a beam with a high slenderness ratio, the displacement, as well as electric potential obtained from the linear analysis, deviates from the actual results because of the geometric nonlinearity arising. Also, time comparison is presented in [Table 4](#), which only proves that the theory presented here is computationally efficient.

5. Conclusion

The theory presented here provides us better opportunity to understand the multiphysics systems and their effects while being derived from the exact beam theory having intrinsic quantities. To the best of authors' knowledge, this is for the first time that intrinsic mixed variational theory [\[26,37\]](#) is applied to a 1D electromechanical beam problem. This paper applies both the VAM and intrinsic based mixed variational formulation to develop and analyze smart beam model under static

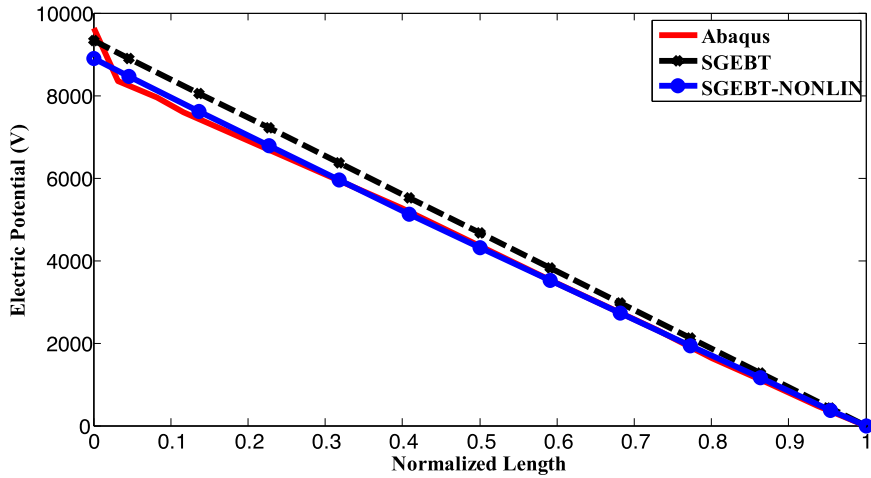


Fig. 10. Nonlinearity effect on electric potential with increased slenderness of beam.

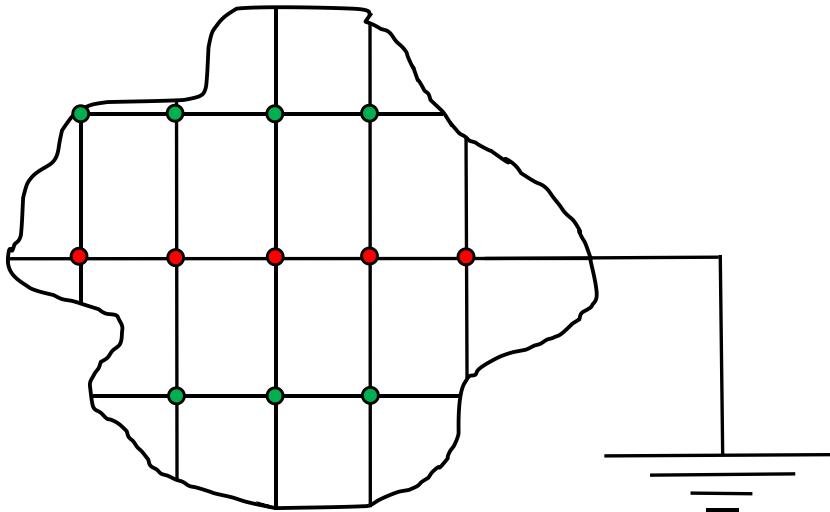


Fig. 11. Meshed cross section. (For interpretation of the references to color in this figure, the reader is referred to the web version of this article).

Table 5
Comparison of electric potential obtained from Abaqus and the present method.

Electrode number	Electric potential V1 (Abaqus)	Electric potential V2 (SGEBT)	Error % (V1-V2)/V1 × 100
1	1450.69	1350.378	6.91479
2	1248.27	1208.175	3.21205
3	1061.42	1065.978	-0.42942
4	934.256	923.7871	1.12057
5	794.118	781.6024	1.57603
6	646.194	639.4242	1.04765
7	500.865	497.2521	0.72133
8	360.727	355.0862	1.56374
9	228.374	212.9261	6.76431
10	80.8304	70.77160	12.4443

loading. Smart GEBT presented here can serve as a general purpose nonlinear tool to analyze the piezoelectric laminated, slender composite structures. The detailed description has been presented for the sensor beam model, clearly providing the steps involved and stating the equations required. The final mixed variational statement is devoid of any rotational and displacement variables making it fully intrinsic. Results were compared with the finite element simulations in Abaqus and the literature [6,22,39], showing good agreement which will lead to the acceptability of the updated theory which will further be enhanced for better future applications like energy harvesting and smart wind turbines, etc. Also, there is

Table 6
Comparison of transverse deflection obtained from Abaqus and the present method.

Length (m)	Transverse Displacement T1 Abaqus)	Transverse Displacement T2 (SGEBT)	Error % (T1–T2)/T1 × 100
0	0.00000000	0.00000000	NAN (no error)
0.00762	0.00000835	0.00000835	–0.5000
0.05334	0.00017012	0.00017905	–5.2464
0.06858	0.00026995	0.00028144	–4.2585
0.08382	0.00038720	0.00040129	–3.6413
0.09906	0.00051690	0.00053543	–3.5853
0.11430	0.00065904	0.00068068	–3.2828
0.12954	0.00081364	0.00083386	–2.4843
0.14478	0.00096077	0.00099180	–3.2301
0.15240	0.00103557	0.00107156	–3.4758

no need to recover the 3D results [23] if only electrical outputs are required along the length of the slender sensor-beam, hence making the computation simpler.

One of the advantages of this theory is high accuracy at a much lower computation time and expense. As observed from time comparison in Tables 3 and 4, the computational cost is much lower than the available finite element software like Abaqus, which will help in simulating the real-time applications. In short, the presented sensor model is one of the fastest. The theory presented can handle sensor model with the arbitrary material, cross-section, and geometry. Thus mathematical theory ensures that it can tackle various problems of single and multilayer Piezoelectric-laminated smart beam problems. Also, the theory presented can act as a platform to check the various beam models for piezoelectric laminated structures to analyze the results and for consistency. Though mathematically rigorous, the model developed here is very efficient computationally, capturing nonlinearities (geometrical) arising from large displacements and rotations while strains being small.

Acknowledgment

We would like to thank Professor Wenbin Yu (Purdue University), and his online platform, ‘Composite Design and Manufacturing Hub’ for their valuable suggestions. We are also thankful to Department of Applied Mechanics (IIT Delhi) for their encouragement and help. The first author acknowledges the financial support as senior research fellowship from CSIR-India under the file No. 09/086(1317)/2K18 EMR-I.

Appendix A. Electromechanical coupled constitutive equations

The zeroth order approximation for electromechanical enthalpy from VAM [23,38] for a sensor model can be expressed as,

$$2\int_0^L \Pi = V^T E V + 2V^T D_{h\epsilon} \epsilon + \epsilon^T D_{\epsilon\epsilon} \epsilon \tag{A.1}$$

where Π_0 is the electromechanical enthalpy, $E = \langle [\Gamma_h S^u]^T C [\Gamma_h S^u] \rangle$, $D_{h\epsilon} = \langle [\Gamma_h S^u]^T C [\Gamma_\epsilon] \rangle$ and $D_{\epsilon\epsilon} = \langle [\Gamma_\epsilon]^T C [\Gamma_\epsilon] \rangle$. While ϵ contains the force and moment strain measures. Here $\Gamma_h, \Gamma_\epsilon$ are the matrices as defined in Roy et al. [21] and are given as

$$\Gamma_h = \begin{bmatrix} 0 & 0 & 0 & 0 \\ \frac{\partial}{\partial x_2} & 0 & 0 & 0 \\ \frac{\partial}{\partial x_3} & 0 & 0 & 0 \\ 0 & \frac{\partial}{\partial x_2} & 0 & 0 \\ 0 & \frac{\partial}{\partial x_3} & \frac{\partial}{\partial x_2} & 0 \\ 0 & 0 & \frac{\partial}{\partial x_3} & 0 \\ 0 & 0 & 0 & 0 \\ 0 & 0 & 0 & -\frac{\partial}{\partial x_2} \\ 0 & 0 & 0 & -\frac{\partial}{\partial x_3} \end{bmatrix}, \Gamma_\epsilon = \begin{bmatrix} 1 & 0 & x_3 & -x_2 \\ 0 & -x_3 & 0 & 0 \\ 0 & x_2 & 0 & 0 \\ 0 & 0 & 0 & 0 \\ 0 & 0 & 0 & 0 \\ 0 & 0 & 0 & 0 \\ 0 & 0 & 0 & 0 \\ 0 & 0 & 0 & 0 \\ 0 & 0 & 0 & 0 \end{bmatrix} \tag{A.2}$$

The total nodal values of the warp field expressed as $\hat{w} = [w_1 w_2 w_3 \phi]^T$ where $\phi(x_1, x_2, x_3)$ is the 3D electric potential, which is different from the 1D electrical variable φ defined earlier. For detail discussion, readers are advised to refer [38]. For any cross-section of arbitrary geometry, the nodal degrees of freedom vector is split into two parts given by,

$$V = V_k + V_u \tag{A.3}$$

Here V_k symbolically expresses the known part of electric potential at specific points (nodes) and V_u is the unknown degrees of freedom (mechanical and electrical). The details have been discussed in previously published work of co-authors of this work [23]. An arbitrary meshed cross-section is shown in Fig. 11, the red colored nodes are the electrically grounded, i.e., assigned as zero voltages.

Discretized form of the warping field can be expressed as,

$$\hat{w}(x_1, x_2, x_3) = S^u(x_2, x_3)V(x_1) \tag{A.4}$$

where S^u is the element shape function and is of $4 \times 4n$ dimension, n being the number of nodes in the element. V refers to the nodal values of the warping and of dimension $4 \times n \times 1$. Applying constraints and solving Eq. (A.1), details solution technique has already been given in Roy et al. [21] we finally end up getting the zeroth order generalized approximation of fully coupled electric enthalpy,

$$2\prod_0 = \epsilon^T S \epsilon - 2\epsilon^T f^a \phi - c_p \phi^2 \tag{A.5}$$

where S is the cross-sectional stiffness of the electromechanical system, f^a is the electromechanical coupling vector and c_p is the capacitance per unit length of the structure. Thus, from Eq. (A.5), the 1D coupled constitutive equations of the sensor model,

$$F^* = \frac{\partial \prod_0}{\partial \epsilon}, \tag{A.6}$$

$$\text{or, } F^* = S\epsilon - f^a \phi \tag{A.7}$$

where F^* is a 6×1 column vector which contains the forces and moments while f^a is a vector consisting of the coupling terms. and,

$$Q = \frac{\partial \prod_0}{\partial \phi} \tag{A.8}$$

$$\text{or, } Q = -\epsilon^T f^a - c_p \phi \tag{A.9}$$

The above equations represent the coupled cross-sectional equations for the sensor model for ‘smart’ beams. In matrix form, the electromechanically coupled constitutive relation is expressed as [38]

$$\begin{Bmatrix} F_1 \\ F_2 \\ F_3 \\ M_1 \\ M_2 \\ M_3 \\ Q \end{Bmatrix} = \begin{bmatrix} S_{11} & S_{12} & S_{13} & S_{14} & S_{15} & S_{16} & -f_1^a \\ S_{21} & S_{22} & S_{23} & S_{24} & S_{25} & S_{26} & -f_2^a \\ S_{31} & S_{32} & S_{33} & S_{34} & S_{35} & S_{36} & -f_3^a \\ S_{41} & S_{42} & S_{43} & S_{44} & S_{45} & S_{46} & -f_4^a \\ S_{51} & S_{52} & S_{53} & S_{54} & S_{55} & S_{56} & -f_5^a \\ S_{61} & S_{62} & S_{63} & S_{64} & S_{65} & S_{66} & -f_6^a \\ -f_1^a & -f_2^a & -f_3^a & -f_4^a & -f_5^a & -f_6^a & -c_p \end{bmatrix} \begin{Bmatrix} \gamma_1 \\ \gamma_2 \\ \gamma_3 \\ \kappa_1 \\ \kappa_2 \\ \kappa_3 \\ \phi \end{Bmatrix} \tag{A.10}$$

Appendix B. Strains and generalized speeds

From Fig. 2, displacement fields [37] are represented by

$$\hat{r} = r + \xi = r + x_2 b_2 + x_3 b_3 \tag{B.1}$$

$$R = R + C.(\xi + w) = r + u + x_2 B_2 + x_3 B_3 + w_i B_i \tag{B.2}$$

where C is the global rotation tensor and $w = w_i b_i$ represents small warping displacement

Also the generalized strains are given by

Force strains

$$\gamma = \begin{Bmatrix} \gamma_{11} \\ 2\gamma_{12} \\ 2\gamma_{13} \end{Bmatrix} = C(e_1 + u'_b + \tilde{k}_b u_b) - e_1 \tag{B.3}$$

where u_b is the column matrix and the elements are the measure numbers of displacement along b_i and $\tilde{()}$ stands for antisymmetric matrix. Also,

$$e_1 = \begin{Bmatrix} 1 \\ 0 \\ 0 \end{Bmatrix} \tag{B.4}$$

Similarly, moment strains are defined as

$$\kappa = \begin{Bmatrix} \kappa_1 \\ \kappa_2 \\ \kappa_3 \end{Bmatrix} = K_B - k_b \tag{B.5}$$

where $\tilde{K}_B = -C^T C + C \tilde{k}_b C^T$

Introducing column matrix of the virtual displacements as

$$\overline{\delta q}_B = C\delta u_b \tag{B.6}$$

Also, antisymmetric matrix of virtual rotations is defined to be

$$\delta \tilde{\psi} = -\delta C C^T \tag{B.7}$$

From Eq. (B.3), the variation of the force strains will give

$$\delta \gamma = \overline{\delta q}'_B + \tilde{K}_B \overline{\delta q}_B + (\tilde{e}_1 + \tilde{\gamma}) \overline{\delta \psi}_B \tag{B.8}$$

Also, from Eq. (B.5), the variation of the moment strains will give

$$\delta \kappa = \overline{\delta \psi}'_B + \tilde{K}_B \overline{\delta \psi}_B \tag{B.9}$$

One can observe that neither displacement variables nor the orientation variables are present in these equations, (B.8) and (B.9), making them *intrinsic* in nature.

The velocity of the deformed reference axis in the deformed frame is given by [37]

$$\dot{V}_B = C(v_b + \dot{u}_b + \tilde{\omega}_b u_b) \tag{B.10}$$

where v_b and ω_b are the linear and angular velocities of the undeformed reference axis of the beam, respectively.

Angular velocity of the deformed cross-sectional frame of the beam is given by [37]

$$\tilde{\Omega}_B = -\dot{C} C^T + C \tilde{\omega}_b C^T \tag{B.11}$$

From Eqs. (B.10) to (B.11), the variations of the generalized speeds and using the definitions of the virtual displacement and rotation will provide

$$\delta V = \overline{\delta \dot{q}} + \tilde{\Omega} \overline{\delta q} + \tilde{V} \overline{\delta \psi} \tag{B.12}$$

$$\delta \Omega = \overline{\delta \dot{\psi}} + \tilde{\Omega} \overline{\delta \psi} \tag{B.13}$$

Eqs. (B.8), (B.9), (B.12) and (B.13) are independent of any displacement or orientation variables.

Appendix C. Finite element method

By transforming all the variables in the global frame, 'a' using the rotation matrices C^{ab} and C^{aB} , electromechanically mixed statement in Eq. (34) can be further written as [26]:

$$\begin{aligned} & \int_0^l \left\{ \delta u'_a{}^T F_a + \overline{\delta \psi}'_a{}^T M_a + \overline{\delta \psi}_a{}^T [\dot{H}_a + \tilde{\omega}_a H_a + \tilde{V}_a P_a - C^{aB}(\tilde{e}_1 + \tilde{\gamma}) F_B] + \delta \phi^T Q \right. \\ & + \delta u_a{}^T (\dot{P}_a + \tilde{\omega}_a P_a) - \overline{\delta F}'_a{}^T [C^{aB}(e_1 + \gamma) - C^{ab} e_1] - \overline{\delta F}'_a{}^T u_a - \overline{\delta M}'_a{}^T \theta_a + \delta Q^T (\phi - \phi^C) \\ & - \overline{\delta M}'_a{}^T \left(\Delta + \frac{\tilde{\theta}_a}{2} + \frac{\theta_a \theta_a^T}{4} \right) C^{ab} \kappa + \overline{\delta P}'_a{}^T (V_a - v_a - \tilde{\omega}_a u_a - \dot{u}_a) \\ & \left. + \overline{\delta H}'_a{}^T \left(\Omega_B - \omega_B - C^{ba} \frac{\Delta - \tilde{\theta}_a/2}{1 + \theta_a \theta_a^T/4} \dot{\theta}_a \right) - \delta u_a{}^T f - \overline{\delta \psi}'_a{}^T m_a \right\} dx_1 \\ & = \left(\delta u_a{}^T \hat{F}_a + \overline{\delta \psi}'_a{}^T \hat{M}_a - \overline{\delta F}'_a{}^T \hat{u}_a - \overline{\delta M}'_a{}^T \hat{\theta}_a \right) \Big|_0^l \end{aligned} \tag{C.1}$$

Since the above mentioned is a mixed variational statement in its weakest form, hence the lowest order of shape functions may be used. For instance, the test function δu_a , $\overline{\delta \psi}'_a$, $\overline{\delta F}'_a$ and $\overline{\delta M}'_a$ can use linear shape functions while others will have the constant shape functions, paving the way for analytical integrations hence avoiding errors from numerical integration. Also, the Jacobian matrix for the system of nonlinear equations is solved analytically hence avoiding the errors generated by numerical differentiation. If ΔL_i is the length of two noded beam element, with 'i' as starting node while 'j' as the ending node, introducing general coordinate η such that

$$\eta = \frac{x_1 - L_i}{\Delta L_i} dx_1 = \Delta L_i d\eta \quad ()' = \frac{1}{\Delta L_i} \frac{\partial ()}{\partial \eta} \tag{C.2}$$

Here L_i is the x_1 coordinate of the starting node. While linear shape functions are introduced as follows:

$$\delta u_a = (1 - \eta) \delta u_i + \eta \delta u_j \tag{C.3}$$

$$\overline{\delta \psi}'_a = (1 - \eta) \overline{\delta \psi}'_i + \eta \overline{\delta \psi}'_j \tag{C.4}$$

$$\overline{\delta F}_a = (1 - \eta)\overline{\delta F}_i + \eta\overline{\delta F}_j \quad (C.5)$$

$$\overline{\delta M}_a = (1 - \eta)\overline{\delta M}_i + \eta\overline{\delta M}_j \quad (C.6)$$

Others including electrical variables have constant shape functions. Whole beam is divided into N elements with 'i' as the starting node while 'i + 1' is the ending node of the ith element and integrating analytically we obtain,

$$\begin{aligned} \sum_{i=1}^N \{ & \delta u_i^T f_{u_i}^- + \delta u_{i+1}^T f_{u_i}^+ + \overline{\delta \psi}_i^T f_{\psi_i}^- + \overline{\delta \psi}_{i+1}^T f_{\psi_i}^+ + \delta \phi_i^T f_{\phi_i} + \overline{\delta F}_i^T f_{F_i}^- + \overline{\delta F}_{i+1}^T f_{F_i}^+ + \overline{\delta M}_i^T f_{M_i}^- \\ & + \overline{\delta M}_{i+1}^T f_{M_i}^+ + \overline{\delta P}_i^T f_{P_i} + \overline{\delta H}_i^T f_{H_i} + \delta Q_i^T f_{Q_i} \} = \delta u_{N+1}^T \hat{F}_{N+1} + \overline{\delta \psi}_{N+1}^T \hat{M}_{N+1} - \overline{\delta F}_{N+1}^T \hat{u}_{N+1} \\ & - \overline{\delta M}_{N+1}^T \hat{\theta}_{N+1} - \delta u_1^T \hat{F}_1 - \overline{\delta \psi}_1^T \hat{M}_1 + \overline{\delta F}_1^T \hat{u}_1 + \overline{\delta M}_1^T \hat{\theta}_1 \end{aligned} \quad (C.7)$$

where (*)⁻ and (*)⁺ are the quantities evaluated at ith and i + 1th node, respectively, given by

$$f_{u_i}^\mp = \mp C^T C^{ab} F_i - \bar{f}_i^\mp + \frac{\Delta L_i}{2} \left[\tilde{\omega}_a C^T C^{ab} P_i + \overline{C^T C^{ab} P_i} \right] \quad (C.8)$$

$$f_{\psi_i}^\mp = \mp C^T C^{ab} M_i - \bar{m}_i^\mp + \frac{\Delta L_i}{2} \left[\tilde{\omega}_a C^T C^{ab} H_i + \overline{C^T C^{ab} H_i} + C^T C^{ab} (\tilde{V}_i P_i - (\tilde{\epsilon}_1 + \tilde{\gamma}_i) F_i) \right] \quad (C.9)$$

$$f_{\phi_i} = \Delta L_i Q_i \quad (C.10)$$

$$f_{M_i}^\mp = \pm \theta_i - \frac{\Delta L_i}{2} \left(\Delta + \frac{\tilde{\theta}_i}{2} + \frac{\theta_i \theta_i^T}{4} \right) C^{ab} \kappa_i \quad (C.11)$$

$$f_{F_i}^\mp = \pm u_i - \frac{\Delta L_i}{2} [C^T C^{ab} (e_1 + \gamma_i) - C^{ab} e_1] \quad (C.12)$$

$$f_{P_i} = C^T C^{ab} V_i - v_i - \tilde{\omega}_a u_i - \dot{u}_i \quad (C.13)$$

$$f_{H_i} = \Omega_i - C^{ba} C \omega_a - C^{ba} \frac{\Delta - \tilde{\theta}_i/2}{1 + \theta_i \theta_i^T/4} \dot{\theta}_i \quad (C.14)$$

$$f_{Q_i} = \Delta L_i (\phi - \phi^C) \quad (C.15)$$

where

$$\bar{f}_i^- = \int_0^1 (1 - \eta) f_a \Delta L_i d\eta \quad (C.16)$$

$$\bar{f}_i^+ = \int_0^1 \eta f_a \Delta L_i d\eta \quad (C.17)$$

$$\bar{m}_i^- = \int_0^1 (1 - \eta) m_a \Delta L_i d\eta \quad (C.18)$$

$$\bar{m}_i^+ = \int_0^1 \eta m_a \Delta L_i d\eta \quad (C.19)$$

Appendix D. Comparison of results obtained from the Abaqus and the present method

Note that the electrode numbering in Table 5 starts from the fixed end of the sensor beam.

References

- [1] C.B. Williams, R.B. Yates, Analysis of a micro-electric generator for microsystems, *Sens. Actuators A Phys.* 52 (1996) 8–11.
- [2] H.A. Sodano, D.J. Inman, G. Park, Comparison of Piezoelectric energy harvesting devices for recharging batteries, *J. Intell. Mater. Syst. Struct.* 16 (2005) 799–807.
- [3] T.H. Ng, W.H. Liao, Sensitivity analysis and energy harvesting for a self-powered piezoelectric sensor, *J. Intell. Mater. Syst. Struct.* 16 (2005) 785–797.
- [4] D.H. Robbins, J.N. Reddy, Analysis of piezoelectrically actuated beam using a layer-wise displacements theory, *Comput. Struct.* 41 (1991) 265–279.
- [5] N.H. Shen, Analysis of beams containing piezoelectric sensors and actuators, *Smart Mater. Struct.* 3 (1994) 439–447.
- [6] C.Y.K. Chee, L. Tong, G.P. Steven, A mixed model for composite beams with piezoelectric actuators and sensors, *Smart Mater. Struct.* 8 (1999) 417–432.
- [7] W. Zhou, A. Khaliq, Y. Tang, H. Ji, R.R. Selmic, Simulation and design of piezoelectric microcantilever chemical sensors, *Sens. Actuators A Phys.* 125 (2005) 69–75.
- [8] L. Ederly-Azulay, H. Abramovich, The integrity of piezo-composite beams under high cyclic electro-mechanical loads – experimental results, *Smart Mater. Struct.* 16 (2007) 1226–1238.

- [9] I.M. Bendary, M.A. Elshafei, A.M. Riad, Finite element model of smart beams with distributed piezoelectric actuators, *J. Intell. Mater. Syst. Struct.* 21 (2010) 747–758.
- [10] S.B. Beheshti-Aval, M. Lezgy-Nazargah, A coupled refined high-order global-local theory and finite element model for static electromechanical response of smart multilayered/sandwich beams, *Arch. Appl. Mech.* (2012) 1–44.
- [11] M. Adnan Elshafei, F. Alraies, Modeling and analysis of smart piezoelectric beams using simple higher order shear deformation theory, *Smart Mater. Struct.* 22 (2013).
- [12] S. Kapuria, M.Y. Yasin, Active vibration control of smart plates using directional actuation and sensing capability of piezoelectric composites, *Acta Mech.* 224 (2013) 1185–1199.
- [13] C. Maurini, J. Pouget, F. dell'Isola, Extension of the Euler-Bernoulli model of piezoelectric laminates to include 3D effects via a mixed approach, *Comput. Struct.* 84 (2006) 1438–1458.
- [14] I. Benedetti, A. Milazzo, Advanced models for smart multilayered plates based on Reissner Mixed Variational Theorem, *Compos. B Eng.* 119 (2017) 215–229.
- [15] D. Legner, J. Wackerfuß, S. Klinkel, W. Wagner, An advanced finite element formulation for piezoelectric beam structures, *Comput. Mech.* 52 (2013) 1331–1349.
- [16] S. Kapuria, N. Dhanesh, Free edge stress field in smart piezoelectric composite structures and its control: An accurate multiphysics solution, *Int. J. Solids Struct.* 126–127 (2017) 196–207.
- [17] V.L. Berdichevskii, Variational-asymptotic method of constructing a theory of shells, *J. Appl. Math. Mech.* 43 (1979) 711–736.
- [18] W. Yu, D.H. Hodges, V. Volovoi, C.E.S. Cesnik, On Timoshenko-like modeling of initially curved and twisted composite beams, *Int. J. Solids Struct.* 39 (2002) 5101–5121.
- [19] W. Yu, D.H. Hodges, Elasticity solutions versus asymptotic sectional analysis of homogeneous, isotropic, prismatic beams, *J. Appl. Mech.* 71 (2004) 15.
- [20] C. Sachdeva, S.S. Padhee, Functionally graded cylinders: Asymptotically exact analytical formulations, *Appl. Math. Model.* 54 (2018) 782–802.
- [21] S. Roy, W. Yu, D. Han, An asymptotically correct classical model for smart beams, *Int. J. Solids Struct.* 44 (2007) 8424–8439.
- [22] M.A. Neto, W. Yu, S. Roy, Two finite elements for general composite beams with piezoelectric actuators and sensors, *Finite Elem. Anal. Des.* 45 (2009) 295–304.
- [23] S. Banerjee, S. Roy, Multiphysics analysis of an asymptotically correct piezoelectric sensor under static and dynamic load, *Int. J. Solids Struct.* 92–93 (2016) 64–75.
- [24] D.A. Danielson, D.H. Hodges, Nonlinear beam kinematics by decomposition of the rotation tensor, *J. Appl. Mech.* 54 (1987) 258.
- [25] D.H. Hodges, A mixed variational formulation based on exact intrinsic equations for dynamics of moving beams, *Int. J. Solids Struct.* 26 (1990) 1253–1273.
- [26] W. Yu, M. Blair, GEBT: a general-purpose nonlinear analysis tool for composite beams, *Compos. Struct.* 94 (2012) 2677–2689.
- [27] P.M.G. Bashir Asdaque, S. Roy, Geometrically exact beam actuator model, in: *Proceedings of the Twenty-fifth International Conference on Composites or Nano Engineering (ICCE-25)*, Rome, 2017 July 16–22.
- [28] C. Sachdeva, M. Gupta, D.H. Hodges, Modeling of initially curved and twisted smart beams using intrinsic equations, *Int. J. Solids Struct.* 0 (2017) 1–11.
- [29] O. Kursu, A. Kruusing, M. Pudas, T. Rahkonen, Piezoelectric bimorph charge mode force sensor, *Sens. Actuators, A Phys.* 153 (2009) 42–49.
- [30] O.Z. Olszewski, R. Houlihan, R. O'Keefe, M. O'Neill, F. Waldron, A. Mathewson, N. Jackson, A MEMS silicon-based piezoelectric AC current sensor, *Proc. Eng.* 87 (2014) 1457–1460.
- [31] R. Ly, M. Rguiti, S. D'Astorg, A. Hajjaji, C. Courtois, A. Leriche, Modeling and characterization of piezoelectric cantilever bending sensor for energy harvesting, *Sens. Actuators A Phys.* 168 (2011) 95–100.
- [32] L. Zhou, J. Sun, X.J. Zheng, S.F. Deng, J.H. Zhao, S.T. Peng, Y. Zhang, X.Y. Wang, H.B. Cheng, A model for the energy harvesting performance of shear mode piezoelectric cantilever, *Sens. Actuators A Phys.* 179 (2012) 185–192.
- [33] I. Payo, J.M. Hale, Sensitivity analysis of piezoelectric paint sensors made up of PZT ceramic powder and water-based acrylic polymer, *Sens. Actuators A Phys.* 168 (2011) 77–89.
- [34] H. Han, J. Kim, Active muscle stiffness sensor based on piezoelectric resonance for muscle contraction estimation, *Sens. Actuators A Phys.* 194 (2013) 212–219.
- [35] D. Buxi, J.M. Redouté, M.R. Yuce, Frequency sensing of medical signals using low-voltage piezoelectric sensors, *Sens. Actuators A Phys.* 220 (2014) 373–381.
- [36] H. Kalantarian, N. Alshurafa, T. Le, M. Sarrafzadeh, Monitoring eating habits using a piezoelectric sensor-based necklace, *Comput. Biol. Med.* 58 (2015) 46–55.
- [37] D.H. Hodges, *Nonlinear Composite Beam Theory*, American Institute of Aeronautics and Astronautics, Reston, Virginia, 2006.
- [38] S. Banerjee, S. Roy, A dimensionally reduced order piezoelectric energy harvester model, *Energy* (2018).
- [39] D.A. Saravanos, P.R. Heyliger, Coupled layerwise analysis of composite beams with embedded piezoelectric sensors and actuators, *J. Intell. Mater. Syst. Struct.* 6 (1995) 350–363.